# In vitro study of membrane remodeling and curvature sensing at the micrometric scale by budding yeast septins

Alexandre Beber

Sorbonne Université

Ecole doctorale Physique en Île-de-France (ED564)

*Institut Curie, Physico-chimie (UMR168)*

*Equipe « Membranes and cellular functions » sous la direction de Patricia Bassereau*

# In vitro study of membrane remodeling and curvature sensing at the micrometric scale by budding yeast septins

Par Alexandre Beber

Thèse de doctorat de Biophysique

Dirigée par Stéphanie Mangenot & Aurélie Bertin

Présentée et soutenue publiquement le 23 novembre 2018

Devant un jury composé de :

| | |
|---|---|
| Manouk Abkarian – chargé de recherche | Rapporteur |
| Gijsje Koenderink – professeure | Rapporteure |
| Sophie Cribier – professeure | Examinatrice |
| Antoine Jegou – chargé de recherche | Examinateur |
| Julien Heuvingh – maître de conférence | Invité |

# *Dédicace*

*A ma deuxième famille, les Fourtets.*

*Serge et Elizbaeth pour m'avoir toujours accueilli à bras ouverts dans votre demeure,*

*Et Allister pour avoir toujours été là pour moi.*

# Acknowlegments

I would like to express my gratitude to all the members of the jury for accepting to take the time to evaluate my work.

I would like to thank all the members of my team, starting with Patricia for always being so insightful. Feng, Ajay for all the advices on experimental procedures and the rest of the team for making my stay here so pleasant.

I would also like to thank Manuela Nania and João Cabral for not only providing us with the patterned substrates but also hosting me at your lab and showing me your fabrication process, Virginie Bazin and Michael Trichet at the IBPS for the SEM pictures. Hervé for the theoretical model he developed.

Manouk, I thank you for allowing me to discover the world of research and putting me in contact with Patricia.

But most importantly, I would like to thank Stéphanie and Aurélie for being amazing PIs by providing me constant support and care. You have taught me so much and I don’t think I could have gotten better supervision.

This work has been supported by:





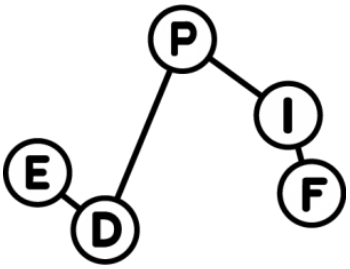



# Table of contents

## Table of abreviations

AD: Alzheimer's disease

cdc: Cell division cycle (also budding yeast septins)

DAG: Diacylglycerol

EM: Electron microscopy

ER: Endoplasmic reticulum

FCS: Fluorescence correlation spectroscopy

FRAP: Fluorescence recovery after photobleaching

GUV: Giant unilamellar vesicle

LUV: Large unilamellar vesicle

MAP: Microtubule-associated protein

MLV: Multilamellar vesicle

MVV: Multivesicular vesicle

NOA : Norland optics adhesive

PD: Parkinson's disease

PDMS: Polydimethylsiloxane

PEG: Polyethylene glycol

PI(4,5)P2: Phosphatidylinositol-4,5-bisphosphate

PI: Phosphatidylinositol

PLC: Phospholipase C

SEM: Scanning electron microscopy

SEPT: Human septins

shs1: Seventh homolog of septin (also budding yeast septin)

SLB: Supported lipid bilayer

SUV: Small unilamellar vesicle

TIRF: Total internal reflection fluorescence

ts: Temperature-sensitive mutant

UVO: Ultraviolet ozonolysis

# Table of figures

## 1.1 1 Introduction

## 1.2 In vivo studies of septins

### 1.2.1 History of the discovery of septins

Septins were first discovered in 1966 by Leland H. Hartwell in the budding yeast *Saccharomyces cerevisiae* when he began isolating a large amount of temperature-sensitive mutants (ts)[1]. Specifically, two mutants affecting cell wall formation during cell division, ts310 and ts471 (later cdc10 and cdc12) were described as displaying elongated cells and unable to achieve cell separation (Figure 1).

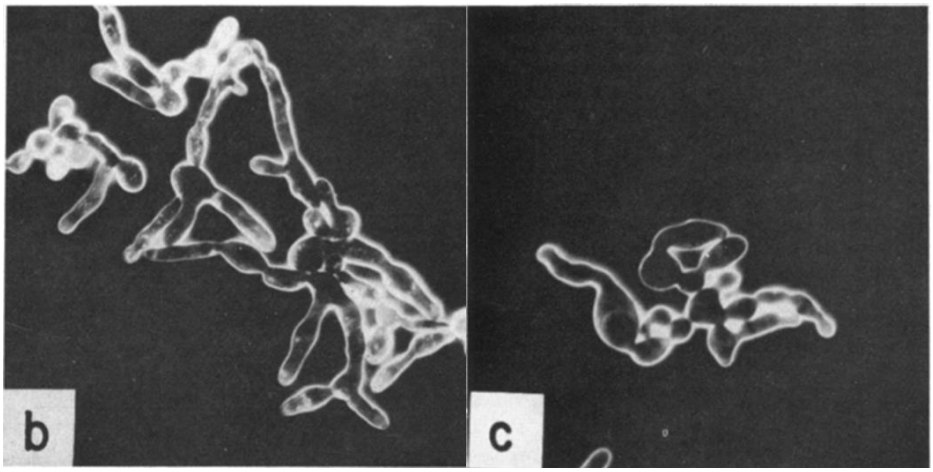


***Figure 1 – temperature-sensitive mutants***

*Dark field phase contrast images of budding yeast cells showing the ts471 mutation (b) and ts310 (c). The cells are elongated and do not undergo cell separation[1].*

Later on, several other genes responsible for the successful completion of cell division were identified and denominated cdc[2,3] (**C**ell **D**ivision **C**ycle). Distinctively, the temperature-sensitive mutants of cdc3, cdc10, cdc11, cdc12 were categorized “cytokinesis defective”. These mutants would display elongated polynucleid phenotypes and a decrease in glusulase-promoted neck scission. Taken together, these findings clearly indicated that these four genes were responsible for the successful proceedings of cytokinesis. Additionally, electron microscopy (EM) studies revealed the presence of filamentous structures formed by these 4 gene products[4,5]. In wild type cells, parallel striations can be found at the bud neck of dividing cells that are about 10 nm in diameter.

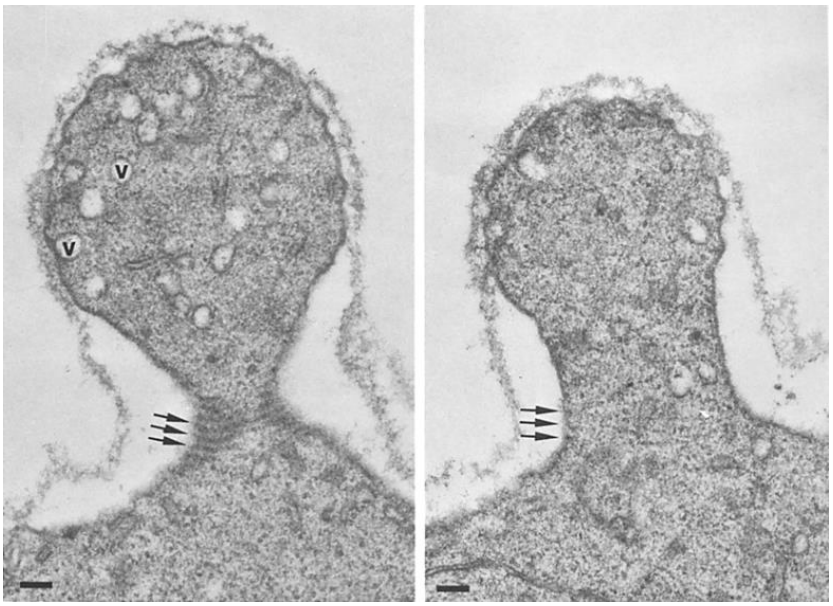


***Figure 2 – Bud neck filaments***

*EM images of 10 nm thick filaments at the bud neck of dividing cells. Left image shows a longitudinal view and right image a transverse view. Scale bare are 0.1 µm*[4]*.*

These filaments were absent in temperature-sensitive mutants of cdc3, cdc10, cdc11 and cdc12. Ten years later, an immunofluorescence study revealed the presence of the cdc11 protein at the bud neck[6] and its presence was lost with the temperature-sensitive mutation of any of the four cdc proteins. Taken together, it became clear that cdc3, cdc10, cdc11 and cdc12 form a complex assembling into these filaments. These findings were confirmed by immunoEM[7], showing the presence of these proteins at the bud neck and exhibiting their close association with the plasma membrane. Sequencing and time lapse microscopy of cdc3 from the budding to the scission of the cells[8] finally sealed the deal to confirm that these proteins as being part of one group and being, in fact, the proteins that constitute the filaments at the bud neck. This family was later named the "septin" family of proteins for their presence throughout the septation of the plasma membrane during cytokinesis. After their discovery in yeast, several homologous proteins have been discovered in almost all eukaryotes including the mammalian septin family sept1-14[9,10,11] and in drosophila (the Pnut/Dsep1-4 family )[12,13] but are absent in plants, except in algae[10]. While different species express a different number of septin genes (two in *Caenorhabditis elegans*, seven in *Saccharomyces cerevisiae* and thirteen in humans), they all share a common basic template as well as some properties and similarities ranging from their primary structure to their supramolecular organization and functions *in vivo*[14]. Specifically, a close comparison between the yeast septins cdc3, cdc10, cdc11, cdc12 and the human septin subgroups sept2, sept6, sept7, sept9 can be made. The primary sequence of septins is conserved from one septin gene to another in the same organism but also between species[10]. A detailed description of the structure of septins will be described in section 1.3.1 but it is worth

mentioning that septins can bind to each other to form non-polar hetero-oligomers. These oligomers can then assemble into filaments. Septins have also the ability to interact with the plasma membrane through a specific affinity for a phospholipid: Phosphatidylinositol-4,5-bisphosphate (PI(4,5)P2). While septins have first been described in the budding yeast for their role in cytokinesis, their polymorphism in organization and subunit numbers allow them to fulfill a wide range of cell function that will be described in the next section.

### 1.2.2 Cellular functions of septins

#### *1.2.2.1 Cell division*

Since their discovery, the functions of septins have been well documented during the cell division cycle in *S. cerevisae*. In budding yeast, several key proteins including septins accumulate (G1 phase) at the future budding site to create the bud (G2). The genetic material is then replicated (anaphase) and cells are separated (telophase)[15]. During all this process, septins are present and are subjected to a lot of rearrangements (Figure 3). The specificity of these rearrangements will be discussed in section 1.2.5.2 but it is clear that septins serve a major role during cell division as septin deficient cells cannot achieve scission and end up elongated and polynucleated (Figure 1).

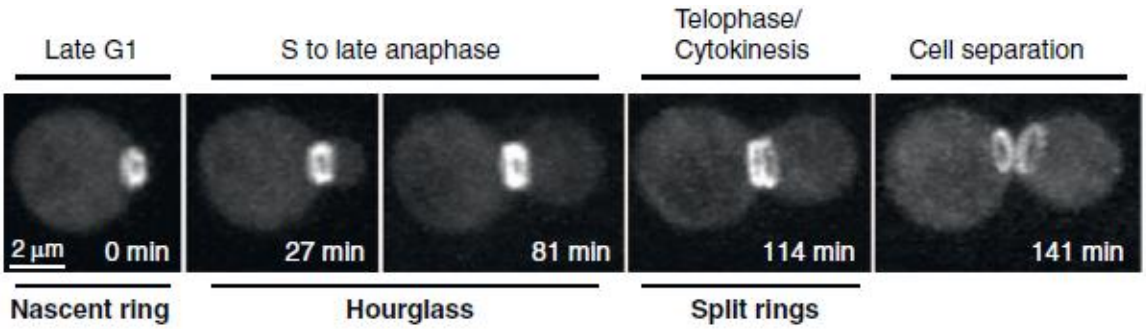


***Figure 3 – Septins in budding yeast throughout the cell division***

*3D time lapse spinning disk microscopy images of budding yeast septins (with cdc3-GFP) during the different steps of the cellular division. Septins accumulate at the onset of budding (late G1) and are present until cell separation).*[16]

In the earlier stages of cell division, a large body of concentrated microtubules called the mitotic spindle is responsible and essential for the separation of the genetic material into two identical sets. There, septins located at the bud neck are able to guide microtubule plus-ends that will drag the mitotic spindle to the budding site[17]. Several proteins necessary for the selection of the budding site and its morphogenesis are also recruited in a septin-dependent

manner. For instance, septin are responsible for the recruitment of Bud4[18,19], an anilin-related protein.

Following the emergence of the bud and the growth of the daughter cell, the narrowing of the connection between the two cells (also called the neck) later leads to abscission and cell separation. This contraction is driven by an acto-myosin ring composed of actin and myosin II (Myo1) which is recruited after bud emergence in a septin-dependent manner[20,21]. Myosin II is not essential for cytokinesis. While septins are responsible for the recruitment of myosin II to the budding site, they do not interact directly with the acto-myosin ring which is located between the two septin rings that split from the hourglass structure[22] (Figure 4).

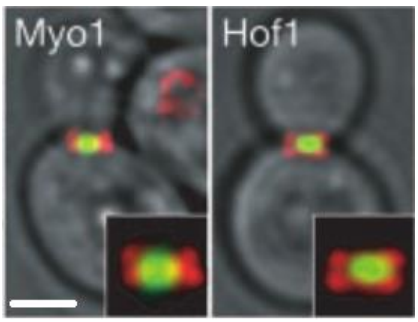


***Figure 4 – Localization of the septin and actomyosin rings during cytokines***

*Confocal microscopy images of dividing budding yeast cells during cytokinesis showing CFP-cdc3 (red) and GFP-Myo1 or GFP-Hof1 (green)[22]. Scale bar is 2 µm.*[22]

In the absence of myosin II, other cytokinetics players such as Hof1 and Cyk3 that also localize with the acto-myosin ring are able to trigger cytokinesis[20,23,24]. This indicates that several pathways are possible to achieve cytokinesis but in both cases, these pathways are septin-dependent. Finally, during cytokinesis, septins are involved in the confinement of several membrane-remodeling related proteins that ensure the scission of the neck by contributing to the formation of a diffusion barrier to membrane proteins. This function will be explained in details in section 1.2.2.6. Septins are responsible for the recruitment of numerous proteins involved in cell division, either by directly interacting with essential factors or by recruiting other crucial elements.

In other model systems, septins also have a role during cell division and embryogenesis although their role has not been as thoroughly analyzed as in yeast. In *Drosophila*, three septins: Pnut, Sep1 and Sep2 are located at the cleavage furrows during cytokinesis[12,25].

While yeast septins act as a recruitment scaffold for a lot of proteins involved in cell division, here they appear downstream in the assembly pathway of the cytokinetic components. Together with anillin, they appear to have a more mechanical role and their presence is not necessary to the recruitment of key components of cytokinesis[26,27]. *Drosophila* lacking the Pnut gene perish at an early stage during gastrulation[28] and show polynucleated cells (pointing to a defect in cytokinesis). Other genome-wide screens showed that Pnut and Sep2 knockdowns resulted in cytokinetic defects but other proteins involved in cell division showed a much more pronounced phenotype with a highest defects count[29,30]. In both mutants, the asymmetry is lost and the embryo divides symmetrically (Figure 5). It seems that in *Drosophila*, the role of septins during cytokinesis is to ensure (along with anillin) the contraction of the acto-myosin ring.

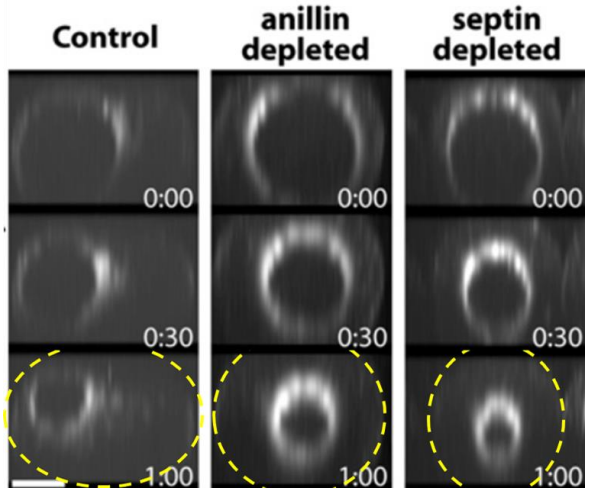


***Figure 5 – Drosophila anillin and septin mutants***

*Confocal images of Drosophila embryos in wild type, anillin and septin depleted mutants at the beginning, after 30 minutes and after 1 hour of furrow ingression. Here, myosin II is tagged with GFP. The yellow dotted shapes denote the plasma membrane of the cells. Scale bar is 10 µm.*[27]

In human cells, septins are also involved in cell division and are required for mitosis[31,32] but their specific function is still unclear. However, some evidences suggest that septins are necessary to the localization of proteins at the mother-bud junction, like the centromere-associated protein E (CENP-E)[33]. The overexpression or depletion of SEPT9 are also responsible for defects in cytokinesis in HeLa cells by preventing the abscission of the midbody[34]. Several studies also show their implication in the establishment of a diffusion

barrier for membrane proteins which this will be discussed in section 1.2.2.6. Septins are also necessary for the recruitment of the ESCRT-III machinery during cytokinesis[35].

Overall, the functions of septins during cell division have been well studied in yeast but remain still unclear in animal cells. Although some evidences indicate that they can serve similar functions as compared with yeast, several studies showed that they can be nonessential for cytokinesis. The functions of septins are not exclusive to cell division and they serve many other purposes.

#### *1.2.2.2 Neuro-morphogenesis*

In multicellular organisms, septins have a role in neurogenesis where they seem to play a role in the generation of new axons and dendrites. Perhaps the most striking example is in the worm *C. elegans* where the only two septin genes unc-59 and unc-61 are expressed in embryonic and larval neurons but are absent in fully developed organisms[36]. Both septin mutants showed mispositioned axons, defective guidance, migration and occasional discontinuities in the ventral cord. These morphologies are all reported in

Figure 6. In the neurons of the embryonic nervous system of *Drosophila*[25], the Pnut-Sep1-Sep2 complex interacts with seven-in-absentia, a gene necessary for neuronal fate in the eye[12]. In *Drosophila* neurons, the function of septins is not restricted to development like in *C. elegans* given they are present throughout all stages[12].

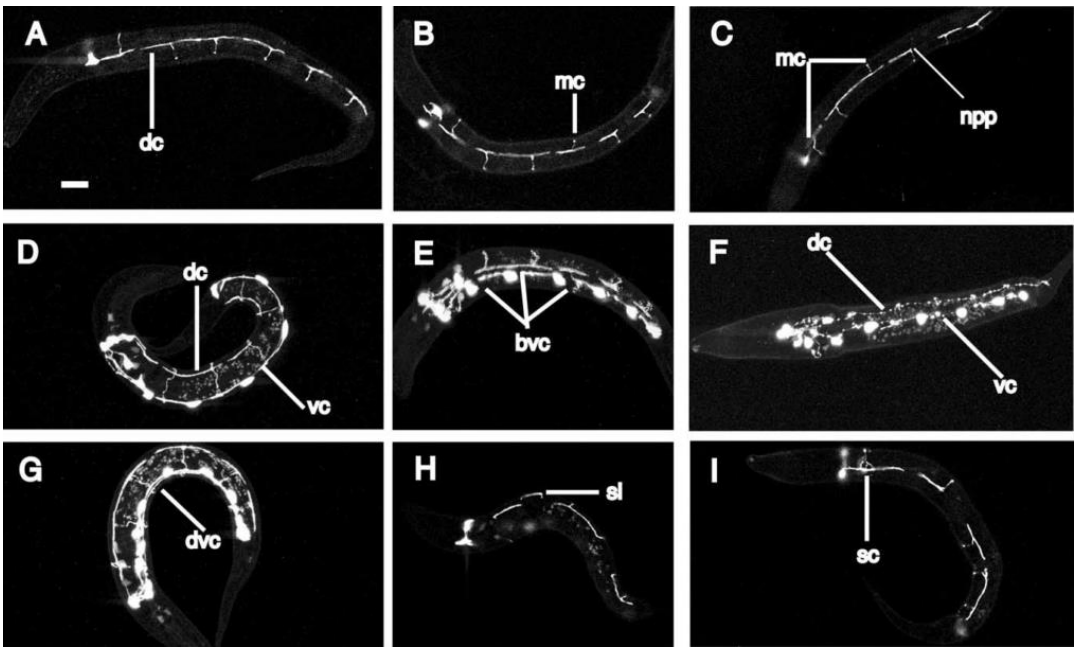


***Figure 6 – Neuronal defects in C. elegans induced by septin mutations***

*Confocal images of Punc-47GFP revealing GABA neurons in newly hatched larvae. (A) WT larva, dc indicates the dorsal cord. (B) Misoriented commissure (mc) in an unc-59(e261) mutant. (C) Misoriented commissures (mc) and failure of the generation of a commissure towards the posterior (npp) in an unc-59(e1005) mutant. (D) Projection of a WT larva, dc indicates the dorsal cord and vc the ventral cord. (E) unc-59(e261) mutant, bvc indicates discontinuities in the ventral cord. (F) unc-61(e228) mutant showing punctate cords. (G) unc-*

*61(e228) mutant showing a defasciculation of the ventral cord (dvc). (H) Process in unc-59(e1005) mutant running in the sublateral (sl), rather than dorsal cord. (I) Split commissure (sc) in unc-61(n3169) mutant.*[36]

In mammals, septins seem to play a key role in the morphogenesis of neurons and dendritic spines as shown by several studies[37–39]. Specifically, SEPT7 is located at the base of dendritic protrusion and dendritic branching points in hippocampal neurons and its overexpression leads to an enhanced dendritic branching and density of dendritic protrusions. Conversely, a knockdown is responsible for a reduced branching and the formation of immature dendrites[38] (Figure 7). At these branching points, SEPT7 also colocalizes and coimmunoprecipitates with SEPT5 and SEPT11 which supports the idea of the existence of the SEPT5/7/11 complex[37]. Furthermore, a loss of SEPT7 in mature neurons results in the same phenotype. The depletion of SEPT7 induces reduced branching and shorter dendrites in growing neurones, highlighting the role of SEPT7 not only in neuronal development but also the regulation of dendritic protrusion at later stages.

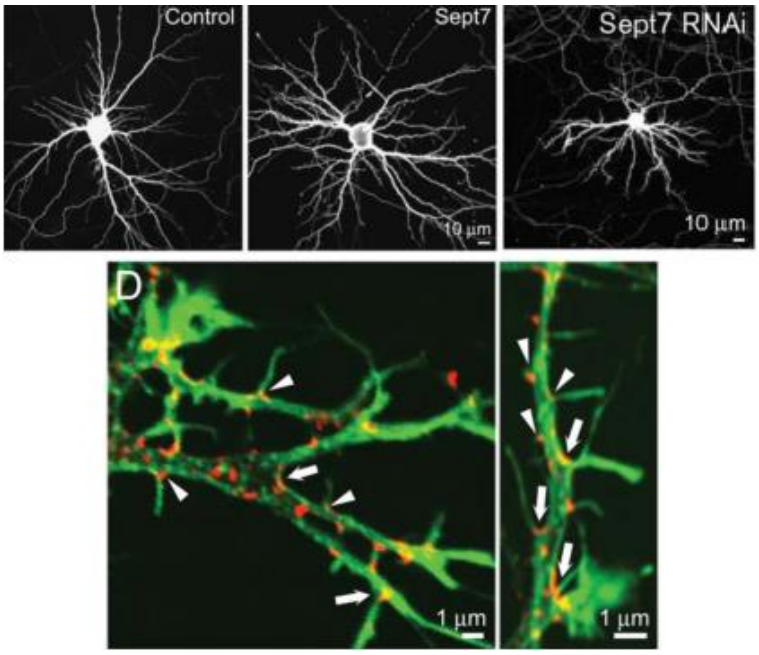


***Figure 7 – Septins in human hippocampal neurons***

*EGFP transfected wild type hippocampal neuron (DIV13) (top left), overexpression of SEPT 7 (top middle) and knockdown of SEPT7 mediated by RNA interference (top right). Immunostaining of SEPT7 (red) and F-actin (phalloidin staining, green), in young hippocampal neurons (DIV7)*[38]*.*

Another study focusing on SEPT6 in similar neurons demonstrated comparable results[40]. SEPT6 form clustered rings of about 0.5 µm in diameter that are co-localized with microtubules. Like SEPT7, these septin structures are localized at branching points of dendrites and it was shown that SEPT2/6/7 are able to form a complex *in vivo*[41]. Similarly, RNA interference of SEPT6 reduced the number of branching and dendritic length. SEPT11 is present in GABAergic synapses accumulated at the collar of dendritic spines and its knockdown leads to the same type of defects[42]. Evidences have revealed two distinct roles of septins in the regulation of dendritic morphology. Septins participate in the establishment of a diffusion barrier at the neck of dendritic protrusion[43] and they interact with other cytoskeletal partners that are responsible for a regular morphology[39,44,45]. These specific functions will be discussed in more details in section 1.2.2.6 and 1.2.3 respectively.

Overall, it seems that septins play a role in the morphogenesis of neurons at different levels but this function is restricted to a specific set of septins only (SEPT7, 6 and 11). They also have a significant role in maintaining the morphology of protrusions called cilia.

#### *1.2.2.3 Ciliogenesis*

Cilia are hair-like structure 1-10 µm in length and 1 µm in diameter holding nine pairs of microtubules arranged into a circle and two additional central microtubules [46]. They act as sensory organs for the cell. They are known to be involved in a lot of different diseases called ciliopathies[47]. In vertebrates, there are two types of cilia: motile cilia and non-motile cilia that are deprived of the two central microtubules also called primary cilia (Figure 8). In humans, cilia are typically found inside the ear, the intestine and at the end of spermatozoids.

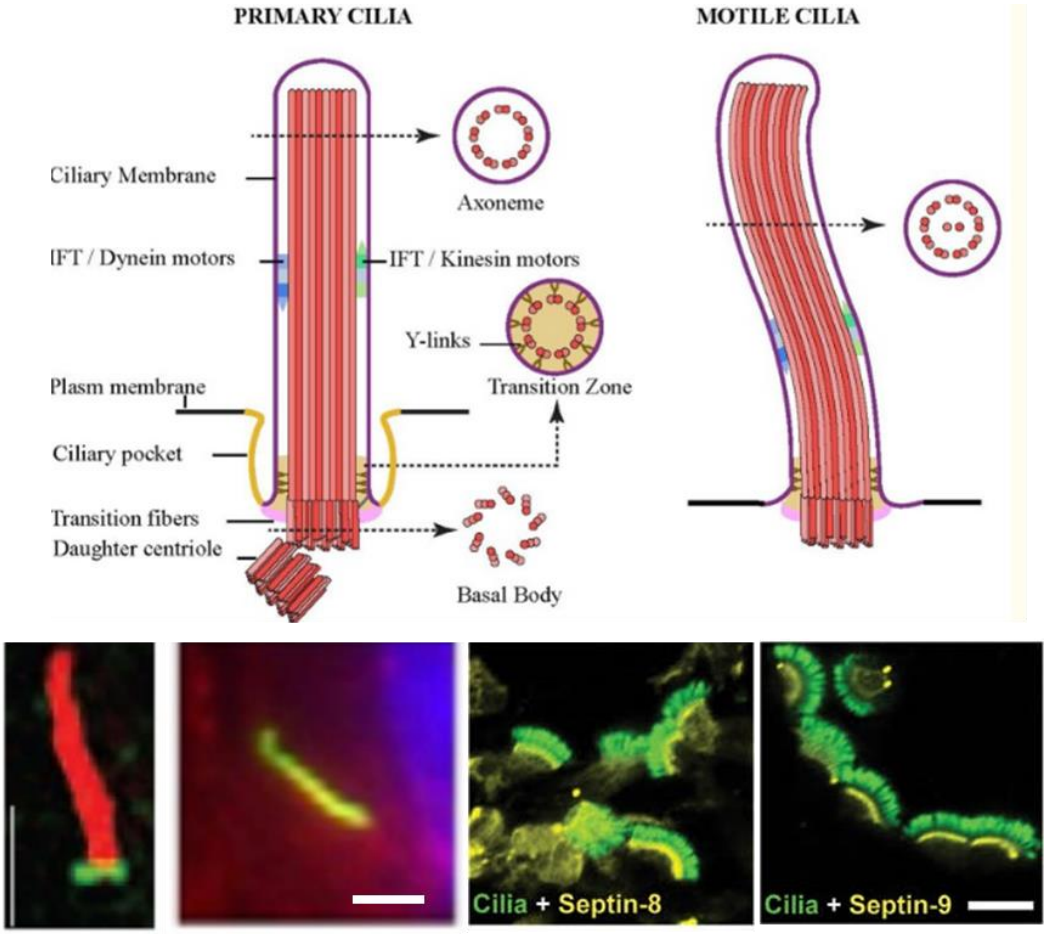


***Figure 8 – Cilia and septin localization***

*Schematic description of the primari and motile cilia (top). Different localization of septins inside cilial cells (bottom row): SEPT2 (green) and acetylated tubulin (red) in the primary cilia of IMCD3 cells*[48] *(left, scale bar is 5 µm). Acetylated tubulin (green) and SEPT7 (red) in the primary cilia of RPE1 cells*[49] *(second left, scale bar is 5 µm). Acetylated tubulin (green) and SEPT8 or SEPT9 in motile cilia of mouse tracheal epithelial cells*[50] *(right, scale bar is 20 µm).*

The location of septins inside cilial cells can vary. For instance in mammalians cells, SEPT2 can be found as part of a ring at the base of primary cilia[48] and SEPT7 along the axoneme[49]. A more systematic immunofluorescence study of epithelial cells revealed that both SEPT2 and SEPT7 are found in the whole cilia, with SEPT4 and SEPT6 at the ciliary base, SEPT9 and SEPT11 in the axoneme, SEPT8 and SEPT9 in ciliary sub-compartments[50]. This suggests the existence of two different septin complexes (SEPT2/4/6/7 and SEPT2/7/9/11). In Xenopus embryos, during ciliogenesis, septins have a role in establishing the planar cell polarity (PCP) pathway[51]. A knockdown of the ortholog of the cytoplasmic protein Fritz responsible for the control of the PCP in *Drosophila*[52] has been shown to induce defective tissue gastrulation and a failure of axis elongation, similarly to SEPT7 and SEPT2 mutants (Figure 9).

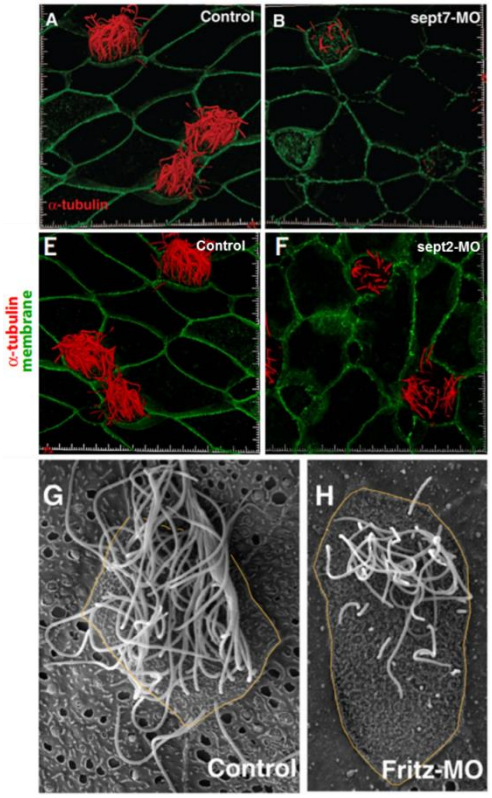


***Figure 9 – Septin and fritz-mediated ciliogenesis in Xenopus***

*Confocal and SEM images of multiciliated cells in wild type Xenopus embryos (A,E,G) and SEPT7 mutant (B), SEPT2 mutant (F) and Fritz mutant (H). The mutants show similar phenotypes*[51]*.*

The SEPT7 gene of cilia in the pronephric tubule of the zebrafish embryo revealed similar results[53]. The Knockdown of SEPT7 also gave phenotypes associated with ciliopathies linked to a malfunction of the glomerular filtration barrier resulting of a reduced cilia activity caused by reduced cilia length, increased tubule diameter, disorganization and misorientation of basal bodies (Figure 10).

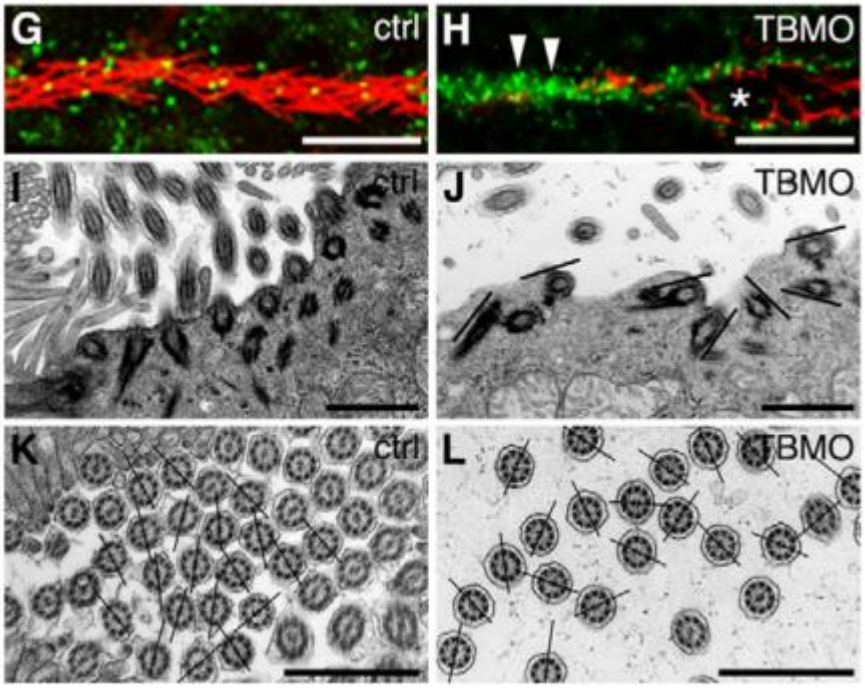


***Figure 10 – Septin-mediated ciliogenesis in Zebrafish***

*Confocal images of cilia in the pronephric tubule in wild type (G) and SEPT7 mutant (H) acetylated α-tubulin is marked in red (axoneme) and γ-tubulin in green (basal body), scale bars are 20 µm. TEM images of the same region in wild type cells (J,K) and SEPT7 mutants (J,L). Mutants show disorganized and misoriented cilia basal bodies. Scale bars are 1 µm.*[53]

Two other functions of septins during ciliogenesis include a diffusion barrier role for key components in ciliogenesis (for more details, see section 1.2.2.6) and microtubule signaling and stabilization since they are known to play a role in cilium formation[54] (for more details, see section 1.2.2.3).

### 1.2.2.4 Spermatogenesis

The spermatozoid is a tapdole-looking cell composed of a head region where the nucleus is located, a neck region composed of dense fibers and mitochondria and a large motile cilium called the flagellum for navigation. In humans, the spermatozoa are about 60 µm long but their size can vary in other species and can measure up to 5 cm in *Drosophila*.

Septins have been identified in the annulus of the spermatozoid which is located at the base of the flagellum[55]. More specifically, SEPT4[56] and SEPT12[57] have been found to form a ring at the annulus (Figure 11). A more recent study showed that three more septins, SEPT2 SEPT6 and SEPT7 were involved in the formation of two distinct septin octamers composed of SEPT2/6/7/12 or SEPT4/6/7/12. SEPT12 is crucial to maintain the stability of these septin complexes and subsequently, the formation of the ring at the annulus. Some septins are located exclusively at the annulus (SEPT4 and SEPT7) while others can be found at different regions inside the neck but always concentrated at either ends (Figure 11). SEPT14 also might play a role in spermatogenesis given this septin is only express in the testis[58].

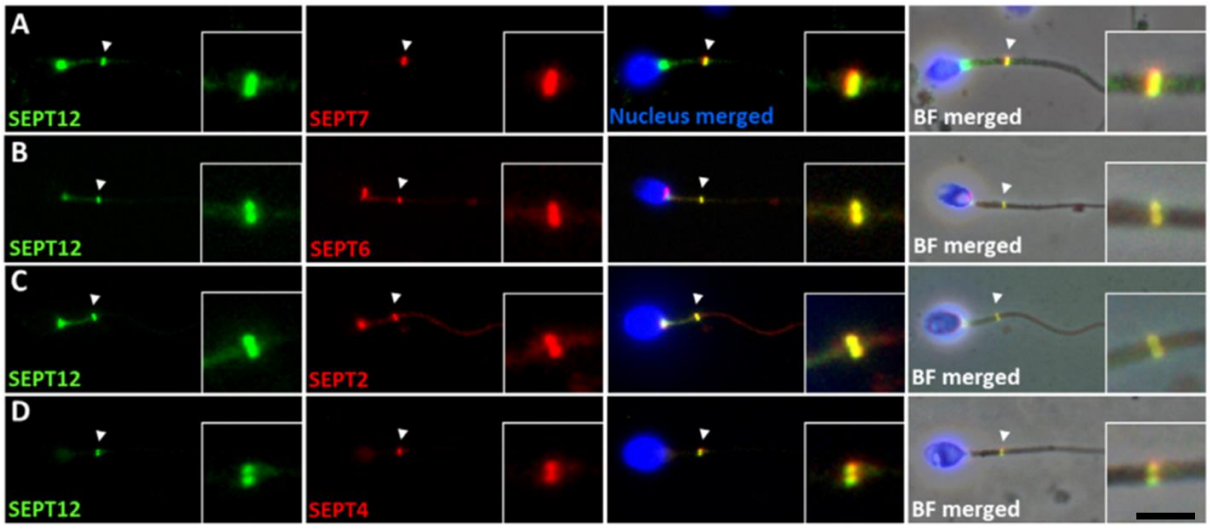


***Figure 11 – Septin localization in human sperm cells***

*Confocal images of immunofluorescence staining of different septin genes in four separate human sperm cells. The first column shows SEPT12 staining in green, the second column shows either SEPT7 (A), SEPT6 (B), SEPT2 (C) or SEPT4 (D) staining in red, the third column shows DAPI staining of the nucleus merged with the two previous channel and the fourth one all the channels merges with a bright field image. Scale bar is 5 µm*[59].

Considering the fact that the sperm flagellum is a very long cilium, it would be reasonable to stipulate that the septin functions are similar. Two separates studies showed that mice sperm cells with a SEPT4 mutation lacked the septin ring at the annulus and showed abnormal tail rigidity with a sharp bend at the beginning of the flagellum, resulting in the inability to swim (Figure 12)[56,60].

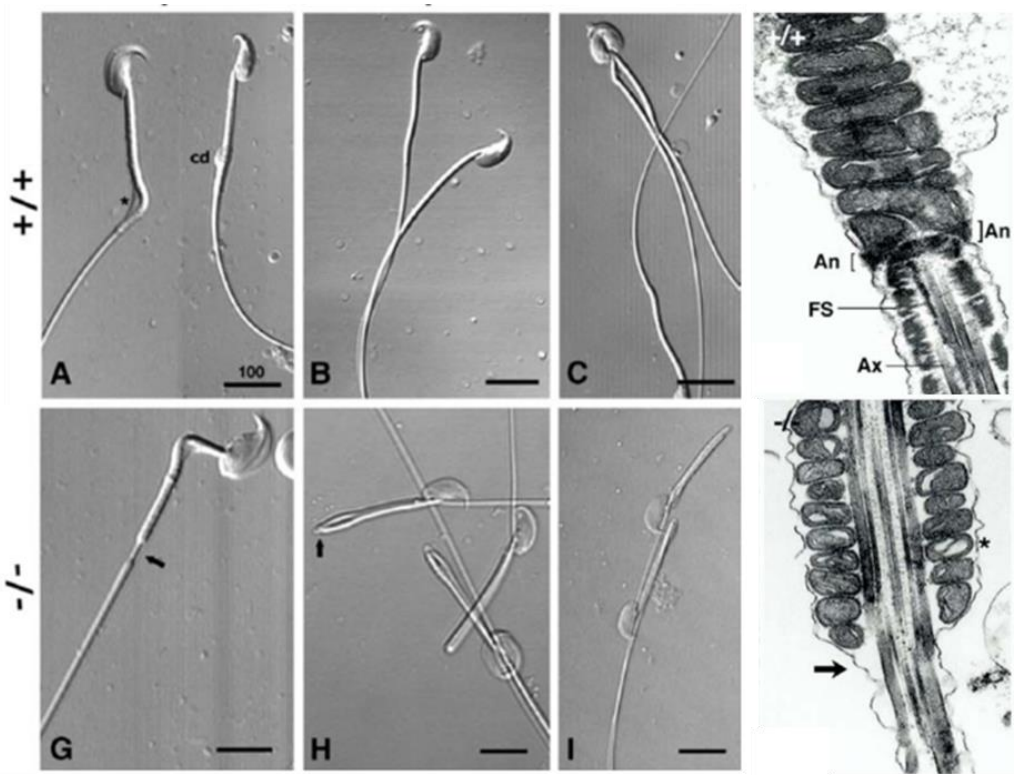


***Figure 12 – SEPT4 mutant in mice sperm cells***

*Bright field microscope images of mice sperm cells at three different increasing maturation stages (caput first column, corpus second column, cauda third column) in wild type cells (A-C) and SEPT4 mutants (G-I). Electron microscopy images of the annulus region in cauda wild type mice sperm cells (top right) and SEPT4 mutant, lacking the ring and showing disorganized mitochondria. An denotes the annulus, FS the fibrous sheet and Ax the axoneme. Magnification is x20,000.*[56]

The first study[56] focused on the mechanical aspect of this abnormal phenotype. The second study[60] focused on the effect of a septin mutant during different maturation stages of mice sperm, indicating a role of SEPT4 only in spermatogenesis especially at later development stages (Figure 12).

Other studies revealed a variety of findings. While mice SEPT6 mutants did not display any pathological phenotype[61], SEPT12$^{+/-}$ mutants showed an even more pronounced effect than SEPT4 mutants[62]. In SEPT4 mutants, the infertility was caused by the lack of sperm motility and an assisted fertilization of oocytes would lead to normal development. For SEPT12 mutants, however, in addition to the lack of motility, fertilized oocytes were not able to develop past the morula stage (a very early embryonic stage), supporting the hypothesis of DNA damage[63]. Taken together, these studies show that septins are involved in spermiogenesis at different levels, whether it is by regulating microtubule dynamics indirectly or via the action of a diffusion barrier. We have described how septins are involved in processes that include drastic membrane remodeling like morphogenesis. In the next part, we will focus on other membrane remodeling processes that are not necessarily related to morphogenesis.

#### *1.2.2.5 Membrane remodeling*

In cells, the membrane shape can be modulated by several processes. Direct reshaping can occur by applying forces locally (binding of naturally curved protein domains such as the BAR domain family[64]) or more globally (cytoskeletal cortex). Cell shape can also be regulated by the addition or removal of membrane by processes known as endo- and exocytosis. The regulation of osmolarity can also lead to changes in the cell volume by either filtering small ions via pores through the membrane or changing the cytoplasmic solution of active substances (by increasing or decreasing the concentration of free amino acids for instance). Finally, the generation of protrusion-like filopodia or lamellopodia (that differ in their internal composition and function) is a key membrane remodeling process that is vital for the survival of the cell.

Septins are involved in membrane remodeling processes through their interaction with key membrane remodeling elements such as the soluble N-ethylmaleimide-sensitive fusion proteins (SNARE)[65]. For instance, SEPT5 (formerly known as CDCrel-1) immunoprecipitates with syntaxin, a protein responsible of the formation of SNARE complexes, by directly interacting with SNARE domains[66]. SEPT5 regulates vesicle secretion by inhibiting the activity of syntaxin, and by directly binding to syntaxin when it is part of the SNARE complex [67]. Other septins also have regulatory roles in the mediation of endo/exocytotic complexes. For example, the mouse SEPT4 physically associates with α-synuclein, a transporter of dopamine and other presynaptic molecules which aggregation results in the formation of Lewy bodies in Parkinson disease[68]. SEPT2 was also shown to promote membrane fusion with endo- and lysosomes, stimulating the fluid-phase cargo traffic in macropinosomes[69]. It

also directly interacts with several other component of the exocytosis machinery such as Munc18-1 (a protein that facilitates SNARE assembly), SNAP-25 and its chaperone Hsc70 (responsible for membrane fusion), promoting exocytosis at different levels[70].

It was shown that septins were also directly involved in membrane remodeling. Perhaps the most striking evidence is an *in vitro* study of the tubulation of giant unilamellar vesicle (GUVs) by porcine and human septins where protrusions are induced on GUVs after their interaction with septins (more details in section 1.3.4). Whether this phenomenon is biologically relevant or not is still an open question but several *in vivo* studies point to a positive answer. For instance, at the onset of blebbing (a detachment of the plasma membrane from the underlying cytoskeleton) septins were shown to have a role in the retraction of the free plasma membrane in human T cells[71]. The blebs were induced by tuning the outward hydrostatic pressure. They were rapidly resorbed in healthy cells. In SEPT7 knockdown cells, however, the blebs persisted and accumulated with cell migration on the surface. Excessive blebbing also revealed that septins rapidly accumulate at the sites of blebbing before retraction (Figure 13).

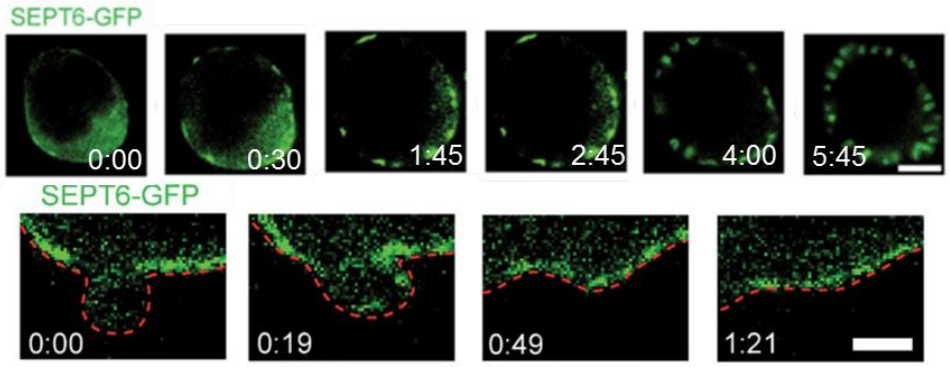


***Figure 13 – Septin localization during blebbing and membrane retraction***

*Time lapse confocal images of SEPT-GFP in T cell where blebbing has been induced by shifting the cells in a 100 mOsm hypotonic media. The red dotted line outlines the plasma membrane (bottom). Scale bars are 10 µm (top) and 2µm (bottom).*[71]

Another example of direct involvement of septins in membrane shaping can be seen in their implication with myelin in mice neurons[72]. Myelin is a mostly lipidic substance wrapped around axons necessary for their protection and the propagation of neuronal signals. SEPT2, 4, 7 and 8 have been found to form filaments binding both sides of the membrane lying longitudinally along the axon axis (Figure 14).

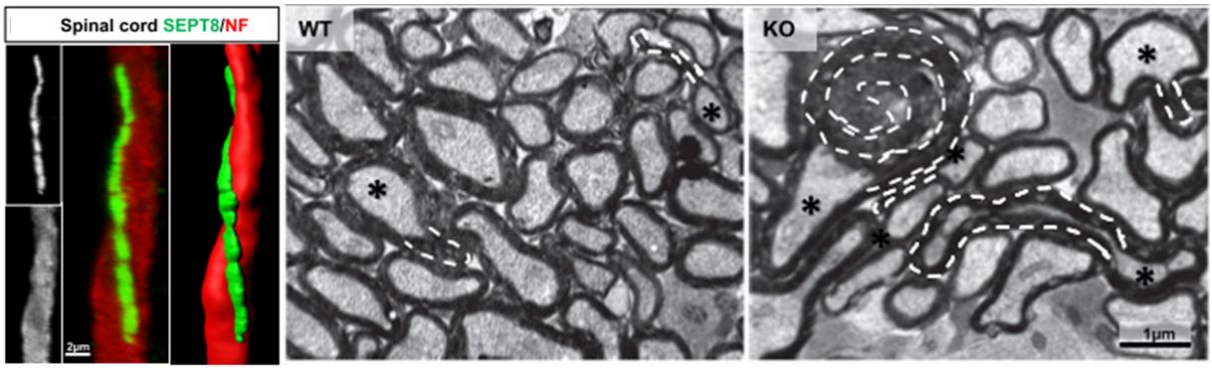


***Figure 14 – SEPT8 localization and myelin outfolding in neurons***

*Confocal images of immunofluorescence signal of SEPT8 (green) and neurofilament (red) in a mouse brain (left). Electron microscopy images of cross sections of wild type mouse optic nerve (middle) and SEPT8 knockdown mutants (right). The dotted white lines highlight the myelin outfoldings and the asterisk the corresponding neurons.*[72]

In SEPT8 mutants, long myelin tubulations caused a depletion of adhesive forces with adaxonal membrane. Those so-called “myelin outfoldings” appeared at much higher frequency and intensity in mutants, indicating a mechanistic role of septins in maintaining the integrity of myelin (Figure 14). PI(4,5)P2 depletion showed similar phenotypes[73]. Knowing the high affinity of septins with PI(4,5)P2, this suggests that PI(4,5)P2 might be required to recruit septins on adaxonal membrane. In tumor cells, SEPT2 and SEPT7 are also essential in the formation of microtentacles by acting as a structural link between the membrane and other components[74]. In *S. cerevisae,* they have a more mechanistical role by providing the stress wall resistance necessary for proper prospore membrane biogenesis[75].

To summarize, septins can be involved in membrane remodelling processes by either interaction with endo-, exocytotic pathways or the cyotoskeleton. They can also have a more direct role by directly reshaping the membrane or offering local stability and modulating its mechanics. This last point will be a central point of focus of this study. The next part will describe another category of septin functions found widely in cells: their role in establishing a diffusion barrier for membrane proteins.

### 1.2.2.6 Diffusion barriers

One of the major functions of septins is to be involved in lateral diffusion barriers for membrane proteins. This is the case in *S. cerevisae* for Ist2, a protein that recruits the ER at the division site during cell division[76]. In wild type cells this membrane protein can freely diffuse in the plasma membrane of the bud where it is restricted (Figure 15.A).

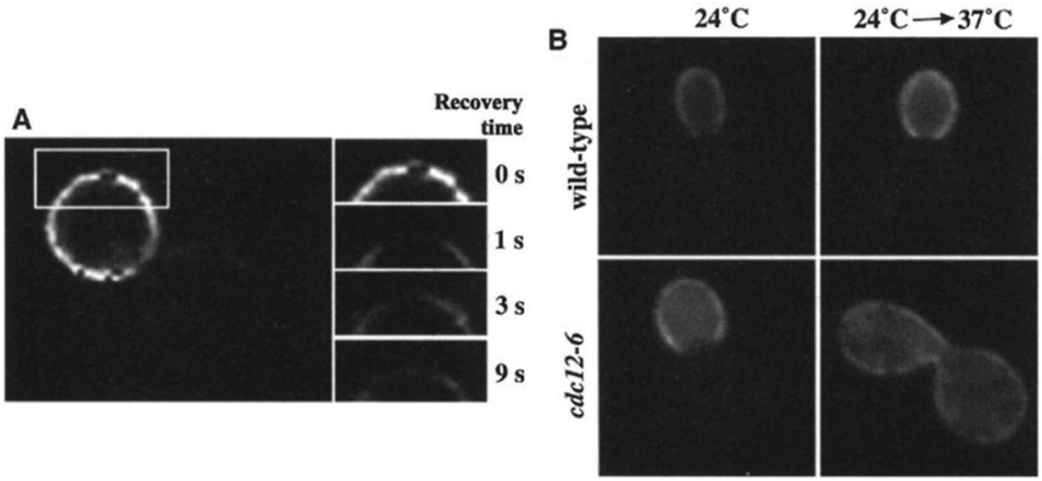


***Figure 15 – Septin-based diffusion barrier in budding yeast***

*FRAP of GFP-Ist2 in budding yeast (A) and activation of temperature-sensitive cdc12 mutants by heating compared to wild type cells (B).*[76]

However, the disruption of the septin network induced the loss of the diffusion barrier (and consequently, the loss of Ist2 confinement in the bud (Figure 15.B). This was confirmed for other *S cerevisae.* membrane-associated proteins like Spa2, Sec3, Sec5 (exocytosis and morphogenesis factor) and Myo2 in another study where compartmentalization was lost after mutation of cdc12 and deletion of swe1 (a division checkpoint able to recover the compartmentalization)[77]. In the ER, it was shown that septins have a role, upstream of sphingolipids, in establishing a diffusion barrier[78]. So far, no clear evidence of a septin-based diffusion barrier has been found in mammalian cells during division but they can serve this purpose in other processes. In mouse sperm cell for instance, where septins have been found to locate at the end of the annulus. SEPT4 mutants lack this ring. A study showed that basigin, a protein restricted to the tail region in early stages of development but relocated at the midpiece during maturation, failed to be compartmentalized in SEPT4 mutants, further supporting the importance of septins in maintaining diffusion barriers (Figure 16)[79].

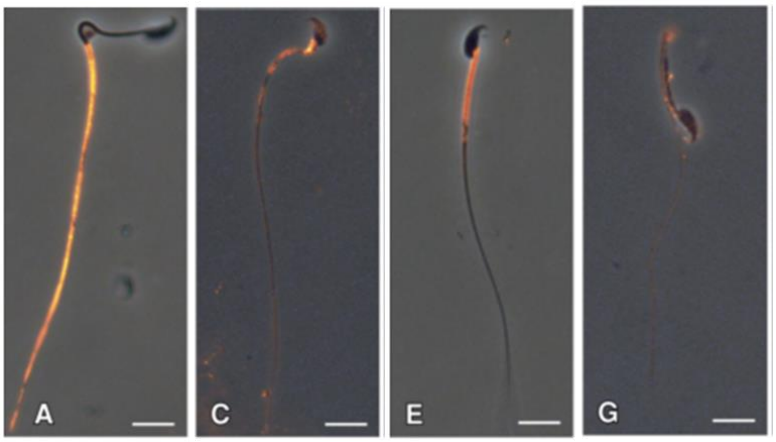


***Figure 16 – Basigin localization in SEPT4 sperm cell mutants.***

*Immunofluoresence of basigin in sperm cells during the caput stage in wild type (A) and SEPT4 mutants (C) and during the cauda in wild type (E) and SEPT4 mutants (G). Scale bars are 10 µm.*[79]

Additionally, in mammals, four cilium-restricted proteins (Htr6, Sstr3, PKHD1 and Smo) also localize in the primary cilium in a septin-dependent manner[48]. Finally, reports for septin-based diffusion barriers have also been found in neurons at the base of dendrites[43]. The septin ring is thus necessary for the establishment of a diffusion barrier. Although the mechanism of formation of this barrier is still unclear, it certainly involves other interaction partners. Their more notable partners are the members of the cytoskeleton, namely actin and microtubules.

### 1.2.3 Interaction with the cytoskeleton

Septins are involved in a lot of different cellular functions and their function is related to other filaments members of the cytoskeleton, namely F-actin and microtubules. Their implication with them is so close that they have been branded “the fourth element of the cytoskeleton”[80].

### 1.2.3.1 Actin

SEPT2 was the first septin identified to interact with actin-based structures in stress fibers at focal adhesion [31]. Further studies on SEPT2 showed that septin filaments organize linearly along actin filaments and can form cytoplasmic rings 0.5 µm in diameter in mouse cells when not associated with actin[81]. When stabilized F-actin was incubated with recombinant mouse SEPT2/6/7 complexes, partial colocalization was observed but no actin organization. The addition of actin bundling proteins (α-actinin, fascin and filamin) triggered F-actin filaments showed bundling but no septin colocalization. However when stabilized F-actin, SEPT2/6/7 and anillin where mixed together, actin was able to form long thick bundles and colocalize with septins indicating that anillin, an actin adaptor protein, is able to recruit septins to actin to be organized into bundles. A more recent study showed that the human complex SEPT2/6/7 as well as the *Drosophila* Sep1-Sep2-Pnut complex could directly bind to actin filament and bundle them, creating loops (Figure 17)[82].

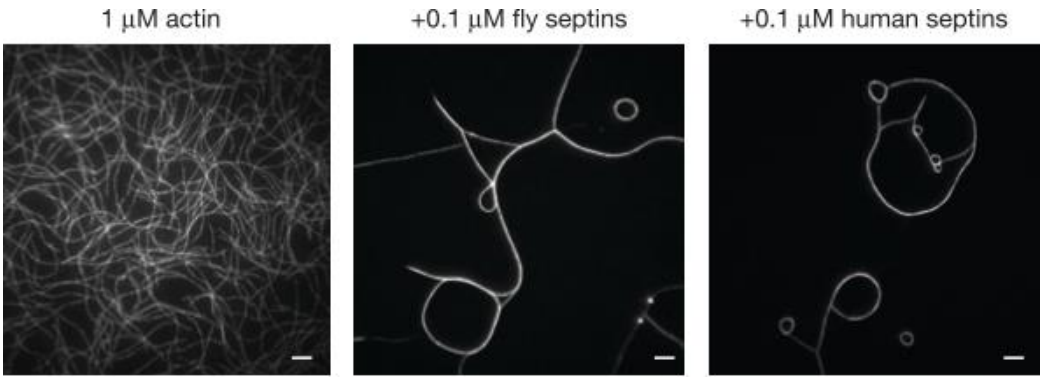


***Figure 17 – Actin bundling by fly and human septins***

*TIRF images of Axlega488-tagged F-actin co-polymerized with Drosophila Sep1-Sep2-Pnut and human SEPT2/6/7. Scale bars are 5 µm.*

The integrity of these actin bundles *in vivo* highly depends on the septin network. Indeed, a truncated version of the polybasic region of SEPT2 can induce a loss of actin bundles while the addition of the truncated GTPase domain preserved them[83]. Similar results were found in *Drosophila* embryo where deletion of the Pnut septin gene would give disorganized actin rings with non-circular shape and dispersed diameter. *In vitro* assays showed that human and *Drosophila* septins alone were enough to organize actin into bundles[82]. Overexpression of actin in *S. cerevisae* revealed the presence of an actin belt during cell division, distinct from the acto-myosin ring that initiates the neck constriction[84]. In breast cancer cells, SEPT9_i2 (a SEPT9 isoform) has been identified for having a major role in regulating the actin network[85]. In these cells, SEPT9_i2 and SEPT9 depletion has been observed in other

type of cancer cells[86,87]. In neurons from chicken embryos, different septins seem to interact with actin to promote the formation of axonal filopodia[88]. SEPT6 colocalized with actin patches responsible for the nucleation of filopodia and SEPT7 was found on the sides with little overlap with actin patches (Figure 18). Further *in vitro* experiments confirmed that recombinant SEPT6 binds to actin filaments and the number of branching points increases in the presence of Arp2/3.

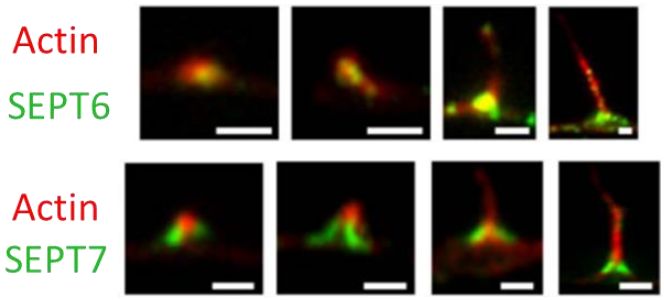


***Figure 18 – Septins in a nucleated axonal filopodia***

*Fluorescence images of actin (red) and SEPT6/7 (green) in a nucleating filopodia in chick embryo cells. Scale bars are 1 µm.*[88]

Other examples where septins are responsible for the organization of branched actin networks can be found in lamellipodia of squamous carcinoma and melanoma cells where SEPT1/5 form a complex and their inhibition leads to an inability for the cells to spread[89]. Phagosome formation requires the activity of the branched actin network. The stability pf phagosomes is impaired with with SEPT2 and SEPT11 mutations [90]. Another study revealed that SEPT9 is able to bind F-actin via three different modes[91]. Two of these three modes overlap with myosin II and cofilin binding sites involving the basic domain region of SEPT9 but not its GTP binding domain. Additionally, SEPT9 is able to decrease the rate of depolymerization induced by cofilin or myosin II[92], suggesting a competition between them at two specific binding site. The activity of myosin II is essential for the establishment of the acto-myosin ring and its later contraction. Overall, septin are able to organize actin filaments at different level and their function has severe implication in the associated cellular functions.

#### *1.2.3.2 Microtubules*

The interaction of septins with microtubules was less documented until recently. They have been shown to localize with specific subsets of microtubules like perinuclear, ciliary or golgi-associated microtubules in epithelial cells[49,50,93] and spindle poles, central spindle or the midbody microtubules in dividing cells[32,94–97]. It has also been revealed that SEPT9 can

directly bind to microtubules and mediate their assembly (Figure 19)[98]. SEPT9 possess a motif that is commonly found in microtubule associated proteins (MAP) composed of Lys/Arg-Arg/x-x-Asp/Glu[99] and located inside its basic N-terminal region. It allows septins to directly bind to the acidic C-terminal tail of β-tubulin and bundle microtubules *in vitro.*

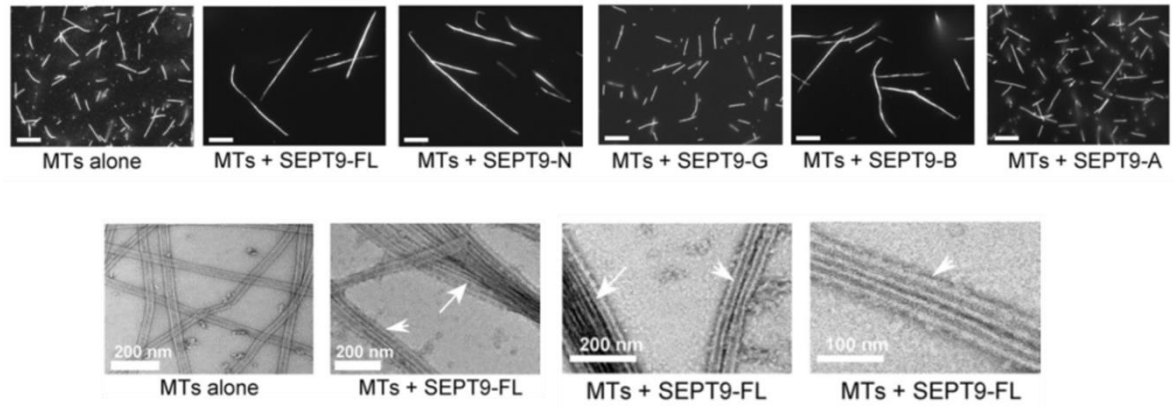


***Figure 19 – In vitro assays of SEPT9 and microtubules***

*Confocal images of microtubules in solution with full length (FL) and truncated (N,G,B,A) versions of SEPT9 (top row, scale bars are 10 μm). Electron microscopy images of microtubules and full length SEPT9. (bottom row).*[98]

By using SEPT9_i4, an isoform that is deprived of the MAP motif, it was shown that the MAP domain is necessary for microtubule-septin interaction. SEPT7 also has a role in guiding microtubules in axonal filopodia and in promoting their nucleation[88]. Several studies seem to support the later hypothesis. For example HDAC6, an enzyme responsible for the acetylation of α-tubulin, has been revealed to function in a septin dependent manner[39]. Microtubule deacetylation induces more stable filaments and an improved dendrite growth. Another example of post translational modification of microtubule targeting mediated by septins is found in epithelial cells. SEPT2 colocalizes with polyglutamylated microtubules during Golgi to plasma membrane transport of vesicles[100]. The mechanism of action of septins seem to be to act as an antagonizing molecule to MAP4, a microtubule-associated protein that has an inhibitory role in vesicle trafficking. *In vitro*, MAP4 is able to bundle microtubules but their interaction is stopped when adding recombinant SEPT2/6/7 showing again the competitive binding of the two proteins to microtubules[101]. SEPT9 has also been reported to interfere with microtubule motors, namely the kinesin KIF17 and inhibit its binding to a specific cargo, mLin-10 without affecting its motility[45]. Since kinesins are able to modulate microtubule dynamics, it is possible that this could have an indirect effect on microtubule stability[102].

In the two previous parts, we have seen that septins are involved in numerous cellular functions where they are often essential. Their roles are very versatile and involve different septin complexes in mammals. In the next part, we will see how these phenotypes translate into diseases in humans.

### 1.2.4 Septins in pathologies

#### *1.2.4.1 Cancer*

The first examples of septins being involved in cancer were discovered in the early 2000s in three independent studies all implicating the SEPT9 gene[86,87,103]. Following these findings, SEPT9 and its various isoforms have been identified to be overexpressed in numerous tumor types, with ovarian and breast cancer being prevalent[104]. SEPT4 has also been found to be down-regulated in acute lymphoblastic leukemia[105] and altered levels of its expression are found in kidney, brain, skin, prostate, colorectal, and lung tumours[106]. Their presence in some cancers is so predominant than two diagnosis tests based on the measurement of a SEPT4 isoform in urine and the methylation of the SEPT9 gene in the blood have been developed to screen for urothelial and colorectal cancers respectively[107,108]. Although septin expression is enhanced in a large number of cancers, few of them arise from mutations and mutations often concern oligomerization domains such as the GTP-binding domain and the G-G and N-C interfaces[109].

Regarding their role in cytokinesis, septin mislocalization might be responsible for the creation of an environment favorable for cancer development[110]. Overexpression of SEPT9 promotes cancer development by reducing ubiquitin-related degradation[111]. SEPT2 and the receptor tyrosine kinase ErbB2 (an important target for cancer treatment) are also overexpressed in gastric cancer cells[112]. Considering their close interactions *in vivo* with actin filament and their role in organizing and stabilizing them (especially with stress fibers), it has been hypothesized that septins might contribute to metastatic cancer cell migration and invasion. Indeed, several septin knockdowns (SEPT9 and SEPT7) were directly linked to defective motility in epi- and endothelial cells[113,114]. Similarly, MCF7 breast cancer cells over-express the SEPT9_i4 isoform and disturbs the activity of SEPT9 which increases neoplasia and cell motility[115]. A crucial step towards the nucleation of the metastatic process in many cancers is the transformation of epithelial cells to a mesenchymal state, with the apparition of many actin-dependent pseudopodia. Knockdown of SEPT9 in 6 different cancer cell lines resulted in pseudopodia retraction and subsequently decreases motility[116]. A possible pathway of septin regulation has been linked to extracellular matrix[117]. In addition to enhance

cancer cell proliferation and migration through the actin cytoskeleton, septins have been revealed to interfere with several microtubule-associated cancer treatments. Several chemotherapy drugs have been engineered to specifically target microtubules and tamper with its division-associated functions[118]. For instance, SEPT10 (which is a regulator of microtubule stability) overexpression has been linked to an increase in sensitivity to paclitaxel (also known as taxol, an anticancer agent that blocks cell mitosis and kill tumor cells) while overexpression had the opposite effect and low level of SEPT10 where found in drug-resistant tumors[119]. Conversely, the overexpression of SEPT9 and its isoform SEPT9_i4 are responsible for taxol and 2-methoxyestradiol resistance in several cancer lines[120–122]. Finally, some evidences have revealed that septin might play a role in tumor suppression. The SEPT4_i2 isoform (also called ARTS) was shown to be essential in activating caspase 3 and induce apoptosis[123]. These findings led to the development of an ARTS-based therapy for cancer stem cells[124].

#### *1.2.4.2 Neurological disorders*

As we saw in section 1.2.2.2, septins are responsible for several neurological functions and especially neuro-morphogenesis. Septins were first linked to Parkinson disease (PD) through the findings that SEPT5 can bind to Parkin (an ubiquitin ligase which mutation can cause a form of autosomal recessive juvenile PD) both *in vitro* and in cultured cell[125]. Furthermore, the overexpression of SEPT5 in rat neurons[126] resulted in cytotoxicity and reduced motor function. Another septin, SEPT4, has been associated with PD and found in α-synuclein-positive cytoplasmic inclusion (pathological hallmarks of neurogenerative diseases including PD and Lewy bodies dementia) consistently while other septins (SEPT2,5,6,7,8) were not[127]. Modified level of septin expression can also be found in Alzeimer disease (AD) with lower SEPT2,3 levels and higher SEPT5 levels[128]. SEPT2 and SEPT4 also localize in neurofibrillary plaques and tangles, structure associated with AD[129]. SEPT2 and SEPT4 can self-assemble of into large amyloid filaments[130,131]. This provides some evidence that a misregulated aggregation of septin might be a mechanism by which AD-related structures are generated. Overall, the role of septins in neurodegenerative disease is not well understood but their altered expression in several disorders and their close relation to endo-exocytotic complexes described in section 1.2.2.5 leads to believe that they serve a function and deserve to be more studied in the context of neuropathologies.

### 1.2.4.3 Bacterial infection

Septins are involved in bacterial infection at different level. For instance during *Listeria monocytogenes* and *Shigella* invasion[132].

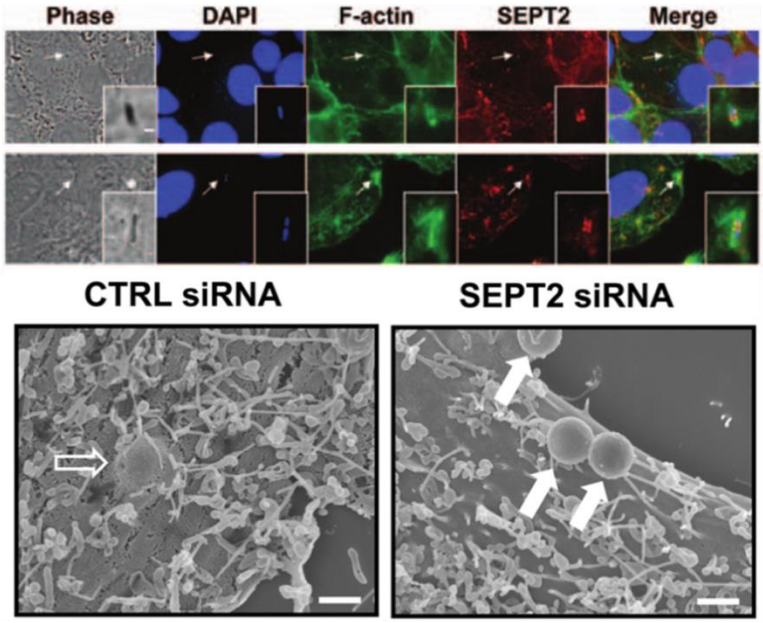


***Figure 20 – Septin-mediated bacterial invasion***

*Confocal images of Listeria. monocytogenes (top) and Shigella (middle) invasion in JEG-3 cells. Scale bar is 1 µm. SEM images of InlB coated beads in wild type cells (bottom left) and SEPT2 mutants (bottom right). Scale bars are 1 µm.*[133]

By using beads coated with InlB (the bacterial receptor necessary to nucleate bacterial invasion), it was shown that SEPT2 is necessary for the internalization of bacteria (Figure 20). The colocalization of actin and septins at the entry site suggests a conjoint function. Another possible septin-regulated mechanism during invasion might be the formation of macropinosomes (cellular extensions whose function is primarly the uptake of solutes in the extracellular environment) since they have recently been shown to have a role in *Listeria* invasion[134] and given septins are involved in their maturation[69]. Additionally to their role in bacterial invasion, septins and actin are also recruited to the membrane of internalized bacteria by forming a cage-like structure of alternative septin and actin rings (Figure 21)[135].

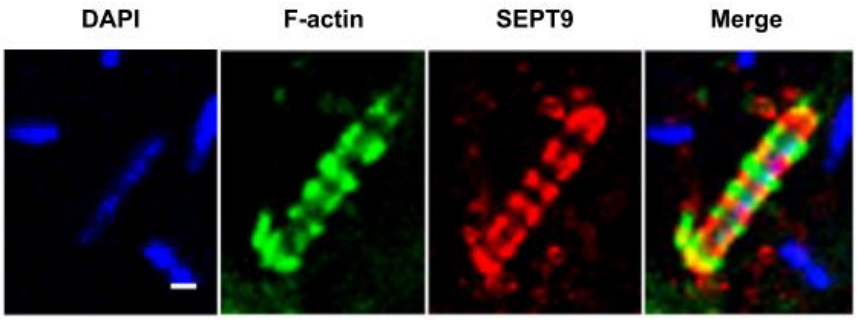


***Figure 21 – Bacterial septin and actin cage***

*Immunofluorescence images of HeLa cells infected with Shigella flexneri. Scale bar is 1µm.*[135]

The entrapment of bacteria by these septin-actin structures resulted in the loss of their actin tail (actin from the host cell utilized by the bacteria to navigate) and subsequently a loss of motility while non-entrapped cells were free. Moreover, trapped bacteria were later targeted for autophagy, revealing a defense mechanism in which septins and actin impede the motility of invading cells so they can be easily targeted. Examples of septin cages have been found in other species and seem to be a conserved defense mechanism against actin-tailed bacteria[136,137]. Finally, *Chlamydia trachomatis* utilizes the actin cytoskeleton as well as intermediary filaments to generate large vacuoles during replication[138]. A study showed that septins were involved in stabilizing the actin cytoskeleton to promote the generation of those vacuoles by forming rings around the inclusion site[139].A systematic depletion of either SEPT9 or SEPT2/6/7 greatly reduced the number of extrusion in infected HeLa cells. It seems that septins are involved in bacterial-related functions at different levels. One common feature found in these functions is the apparition of a ring-like structure induced by septins. The existence of this ring seems to have an essential biological function. In the following part, we will see how septin dynamically assemble into rings *in vivo* and describes other types of septin supramolecular structures.

### 1.2.5 Septin organization *in situ*

#### *1.2.5.1 Observing septins in situ*

To achieve their diverse functions, septins need to be able to oligomerize and later polymerize to assemble into supramolecular structures[140]. Septin filament formation shows some plasticity and not every subunits are essential to generate functional filaments. For instance in budding yeast where septins form the hetero-octamer cdc11-cdc12-cdc3-cdc10-cdc10-cdc3-cdc12-cdc11, cells lacking either cdc10 or cdc11 are still able to perform cytokinesis because the two other subunits (cdc3 and cdc12) are able to mutate, dimerize and form higher order structures. However, mutation of the alpha helix at the NC interface of cdc11 that normally allows filament formation ultimately leads to cell death. These findings support the evidence that filamentous septins (as opposed to monomeric septins) in yeast are necessary to perform their functions, especially during cell division.

Several studies showed similar findings in mammalian cells. For instance, in sperm cells, a deletion of SEPT12 or SEPT4 leads to an absence of the septin ring localized at the base of the tail and consequently a loss of septin function while mutations of the other septins SEPT2,6,7 does not impair septin functions[59]

Given these findings, the observation of septin filaments at a high resolution has sparked a lot of interests during the recent years. The first example of septin filament visualization *in vivo* dates back to 1976 where they were identified in budding yeast as 10 nm thick filaments spaced regularly by 28 nm[4]. It was later revealed, in numerous *in vitro* studies, that these filaments were actually pairs of septin filaments and that single septin filaments are 4 nm in diameter. Because of this, septin filament visualization requires higher resolution that the diffraction limit imposed by light microscopy. Therefore, electron microscopy and super resolution microscopy remain the best tools to achieve that. So far, two studies using two different types of electron microscopy were able to reveal septin filament organization in the budding yeast. Using electron tomography of freeze-substituted cells, a study revealed the presence of different orientation of filaments at the neck during cell division (Figure 22)[141].

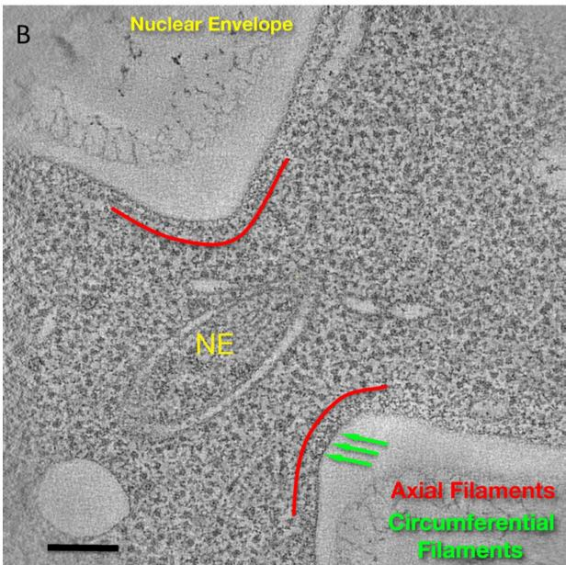


***Figure 22 – Electron tomogram of dividing S. cerevisae***

*Electron tomograph of a dividing S. cerevisae cell showing axial and circumferential filaments at the bud neck. Scale bar is 100 nm.*[141]

This method allows for the visualization of cell architecture by reconstructing slices at different depth in 3D models of cells[142]. The other method is based on scanning electron microscopy (SEM) and requires a metallization process (for a more detailed SEM introduction, see section 2.6.3). The inner morphology of cells has to be uncovered. Because of this, spheroplasts are used. A spheroplast is a cell where the plasma membrane has been removed. The remaining cell material is subsequently deposited on a plate, similar to a dissection. Spatial distribution of septins subunits in yeast and mammalian cells within filaments was resolved thanks to super resolution fluorescence microscopy[143,144]. Although the specific arrangement of these particular complexes was already known, the development of these techniques opens the door for much advancement in resolving the organization of other septin filaments. Finally, polarized fluorescence microscopy can also be used to identify septin structures *in vivo* and have an insight on their orientation[145] but the resolution remains lower than electron microscopy, even though super resolution microscopy is a growing and very promising field. Recently, super resolution in live model animals has permitted the observation of septin activity in zebrafish[146]. In the following section, we will see how these methods have been used to describe with accuracy the organization of septin filaments in a precise example: budding yeast division.

### 1.2.5.2 Septin organization during S. cerevisae division

Cell division is a very dynamic process in which septins, among other proteins, are essential[16]. In budding yeast, septins are recruited at the budding site and form a primitive ring that evolves into an hourglass structure as they accumulate. This hourglass later splits into two rings during cytokinesis, with each ring being located on each side of the scission site (Figure 23).

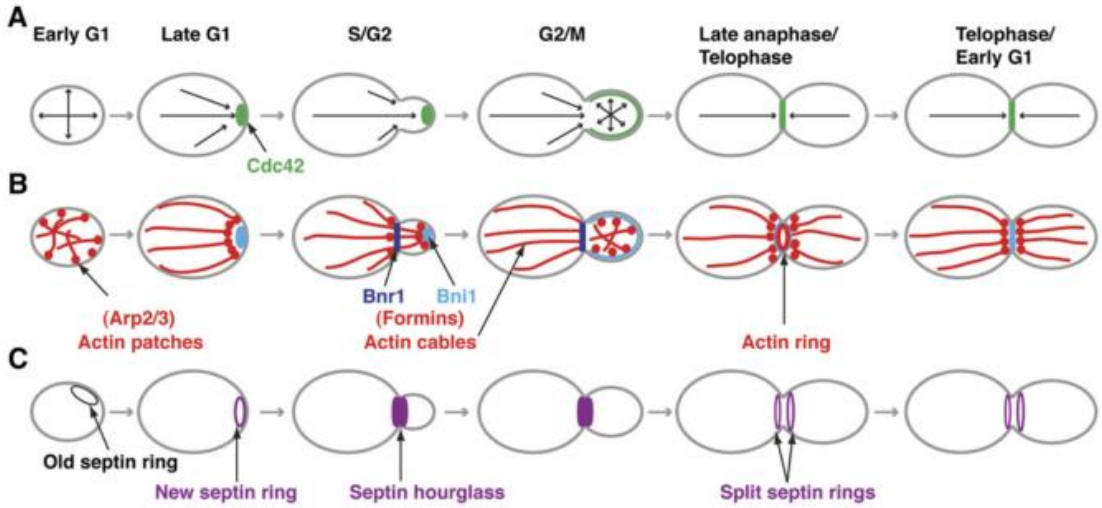


***Figure 23 – Septin organization during cell division***

*Cartoon of the organization of Cdc42 (A), actin (B) and septin (C) in S. cerevisae division.*[16]

These dynamic changes require a lot of reorganization of the septin network and coordination with other partners such as the actin cytoskeleton. Evidence of this reorganization was obtained using polarized fluorescence microscopy in living budding yeast cells[145]. By using GFP-fusion mutants of cdc3 and cdc12, this study showed that septins first accumulated at the budding site in a radial arrangement to organize in the hourglass structure and rotate by 90° during the hourglass-to-rings transition, finishing in a circumferential arrangement. Not only did that experiment confirmed that septins assemble into an anisotropic fashion but that they are also rotationally constrained and are only able to globally rotate during a controlled step. This remodeling requires that the septin filaments are disassembled to be able to reorient and assemble into two rings, suggesting the existence of machinery able to control membrane-bound septins. Using SEM, another study was able to show precise organization of septins at different steps and to identify different types of filaments by observing spheroplasts synchronized at different steps of cell division.[147].

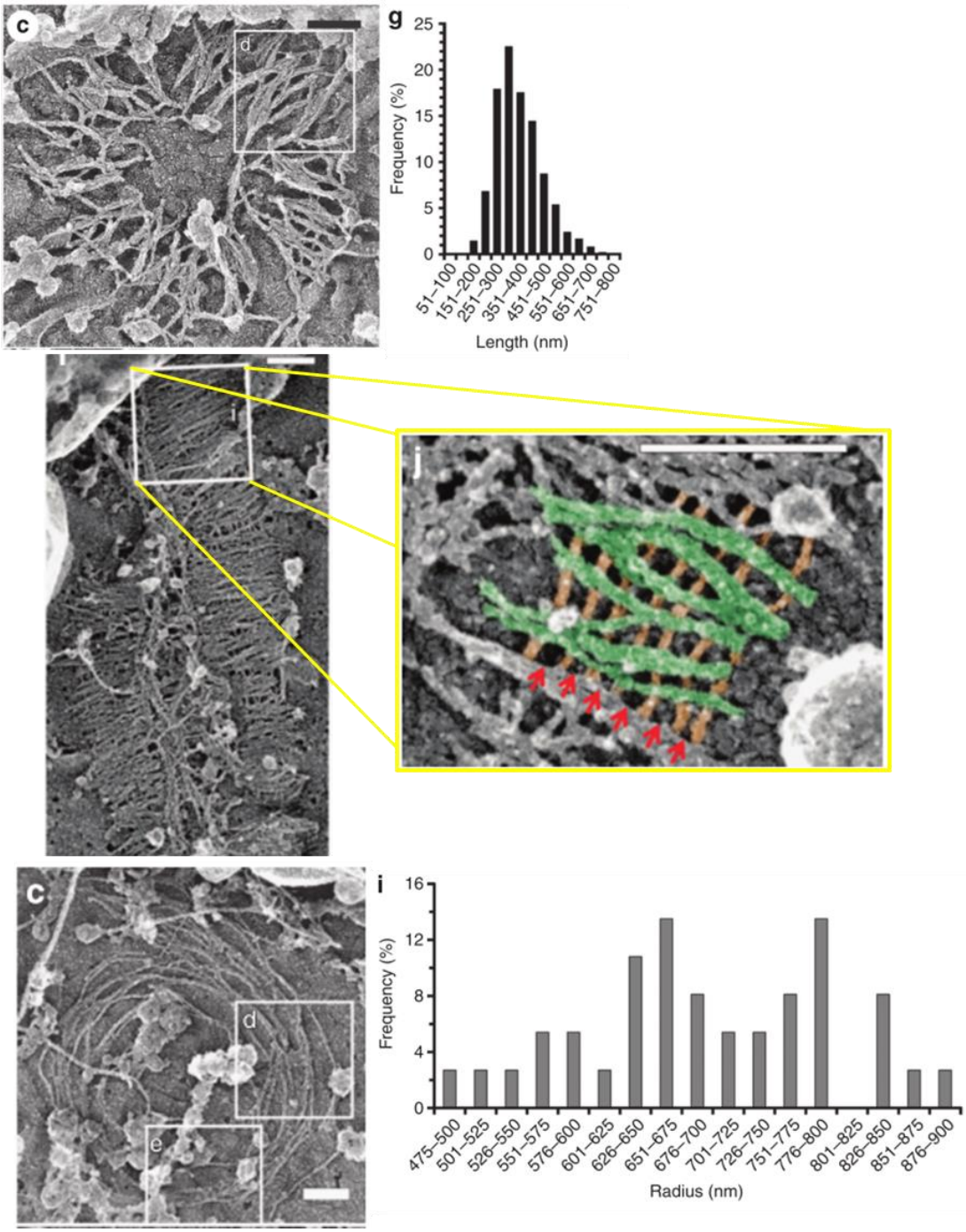


***Figure 24 – Septin filaments during budding yeast division***

*SEM images of septin filament during S. cerevisae cell division at different steps and the corresponding size distribution of filaments. Top – at the onset of the hourglass structure, middle – during the transition, bottom – after the transition to rings. Scale bars are 200 nm.*[147]

At the onset of division, short (400 nm in length) double septin filaments assemble radially and form the hourglass structure (Figure 24, top). The filaments are parallel to the mother bud axis and some filaments are connected to each other, which might contribute to the

immobility of the septin structure. During the transition, double septin filaments are denser and single filaments as well as thick filaments are decorating them (Figure 24, middle) with double filament representing 75% of the filaments, single filaments 17% and thick filaments 7%. The double filaments are still oriented along the mother-bud axis and covered with circumferential cross-linking filaments towards their membrane-proximal side. The thick filament bundles located between the two rows of septin filaments have been identified as the actomyosin ring, as confirmed by their absence in ∆myo1 mutants. Finally, once the transition occurred, only circumferential single septin filaments were present with radii of varying size. Interestingly, during the transition in ∆shs1 mutants (shs1 being another subunit able to replace the terminal cdc11 and assemble into rings *in vitro*), filaments were highly disorganized and filament length less controlled, indicating a possible coexistence of two different filament populations in the structure. Additionally, FRAP experiments of the hourglass structure during the transition in the same study gave several insights on the dynamics of septin reorganization. Bleaching only half the hourglass showed low levels of recovery restricted to the end of the hourglass indicating that it might be the site of the assembly of the rings. Secondly, the fluorescence signal decreased rapidly in the unbleached half before the beginning of cytokinesis indicating that septin disassemble and leave the site. While this study was quite informative and revealing, the method of preparation implies a destruction of a cell wall that could ignore some of the septin architecture found in living cells.

The idea that septins regulators are necessary to ensure the integrity of the septin structure throughout cell division was thoroughly explored in a study using polarized fluorescence microscopy[148]. Several shs1 mutants were tested as it was shown that the have a role in organizing septin filaments during cell division[147]. In full ∆shs1 mutants, both the hourglass and double rings structure were highly disorganized and the transition happened slowly in a single phase. In less drastic mutants like shs1∆C, where the highly phosphorylated C-terminal region was removed, the structures were as disorganized but the rate of disassembly remained the same as in wild type cells, indicating the role of this C-terminal region in the organization of septin filaments but not their disassembly. Similar results were found in four other shs1 mutants where specific phosphorylation sites were targeted. All these findings are summarized in

Figure 25.

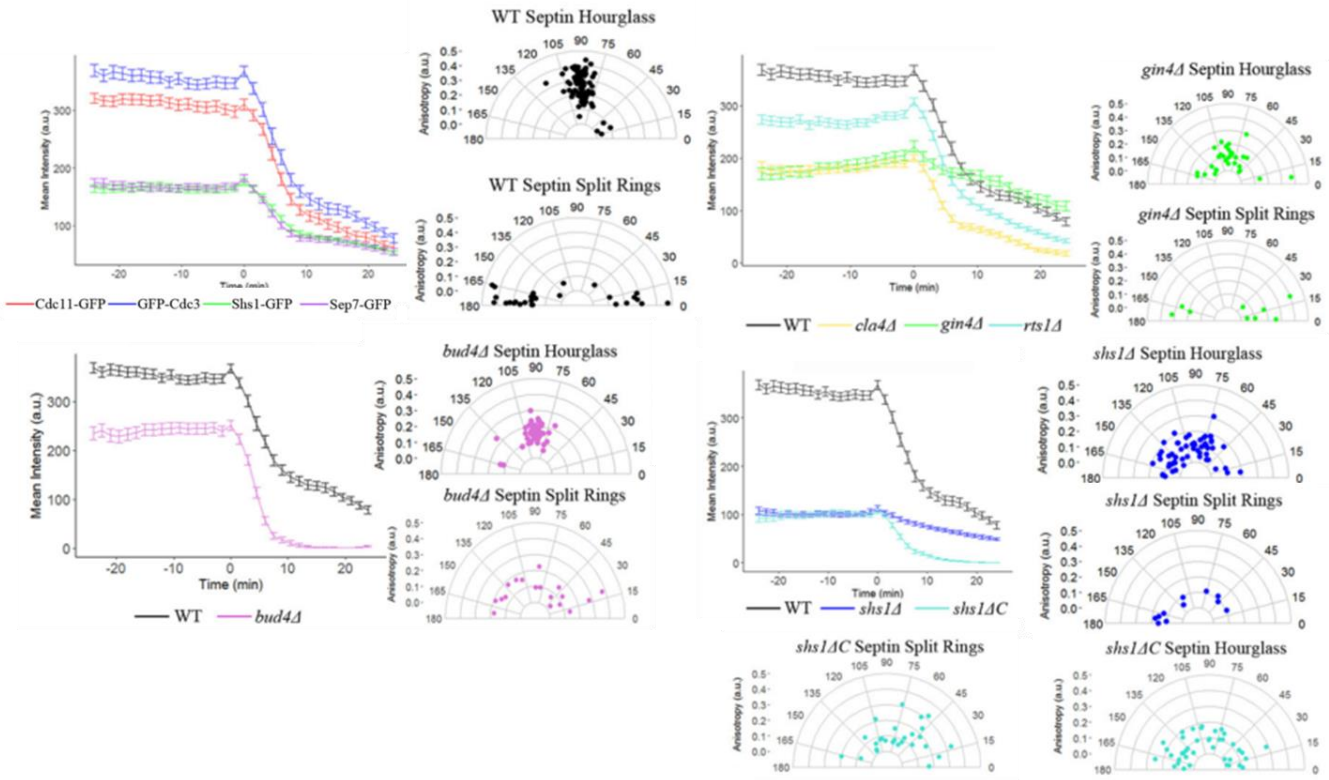


***Figure 25 – Hourglass to double rings transition in different yeast mutants***

*Rate of disassembly (curves) and anisotropy levels (angular distribution) of GFP-cdc3 in different mutants of proteins associated with cell division during the hourglass to double rings transition.*[148]

This study confirms the dynamic nature of the transition and the requirement for several septin-interacting partners to achieve a correct transition. Post-translational modifications of septin filaments also play an important role. SUMOylation (small ubiquitin-like modifications) also regulates ring assembly at the previous division site by removing the old septin rings[149,150]. They have a deeper role in human cells where non-SUMOylatable mutants of SEPT6 and SEPT7 show aberrant septin bundle formation and defects in cell division after the ingression[151], indicating that they might also play a role in the disassembly of the filaments during the transition. At least 4 septin subunits are acetylated in yeast (cdc3, cdc10, cdc12 and shs1) by the lysine acetyltransferase NuA4[152] and decreased acetylation of shs1 or NuA4 mutants show the same phenotypes with localization and collar formation defects. All these findings point out to the fact that septin assembly and function is a complicated issue. In the next chapter, we will describe thoroughly how septin assemble and interact *in vitro* to better understand the role of these supramolecular structure in cells.

## 1.3 In vitro studies of septins

### 1.3.1 Primary sequence and septin filaments

Septins form a family of proteins homologous in their primary sequences. Different species possess a different number of septin subunits. For instance, there are 5 mitotic yeast septins (cdc3, cdc10, cdc11, cdc12 and shs1). In human, they amount to 13 (SEPT1 to SEPT12 and SEPT14) that can be divided into four groups: SEPT1/2/4/5 form the SEPT2 group; SEPT6/8/10/11 the SEPT6 group; SEPT3/9/12 the SEPT9 group and SEPT7 is alone in its group. Septins within the same group are more homologous and can often be substituted in oligomers. These homologies can also be made between species. For instance, the 5 septins of *S. cerevisae* can be associated with the different human septin groups. cdc3 with SEPT2; cdc10/shs1 with SEPT6, cdc11 with SEPT7 and cdc12 with SEPT9. The primary structure of septins holds 3 domains: The N-terminal domain, the GTP-binding domain and the C-terminus domain. They all vary in size depending of the subunit but all share some properties.

The N-terminal domain is an intrinsically disordered domain that shows few secondary structures[153]. Contacts between different N-terminal regions are made to promote end-to-end interactions[154]. It is also able to bind to cytoskeletal partners like F-actin and microtubules[91,98] and to bind to phospholipids with a high specificity for PI(4,5)P2 through its polybasic region located at the frontier with the GTP-binding domain[155]. It can also interact with the C-terminal region of a neighboring septin subunit in the complex which participates in the formation of oligomers by forming what is called a NC interface. In the case of cdc3, the N-terminus can inhibit its association with cdc10 until its prior association with cdc12, showing a hierarchy in the order of subunits association in the octamer[156]. The central domain corresponds to the GTP-binding domain which is the largest and most conserved in all septins. GTP binding induces conformational changes[157,158] which might trigger oligomerization and later filament assembly of septins by the interaction of two adjacent septins[159,160]. GTP hydrolysis is uneven between different septins and occurs mainly at the GTP binding site of cdc10 and cdc12 for the budding yeast[160] while it occurs for the SEPT7[161] and SEPT2[162] family in mammalians. A recent *in vitro* study showed that yeast septin filaments were able to bundle on a poly(ethylene glycol) (PEG) surface or on a supported lipid bilayers by the addition of either GTP or GDP. The alteration of the phosphorylation site modifies filament length and cell morphology[163]. More importantly, the state of the bound nucleotide can guide the step-by-step process of oligomerization and control the incorporation of different subunits[156]. The consequence is that GTP and GDP levels are able to control filament length and rigidity by

controlling the stoichiometry of different bound subunits. While highly conserved[9,10], the function of the septin unique element has yet to be understood. It is related to the specificity of each septin and distinguishes them from other small GTPases. Finally, septin possess a coiled coil domain at their C terminal region that can vary in length depending on the specific septin subunit. For instance, septin from the SEPT6 and SEP7 have a long terminal domain with more than 100 residues while the ones in the SEPT3 group are the smallest with a few dozen residues. These coiled-coils are involved in oligomerization and filament assembly[164,165] and are excluded in homodimerization interactions[166]. This domain also has a role complex formation as well as mediating lateral interactions that allows for pairing of filament and rings[165,141,166].

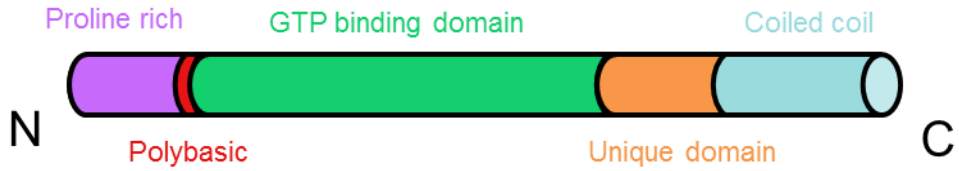


***Figure 26 – Cartoon of the primary structure of septins***

*Schematic of a septin subunit from N to C terminal. Septins contain a proline rich region, a polybasic domain, a GTP binding domain, a highly conserved unique domain and a coiled coil region of varying length. N and C denote N and C termini.*

### 1.3.2 Higher-order structures

One of the specificity of septins is their ability to assemble into palindromic oligomers that can later polymerize into filament. For instance, the human septin complex constructed by SEPT7, SEPT6 and SEPT2 will assemble into the following order: 7-6-2-2-6-7[154]. The subunits are brought together end to end, creating a rod-like shaped complex that is nonpolar by construction. Several other septin complexes have been identified in different species including yeast and humans[13,167,168,169]. Perhaps the most studied and well-characterized septin complex is the one consisting of cdc3, cdc10, cdc11 and cdc12 in *S. cerevisae*. The octamer consists in two copies of each subunit arranged into a palindromic order as follows: cdc11-cdc12-cdc3-cdc10-cdc10-cdc3-cdc12-cdc11. It has been purified and studied by electron microscopy under high salt concentration and its structure revealed at high enough resolution to be able to distinct each separate subunit[165] (Figure 27).

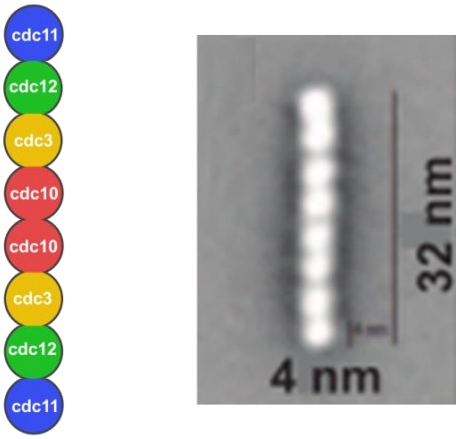


***Figure 27 – The yeast septin octamer***

*Schematic representation of the budding yeast septin octamer composed of the cdc3, cdc10, cdc11 and cdc12 subunits (left). Electron microscopy image of the same complex*[165]*.*

The complex appears as a 32 nm long rod-like structure composed of 8 globular elements of 4 nm in diameter which corresponds to the 8 subunits. Analyzed on a gel, a 2:2:2:2 stoichiometry is present in the octamer. Septin filament formation occurs by end-to-end polymerization of such complexes through homodimerization of the cdc11 subunit[140,170]. More interestingly, the polymerization ability of this complex is salt-dependent. A high enough salt concentration (>150 mM NaCl) screens electrostatic interactions and prevents its polymerization which keeps the septins into their octameric form. Conversely, lowering the ionic strength triggers polymerization of micrometric long filaments. Moreover, the filaments associated into pairs display electron-dense material in between filaments, located periodically every 30 nm, resembling a railroad track. This ensures lateral interactions between septins (Figure 28). This electron-dense material between the two filaments has been identified as the C-terminal coiled-coil region of cdc3 and cdc12 arranged into a four helix bundle.

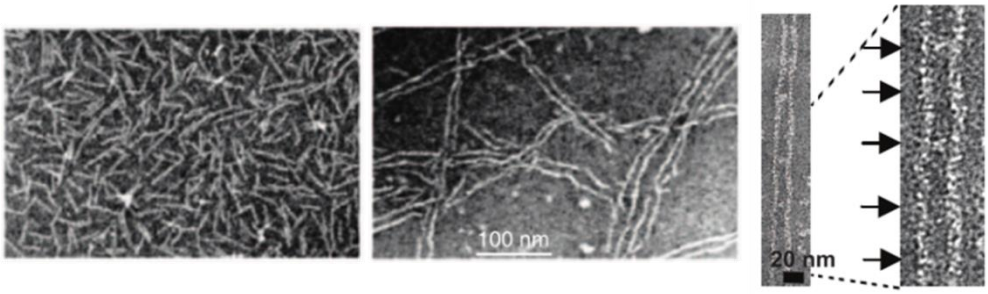


***Figure 28 – Solutions of budding yeast septin filaments***

*Solution of cdc11/12/3/10 septins at low (50 mM) NaCl concentration (left) and high (300 mM) NaCl concentration (middle, right). Right picture is a zoom on a pair of filaments showing the railroad-like structure.*[165]

Besides, septins can assemble into a variety of ultrastructures. They can also form rings when substituting the terminal subunit (cdc11) with another one (shs1)[97]. The minimal complexes obtained with the shs1 substitution were very similar to the cdc11 ones displaying 8 globular subunits 4 nm in size aligned in a 32 nm long rod-like arrangement (Figure 29). In the same fashion as for cdc11-terminal complexes, shs1-terminal complexes only polymerize under low salt conditions (<150 mM NaCl) and form rings formed by curved bundles about 500 nm in diameter and 100 nm thick (Figure 29). Removal of the α0 helix at the N-terminal or the whole C-terminal region resulted in the inability for these octamers to polymerize, highlighting the importance of both regions to generate these structures.

Interestingly, in solutions where cdc11 and shs1 were mixed together, the stoichiometry of the two subunits played an important role on the morphology of the ring. At a 2:1 ratio (shs1/cdc11), the filaments were still able to form railroad tracks but with much thicker filaments. At a 3:1, septin started to assemble into ring and increasing the shs1 concentration would result in thicker rings of similar diameters (Figure 29). Overall, this suggests that septin assembly is highly related to the stoichiometry of the different complexes and their state. The plasticity of these septin structures is even more pronounced in mammals where the 13 subunits form 4 different groups with some being cell-specific and can assemble into tetramers, heptamers and octamers. The stoichiometry is not the only regulatory mechanism of septin assembly since several *in vitro* studies have shown that septin can behave very differently in the presence of the plasma membrane.

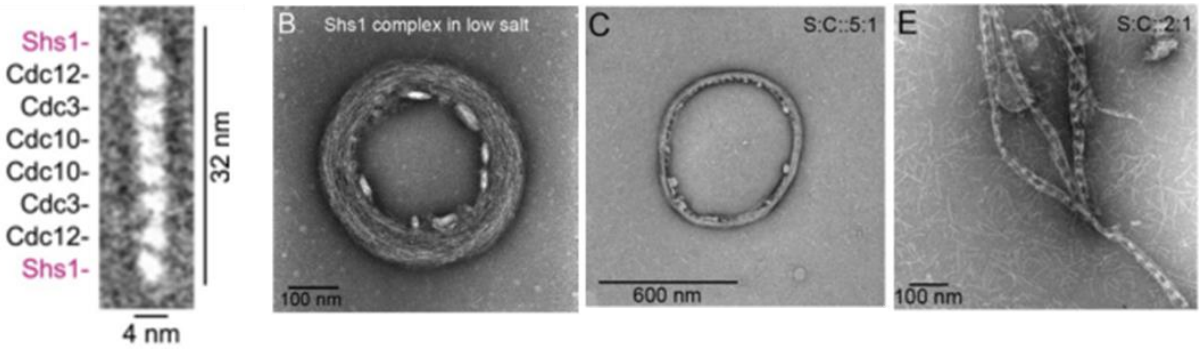


***Figure 29 – Solution of septin filaments with varying amounts of shs1 and cdc11***

*The septin octamer made of shs/cdc12/3/10 is similar to the one with cdc11 (left). The shs1/cdc12/3/10 complex organizes into thick rings at low salt concentration (B). The thickness of the rings decreases as cdc11 is mixed with shs1 (C, ratio = 5:1) up to the point where filaments switch to a railroad tracks structure (E, ratio = 2:1).*[97]

### 1.3.3 Septin-lipids interaction

Since the discovery of septin filaments, it was hypothesized that they were able to interact with the plasma membrane. Cell fractionation revealed that septin co-fraction with the plasma membrane[171]. The extraction of septins from cells usually results in a soluble fraction and a membrane-bound fraction (at equal quantity). Additionally, septins *in vivo* form rings and localize at region of micron-sized curvature such as the basis of cilia or the neck of dividing cells. Furthermore, a direct interaction with the membrane has been observed with the human SEPT4 and the four *S. cerevisae* subunits cdc3, cdc10, cdc11 and cdc12[155,172]. The polybasic region serves the same function in budding yeast septins and mutations lead to mislocalized rings and failure to bind to the membrane. Another important element is the high specificity of the interactions between septins and lipids.

A study showed that budding yeast septins were able to bind to DOPC lipid monolayers only when it was doped with PI(4,5)P2[173]. The presence of another phospholipid: phosphatidylinositol-4-phosphate (PIP) did not result in any binding even at concentration up to 20% and only the addition of PI(4,5)P2 or PI(3,4,5)P3 at concentrations as low as 2.5% would allow for septins to bind. The same result was found in this study using PI(4,5)P2 doped vesicles and it will be described in more details in section 3.1. On PI(4,5)P2 monolayers, the organization of septin filaments as compared with their organization in solution is different. At equivalent concentrations, septin filaments have a tendency to form flat bundles on PI(4,5)P2 monolayers instead of railroad tracks as seen in Figure 28. These bundles were made of long filaments (several µm) parallel to each other with a sheet-like organization (Figure 30). On PI(3,4,5)P3 monolayers, however, filaments were still able to bind but were less organized and assembled into aggregates, suggesting that PI(4,5)P2 has a specific role in organizing septin filaments. In addition, septin octamers in an environment that would normally prevent filament formation (for instance, at salt concentration higher than NaCl 150 mM) are able to assemble on a monolayer and polymerize in the same fashion as described previously. This is even more striking using Δ(2-18)cdc11, a mutant that is deprived of the N-terminal α0 helix. This mutant is unable to assemble in solution, even at salt concentrations as low as 50 mM NaCl which would be low enough to trigger the polymerization of wild type septins. When these mutants were incubated with a PI(4,5)P2 monolayer, they were able to assemble once bound to the membrane in the same fashion as wild type septins.

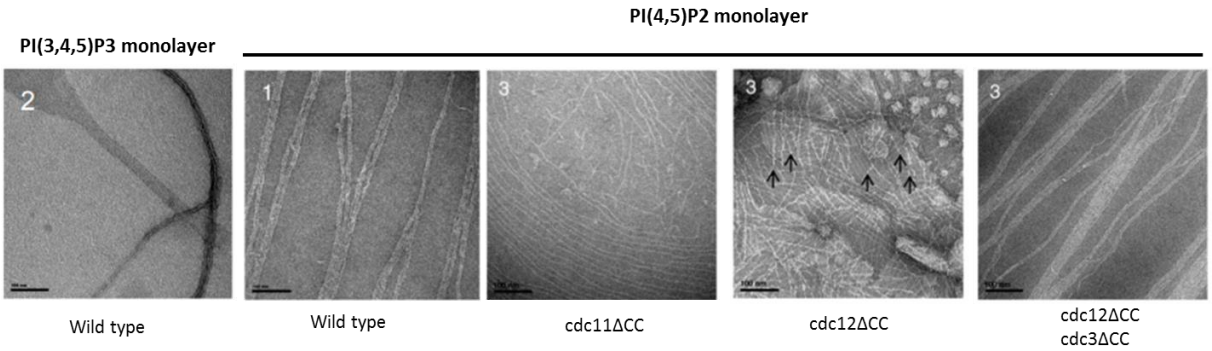


***Figure 30 – Septins on phospholipid monolayers***

*Assembly of septins on either PI(3,4,5)P3 or PI(4,5)P2 monolayers. The two left images correspond to wild type and the three other to different mutants.*[173]

Several other mutants have been engineered to test the influence of specific residues on septin filament organization on monolayers. For instance, the deletion of the C-terminus (ΔCC) of cdc11 would lose the ability to bundle but still formed long filaments that still organized (Figure 30, middle). These findings strongly suggest that septins can assemble into filament by several processes. At least one of these processes is membrane-mediated and utilizes the three different septin domains. Interestingly, the binding of GTP can also alter filament assembly as another study has shown in greater detail[163]. Additionally to GTP and GDP, $Mg^{+2}$ can also promote septin filament bundling and organization. On PEG surfaces, the filaments were able to bundle even more, sometimes up to a single giant bundle of septin filaments. Using total internal reflection (TIRF) microscopy, it was shown that septins on membrane are able to polymerize by connecting short segments of filament in a process called "annealing"[174]. By using fluorescence correlation spectroscopy (FCS), they first showed that cytosolic septins in *S. Pombe* assemble into oligomers but do not polymerize into filaments. Once they are bound to the membrane, septin oligomers can freely diffuse and assemble to form higher-order structures. Similar results were found when switching to *in vitro* supported lipid bilayers doped with 4% nickel-tagged lipids put in a solution containing cdc3,10,11,12(His) or PI(4,5)P2. Small octamers would first bind to the membrane and be able to diffuse freely. Collision of two ends of septin short filaments would results in the fusion of those two filaments to generate a bigger one (Figure 31, top).

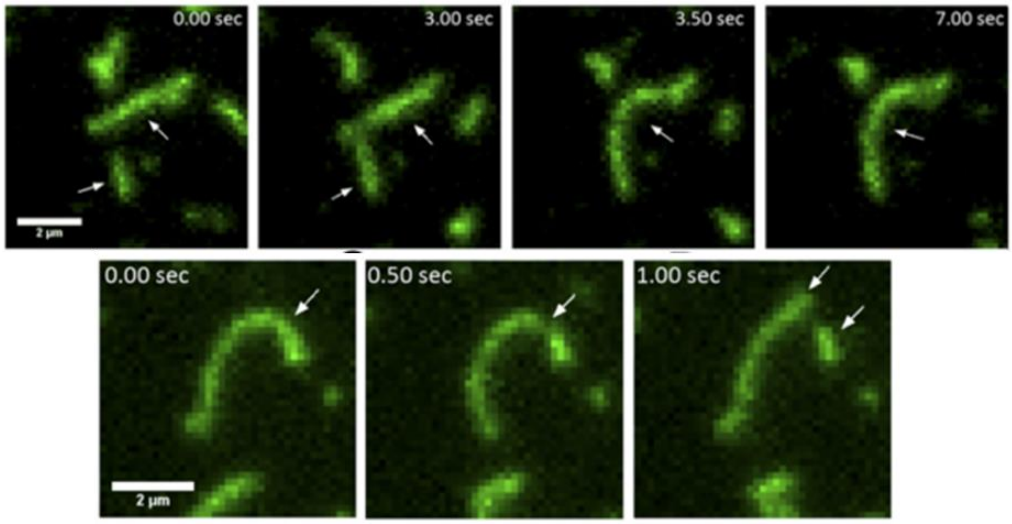


***Figure 31 – Septin annealing on a supported lipid bilayer***

*Budding yeast septin filaments attached to a supported lipid bilayer diffuse and assemble (top) and can also detach (bottom).*[174]

Small filaments were able to grow as they annealed and this, independently of the direction of the filament. Additionally, fragmentation of already formed filament sometimes happened, resulting in the splitting into two smaller filaments (Figure 31, bottom). This mode of filament assembly is not specific to septins and has also been observed for F-actin and microtubules[175,176]. Additionally, filaments were able to curve and fluctuate on the membrane which allowed them to measure a persistence length of 12 µm. The idea that septin filament can be curved is consistent with *in vivo* observation of septin rings. This has led people to hypothesize that septin filaments might recognize the curvature of plasma membrane.

### 1.3.4 Curvature and septins

Since numerous studies have shown that septins localize at branching points in living cells, like the division neck or the basis of cilia where the curvature is in the micrometric range, it has been hypothesized that septins are able to sense curvature and localize specifically to these parts. A recent study using lipid-coated beads was able to demonstrate that purified septins can discriminate between different curvature radii[177]. In this study, *S. cerevisae* septins were put in a solution of lipid-coated silica microbeads of diameter ranging from 0.5 to 6.5 µm. Using confocal microscopy, they showed that septins accumulate on beads of higher diameter with a maximum around 0.5 µm. The presence of this maximum was independent on the bulk septin concentration (Figure 32).

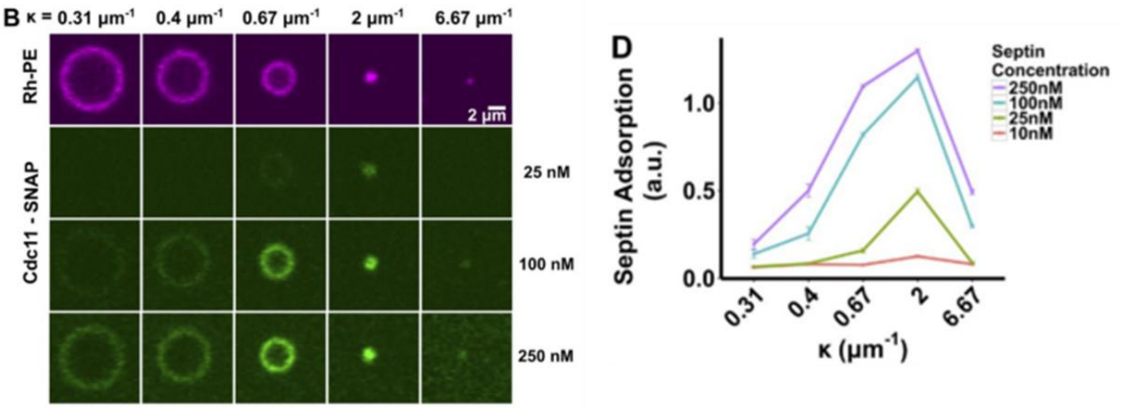


***Figure 32 – Septins on lipid-coated beads***

*S. cerevisae septins in a solution of lipid-coated beads shown by confocal microscopy (left) and the corresponding absorption versus curvature curve at different concentrations.*[177]

Interestingly, mutation of the α6 helix of cdc11 would show similar results. These mutants remained in octameric form even when bound to a PEG surface (which usually promote filament polymerization) but were still able to discriminate between different curvature radii. This suggests that filaments are not necessary for septins to sense curvature. This study does not investigate the presence of several curvature axes by using spheres. In that regard, we developed during my PhD a novel tool to be able to investigate different curvatures and geometries using patterned supported lipid bilayers (this will be explained in details in section 3.3). Membrane deformation is related to curvature as several curvature-sensing proteins like endophilin and α-synuclein are also able to generate protrusion on lipid membranes[178,179]. Evidences of membrane deformation by human septin have shed light on the relationship between septin organization and membrane curvature[180]. This study focused on the deformation induced by the SEPT2/6/7 complex on GUVs doped with phospholipids. On vesicles lacking phospholipids, no deformation could be observed while phosphoinositide-doped vesicles showed large tubulations. Finally, EM studies of the tabulated GUVs and SEPT2/6/7 complexes revealed that septin filament assemble circumferentially along the tube main axis which suggests that septins constrain the membrane by organizing into rings of fixed size. Yet, to completely understand this behavior, it seems necessary to explain the role of this distinct phosphoinositide in membranes.

## 1.4 Role of PI(4,5)P2 in cells

### 1.4.1 PI(4,5)P2 synthesis and degradation

Being a phosphoinositides, PI(4,5)P2 is synthesized from phosphatidylinositol (PI), a glycerol-lipid[181]. This lipid is concentrated at the inner leaflet of the plasma membrane and is less abundant than other phospholipids like phosphatydilcholine or phosphatidylserine where it contributes to 1-2% of the total phospholipids pool. While several isoforms of this molecule exist in cells, the major isoform found in mammalian cells is *myo*-D-inositol. It possesses three phosphorylation sites which can give rise to seven phosphoinositides (Figure 33, bottom) with PI(4)P and PI(4,5)P2 being the most prevalent ones *in vivo* (chemical structure,Figure 33, top). In mammalian cells, PI(4,5)P2 can be synthesized by two pathways via a PI(4)P or a PI(5)P intermediate through kinases, although PI(5)P is scarcely found in membranes and the main mechanism of PI(4,5)P2 synthesis is PI(4)P phosphorylation[182]. In *S. cerevisae*, homologues of these kinases (MSS4 and FAB1) have been identified to have a similar role in biogenesis of phosphoinositides[183,184].

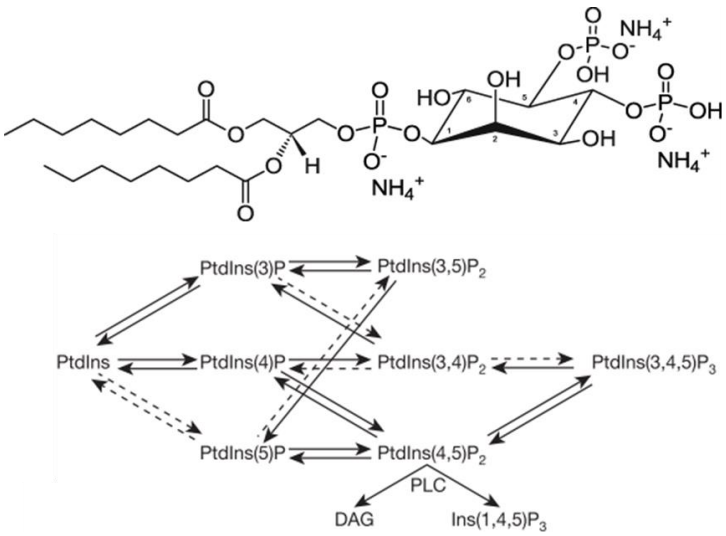


***Figure 33 – Phosphatidylinositol and its different pathways***

*Chemical structure of PI(4,5)P2 (top). Different pathways of phosphoinositides synthesis (bottom). The dotted arrows represent a reaction that has been observed in vitro but which biological existence is still not clear.*

In mammalian cells, the degradation of PI(4,5)P5 occurs during its hydrolysis by either phosphatases or phospholipases. Phosphatases 4' and 5' are mainly involved in controlling the local concentration of PI(4,5)P2 and only take away one phosphorus atom from the headgroup while phospholipases (specifically phospholipase C or PLC) serve another role as

they cleave two byproducts: inositol triphosphate (IP3) and diacylglycerol (DAG) which are important in the inositol lipid signaling system. Another fate of PI(4,5)P2 is its conversion to PI(3,4,5)P3 primarily by class I phosphoinositide (3)kinases (PIP3K). This lipid is present in negligible amounts in resting cells, but can transiently and dramatically increase in response to growth factor stimulation. Out of all the phosphoinositides, PI(4,5)P2 is the most abundant and play a pivotal role in numerous cell functions.

### 1.4.2 PI(4,5)P2 functions *in vivo*

As described previously, PI(4,5)P2 can be degraged by two family of enzymes and these two mechanisms of dephosphorylation give rise to two fundamentally different functions. Cleavage by phospholipases produce metabolites that are able to amplify and propagate signaling primarily, controlling the activity of calcium channels[185]. PI(4,5)P2 is also directly involved in the regulation of ion channel and signal transduction by increasing channel activity (consequently, its hydrolysis reduces channel activity)[186,187]. These processes are very sensitive to local PI(4,5)P2 concentrations. However, the mechanisms of regulation are still not fully understood. One of the properties that makes PI(4,5)P2 unique and so essential is highly charged headgroup (-3 at physiological pH). Therefore it can interact with polycationic proteins. It can also bind more specifically to PI(4,5)P2-related domains such as PH, ENTH and FERM domains. It is therefore a good candidate for the regulation of the activity of GTPases, including septins. For example, PI(4,5)P2 is essential for clathrin-mediated endocytosis (CME)[188]. Several proteins (endophilin, amphiphysin and AP2 (an adaptor that recognizes cargo and also binds to clathrin)) involved in this process are recruited at the endocytosis site by interacting directly with PI(4,5)P2. Several methods regulating PI(4,5)P2 levels by either inhibiting kinases or overexpressing phosphatases have been reported to inhibit CME[189]. The depletion of PI(4,5)P2 in clathrin-coated pits by hydrolysis (mainly by phosphatases) is also necessary to ensure the disassembly of the coat and the final scission. Similarly, PI(4,5)P2 is involved in the formation of phagosomes. The density of PI(4,5)P2 increases as the membrane interacts with the target[190]. Subsequent depletion of PI(4,5)P2 is largely mediated by the phospholipase PLC as its deactivation ablates phagocytosis. The phosphorylation by PIP3K and dephosphorylation by phosphatases 4' and 5' also contribute to PI(4,5)P2 depletion, necessary for pseudopod extension but to a lesser extent than PLC. Finally, PI(4,5)P2 is also involved in macropinocytosis where it accumulates during membrane ruffling and disappear during the membrane closure[191]. Interestingly, a study also showed that the depletion of the PIP3K kinase resulted in failed ruffling and macropinocytosis[192].

## 1.5 Biological membranes

The membranes are essential components of living cells and organelles because they allow the compartmentalization of objects as well as transport, signaling and exchange with the environment or other cells. Cell membranes are complex objects mainly composed of lipids and proteins. The average lipid to protein ratio in the plasma membrane is 50:1 in molar fraction and 1:1 in mass fraction. Lipids combine a hydrophilic head with a hydrophobic tail. In living cells, lipids are mainly made of lipid bilayers. Bilayers are assembled by having two sheets of lipids stacked together with the lipid heads facing outwards and the tails facing inwards. The tails are trapped between the two sets of heads, allowing for the separation of two mediums. The composition of natural bilayers is usually asymmetrical as lipids synthesized are added to the cytosolic face when considering the plasma membrane. Lipids can exist in two phases: liquid or solid (gel) and each lipid has a different liquid-solid temperature transition and it ranges from - 10°C to +90°C for phospholipids[193]. Those two phases can coexist since lipid bilayers are usually made out of a diversity of lipids. This polymorphism can be used to partition proteins[194]. Within living systems, bilayers are highly dynamic with both lipids and proteins diffusing laterally. Mechanics of the membrane play an important role in regulating several biological functions such as cell division and endo/exocytosis.

### 1.5.1 Membrane mechanics

Membranes undergo drastic changes in shape in the course of biological processes. For instance, during cytokinesis, the membrane is highly curved at the neck between the two cells and this site undergoes signaling and trafficking mechanisms. Thus, understanding the mechanics of membrane is crucial to understand the underlying biological functions.

The first model on membrane elasticity was proposed in 1973 by W. Helfrich and P Canham[195]. In this model, the membrane is considered to be an infinite 2D sheet of negligible thickness, which is reasonable when comparing the thickness of the plasma membrane (~ 10 nm) and the cell radius (~ 10 µm). The important parameters are its tension $\boldsymbol{\sigma}$ and its two main curvatures $\mathbf{C_1}$ and $\mathbf{C_2}$ as well as its Gaussian curvature $\mathbf{C_g}$ which is the product of the two (Figure 34).

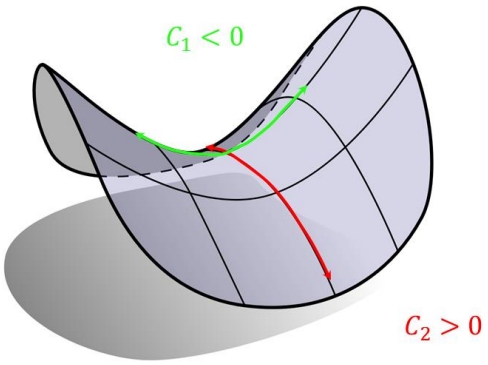


***Figure 34 – Two main axes of surface curvature***

*The two main curvature axes on a saddle surface. One is positive and the other is negative, making the Gaussian curvature negative in this case.*

The model is used to explain the different shapes that a membrane can adopt considering the applied stress. The stress can be decomposed into two components: ***bending*** and ***stretching***.

Bending occurs when forces parallel to the surface vector are applied on both sides of the membrane (Figure 35, left). It results mostly in a variation of the angle between adjacent lipids. It can be described by the bending modulus $\boldsymbol{\kappa}$ and the Gaussian bending modulus $\boldsymbol{\kappa_g}$ expressed in Joules or more commonly for cell membranes in $\boldsymbol{k_bT}$ where $\boldsymbol{k_b}$ is the Boltzmann constant and $\boldsymbol{T}$ the temperature and its value ranges from 10 to 100 $k_bT$[196] depending on the membrane composition. The energetic cost per unit of area to bend a membrane to a mean curvature $\boldsymbol{C = C_1 + C_2}$ can be expressed as:

$$F_c = \frac{1}{2}(C - C_0)^2\boldsymbol{\kappa} + C_1C_2\boldsymbol{\kappa_g}$$

Where $\mathbf{C_0}$ is the spontaneous curvature in the absence of stress which is expected to be flat in the case of a symmetrical membrane and can be non-zero depending on the type of lipids and the insertion of curvature generating proteins. As long as the topography remains unchanged, the Gauss-Bonnet theorem stipulates that the Gaussian curvature is constant. Therefore, the term can be simplified as:

$$F_c = \frac{1}{2}(C - C_0)^2\boldsymbol{\kappa}$$

Stretching occurs when forces are applied perpendicular to the surface vector of the membrane (Figure 35, right). In that case, the relative position of the lipids is modified. It can be described by its stretching modulus $\boldsymbol{S}$ expressed in N.m$^{-1}$. The stretching energy is related to the relative change of area $\frac{\Delta \boldsymbol{A}}{\boldsymbol{A}}$ by a simple Hookean law:

$$F_s = \frac{1}{2}\frac{\Delta A}{A}\boldsymbol{S}$$

Although shear stress is another type of deformation that is likely to occur, for cell membranes it can be neglected given the intensity of shearing involved are very small compared to the two other components[197].

Cell membranes are relatively soft object and are subjected to thermal fluctuations. These fluctuations give rise to entropic-driven membrane tensions which increase with the straightening of the membrane because it reduces the number of possible configurations and is opposed to such a change. In that case, the tension-based energy can be expressed as:

$$F_t = \frac{\Delta A}{A}\boldsymbol{\sigma}$$

With $\boldsymbol{\sigma}$ being the membrane tension. As explained in the following paragraph, the thermal fluctuations imply two possible regimes of stretching of the membrane. At low tensions (typically < 0.5 mN.m$^{-1}$), the fluctuations are still present and a further increase of the tension leads to a smoothing of the membrane. At higher tensions, the fluctuations have disappeared and an increase in tension induces a stretching of the membrane that display an exclusively elastic behavior[196].

The resulting Hamiltonian combining the stretching and the bending energy are sufficient to describe membrane mechanics and has been extensively studied experimentally[195,196,198,199]:

$$H = \int_S \left(\frac{1}{2}(C - C_0)^2\kappa + \sigma\right) ds$$

A Fourier analysis of the Hamiltonian permits to rewrite the relative area variation of the membrane $\frac{\Delta \boldsymbol{A}}{\boldsymbol{A}}$ as[200,201]:

$$\frac{\Delta A}{A} = \frac{k_b T}{8\pi\kappa} ln \frac{\frac{\pi^2}{a^2} + \frac{\sigma}{\kappa}}{\pi^2 L^2 + \frac{\sigma}{\kappa}}$$

Where $\boldsymbol{L}$ is the macroscopic length of the membrane (typically 10 µm), $\boldsymbol{a}$ is the microscopic length of the membrane (typically 1 nm). This expression can be simplified in the case of low or high tensions.

***Low tension: entropic regime***

If we consider tensions low enough, the relation $\sigma \ll \frac{\kappa\pi^2}{a^2}$ implies:

$$\frac{\Delta A}{A} \approx \frac{k_b T}{8\pi\kappa} ln \frac{\pi\kappa}{\sigma a^2}$$

Now, considering a reference state of tension $\boldsymbol{\sigma_0}$, corresponding to an initial area $\boldsymbol{A_0}$ the equation becomes:

$$\frac{\Delta A}{A_0} \approx \frac{k_b T}{8\pi\kappa} ln \frac{\sigma_0}{\sigma}$$

The area expansion $\frac{\Delta \boldsymbol{A}}{\boldsymbol{A_0}}$ depends logarithmically on the tension and is inversely proportional to the bending modulus $\boldsymbol{\kappa}$ for tension low enough (up to ~0.5mN.m$^{-1}$ when considering GUVs). A method to observe these fluctuations is called Flicker spectroscopy. It allows for a measurement of the bending modulus of the membrane of a vesicle by Fourier analysis of the membrane fluctuations[202,203]. Another method to measure the bending modulus consists in directly applying tension on the vesicle with a micropipette. The latter method will be discussed more precisely in section 2.7.1.

***High tension: elastic regime***

A more general expression includes both thermal fluctuation and lipid area expansion. The bending and stretching moduli can thus be derived:

$$\frac{\Delta A}{A_0} = \frac{k_b T}{8\pi\kappa}\left(1 + c\sigma\frac{A}{\kappa}\right) + \frac{\sigma}{S}$$

Where $\boldsymbol{c \approx 0.1}$ is a constant depending on the type of modes (planar or spherical) used to describe the membrane undulations. This equation can be used to describe simple membrane mechanics as being a competition between thermal fluctuation and lipid-lipid interactions in response to stress at equilibrium. At high tension, the excess membrane area that was previously stored in the thermal fluctuations vanishes. Once all the excess area has been smoothened by tension, a further increase leads to stretching and the lipid density decreases. In that case, thermal fluctuations are too weak and this equation can be simplified as:

$$\frac{\Delta A}{A_0} = \frac{\sigma}{S}$$

The membrane area expansion depends linearly on the membrane tension and is inversely proportional to the stretching modulus $\boldsymbol{S}$. This model of membrane mechanics is well-suited to describe simple membrane and model systems such as giant unilamellar vesicles which are widely used as a biomimetic tools to understand the mechanical behavior of cell membranes.

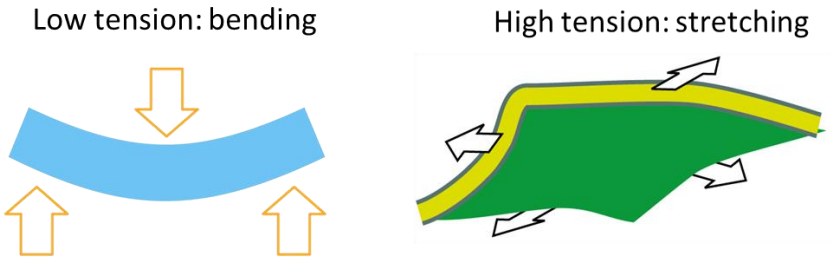


***Figure 35 – Membrane deformations***

*Drawings of the two main stress components present in membrane deformation. At low tensions (< 0.5 mN.m$^{-1}$), deformations are mainly governed by bending and the area expansion depends logarithmically on the tension σ. At high tensions (> 0.5 mN.m$^{-1}$),deformations arise mainly from stretching and the area expansion depends linearly on the tension σ.*

### 1.5.2 In vitro systems

Recently, model systems have sparked a lot of interest for their ability to control parameters as compared with living cells. Recent advances in biochemistry and biophysics have permitted to understand better the formation mechanisms of model membrane systems. Besides, novel techniques have allowed the creation of more complex systems[204–207]. Two main model systems are usually used to investigate membrane associated processes: vesicles and lipid bilayers. These are the model of choice when investigating the property of membrane-associated proteins *in vitro*.

***Vesicles***

Also called liposomes, vesicles are composed of a lipid bilayer arranged into a spherical arrangement, compartmenting the inside which contains the internal or growth buffer from the outside medium containing the external or observation buffer. They can be used to mimic the plasma membrane or lipid cargos. Small unilamellar vesicles (SUV) are vesicles measuring less than 100 nm in radius, while giant unilamellar vesicles (GUV) are typically much bigger with radii higher than 1µm and large unilamellar vesicles (LUV) correspond to the intermediate size. Multilamellar vesicles (MLV) and multivesicular vesicles (MVV) are byproducts of unilamellar vesicle formation and not ideal model systems due to their complexity (Figure 36). This wide range of sizes allows for the modelling of cell membrane (~10µm), exocytosis vesicles (~100 nm) and lipid cargos (~100-1000 nm). Under isotonic conditions, vesicles are spherical but can still fluctuate. These fluctuations can be controlled by adjusting the osmolarity of the external buffer. In this study, we were interested in GUV and SUV formation.

The first protocol of GUVs formation included swelling of a phospholipid film inside a stream of water-saturated nitrogen[208]. Since then, several other methods have been developed to grow vesicles at high yield with more complex lipid compositions. For instance, microfluidics assisted GUV formation can be achieved by jetting an internal buffer from a micropipette at a pre-assembled bilayer at a water-oil interface. The size of the vesicles is controlled by the injection flow. However, this method allows for a residual amount of oil inside the hydrophobic part of the vesicle, leading to changes in the mechanical and diffusive behavior of the bilayer[209]. Another type of microfluidic assisted GUV formation consists in trapping droplets of water inside a drop of oil which is itself embedded in a water medium effectively creating a double emulsion[210]. The solvent contained in the oil phase is then evaporated to obtain a GUV out of these droplets. This method presents the same drawback as the jetting

method given oil molecules are trapped between the two bilayer sheets[211]. Nevertheless recent advancements in the field have removed this artifact by applying a flow across a rotating chamber (cDICE)[212]. Other growth methods such as gel-assisted and electroformation have been developed and enhanced in the past year and allow for high-yield and a good quality of vesicles. These methods have all been tested during my PhD and will be described in details in section 2.5. SUVs are easier to obtain because of their small size and are usually obtained by drying a lipid film, rehydrating it then vortexing and sonicating the solution.

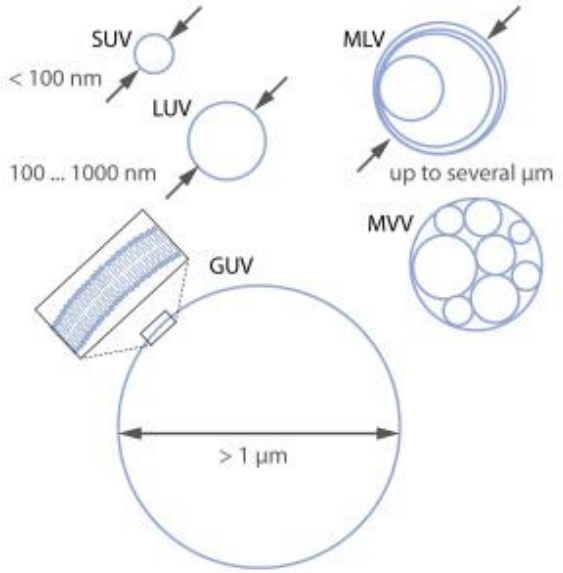


***Figure 36 – Classification of artificial vesicles***

*Sketches of the different types of vesicles.*

***Supported lipid bilayers***

Supported lipid bilayers (SLB) consist of two sheets of lipids arranged in a bilayer deposited on a solid surface (glass, mica…), allowing only the top layer to be in contact with the solution. Other types of surface-confined model systems include additional surface treatment but keep the same principle of having a thin double layer of lipids deposited on a surface (Figure 37).


***Figure 37 – Different types of surface-attached membranes***

*Sketches of the different types of bilayers. (A) solid-supported lipid bilayer; (B) polymer-cushioned lipid bilayer; (C) hybrid bilayer, consisting of a self-assembled monolayer (e.g., thiols onAu or silanes on glass or silica) and a lipid monolayer; (D) tethered lipid bilayer*[207]*.*

The formation of SLB by spreading small vesicles on an hydrophilic surface was pioneered by McCornell in 1984 and is the simplest way to create a bilayer with different lipid compositions[213]. Small vesicles rupture once they reach the surface assuming the gain in adhesion energy is greater than the cost of curvature energy (which is dependent on the lipid composition). The adhesion energy can be strongly influenced by electrostatic interactions and thus depends on the charge of the vesicles. Modifying the pH or the ionic strength of the buffer are simple means to tune this adhesion energy. Divalent ions and more specifically calcium ions can interact with lipids. They can thereafter promote adsorption and rupture of vesicles even at very low concentrations (1 mM)[214]. Finally, the nature of the substrate is important to ensure vesicle adhesion. Although SLB can be deposited on metal surfaces like gold, $SrTiO_2$ or platinum with moderate success; the most common ones remain silicon-based material and mica. Surface roughness can influence SLB formation but the most important parameter is the hydrophobicity of the surface which can be improved, on silicon surfaced for example, by hydroxylation of the surface via plasma treatments[215].

Once the vesicles have successfully ruptured, the resulting lipid patch spreads on the surface exposing lipids to the medium at the edges of the patch. These edges are thermodynamically unfavorable and will interact with adjacent lipids by coalescing with other patches or promoting the rupture of neighboring vesicles. These events can lead to a cascade of events that rapidly triggers the fusion of many vesicles and the formation of the full SLB, given the vesicles coverage is sufficiently high. The quality of the whole bilayer can be determined using quartz cristal microbalance with dissipation (QCM-D) or ellipsometry but atomic force microscopy is needed to visualize local defects such as holes and unfused vesicles. The fluidity of the bilayer can also be tested by fluorescence recovery after photobleaching (FRAP) experiments.

### *1.5.3* Probing membrane mechanics *in vitro*

Membrane mechanics are important in many biological processes, especially highly dynamics one where the membrane undergoes remodeling such as cell division. Many membrane-bound molecules are regulated by membrane mechanics like membrane pore that can close or open depending on the surface tension. For this reason, several methods have been developed in the recent years to be able to probe the mechanics of membrane in model systems.

#### *1.5.3.1 Micropipette aspiration*

Micropipette aspiration is a technique developed by Evans and Kwok in 1979[198] and introduced as a mean to manipulate and study the mechanical properties of micron-sized objects such as cells and vesicles. The micropipette can also be used to apply tension on the vesicle. Considering a vesicle of diameter $D_v$ held by a pipette of diameter $D_p$ (Figure 38).

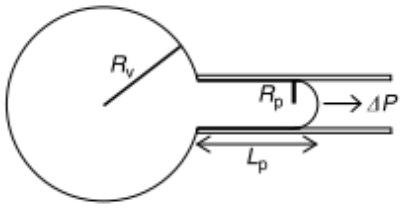


***Figure 38 – Micropipette aspiration assay***

*Drawing of a vesicle sucked by a micropipette via a pressure difference ΔP. The part inside the pipette is called the tongue and its length is Lp.* $\mathrm{R_v}$ *and* $\mathrm{R_p}$ *are the radius of the vesicle and the pipette respectively.*

At equal osmolarity between the inside and the outside of the vesicle, the pressure difference $\Delta P = P_{ext} - P_{in}$ is only driven by the micropipette. By applying the Young-Laplace relationship at both interfaces (between the inside of the pipette and the tongue, and the medium in the chamber and the spherical part of the vesicle), we can express the tension of the vesicle $\sigma$ as a function of the pressure difference.

$$P_{ext} - P_v = \frac{4\sigma}{D_v} \qquad P_v - P_{in} = \frac{4\sigma}{D_p}$$

Where $P_{in}$ is the pressure inside the chamber and equal to the 1 atm. This leads to the following relationship for the tension:

$$\sigma = \Delta P \frac{D_p}{\left(1 + \frac{D_p}{D_v}\right)}$$

Considering the vesicle at equilibrium, the tension is equal at all point of the surface. To have access to the mechanical properties of the vesicle, we measure the evolution of the projected area $\Delta A = A - A_0$ in response to a variation of applied tension. The projected area is calculated from geometrical considerations by separating the GUV into three parts of simple shapes.

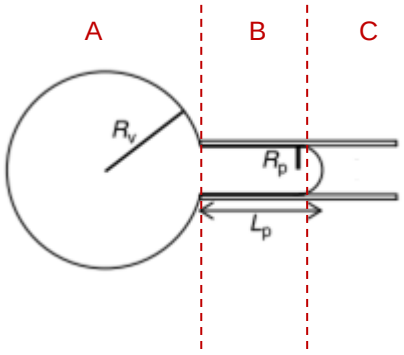


***Figure 39 – Geometry of a micropipette-aspirated vesicle***

*A vesicle sucked by a micropipette is separated into 3 regions: a sphere (A), an open cylinder (B) and a half-sphere (C).*

The region A is a sphere of radius $R_v$ and its area is equal to $4\pi {R_v}^2 - \pi {R_p}^2$ where the second term corresponds to the area where the region A and B connect. The region B is an open cylinder of radius $R_p$ and length $L_p - R_p$ and its area is equal to $2\pi R_p(L_p - R_p)$. The region C is a half-sphere of radius $R_p$ and its area is equal to $2\pi {R_p}^2$. As the tension is increased, the tongue length inside the pipette will also increase while the volume of the vesicle remains constant for low (<10%) area changes. This is due to the fact that the excess area contained in the fluctuations is being used to increase the surface. Taking this into account, the change in area $\Delta A$ can be approximated, using a first order development as[199]:

$$\Delta A \approx 2\pi R_p \left(1 - \frac{R_p}{R_v}\right) \Delta L_p$$

Thus, a measurement of the variation of the tongue length can be directly linked to a change of area as the variation of the vesicle radius $R_v$ is negligible. The advantage of this technique is that it allows to measure small (~1%) area changes. For instance, if a GUV of radius $R_v = 10$ µm aspirated by a pipette of radius of $R_p = 2$ µm is subjected to an increase in tongue length $\Delta L_p = 1$ µm, it would result in a relative area change of $\frac{\Delta A}{A_0} = 0.8\%$. The same area change applied homogeneously on the same free (i.e. not held by a pipette) GUV, for instance, by applying a pressure difference by osmotic shock, would result in a radius change of $\Delta R_v = 39$ nm. While 1 µm is easily observable by optical microscopy, a change in radius of 39 nm is too small to be seen.

#### *1.5.3.2 Optical tweezers and tube pulling*

In 1970, Arthur Ashkin developed a way to manipulate micron-sized dieletric materials (such as glass beads) with a high-powered laser[216] (typically, several watts) called optical trapping (or optical tweezers). In 2018, he was granted the Nobel Prize in physics along with Gérard Mourou and Donna Strickland for their advancement in developing high-intensity laser pulses. The bead is subjected to three forces: a refraction force, resulting from a change of momentum of the passing refracted light that is transfected to the material by the conservation of momentum, an electric field gradient force arising from the non-homogeneous profile of the laser and a radiation pressure coming from the reflected light. These three forces equilibrate and result in a local force maximum located at the focus point of the laser. As the bead is moved away from this point, the laser exerts a force on it proportional to its displacement as a spring would (see Figure 40) with a stiffness which is typically in the range of tens to hundreds of pN.µm$^{-1}$ which leads to the measurement of pN forces. The sensibility of the system is then fixed by the resolution of the microscope.

Since their development, optical tweezers have become a very useful tool in the biological field as it allows for force measurement at the right scale and has been used to measure parameters such as the forces applied by mechanical motors and mechanical properties of filaments[217–219].

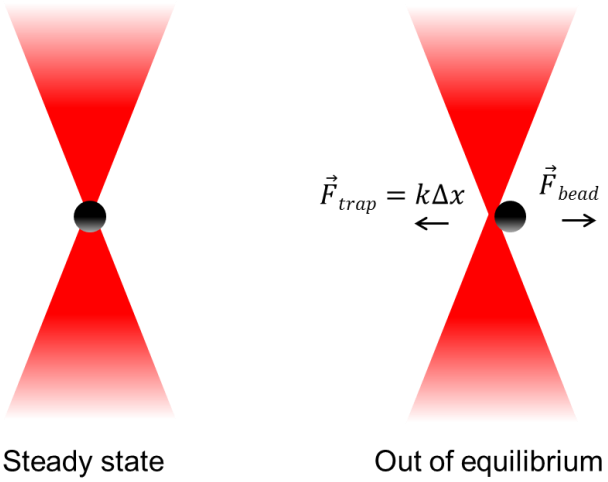


***Figure 40 – Optical tweezers***

*Cartoon of optical tweezers. In the steady state, the bead is trapped in the focus point of the laser. When the bead is driven out of this state by an external force, the laser acts as a spring with a stiffness* k *and a rest position at the focus point.*

One particular usage of optical tweezers for biological purpose, routinely used in our laboratory, is the generation of membrane nanotubes either on biomimetic membranes[220] or living cells[221]. This is achieved by sticking a streptavidin-coated bead to a GUV containing biotinylated lipids. Concretely, a GUV is held by a micropipette and a bead is trapped by the optical tweezers (Figure 41.A). The bead is brought in contact with the membrane and adheres (Figure 41.B). The GUV is then carefully pulled back from the bead and a membrane tube about 50-200 nm in diameter will be formed between the bead and the GUV (Figure 41.C).

The resting position of the bead inside the optical tweezers is different from the center of the trap as a force is necessary to sustain the tube because of the membrane tension coming from the GUV and equal to $F_{tube} = k\Delta x_{tube}$ and is related to the applied membrane tension by the following relation:

$$F_{tube} = 2\pi\sqrt{2\kappa\sigma}$$

Where σ is the tension of the membrane and κ is the membrane bending modulus.

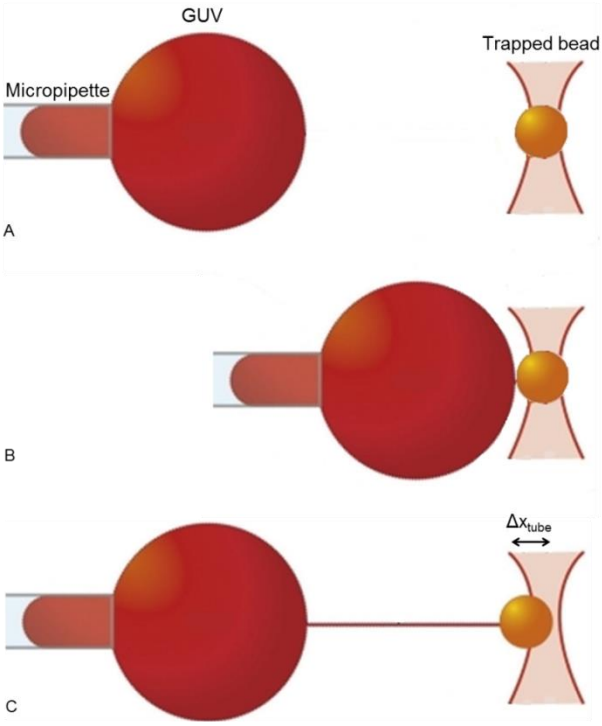


***Figure 41 – Pulling a membrane nanotube out of a GUV***

*A GUV doped with biotinylated lipids is held by a micropipette while a bead coated with streptavidin is trapped in an optical tweezers (A) and brought together in contact (B) then pulled back once the adhesion has occurred and a tube is formed (C). The equilibrium force to sustain the tube is equal to* $\mathrm{F_{tube}} = \mathrm{k}\Delta\mathrm{x_{tube}}$ *where k is the trap stiffness.*

Thus, optical tweezers can be used on systems such as GUVs not only to generate nanometric structures and measure forces in the piconewton range but also to measure their mechanical properties. It is worth mentioning that the two methods described can also be applied to living cells, although the heterogeneity of the cell plasma membrane makes it difficult to interpret some of the results.

### 1.5.4 Membrane deformation by proteins

The deformation of membranes by proteins in time lapses can be observed using bright field or confocal microscopy on GUVs. As it was described in section 1.3.3 with the human SEPT2/6/7 complex, membrane-remodeling proteins can induce tubulations on free membranes that can be resolved with classical microscopy. Although this method is only

qualitative to determine the spontaneous curvature of the protein (if any), this remains a hallmark feature for a membrane-remodeling protein. Recently, a method using a micropipette aspiration assay has been developed to study more quantitatively those deformations and has been applied to study two specific proteins: endophilin and α-synuclein[179,222]. In both studies, GUVs were put in an observation buffer to be held at a constant tension by a micropipette and transferred into another observation buffer containing the protein of interest. By collecting images at different time points, they were able to measure in time lapse the binding of the protein and the change in membrane area through the evolution of the tongue length (Figure 42).

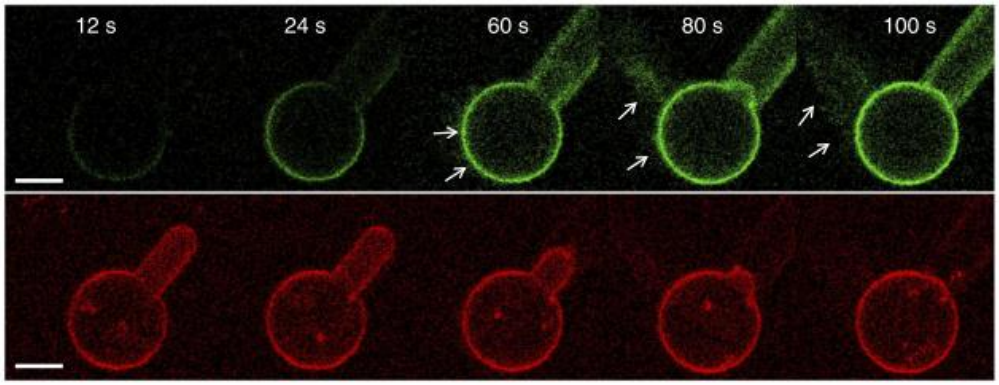


***Figure 42 – Membrane remodeling by endophilin***

*Confocal images of the the lipids of a GUV held by a micropipette (red) and the bound N-bar domain after displacement into the buffer containing the proteins (green). Scale bars are 10 µm.*

Their findings revealed that a minimal amount of bound N-bar domain would trigger the retraction of the tongue. This was combined by the apparition of membrane tubulations that were more frequent as the area of the vesicle decreased while the concentration of bound protein increased. This phenomenon was tension-dependent. A model was therefore designed to accurately describe how membrane tension is lowered by the addition of such membrane-remodeling proteins. In the case of α-synuclein, the vesicles undergo an expansion phase later followed by tubulations. The expansion has been attributed to membrane thinning, another process that can control the membrane shape by the addition of membrane-remodeling proteins. This method of probing membrane deformation at fixed tension has been used during my PhD and will be discussed in section 3.2.2.

### 1.5.5 Methods to analyze curvature sensing

Curvature sensing of a protein can be elucidated by comparing its enrichment at different curvatures. The most widely used tool is the tube-pulling method described previously that allows for a *nanometric* tube and a *micrometric* vesicle to be connected. Curvature sensing of IRSp53[223], a protein from the I-BAR family, has been studied as well as several other proteins including dynamin[224] and cholera toxin[225]. Using confocal microscopy, one can measure the amount of protein bound on the tube and the amount of protein on the vesicle. The calculation of the sorting ratio $S = \frac{[protein]_{tube} / [lipids]_{tube}}{[protein]_{GUV} / [lipids]_{GUV}}$ (the ratio of protein over lipid intensity on the tube versus protein over lipid intensity on the GUV) allows for a quantitative measurement of the curvature preference of the protein. Values of $S > 1$ indicates that the protein binds preferentially to nanometric curvatures while values of $S < 1$ reflects that the protein is enriched at the vesicle. Values of $S \approx 1$ indicates a homogeneous repartition. By using GUVs encapsulated with labeled IRSp53, Prevost et al. were able to show that this protein is strongly coupled with negative curvature and sort with a maximum tube radius of 18 nm while it shows no coupling for positive (outside medium) curvatures (Figure 43).

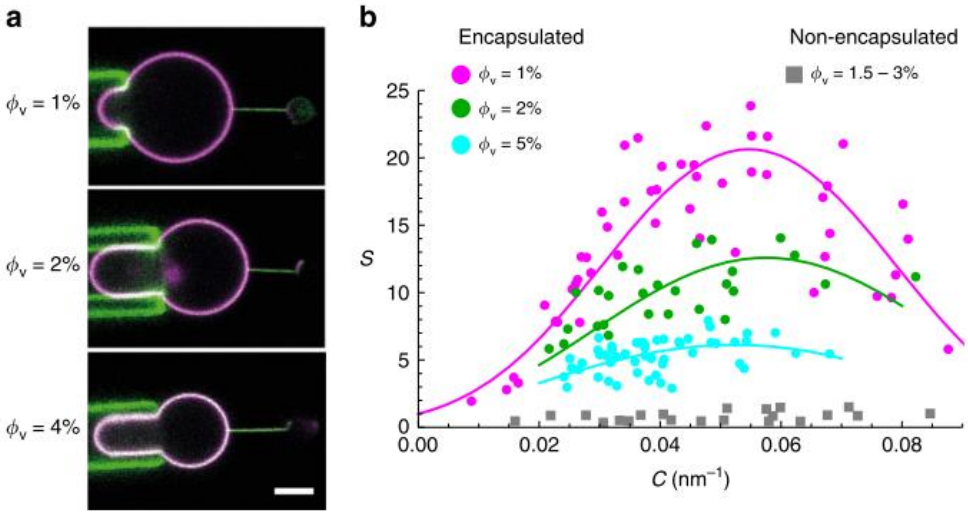


***Figure 43 – Sorting by the IRSp53 proteins***

*Confocal images of a tube pulled out of a GUV (a). Lipids are in magenta and proteins in green. Scale bar is 5 µm. Sorting ratios for different molecular fractions φ.*

They also demonstrated that IRSp53 can phase separate along the tube. The advantage of this tool is that it can couple the generation of small curvatures with membrane mechanics by playing with the applied tension. To probe curvature at different scales, other tools have been developed. For instance, beads of radii ranging from 0.15 to 3 µm coated with a lipid bilayer have been used to investigate yeast septins curvature sensitivity as described in section 1.3.4. Another study used glass microfibers coated with a lipid bilayer to understand the mechanism of polymerization of FtsZ, a bacterial homologue of tubulin, on a micrometric scale[226]. Confocal and SEM analysis of FtsZ filaments bound on these microfibers have revealed that the filaments arrange helicoidally to the main axis of the fiber with an angle depending on its radius (Figure 44).

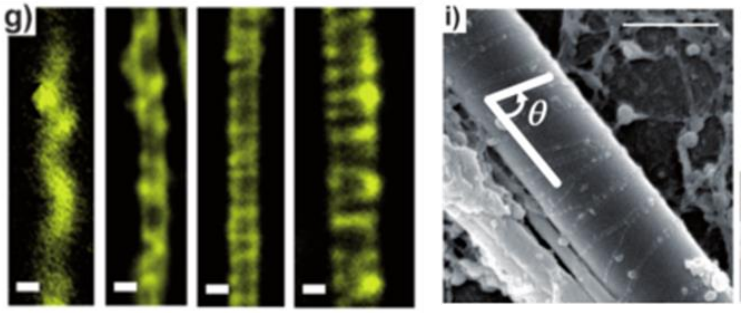


***Figure 44 – Helicoidal binding of FtsZ on micron-sized tubes***

*Confocal images (g) and SEM images (i) of FtsZ filaments bound to glass microfibers coated with a lipid bilayer. Scale bars are 1 µm.*

This gives some insights on how filaments can adapt to geometrical constraints imposed by its intrinsic curvature. Another study using a similar approach has been conducted on DivIVA, a membrane protein that recruits other factors to the cell division site[227]. Instead of using glass capillaries, they coated the surface of a conical glass micropipette, giving a curvature gradient. They were able to show that DivIVA accumulates at the tip of pipettes in lipid-coated micropipette but had a homogeneous distribution on uncoated ones. The advantage of this configuration as compared with the “glass fiber” methodology is the presence of a curvature gradient. It also allows for the screening of both positive and negative curvatures because the outer and the inner sides of the pipette can be both coated with a bilayer. Similarly, PDMS substrates with a sinusoidal pattern can be used to investigate curvature sensing. This was used for a study involving several proteins including proteins that bind preferentially to positive and negative curvatures and proteins with no preferences (Figure 45)[228].

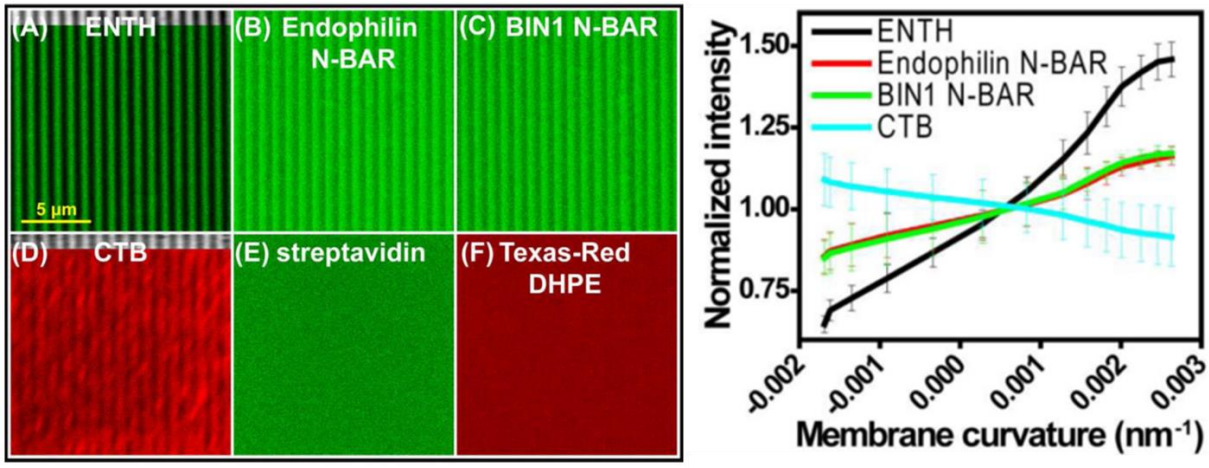


***Figure 45 – Curvature sorting of several proteins on wavy substrates***

*Confocal images of fluorescently-labeled proteins on lipid-coated wavy substrates (left) and the corresponding sorting curves (right).*

The authors were able to show that these proteins show different curvature sensitivities, with the ENTH domains strongly binding to positive curvatures while CTB prefers negative curvatures. During my PhD, I used a similar model system. However, the substrates were made using PDMS microfabrication and not capillary lithography, which is more convenient and less costly. The details of the pattern formation are discussed in section 2.4 and the results obtained in section 3.3.

## 1.6 Summary of the PhD project

The goal of the project is to study the membrane-remodeling and curvature-sensing abilities of the cdc11/12/3/10 complex of *S. cerevisae*. Increasing evidences of these two properties have been found *in vivo.* So far, only a handful of *in vitro* studies have been carried out in the field.

First, we wanted to understand how septins can reshape the membrane and how they can affect its mechanical properties. To do that, we used GUVs as model systems incubated with purified GFP-tagged septin complexes. The first part of my PhD was focused on learning how to reconstitute model lipid systems and optimize them to obtain the best interaction with the septins in a reproducible way.

Once it was achieved, we used a micropipette aspiration assay to assess how septins would tune the biophysical properties of membranes. We thus fixed the tension of GUVs and recorded variations in the projected area of vesicles, inspired by two studies on $\alpha$-synuclein

and endophilin[178,222]. We observed a decrease of the area induced by the presence septins. This led us to formulate two hypotheses: either septins can modify the mechanical properties of the associated membranes by rigidifying it or they could reshape the membrane by utilizing the membrane reservoir present at the low tensions involved. Initial osmotic shock experiments revealed that septin-coated GUVs were able to resist more pressure differences than control GUVs could, strengthening the first hypothesis.

We then decided to quantitatively measure two different mechanical parameters of GUVs in the presence or not of septins: the bending and stretching modulus. To do that, we used a micropipette aspiration and tube pulling assays. Surprisingly, we did not record any significant difference of the bending modulus on septin-coated GUVs and this independently of the method used. We did record however a drop in the stretching modulus in the presence of septins (~ -50).

We then decided to test the second hypothesis, seeing that GUVs incubated with relatively a low concentration of septins (~200 nM) could appear deformed and faceted instead of being spherical. We were able to show that a high concentration of septins (>400 nM) can induce strong membrane remodeling by imposing spike-like deformations with conserved features that we characterized well. Membrane deformation is often associated with curvature sensing as recognized for N-bar domains proteins[229].

To investigate the curvature-sensing ability of septins, we used SLBs deposited on a patterned substrate. These substrates allowed us to investigate curvature ranging from $-5.3$ to $+5.3$ µm$^{-1}$ and observe how septin behave at those curvatures. With confocal microscopy, we were able to show that septins accumulate at positive curvatures compared to negative ones with a maximum around 2µm$^{-1}$. Using SEM, we were able to directly observe how septin filaments assemble and orient on a cylindrical topography curved at the micron scale. On positive curvatures, septin filaments will lay flat and assemble closely together while on negative curvatures, the filament will bend and follow the main axis of curvature. This result, taken together with the confocal data clearly indicates that septins can discriminate between positive and negative curvatures.

With the help of Hervé Isambert, a theoretician at the Curie institute, we developed a model based on filament mechanics and geometry that attempts to describe these results. In this model, we compare the free energy of a number $n$ of flat filaments and the free energy of a number $n$ of bent filaments and can predict different regimes of membrane-associated

septins. We found a minimum of energy for bent filaments around 1 $\mu m^{-1}$ for single and double filaments, which could be related to the micrometric spikes we observed on GUVs. We extended the model to less specific shapes, with two axes of main curvature and predicted that the filaments switch from circumferential to radial orientations as we increase the curvature. This could explain why septin filaments are found adopting different orientations during cell division as the neck constricts. All the results are shown in detail in section 3. With this study, we have achieved a better understanding of the remodeling of septin filaments *in vivo* by providing evidences of different septin behaviors on model membranes.

# 2 Material and methods

## 2.1 Reagents

Common reagents (ethanol, acetone, chloroform, and methanol) were purchased from VWR chemicals. The following lipids were purchased from Avanti polar : 1,2-dioleoyl-sn-glycero-3-phosphoethanolamine **(DOPE, ref 850725P)**, 1,2-dioleoyl-sn-glycero-3-phospho-L-serine **(DOPS, ref 840035)**, L-α-phosphatidylinositol-4,5-bisphosphate **(PI(4,5)P2, ref 840046P)**, L-α-phosphatidylcholine **(EPC, ref 840051P)**, cholesterol **(ref 700000P)**, 1,2-distearoyl-sn-glycero-3-phosphoethanolamine-N-[biotinyl(polyethylene glycol)-2000] **(DSPE-PEG2000-Biotin, ref 880129P)**. The following lipids were purchased from Invitrogen: 1,2-Dihexadecanoyl-sn-Glycero-3-Phosphoethanolamine **(DHPE-Oregon green 488, ref O-12650)**, Bodipy TR-Ceramide **(ref D-7540)**. All lipid powders were stored in a freezer at -80°C. When needed, the powders were solubilized in chloroform and aliquoted then stored in a freezer at -20°C with the exception of PI(4,5)P2 which was solubilized in 70% chloroform and 30% methanol. Aliquots also contained Argon to prevent oxidation of the lipids.

## 2.2 Septin purification

Septin purification was performed by Aurélie Bertin using the following protocol: a GFP-cdc10 mutant has been designed by adding a GFP sequence a C-terminal region of the native yeast cdc10. Yeast septin including cdc11, GFP-cdc10, $(His)_6$-cdc12 and cdc3 were expressed in *E. coli*. A derivative of pACYCDuet-1 (EMD Biosciences) carrying cdc3 and cdc11 and a derivative of pETDuet-1 (EMD Biosciences) carrying cdc10 and $(His)_6$-cdc12 were introduced by DNA-mediated transformation into *E. coli* BL21(DE3). The resulting cotransformants were grown in LB medium containing ampicillin and chloramphenicol to an $A_{600\ nm}$ = 1 and then induced for 20h at 16°C or 3h at 37°C. The cells were then harvested.

After resuspension in 300 mM NaCl, 2 mM MgCl2, 40 mM GDP, 1 mM EDTA, 5 mM β-mercaptoethanol, 0.5% Tween-20, 12% glycerol, 50 mM TrisHCl (pH 8), and lysis of the cells by lysozyme (0.5 $mg.ml^{-1}$) treatment and sonication, the resulting extract was clarified by centrifugation at 10,000 x g for 30 min at 4°C. The $(His)_6$-cdc12-containing septin complexes in the clarified extract were captured by Ni2-affinity chromatography by using either nitrilotriacetic acid-agarose beads (Qiagen) or a HIS-Trap FPLC column (GE Healthcare). After elution with 0.5 M imidazole and 0.5 M NaCl, the eluate was desalted and equilibrated with 50 mM Tris-HCl (pH 8) containing 150 mM NaCl and 0.01% thioglycolate (TCEP) by passage over a PD-10 column (GE Healthcare) preequilibrated with the same buffer. The resulting material was further purified by size exclusion chromatography in the same buffer by using a Superdex 200 column (GE Healthcare). The fractions containing the bulk of the protein were pooled and desalted against 50 mM Tris-HCl (pH 8) by passage over a PD-10 column. The resulting protein sample was applied to a Resource Q anion exchange column (GE Healthcare), which was eluted with a linear salt gradient in the same buffer. The septin complex, containing equimolar amounts of Cdc3, Cdc10, Cdc11, and $(His)_6$-cdc12 eluted at 300 mM NaCl, preventing polymerization of complexes. Purified complexes (yield ≈ 1 mg per liter of LB culture) were used immediately or were flash-frozen and stored at 80°C, at concentrations between 1 µM and 2.5 µM before examination in confocal or scanning electron microscopy.

## 2.3 Formation of SUVs and lipid bilayers

Lipid bilayers were formed by fusing small unilamellar vesicles (SUVs) onto a hydrophilic surface (either glass, polydymethylsiloxane (PDMS) or NOA81 from Norland optics, USA).

To generate the SUVs , 500µg of a lipid mixture (EPC 56.5%, PI(4,5)P2 8%, DOPS 10%, DOPE 10%, cholesterol 15%,Bodipy TR ceramide 0.5%) at 10 $mg.mL^{-1}$ was prepared then dried under nitrogen for 5 min then under vacuum for 30 min to remove any trace of chloroform. The lipids were rehydrated with 125 µL of a (KCl 150 mM, citrate 20 mM pH 4.8) solution for at least 30 min to reach a lipid concentration of 5 $mg.mL^{-1}$. The mixture was vortexed for a few seconds until a white opaque solution was obtained then sonicated using an Elsmasonic s10h ultrasonic cleaning unit (Elma, Germany) until the solution became transparent again. This last step can take from 15 to 45 min. The lipid mixture was then aliquoted into 5 aliquots and stored a -20°C for up to 4 weeks.

To generate the bilayers, an aliquot of SUVs was thawed and 125 µL of the same buffer was added with 1.5 µL of $CaCl_2$ 500 mM for a final lipid concentration of 1 $mg.mL^{-1}$. The glass coverslip was washed with ethanol, water, ethanol again and plasma cleaned for 2 min. A 1x1 cm paraffine square presenting a 0.9x0.9 cm hole was deposited on the glass coverslip to enclose the bilayer. 75 µL of the SUV solution was then deposited on the surface for 1 hour. The glass coverslip was thoroughly washed with the observation buffer at least 5 times and used immediately for observation by adding a septin solution on the bilayer and closing the chamber with a second glass coverslip.

## 2.4 Formation of the patterned substrates

To investigate the ability of septins to binds differently to various curved membranes, we used a novel system developed by the team of Joao Cabral at the Imperial College London. It consists in a PDMS substrate showing a sinusoidal pattern at the surface (Figure 46).

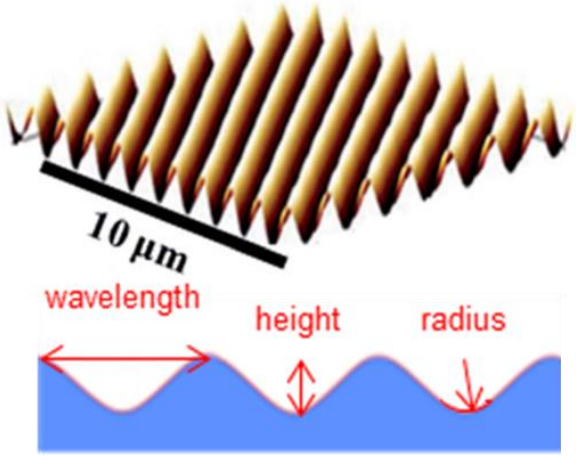


***Figure 46 – Patterned substrate***

*Substrate with a sinusoidal pattern at the micrometric scale on the surface (top) and side view of the substrates highlighting the different characteristics.*

These substrates were obtained by straining a piece of PDMS by 5-30% using two clamps and irradiating it with either Ultraviolet ozonolysis (UVO) (30 to 60 minutes) or plasma (5 to 15 minutes). By cleaving Si-$CH_3$ groups to $SiO_x$, an upper layer with glass like properties is formed. The resulting biphasic material presents two regions of different mechanical properties with a thickness for the top layer ranging from 10 nm after plasma irradiation to 100 nm after UVO irradiation. A release of the stress would result in imprinting a sinusoidal pattern on the surface of the PDMS piece with the following wavelengths: $\lambda_{plasma} = 0.01 - 10$ µm and $\lambda_{UVO} = 10 - 100$ µm. The wavelength and amplitude of the undulations can be

finely tuned by adjusting the irradiation time, gas pressure, irradiation frequency, power and amount of strain. For instance, at a fixed strain, the wavelength of the sample depends logarithmically on the exposure time, and the logarithm rate scales with the power. A more detailed explanation on the relationship between the different applied parameters and the dimensions of the substrates can be found in the literature[230–232].

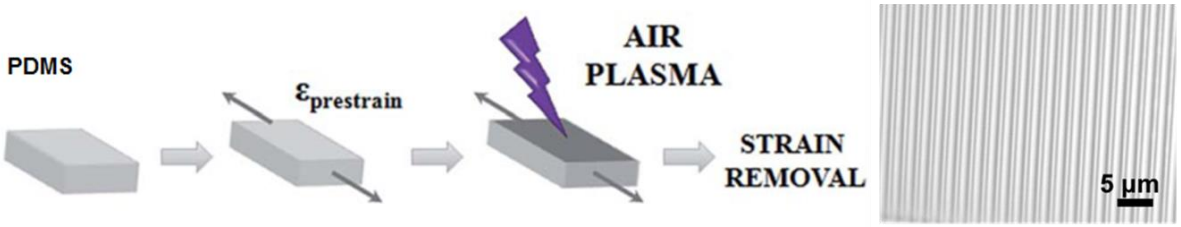


***Figure 47 – The different steps to obtain a patterned substrate***

*Left - Cartoon showing the steps of obtaining the patterned substrates. First a PDMS piece is strained then plasma or UV light is irradiated on it for a certain time. After strain removal the PDMS will keep a sinusoidal pattern at its surface[231]. Right – optical microscopy image of a sample (dimensions are wavelength = 2.12 µm, height = 0.64 µm).*

The substrates were characterized by our collaborators by optical microscopy (Figure 47, right) and their dimensions checked again with confocal microscopy once we received them. I also traveled to London to meet our collaborators for one week and got familiar with the technology. Table 1 shows the characteristics of the samples that were engineered during this stay. Figure 46 shows a definition of the different parameters. The local curvature for each position is the most important parameter. Indeed, we aimed at investigating how septin filaments assemble at a given curvature in the micrometer range.

Since the profile of a cross section of the sample can be described by a simple mathematical function (sine or cosine), we can easily calculate the local curvature of a given function *f(x)* with the following formula:

$$C = \frac{|f''(x)|}{(1 + f'(x)^2)^{\frac{3}{2}}}$$

| Wavelength [µm] | Height [µm] | r [µm] | $C_{max}$ [µm$^{-1}$] |
|---|---|---|---|
| 1.155 | 0.353 | 0.192 | 5.22 |
| 1.818 | 0.595 | 0.282 | 3.55 |
| 2.231 | 0.77 | 0.328 | 3.05 |
| 4.051 | 0.78 | 1.067 | 0.94 |
| 2.52 | 0.512 | 0.629 | 1.59 |
| 15.068 | 2.118 | 5.411 | 0.18 |

***Table 1***

*Different samples and their characteristics. The curvature of the sample is calculated at the top or the bottom of the samples as indicated in Figure 46*

With ‘ and ‘’ denoting the first and second derivative with respect to x respectively. Considering $f(x) = \frac{H}{2}\sin\left(\frac{2\pi}{\lambda}x\right)$ with **H** being the height of the sample and **λ** being its wavelength, the local curvature can be expressed as:

$$C(x) = \frac{\left|\frac{2\pi^2 H}{\lambda^2}\sin\left(\frac{2\pi}{\lambda}x\right)\right|}{\left(1+\frac{\pi^2 H^2}{\lambda^2}\cos\left(\frac{2\pi}{\lambda}x\right)\right)^{\frac{3}{2}}}$$

By using the variable change $x = \frac{\lambda}{2\pi}\sin^{-1}(2\pi z)$, we can also express the curvature as a function of the vertical position $z$:

$$C(z) = \frac{\frac{4\pi^3 H}{\lambda^2}\,z}{\left(1+\frac{\pi^2 H^2}{\lambda^2}\sqrt{1-(2\pi z)^2}\right)^{\frac{3}{2}}}$$

When calculating the maximum curvature at $x = \pm\frac{\lambda}{4}$ or $z = \pm\frac{H}{2}$, which corresponds to the top or the bottom of the sample respectively, the expression becomes:

$$C_{max} = \frac{2\pi^2 H}{\lambda^2}$$

Finally, the samples were obtained by using the original PDMS substrates as a stamp, allowing us to replicate them multiple times. To do that, a glass coverslip was washed with ethanol, water and ethanol again. A small drop (< 5µL) of NOA81 (Norland optic adhesive, USA) was deposited at its center. The original substrates were used as a stamp by pressing the patterned side on the glass coverslip to create a thin layer of NOA81. The resin was exposed to UV light for 10 min and the stamp was removed by carefully peeling it from the glass coverslip. The replicate could then be stored for later use.

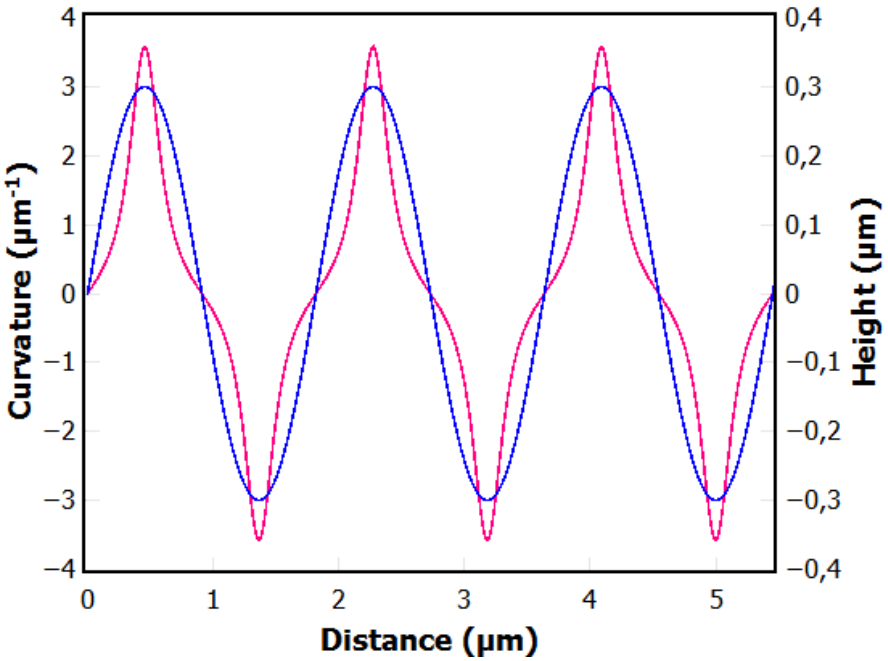


***Figure 48 - Patterned sample profile***

*Height (blue) and curvature (red) of a patterned sample as a function of the distance along the sample. Dimensions are total height* $\mathrm{H} = 0.6$ *µm and wavelength* $\lambda = 1.818$ *µm.*

## 2.5 Formation of Giant unilamellar vesicles

Several methods of GUVs formation have been tested in this study in order to maximize the efficiency of the interaction between septins and the lipid bilayer and will be detailed in the following chapter. The simplest method, and historically the first method, called gentle hydration, consists in depositing a lipid film on a surface and rehydrating it after drying. However this crude method creates a very polydisperse and multilamellar population of vesicles[233], pushing the need for more refined methods to obtain unilamellar vesicles such as gel-assisted swelling or electroformation methods. Microfluidics methods also exist but will not be discussed here as they have not been used during this study.

### 2.5.1 Electroformation on ITO plates

Electroformation methods consist in applying an alternative electrical field on a medium in contact with a lipid film. During electroformation, lipids are first hydrated and self-assemble into a thin film. Then, then film swells dues to forces perpendicular to the film like osmotic forces, line tension and electric fields, leading to the formation of small vesicles. Finally, mechanical stress drives adjacent vesicle to fuse and form GUVs. A method using Indium-tin oxide (ITO) coated glass as electrodes has been proposed in 2011 as a method to produce GUVs on a rather inexpensive material[234]. ITO-coated glass cloverslip (purchased from Sigma Aldrich, USA) were first cleaned with soap then rinsed with ethanol, water and ethanol again. 10µL of the lipid mixture at 1 $mg.mL^{-1}$ were deposited at the center of each plate on the ITO-coated face and spread gently. The plates were then dried under vacuum for 30 min. The two plates were brought together and sealed using capillary sealing paste from Vitrex (GmbH, Germany) (Figure 49).

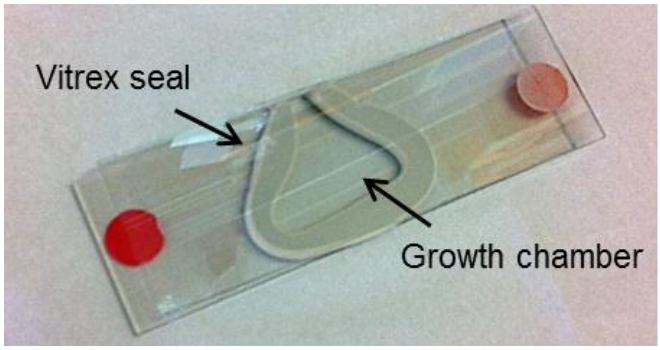


***Figure 49 – ITO plates***

*Growth chamber delimited by a vitrex seal on ITO plates.*

Low salt growth buffer (NaCl 10 mM, sucrose 130 mM, Tris pH 7.6 10 mM) was injected inside the growth chamber which was then sealed hermetically with more Vitrex. Alternative current at 1V and 10Hz was applied for 1 hour at room temperature under a sheet of aluminum to prevent bleaching of fluorescent lipids. The solution containing the growth buffer and the GUVs was collected with a pipette to be observed immediately. While this method is quick and easy, it allows only for low salt concentrations in the growth buffer (<10 mM NaCl). This non-physiological condition is not appropriate for charged lipids[235] and is thus not suitable for large amounts of PI(4,5)P2 which is negatively charged. Although some progress has been made to increase the fraction of charged lipid by using a mixture of extracted lipids and native membranes, the yield and size of vesicles remains low[236]. The electroformation on platinum wires was thus the preferred method of GUV growth.

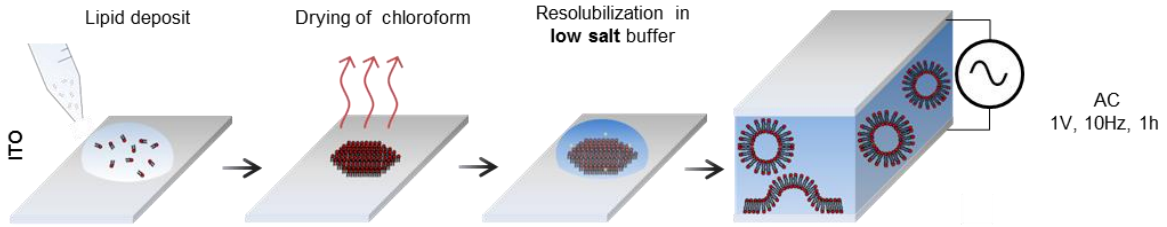


***Figure 50 – ITO method***

*Cartoon of the 4 steps for the formation of GUVs by electroformation between two ITO plates. First, lipids are deposited on a clean ITO plate then dried and resolubilized in the growth buffer. Finally, an AC is applied and GUVs collected.*

### 2.5.2 Electroformation on platinum wires

Needing a method that can incorporate more physiological buffers at higher salt concentration, we decided to turn to electroformation on platinum wires. With this method, platinum wires were used as electrodes[237]. Platinum wires of 0.5 mm in diameter were inserted inside a Teflon chamber equipped with wells to contain the buffer (Figure 51). It utilizes the same principles as the method using ITO plates except that it allows for a higher salt concentration in the growth buffer and higher frequencies while needing lower voltages.

***Figure 51 – Teflon chamber***

*Two platinum wires inserted inside a teflon chamber connected to an AC generator.*

Droplets of the lipid mixture at 3 mg.mL$^{-1}$ were deposited on the wires for a total of 5 µL. The chamber was put under vacuum for 30 minutes to evaporate any residual solvent. A 22x44 mm² coverslip (Menzel-Gläser, Germany) previously cleaned was connected to the bottom with vacuum grease and Vitrex capillary paste was put on the sides of the chamber to prevent any leakage. The growth buffer (NaCl 50 mM, sucrose 50 mM, tris pH 7.6 10 mM)

was injected inside the three wells and the chamber was sealed with another 22x44 mm glass coverslip fixed with vacuum grease. The chamber was connected to an AC generator at 500 Hz and voltages ranging from 250 mV to 600 mV for 6 to 14 hours. These growth conditions have been optimized and will be discussed in section 3.1. GUVs were then collected by gently aspirating the buffer with a pipette at the surface of the wires and used immediately for observation.

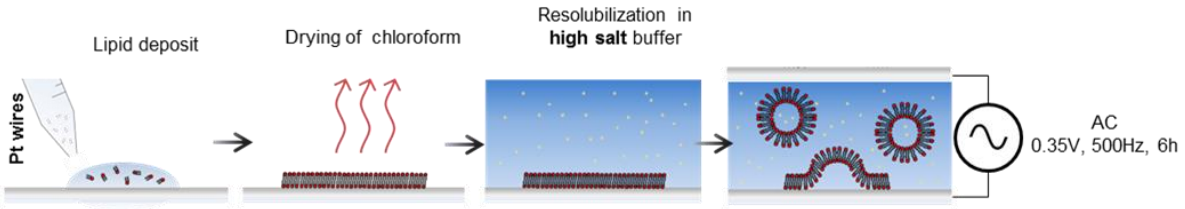


***Figure 52 – Platinum wires method***

*Cartoon of the 4 step for the formation of GUVs by electroformation between two platinum wires.*

Because vesicles have a strong interaction with glass, the coverslip had to be passivated before their observation by microscopy. Glass coverslip were passivated with a β-casein (98% extracted from bovine milk, purchased from sigma Aldrich) solution composed of β-casein 5 mg/mL, NaCl 100 mM, Tris pH 7.4 10 mM for 15 minutes before rinsing twice with a NaCl 75 mM, Tris pH 7.4 10 mM buffer.

### 2.5.3 Gel swelling on PVA

In the recent years, a method to grow GUVs based on gentle hydration of lipids has been developed using an agarose gel as a substrate[238]. Similarly to the method described previously, it allows for physiological buffers at various salt concentrations. The advantages of this method are its simplicity and fast implementation. The protocol we used substituted the agarose gel for a polyvinyl alcohol (PVA) gel[239]. First, the PVA gel (PVA 5% mass, Sucrose 300 mM, NaCl 100 mM) was prepared by heating PVA crystals (purchased from Merck Schuchardt OHG, Germany) in water at 90°C until total solubilization. The gel was then deposited on a 22x22 mm² glass coverslip (VWR international, France) that has been cleaned by rinsing with ethanol, water and ethanol then plasma treated (PDC-32G, Harrick) for at least 1 min. The PVA gel was spread evenly on the coverslip and the excess gel was removed to create a thin, homogeneous 0.5 mm thick layer and heated at 60°C for 50 min. 10 µL of the lipid mixture at 1 $mg.mL^{-1}$ kept in chloroform was deposited on the gel using a

glass Hamilton syringe as slowly as possible to create and thin and homogeneous layer. Lipids were dried for 30 min under vacuum to remove the excess solvent. Lipids were then rehydrated by depositing 1 mL of the growing buffer on the coverslips. After 1h, swelling occurred under a sheet of aluminum to prevent the bleaching of fluorescent lipids. GUVs were finally collected with a pipette for further use.

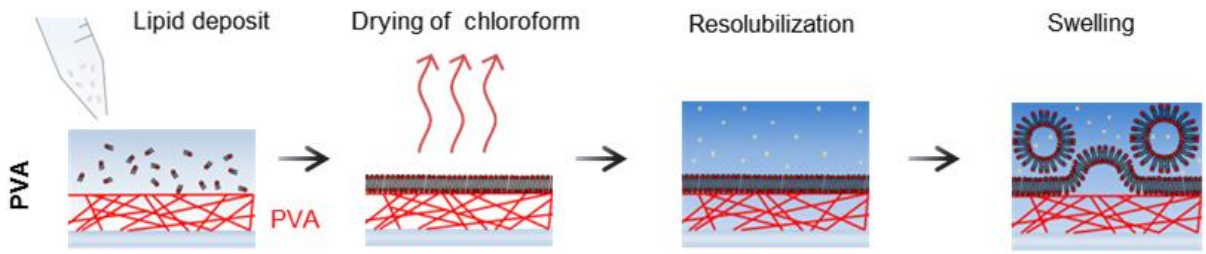


***Figure 53 – PVA method***

*Cartoon of the 4 steps for the formation of GUVs by swelling on a PVA gel. First, the lipid mixture is deposited on a glass coverslip coated with PVA, the lipids are dried then resolubilized in the growth buffer and the GUVs collected after natural swelling.*

## 2.6 Imaging

### 2.6.1 Confocal microscopy

In optical microscopy, the resolution of the system depends on the numerical aperture $NA$, the refractive index of the medium used for the objective $n$, the excitation wavelength $\lambda_{ex}$ and can be expressed through a function called the point spread function (PSF). It corresponds to the image of a single point obtained by the microscope and can be usual ly described by a Gaussian volume with width in the x,y,z directions:

$$\Delta_{x,y} = \frac{\lambda_{ex}}{8n\sin(\alpha)} \; ; \; \Delta_z = \frac{\lambda_{ex}}{4n(1-\cos(\alpha))}$$

With $\alpha = \arcsin\left(\frac{NA}{n}\right)$. A good theoretical estimation of the PSF can be found on the following website: https://svi.nl/NyquistCalculator which also takes into account the type of microscopy.

Our experimental setup is composed of an inverted microscope (Eclipse TE2000, Nikon, Japan) with two objectives (x60 water objective NA=1.27 WD=0.18 mm, and x100 oil objective NA=1.3 WD=0.2 mm) equipped with a C1 confocal head (Nikon, Japan), two lasers (λ= 488 nm argon, λ=543 nm He-Ne) and a photomultiplier tube as detector with two filters (515-30 bandpass nm and 570 longpass) mounted on a dichroic mirror. A third laser line (λ= 1070 nm, P=5W, ytterbium fiber laser) is used to perform optical trapping of small particles (see section 2.7.2). It is also equipped with a halogen lamp used for bright field microscopy, allowing us to look at samples and manipulate them and an infrared camera. Figure 54 shows a schematic of the setup. Images were acquired using the EZ-C1 software developed for this microscope by Nikon. The theoretical dimensions of the PSF for our experimental setup are $\Delta_{x,y} = 46$ nm, $\Delta_z = 119$ nm. It is usually recommended to sample images at a rate 60% lower than the theoretical value, thus we used a vertical spacing of 200 nm to ensure a good sampling.

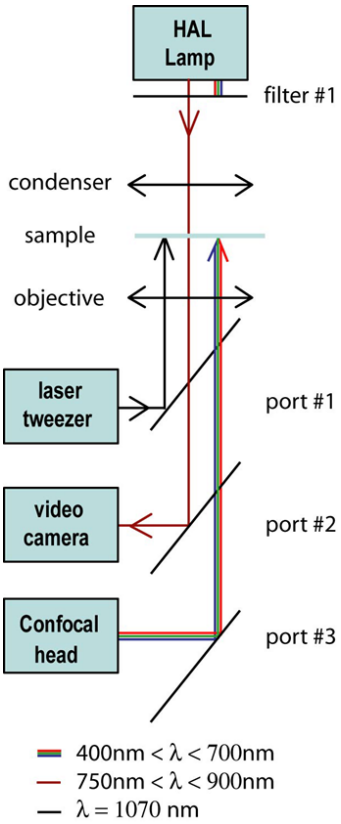


***Figure 54 – Confocal microscope schematics***

*Schematics of our confocal microscope showing the different laser path and filters.*[240]

### 2.6.2 Spinning disk microscopy

Spinning disk microscopy is similar to confocal microscopy but solves the low scanning speed limitation by possessing two disks, one including several pinholes placed before the objective lens and one including several microlenses located after the laser source co aligned with the pinholes, spinning. This creates a planar image of the sample, like a confocal microscope would do, but at several positions simultaneously, thus removing the requirement to scan and providing faster 3D imaging and resolution as compared to classical confocal microscopy.

The spinning disk microscope used was an inverted spinning disk confocal Roper/Nikeon equipped with an EMCCD camera from Andor technology UK, a x100 oil immersion objective (NA=1,4, WD=0,13 mm) and 3 lasers (λ = 491, 561 and 633 nm) as well as 3 filters (ET 525/50m Emission Filter 25mm, ET 595/50m Emission Filter 25mm and ET 655LP Emission Filter 25mm). The experiments were carried out at the BioImaging cell and tissue facility located at the Curie Institute, members of the France-BioImagine national research infrastructure. The dimensions of the theoretical PSF are $\Delta_{x,y} = 43$ nm, $\Delta_z = 131$ nm.

### 2.6.3 Scanning electron microscopy

Conventional optical microscopy is limited in resolution by diffraction as the size of the observed objects becomes comparable with the wavelength of the incoming light (~200 nm). In scanning electron microscopy, electrons are shot through an electron gun by heating and focused through a set of condenser lens to finally interact with the sample where they end up being scattered and deflected towards a detector. The wavelength of the incoming electrons can be expressed by the following relativistic formula:

$$\lambda = \frac{1}{\sqrt{1 + \frac{eU}{2m_0c^2}}} \frac{h}{\sqrt{2m_0eU}}$$

Where e is the elementary charge, $m_0$ the electron mass, c the speed of light, h the planck constant and U the accelerating potential (usually several kV). In our case, we used an accelerating potential of 3 kV resulting in a wavelength of $\lambda_{20kV} = 4.1$ pm which is well below the light diffraction limit. SEM consists in scanning the sample with a focused beam of accelerated electrons. Electrons travel through vacuum before reaching the sample which needs to be a conductive. Thus, the sample necessitates a chemical fixation as well as a

metallization. As incoming electrons interact with the sample, several types of electron (but mainly secondary electrons) are emitted and collected through an electron detector. The contrast and topography are a result of the numbers and angles of the detected electrons.

For chemical fixation, samples were fixed with Glutaraldehyde 2% in sodium cacodylate 0.1M for 15 minutes. The samples were washed three times with sodium cacodylate 0.1M and incubated for 10 minutes with a second fixative (Osmium tetroxide 1% in sodium cacodylate 0.1M). After three washes with water, the samples were incubated with tannic acid 1% for 10 minutes and subsequently washed three time with water before being incubated with Uranyl acetate (1% in water) for 10 minutes. The samples were then dehydrated using baths with increasing ethanol concentrations (50%, 70%, 95%, 100%) and processed using a critical point dryer (CPD 300, LEICA). After being mounted on a sample holder, the samples were coated with 1.1 nm of either tungsten or platinum (ACE 200, LEICA). SEM imaging was performed using a GeminiSEM 500 microscope from Zeiss, Germany at the Institut biologie Paris Seine (Sorbonne Université).

## 2.7 Micromanipulation techniques

### 2.7.1 Micropipette aspiration

The experimental setup used for these experiments is the same confocal microscope as described in section 2.6.1. The microscope in equipped with two micropipette holders bound to 3 microscrews connected to a piezoelectric material that allows manipulating the pipettes inside the observation chamber in 3D, with sub-micrometric precision. The two micropipettes are connected to a water reservoir to apply pressure differences from 2 Pa up to 1000 Pa. These pressures translate into tensions ranging from $10^{-6}$ to $10^{-3}$ $n.m^{-1}$ when applied on GUVs, depending on the different geometrical parameters of the GUV (see section 1.5.3.1 for detailed explanation). The micropipettes were obtained by pulling borosilicate capillaries (1 mm outer diameter, 0.58 inner diameter, Harvard apparatus) with a micropipette puller (P-2000, Sutter instrument) and later forged with a MF-830 microforge (Narishige) with diameters from 2 µm up to 10 µm by melting the tip of the pulled pipette. Typically, one pipette is used to manipulate and apply tension on GUVs while the other is filled with septins and used to locally inject them. For the experiments, the observation chamber was prepared with a 9x35 mm coverslip (VWR International) for the top of the chamber and a 10x30 mm coverslip (VWR International) for the bottom part. The chamber and the micropipettes were

first passivated with a solution of β-casein 5 mg/mL, NaCl 100 mM, Tris pH 7.4 10 mM for 15 min and rinced with the observation buffer NaCl 75 mM, Tris pH 7.4 10 mM. Once the GUVs were added to the medium, the observation chamber was sealed by coating the sides of the chamber with oil, thus preventing evaporation that would lead to concentration changes. A picture of the experimental setup can be found below.

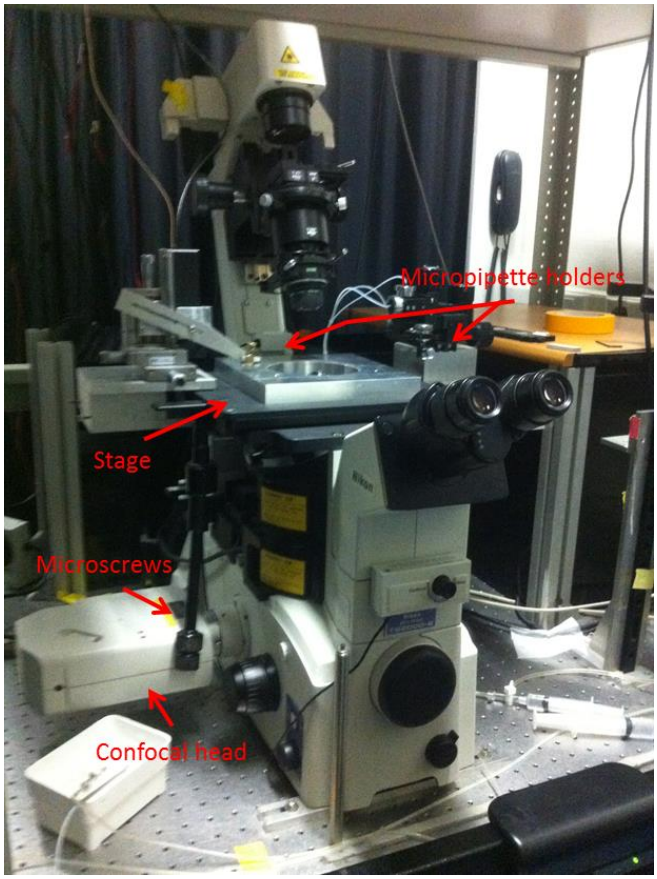


***Figure 55 – Photography of the setup***

### 2.7.2 Optical tweezers

The setup used for optical trapping is the same as described in section 2.6.1. The infrared laser (λ=1070 nm, P=5W) is used to trap the beads. Our optical tweezers were calibrated by measuring the drag force on a trapped bead. The bead was trapped by the optical tweezers and the stage was moved at different frequencies. Knowing the viscosity of the medium $\gamma$, the size of the bead $R_{bead}$ and the velocity of the stage $v$, the drag force can be written as :

$$F_{drag} = 6\pi\gamma R_{bead} v$$

By measuring the displacement of the bead for increasing stage velocities (from 0.1 Hz to 2 Hz), we were able to measure the optical tweezers stiffness at 48 pN.µm$^{-1}$.W$^{-1}$. To pull membrane tubes, we used commercially available streptavidin-coated beads (ThermoFischer) and GUVs doped with 0.5% biotinylated lipids (1,2-dioleoyl-sn-glycero-3-phosphoethanolamine-N-(biotinyl)).

## 2.8 Image analysis

### 2.8.1 Calibration of septin fluorescence and density calculations

In our experiments, it was necessary to be able to measure the concentration and/or density of fluorescent septins present either in the observation chamber or bound to membranes. To calculate the density of GFP-tagged septins from a fluorescence measurement, a calibration step is then necessary to extract the proportionality coefficient between these two values. Indeed, the relationship between the density of fluorescently tagged proteins bound to a GUV $D$ and the measured intensity $I$ can be expressed as:

$$D = \frac{I}{N_f \, a \, I_0}$$

Where $N_f$ is the number of fluorophores per protein (in our case, we have $N_f = 2$ as only cdc10 is tagged with a GFP and each complex contains two copies of each septin subunits), $a$ is the effective GUV area in the confocal volume and $I_0$ is the intensity of a single fluorophore. Since the experimental determination of the product $aI_0$ can be quite challenging, a method was developed using a reference fluorescent lipid incorporated into GUVs with a known density[241]. The fluorescence intensity of the reference lipid compared to the fluorescence intensity of the fluorescent protein in bulk either on micelles or SUVs. In that case the density can be expressed as:

$$D = \frac{I}{N_f \, F \, M_{ref}}$$

Where $F$ is the relative intensity between the protein and the reference lipid and $M_{ref}$product of the area and fluorescence of the reference fluorophore. In dilute solutions, fluorophores follow the Beer-lambert law which can be summarized as a linear relationship between the measured intensity and the concentration in the observed medium. The value of $F$ can then be obtained by comparing the linear coefficient $\alpha$ of two fluorophores of interest.

To perform this calibration, we used Oregon green 488 (OG488) linked to 1,2-Dihexadecanoyl-*sn*-Glycero-3-Phosphoethanolamine (DHPE) purchased Invitrogen (product number O12650) as a reference fluorescent lipid. Our confocal setup as was used (see section 2.6.1). GUVs (composition EPC/Cholesterol 15%/DOPS 10%/ DOPE 10%/ PIP2 8%/OG488 x%) with the reference lipid were prepared using the electroformation on platinum wires method with OG488 densities $x$ varying from 0.1% to 1% and at least 40 GUVs were analyzed for each density (Figure 56, top). The fluorophore density was then calculated assuming a lipid head size of 0.7 ± 0.1 nm² which corresponds to the size of the head of EPC lipids[242]. Taking into account the two leaflets of the bilayer, the density of OG488 is then 2.9 ± 0.4 x$10^6$ lipids per micron squared. This allowed the estimation of $M_{ref} = 0.106 \pm 0.06$ µm². To compare the bulk fluorescence of septins to the bulk fluorescence of OG488, we used SUVs containing OG488. The SUVs were obtained using the protocol described in section 2.3. In that case, Bodipy TR-Ceramide 0.5 % was replaced by 0.5% OG488 (molar fractions) and the solution of SUVs was mixed with the observation buffer (NaCl 75 mM, Tris pH 7.4 10 mM) at concentrations ranging from 0 to 650 nM. The fluorescence of the solution of OG488 was then compared to the fluorescence of fluorescence septin in bulk measured from 0 to 600 nM. The extracted fluorescence yield $F = \frac{\alpha_{GFP}}{\alpha_{OG488}} = 0.57 \pm 0.7$ corresponds to the ratio of the slopes of the two bottom curves presented in Figure 56.

Using those measurements, we were able to extract the proportionality coefficient $\alpha = \frac{1}{N_f F M_{ref}}$ between the septin density and fluorescence $\alpha = 2.6 \pm 0.5$ µm$^{-2}$. This value was measured for a fixed set of parameters (gain, dwelling time, pinhole size and laser power) that were kept the same in all experiments. Thus, a measurement of septin fluorescence can be directly translated into a bound septin density.

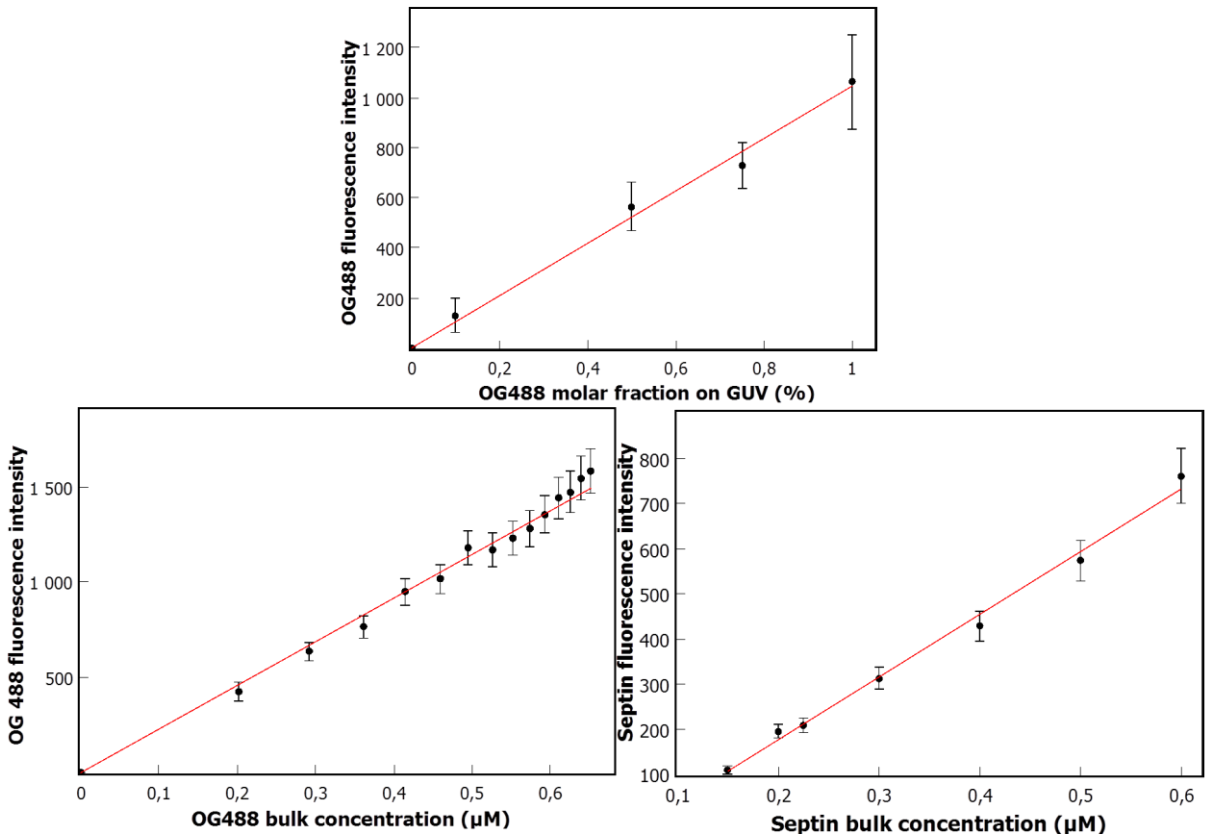


***Figure 56 – Calibration of septin density***

*Top, OG488 fluorescence intensity in GUVs as a function of the density of OG488 incorporated into the GUVs. Bottom left, fluorescence intensity of OG488 micelles in solution as a function of the concentration. Bottom right, fluorescence intensity of septins in solution as a function of the concentration.*

### 2.8.2 Measurement of the dissociation constant $K_d$ for GUVs and SLBs

The microscopic dissociation constant $K_d$ was measured for both GUVs and SLBs to make sure that our systems were never depleted in septins. It corresponds to the septin concentration at which half of the ligands (here, PI(4,5)P2 lipids) are bound to septins. To measure the constant for the two systems, we grew GUVs or coated glass slides with SLBs and mixed them with a solution of septins at increasing concentrations from 0 nM to 900 nM. We then measured the bound septin density with our confocal microscope. Figure 57 shows the result of these experiments. To extract the dissociation constant from these data, we used a standard model and fitted with a Hill equation which can be written as following:

$$[septin]_{bound} = \frac{S_{sat}}{\left(\left(\frac{K_d}{[septin]_{bulk}}\right)^n + 1\right)}$$

Where $[septin]_{bound}$ is the concentration of bound septin, $S_{sat}$ is the saturation concentration, $[septin]_{bulk}$ is the septin concentration in bulk and $n$ is the Hill coefficient. To fit this equation, we used the fitting tool of QtiPlot, a graph plotting software. We were able to extract the following parameters: $K_d GUV = 73 \pm 9$ nm , $S_{sat} GUV = 9200 \pm 400$ µm$^{-2}$ and $n = 1.3$ for GUVs and $K_d SLB = 220 \pm 27$ nm $S_{sat} SLB = 7500 \pm 300$ µm$^{-2}$ and $n = 4$ for SLBs. The dissociation constant is higher in the case of SLBs. This is due to the fact that SLBs are formed by the fusion of SUVs onto the surface. These SUVs are formed by simply mixing the lipid solution and applying mechanical forces by sonication (detailed protocol section 2.3), which is not optimal for a maximized incorporation of PI(4,5)P2 lipids. Hence, less PI(4,5)P2 might be incorporated within supported lipid bilayers. In contrast, GUVs have been grown using electroformation on platinum wires, which protocol has been optimized for the incorporation of charged lipids and the usage of physiological buffers. Knowing the dissociation constant work both our systems, we conducted all of our further experiments at septin concentrations above those values.

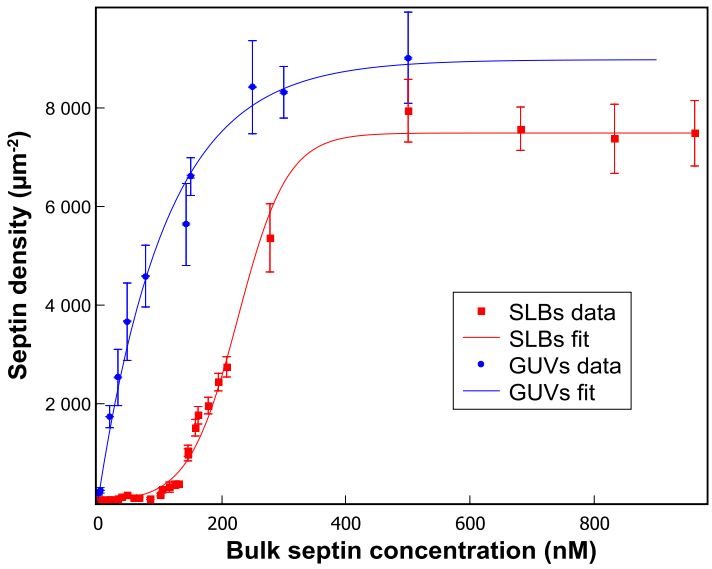


***Figure 57 – Extracting the dissociation constant***

*Bound septin density on GUVs (blue circles) and SLBs (red squares) as a function of the bulk septin concentration and their respective fits using a Hill equation.*

### 2.8.3 Measurement of the persistence length of septin filaments

To obtain the value of $L_p$, we measured the fluctuation of septin filaments constrained on a surface. To do that, budding yeast septins were diluted at 5 nM into a low salt buffer including methylcellulose (20 mM imidazole-HCl at pH 7.4, 1 mM dithiothreitol, 0.1 mM MgATP, 50 mM KCl and 2 mM MgCl2, 1 mM Trolox, 2 mM protocatechuic acid, 0.1 µM protocatechuate 3,4- dioxygenase and 0.1% (w/v) methylcellulose) and inserted into a imaging chamber which surface had been passivated for 45 min using KOH 1M followed by 45 min PLL-PEG 0.2 mg/mL. The filaments were observed using TIRF microscopy. The experiments were conducted by Feng Tsai-Ching and the time-lapse movies shared with us for analysis. To obtain a measurement of the persistence length of a fluctuating filament, we considered a vector $\overrightarrow{A_0}$ at position 0, tangent to the filament and a vector $\overrightarrow{A_L}$ tangent to the filament positioned at an arc length L of $\overrightarrow{A_0}$.Noting $\theta$ the angle between those two vectors, the orientation persistence along the filament can be described as:

$$\langle cos\theta \rangle = e^{\frac{-(d-1)L}{2L_p}}$$

where the brackets denote the average over all starting position 0, d is the dimension (here d=2) and $L_p$ is the persistence length of the filament. The filaments were tracked using the JFilament plug-in of imageJ.

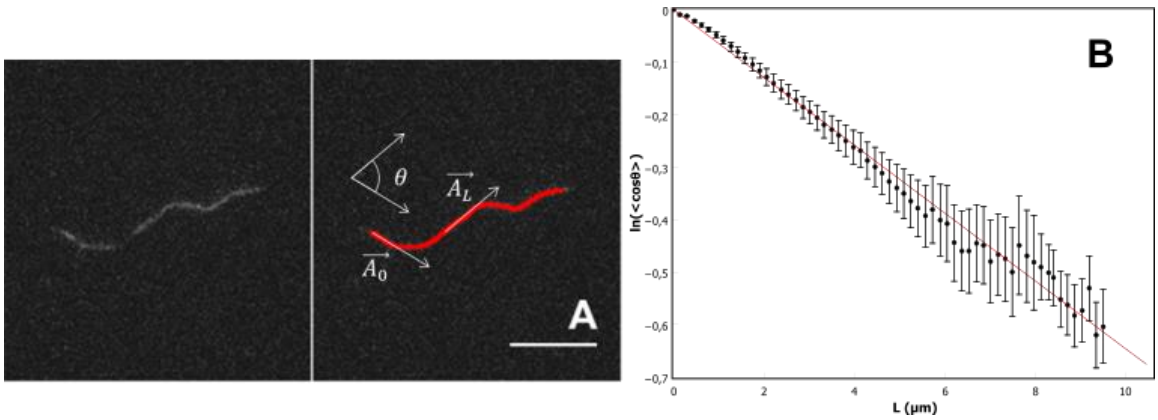


***Figure 58 – Tracked filament***

*A - TIRF image of a septin filament fluctuating on a passivated surface (left) and the same filament tracked with the Jfilament plugin displaying the vectors $\overrightarrow{A_0}$ and $\overrightarrow{A_L}$ as well as the angle θ between them. Scale bar is 5 µm. B – Logarithm of ⟨cosθ⟩ as a function of the arc length L. The slope of the curve gives a*

Figure 58.A shows a raw image of a septin filament and the same filament tracked by the software. This gives 2D coordinates for all points along the tracked filaments. With a MatLab script, we extracted from these coordinates the tangent vectors and calculated $\langle cos\theta \rangle$ for each value of L. We then plotted $\langle cos\theta \rangle$ against L in a semi-log scale and extracted the persistence length value from the slope. Figure 58.B displays the final curve, resulting from an averaging over 300 images corresponding to 12 different septin filaments. We were able to extract the value $L_p = 7.8 \pm 1.1$ µm.

### 2.8.4 Confocal image analysis of GUVs

The fluorescence intensity profiles of GUVs were obtained using the "Radial profile" (source: https://imagej.nih.gov/ij/plugins/radial-profile.html) plug-in of ImageJ. Given a drawn circle on an image, this plug-in calculates the integrated intensity on concentric circles of increasing radii starting from the center of the circle to the outlines of the drawn circle (Figure 59).

GUVs were analyzed by drawing a circle centered on the GUV. A good centering was ensured by looking at the intensity profile. Indeed, an uncentered position of the circle wouldn't give a sharp distribution corresponding to the integrated intensity profile on the GUV. As seen in Figure 59 (middle row), the distribution is not as sharp and slightly skewed towards the outside. This method was used to analyze both the lipid and the septin intensities. For the lipid intensity, a distribution of intensities of the GUVs was plotted. This allowed us to discriminate between single and multilamellar vesicles by comparing the value of the intensities. A baseline value was extracted (corresponding to the intensity value unilamellar vesicles) and any multiple of this value were considered multilamellar. The graph in Figure 59 (bottom) is a distribution of lipid fluorescence intensity and shows two peaks corresponding to unilamellar vesicles and bilamellar vesicles. The mean value for unilamellar vesicles is about 700 a.u. and about 1250 a.u. for bilamellar ones. This corresponds to an average over 262 vesicles and 5 separate experiments. To ensure continuity of these values between experiments, the same imaging conditions have been used throughout my PhD.

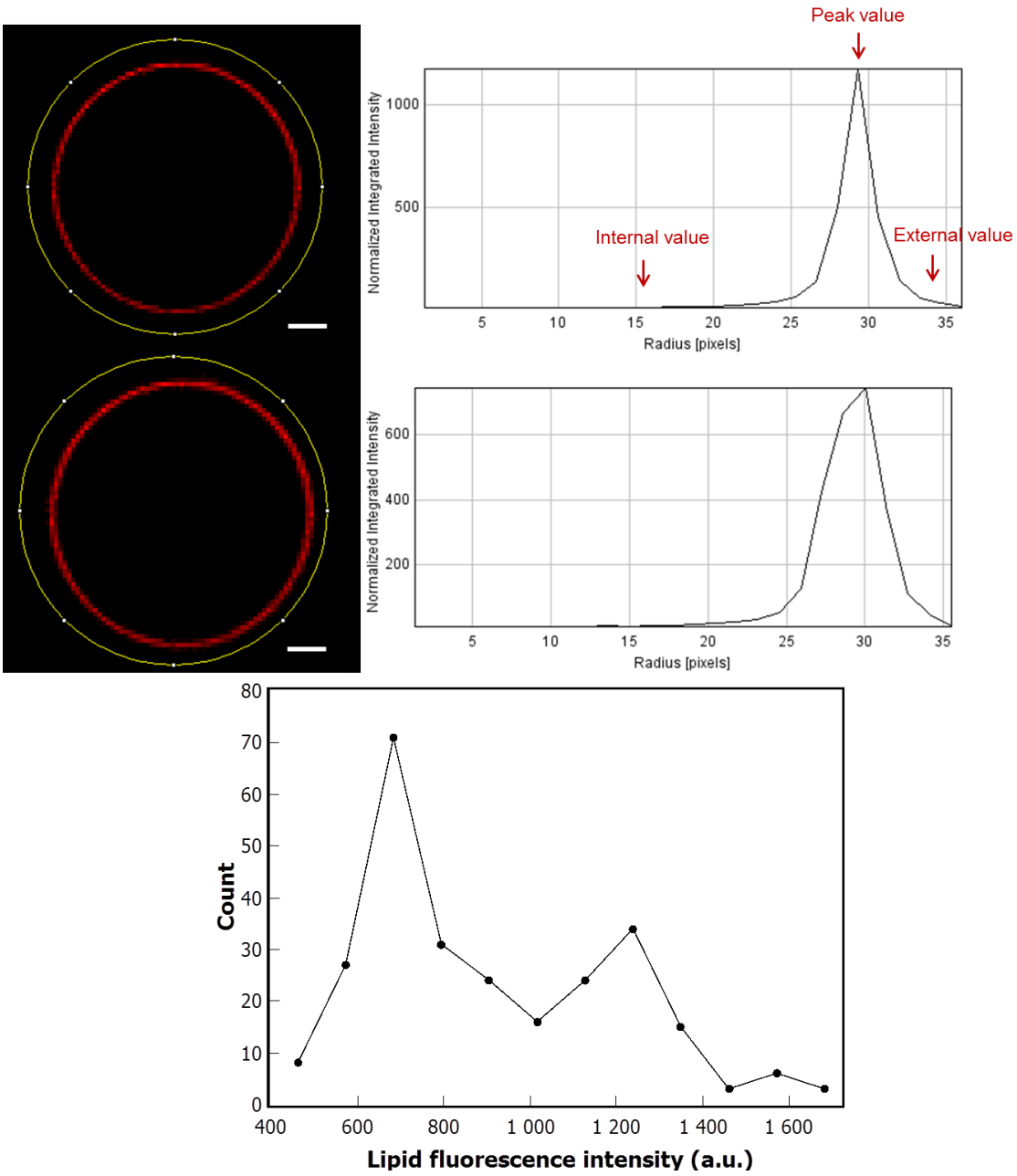


***Figure 59 – Analyzing a GUV fluorescence intensity with ImageJ***

*Left, confocal images of a fluorescent GUV and a circle drawn with the ImageJ software, scale bar = 5µm. Radial intensity profiles obtained by the radial profile plug-in of ImageJ with a centered circular selection (top right) and circular selection slightly off centered (middle right). The internal values correspond to the signal inside the GUV. The peak value corresponds to the signal on the contour of the GUV. The external values correspond to the signal outside the GUV. Bottom, Lipid fluorescence intensity distribution showing two-peaks corresponding to a population of unilamellar vesicles and bilamellar vesicles (N=262).*

### 2.8.5 Confocal image analysis of micropipette aspirated GUVs

To measure the mechanical properties of GUVs (bending and stretching moduli) with the micropipette assay, confocal images of GUVs under different states of tension were analyzed using the EZ-C1 FreeViewer software. Different portions of the GUV were measured (GUV radius, tongue length and micropipette radius) using the built-in measuring tool and the projected area was calculated from these parameters (details of the calculations in section 2.7.1).

### 2.8.6 Confocal image analysis of the patterned substrates

Z-stacks of confocal images of patterned substrates coated with a SLB and septins were analyzed using a MatLab script written specifically to process these images. First, the images were noise filtered by subtracting an image of the recorded noise averaged on 5 frames to the images of interest using ImageJ. Starting with the image corresponding to the top of the sample where the maximum positive curvature is located, images were rotated so that the stripes of the pattern would be vertical (see Figure 60). The position of the first stripe was identified by calculating the local maxima in the Y direction. To achieve that, binning was done by gathering pixels in group of 5 by selecting the 4 closest neighbors and averaging the intensity value. This group of 5 pixels will be referred as the pixel group. Pixel groups were used to partially eliminate bright spots that could punctually be found throughout the sample. Pixel groups were averaged over the full height of the image for different starting position until a local maximum was found. This starting position $[x_i ; y_i]$ would be identified as the position of the first stripe. Knowing the wavelength $\lambda$ of the sample, the intensity of the pixel group would be calculated at every wavelength distance from the starting position $[x_i + n\lambda ; y_i]$ with n being an integer, until the full width of the image was reached. This process was repeated for the starting positions $[x_i ; y_i + 3m]$ with m being another integer until the full image was covered. This would give us a distribution of septin fluorescence intensity at a given curvature from which we would extract a mean value.

Once the first image was analyzed, the process was repeated for the following image in the Z-stack taken at a z-distance of ~300 nm from the previous one and knowing the relationship between the curvature of the sample and the vertical position $z$:

$$C(z) = \frac{\frac{4\pi^3 H}{\lambda^2} z}{\left(1 + \frac{\pi^2 H^2}{\lambda^2}\sqrt{1-(2\pi z)^2}\right)^{\frac{3}{2}}}$$

we were able to extract a plot of the bound septin density, calculated from the fluorescence intensity, versus the curvature of the sample.

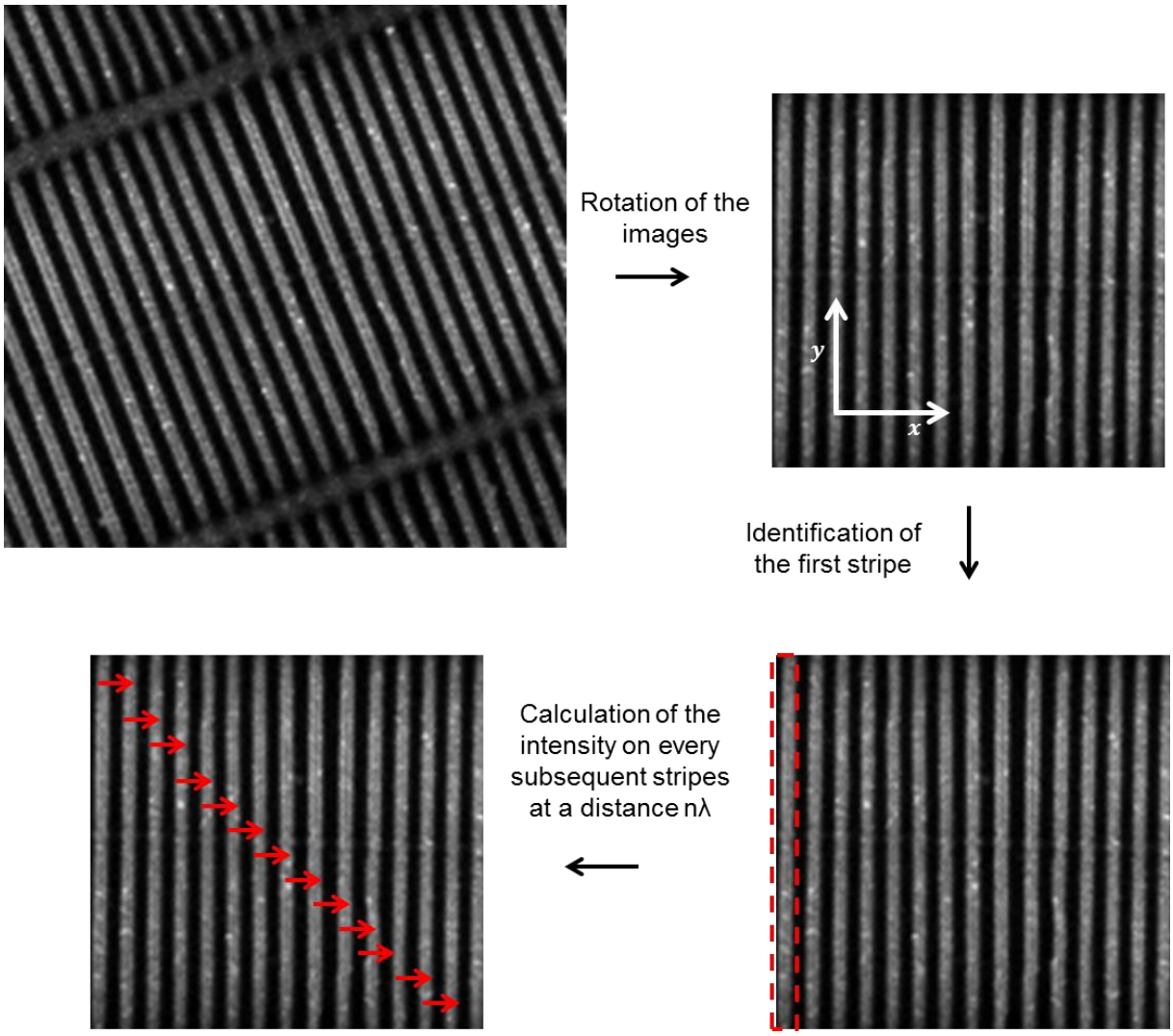


***Figure 60 – Image processing of the patterned substrates***

*Subsequent steps of image processing. First images are rotated then the first stripe containing septin signal is identified at the starting position. Finally, the intensity is calculated and averaged on every position of interest. This process is repeated throughout the Z-stack.*

### 2.8.7 SEM image analysis

SEM images were analyzed to measure the distribution of filament orientation on patterned substrates covered with a SLB and septins. First, impurities formed mainly by unfused vesicles (see Figure 61, top) were filtered from the images. In order to filter the images, ImageJ was used to sharpen the images so that the edges of objects are more easily identifiable by increasing the contrast and the high-frequency information. Then, images were binarized using a manual threshold and segmented to facilitate the identification of objects using the watershed tool. Then, the “analyze particle” tool was used to extract the image of the unfused vesicles from the rest of the image, Figure 62 (bottom) shows a superposition of this image on top of the original image. Circularity range was fixed at 0.3-1 and pixel size at 50 $px^2$ to avoid selecting filaments. The signal of the impurities was then substracted from the signal of the total image, leaving only the signal of the filaments and the surface.

To determine the orientation of both the impurities and the filaments, the plug-in OrientationJ was used (http://bigwww.epfl.ch/demo/orientation). This software allows for a coloration of images depending on the orientation of objects, Figure 62 shows a representation of the same image from Figure 61 color-coded by OrientationJ. To analyze the images, a Gaussian cubic gradient was chosen with a Gaussian windows of 2 pixels, minimum coherency and minimum energy were fixed around 18% and 6% respectively to filter the signal of the surface (although these values could be fixed at different values depending on the natural contrast of the image). Finally, to be able to discriminate the signal coming from the filaments bound to positive curvature (top) and those bound to negative curvature (bottom), the images were segmented and splitted manually in two regions. This allowed us to obtain the angular distribution of pixels belonging to septin filaments either at the top or the bottom of the sample.

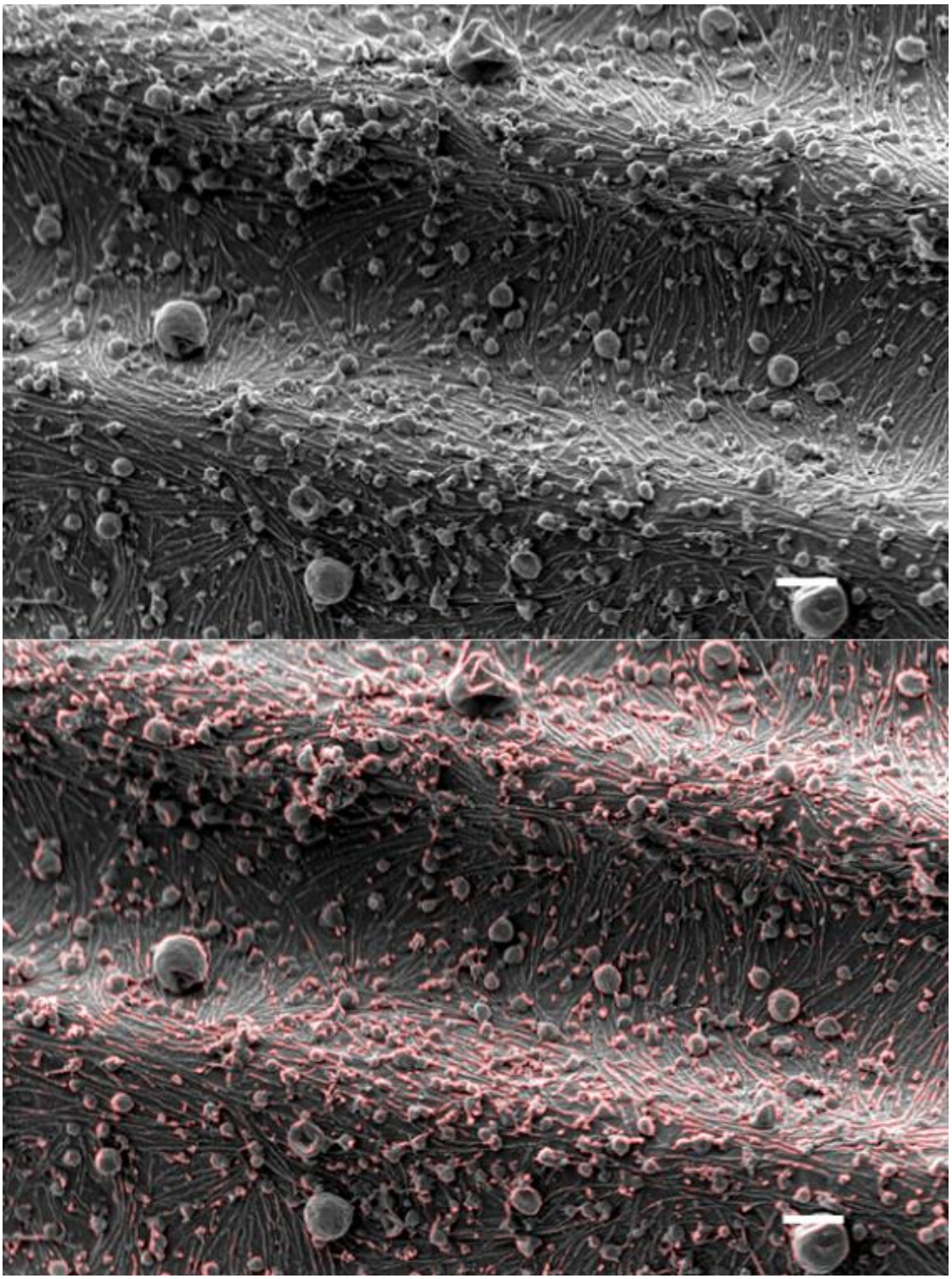

***Figure 61 – SEM image of a patterned sample coated with a SLB and septins***

*SEM images of a patterned sample coated with a SLB and septins. The top corresponds to the raw image and the bottom to the image with the impurities highlighted.*

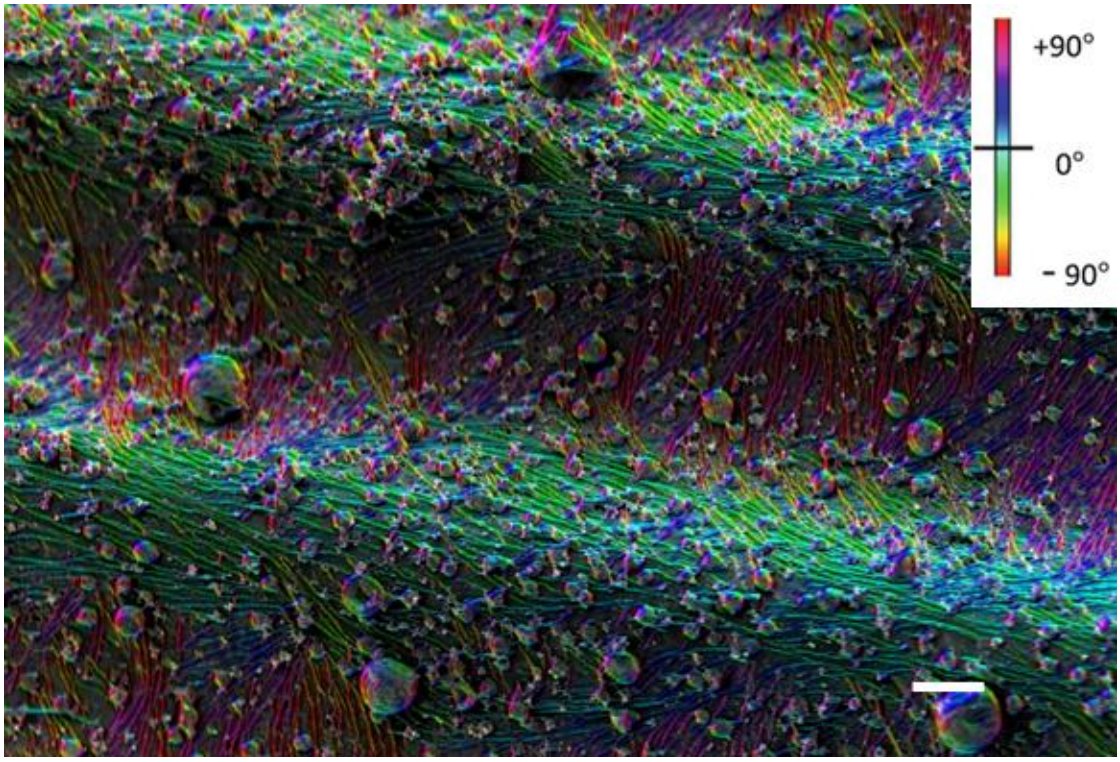


***Figure 62 – Colored coded SEM image***

*Colored coded SEM image of a patterned sample coated with a SLB and septins scale bar = 300 nm.*

# 3 Results

Septins have been shown to be involved in membrane deformations. Consequently, they might have a mechanical role in vivo by maintaining the shape of the membrane[71,72]. Septins also have a preference for specific curvatures both *in vivo* and *in vitro*[177]. However, *in vitro* studies of septin filaments interacting with biomimetic membranes are still scarce. During my PhD, I have used several biophysical model systems to characterize the membrane deformations induced by septins observe how they assemble on micrometric curvatures. In collaboration with Hervé Isambert (PCC, Curie institute), we developed a theoretical model that predicts septin assembly on micrometric structures and their relative orientation and organization.

## 3.1 Optimization of the interaction conditions

The first aim of my work was to optimize the interaction between model membranes and purified septins. Indeed, incorporating PI(4,5)P2 into biomembranes can be quite challenging. In the following chapters, the word “septins” will be used to refer to the cdc11-GFP_cdc10-$(His)_6$_cdc12-cdc3 yeast septin complex. Septins were used as reported to probe the proper incorporation of PI(4,5)P2 into GUVs. This systematic study has been published recently in cytoskeleton as a technical report[243].

### 3.1.1 PI(4,5)P2 incorporation into biomimetic membranes

Phosphoinositides, and especially PI(4,5)P2, are essential for the binding of septins onto membranes and to promote their supramolecullar organization[173]. To optimize the interaction between our systems and purified septins, it was necessary to efficiently incorporate PI(4,5)P2. Additionally, the septin/membrane interaction might be dependent on the concentration of PI(4,5)P2.

We grew GUVs (EPC $64.5 - x$%, Cholesterol 15%, DOPS 10%, DOPC 10%, PI(4,5)P2 $x$%, Bodipy TR-ceramide 0.5%) by electroformation on platinum wires with different amount of PI(4,5)P2 $x$ varying from 0% to 10% in molar fraction. This lipid composition was used to mimic a more physiological composition than a pure EPC/PI(4,5)P2 membrane mixture. GUVs electroformed on platinum wires were incubated with 150 nM septins for 30 minutes. The fluorescence intensity on septin-covered GUVs, proportional to the septin density (see 2.8.2), was then measured. The densities were compared to another reporter: Phospholipase C-δ1 (PLC-δ) known to also specifically interact with PI(4,5)P2 doped vesicles[244]. Relative

fluorescence levels of both septins and PLC-δ were confronted to estimate the quality of the incorporation of PI(4,5)P2 into the GUVs. Figure 63 shows a plot of the mean fluorescence intensity of septins (black circles) or PLC-δ (red squares) on GUVs containing 0%, 3%, 5%, 8% and 10% of PI(4,5)P2 normalized by the mean fluorescence at 10%-PI(4,5)P2 GUVs. The curves show that the relative fluorescence intensity is positively correlated to the amount of PI(4,5)P2 in the GUVs for both reporters as expected. There is relatively little difference between the intensity at 8% and 10% PI(4,5)P2, as seen by the plateau, meaning that growing GUVs with more than 8% of PI(4,5)P2 does not result in the incorporation of more PI(4,5)P2. All subsequent experiments were carried out with a 8% PI(4,5)P2 molar fraction. Surprisingly, we observed a difference between the two reporters incubated with of GUVs in the absence of PI(4,5)P2. Indeed, in the case of septins the signal is undistinguishable from the background noise while using PLC-δ we can observe some signal indicating that there is still some non-specific PLC-δ /membrane interaction even in the absence of PI(4,5)P2. Septins are even more specific to PI(4,5)P2 than PLC- δ. We can thus trust septins as a good reporter for the quality of GUVs doped with PI(4,5)P2.

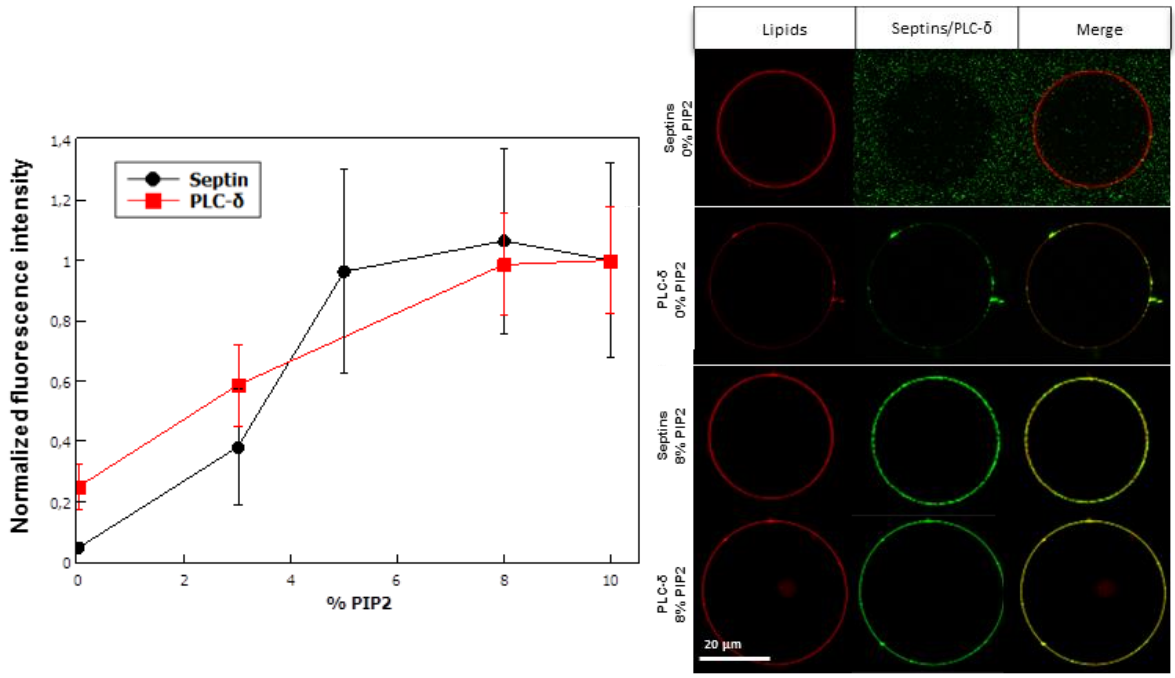


***Figure 63 – Investigating the quality of PI(4,5)P2 incorporation***

*Left graph - Fluorescence intensity of septins (black circles) and PLC-δ (red squares) bound to GUVs doped with different amounts of PI(4,5)P2 normalized by the value at 10%. Each point corresponds to an average over at least 60 GUVs. Right images – Confocal images of GUVs (red) and septins or PLC-δ (green). Septin signal was increased for the top row to indicate the absence of interaction in the clear presence of septins. Scale bare is 20 µm.*

### 3.1.2 Testing of the different growth methods

Using septins as our readout for the quality of our GUVs, we then decided to test different conditions to optimize their interaction starting with 3 different growth methods: swelling in a PVA gel, electroformation on either ITO plates or platinum wires. Each method has its perks and inconvenient in term of yield, growth time and quality and they will be discussed. For each one of them, the same lipid composition was used (EPC 56.5%, Cholesterol 15%, DOPS 10%, DOPC 10%, PI(4,5)P2 8%, Bodipy TR-ceramide 0.5%) as well as the same observation buffer (NaCl 75 mM, Tris pH 7.4 10 mM), septin concentration (150 nM) and microscope settings. For each case, we used two parameters to characterize the quality of the growth: the mean septin density (an indicator of septin binding and indirectly PI(4,5)P2 incorporation) and the proportion of unilamellar, multilamellar and defects-containing vesicles (see Figure 64). A higher septin density and lower defect count indicate a better growth quality.

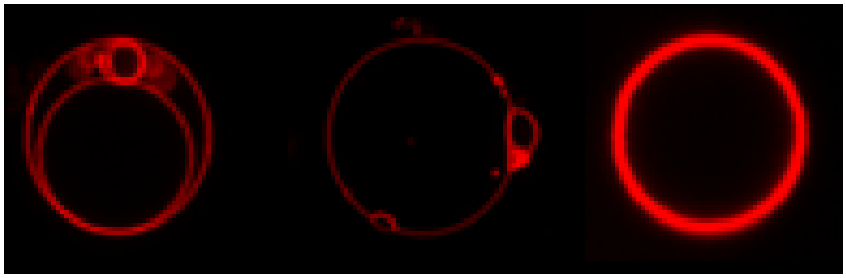

***Figure 64 – Defective vesicles***

*Confocal image of a vesicle containing several objects inside of it (left), a vesicle showing defects on the surface (middle) and a multilamellar vesicle. Such vesicles are not suitable for studying but are unfortunately a byproduct of the growth process.*

We first tested the electroformation method on ITO plates, using a growth buffer composed of 130 mM Sucrose, 10 mM NaCl, Tris pH 7.4 10 mM and applying AC at 10 Hz and 1V for 1h but were unable to obtain any binding of the septins on any of the 4 trials although we did obtain vesicles. This may be due to the fact that this method requires a low salt concentration in the growth buffer (10 mM NaCl) which is not a favorable environment for highly charged lipids such as PI(4,5)P2. Similar results were found with electroformation by platinum wires and PVA-assisted swelling in the absence of salt. Hence, we tested some methods which allow for the usage of higher salt concentrations (50 mM NaCl), namely electroformation on platinum wires and PVA-assisted swelling.

We then decided to compare the electroformation on platinum wires method to the gel swelling on PVA. Electroformed GUVs were grown for 6h at 350 mV and 500 Hz. PVA GUVs were grown in a PVA gel composed of Sucrose 300 mM, NaCl 100 mM, PVA 5% in mass. For both methods the same growth buffer (NaCl 50 mM, Sucrose 50 mM, Tris pH 7.4 10 mM) was used. We found that the mean septin density on GUVs in both case was very similar (5200 ± 600 septins.µm$^{-2}$ for the electroformation and 5500 ± 750 septins.µm$^{-2}$ for the gel-assisted method). However, when we compared the amount of unilamellar and defective vesicles, we found that the electroformation on platinum wire method was much more reliable.

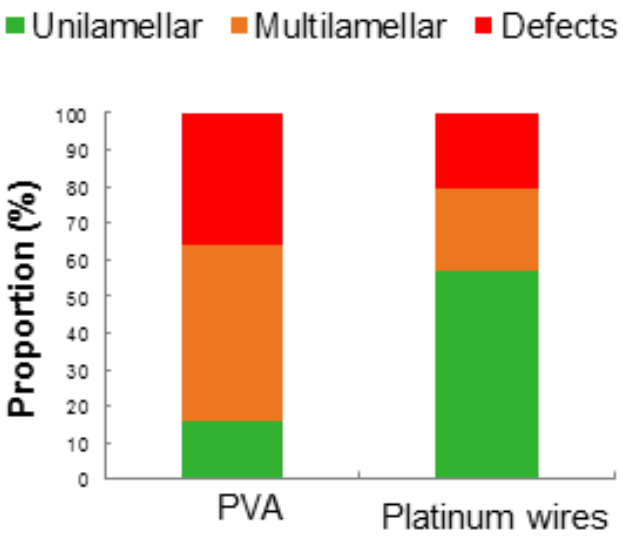


***Figure 65 – Comparing PVA and platinum wires growth***

*Proportion of unilamellar (green), multilamellar (orange) and defective (red) vesicles for PVA-assisted and electroformed on platinum wires grown GUVs.*

For vesicles grown by electroformation on platinum wires, we found 59% of unilamellar, 24% of multilamellar and 17% of defective vesicles while for vesicles grown in PVA the proportion were 18%/48%/35%. This clearly indicates that **growing vesicles on platinum wires is the most adapted method of growth for this lipid composition** and will be the one used throughout the rest of this study.

### 3.1.3 Optimization of the growth conditions by electroformation on platinum wires

After determining the more suitable growth method, we wanted to investigate the effect of different growth parameters: the presence or absence of DOPS, the composition of growth

and observation buffers, the growth time and applied voltage, the drying conditions and finally the observation time after extraction. For all conditions, only the mean septin density was used to make a comparison since the proportions of unilamellar, multilamellar and defective vesicles were relatively constant for all conditions except for the growth time. Figure 66 shows a summary of all the conditions tested.

| **Tested condition** | | | |
|---|---|---|---|
| Drying temperature | Vacuum | Room temperature | 60°C |
| Mean septin density | 5100 ± 700 | 6400 ± 1000 | 2400 ± 300 |
| External buffer composition | 75 mM NaCl | > 300 mM NaCl | > 300 mM sucrose |
| Mean septin density | 5100 ± 600 | 3800 ± 800 | No interaction |
| Negatively charged lipid amount | PI(4,5)P2 0% DOPS 10% | PI(4,5)P2 10% DOPS 0% | PI(4,5)P2 10% DOPS 10% |
| Mean septin density | No interaction | 3300 ± 600 | 5200 ± 600 |

| **Growth condition** | | | | | |
|---|---|---|---|---|---|
| Voltage (mV) for 6h growth | 150 | 250 | 350 | 450 | >450 |
| Mean septin density | 3500 ± 800 | 4200 ± 1000 | 5100 ± 700 | 6400 ± 1000 | No interaction |
| Growth time for 350 mV voltage | 6 | 8 | 10 | 12 | 16 |
| Mean septin density | 4600 ± 500 | 5300 ± 500 | 4100 ± 700 | 4900 ± 900 | 5100 ± 1000 |

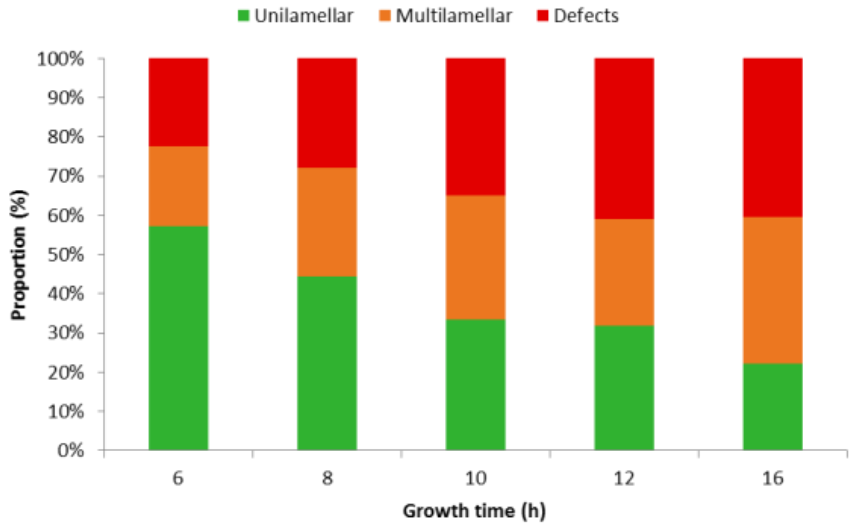


***Figure 66 – Summary of growth conditions for electroformation by platinum wires***

*Mean septin density measured for different conditions of vesicle grown by electroformation en platinum wires. The bottom graph shows the proportions of unilamellar (green), multilamellar (orange) and defectiives (red) vesicles for different growth times at 350 mV. Septin densities are expressed in septins.µm-2.*

The control conditions were used as a baseline. The control conditions correspond to a lipid composition of EPC 56.5%, Cholesterol 15%, DOPS 10%, DOPE 10%, PI(4,5)P2 8%, Bodipy-TR ceramide 0.5% (molar fractions) dried under vacuum for 30 minutes then grown at 350 mV and 500 Hz for 8h in Sucrose 50 mM, NaCl 50 mM, Tris pH 7.4 10 mM. The standard observation buffer is composed of NaCl 75 mM, Tris pH 7.4 10 mM.

One of the crucial steps towards the formation of proper GUVs is the formation of an homogeneous dried lipid film. We decided to compare three drying condition: under vacuum (using a Model 400-14 vacuum pump from VRL), under a hood at room temperature and inside an incubator at 60°C for 30 minutes each time. For a drying under vacuum or a room temperature, the mean septin density was comparable but the overall quality of the growth was lower when dried at room temperature (60% unilamellar vesicles for the drying under vacuum and 40% for the drying at room temperature). Concerning the drying at 60°C, a temperature well above each lipid phase transition, the mean septin interaction was reduced twice.

Second, the effect of the external buffer composition was tested since the the septin-membrane interaction could be regulated by electrostatic, given that PI(4,5)P2 is negatively charged. We tested different amount of NaCl in the observation buffer (each time by balancing the internal buffer to obtain the same osomlarity for both buffers). We also tested different amount of sucrose in the observation buffer as it is known to interact with membranes and proteins[245,246]. For salt concentrations under 300 mM we didn't record any drastic change in the mean septin density while for concentrations above 300 mM it started decreasing. Thus, electrostatic interactions play a role in the septin-PI(4,5)P2. Interestingly, the mean septin density decreased more and more as the sucrose concentration increased in the observation buffer up to the point of screening all the interaction once it reached concentrations above 300 mM. Similarly, sugar is known to inhibit biot-streptavidin/avidin interactions[246].

Next, we tested the influence of another negatively charged (albeit less) lipid: DOPS. As we already discussed, bringing the molar fraction of PI(4,5)P2 to 0% prevents any septin-membrane interaction even in the presence of DOPS 10%. Doping the vesicles with only PI(4,5)P2 and no DOPS resulted in lower mean septin density than with both negatively charged lipids (see Figure 66). It is possible that incorporating monovalent anionic lipid into the membrane facilitates the incorporation of PI(4,5)P2 into the membrane.

Finally, we tested different parameters related to the growth process, namely the voltage and the growth time. Starting at 150 mV, we increased the voltage up to 800 mV and found that the measured mean septin density would increase up to around 6000 septins.$\mu m^{-2}$ for voltages around 400 mV and the interaction would be hindered for voltages above those values. For different growth times from 6h to 16h at 350 mV, the mean septin density was rather similar but the proportions of unilamellar, multilamellar and defective vesicles increased with time (Figure 66). Eventually, we have been able to optimize the GUVs growth, lipid and buffer composition. The following conditions will be used throughout the whole study unless specified otherwise: EPC 56.5%, Cholesterol 15%, DOPS 10%, DOPE 10%, PI(4,5)P2 8%, Bodipy-TR ceramide 0.5% (molar fractions), drying under vacuum for 30 minutes then grown at 350 mV and 500 Hz for 8h in Sucrose 50 mM, NaCl 50 mM, Tris pH 7.4 10 mM. Observation buffer is  NaCl 75 mM, Tris pH 7.4 10 mM.

### 3.1.4 GUV degradation over time

While optimizing the growth conditions, I have noticed that GUVs did not interact with septins after a significant time following their preparation. To clarify this timeframe over which GUVs are still usable, we tested the stability of our GUVs over time. Guvs were incubated with septins right after production of every hour after. The mean septin density was measured each time. Between each experiment, only a fraction of the GUVs was extracted for observation and the rest was stored at +4°C to minimize degradation.. The results are reported in Figure 67.

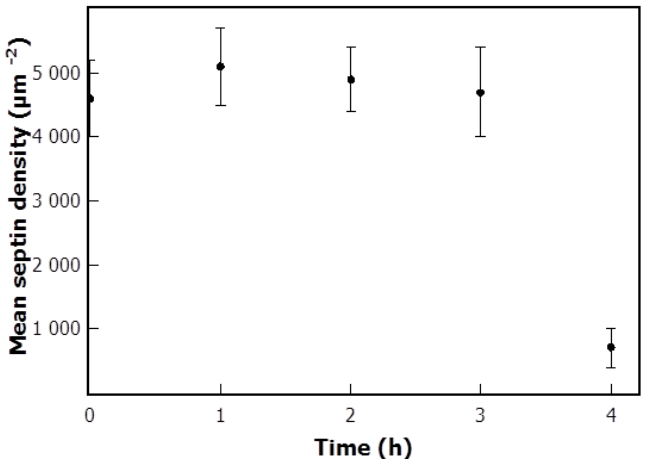


***Figure 67 – GUVs degradation over time***

*Mean septin density measured on GUV at different times after extraction showing a significant drop around 4h.*

The septin density remained constant up to 3 hours after GUVs production but after 4 hours, the GUVs started to show a drastic decrease of the bound septin density, down to 700 septins.$\mu m^{-2}$, thus indicating very weak interaction. Therefore, after 4 hours, the GUVs were altered. This was consistent over 3 different trials. We investigated the nature of this fast degradation. Since septins interact with PI(4,5)P2 specifically, one could reasonably assume that the altered interaction over time could be linked to a degradation of PI(4,5)P2. One could also hypothesize that PI(4,5)P2 leaves the GUVs out and is solubilized. To test this hypothesis, GUVs doped with 0.5% fluorescent and 7.5% non-fluorescent PI(4,5)P2 were produced. We then recorded the changes in fluorescence over time. As a control, we used the standard conditions and recorded the changes in fluorescence of Bodipy TR-ceramide GUVs. Results are shown in Figure 68.

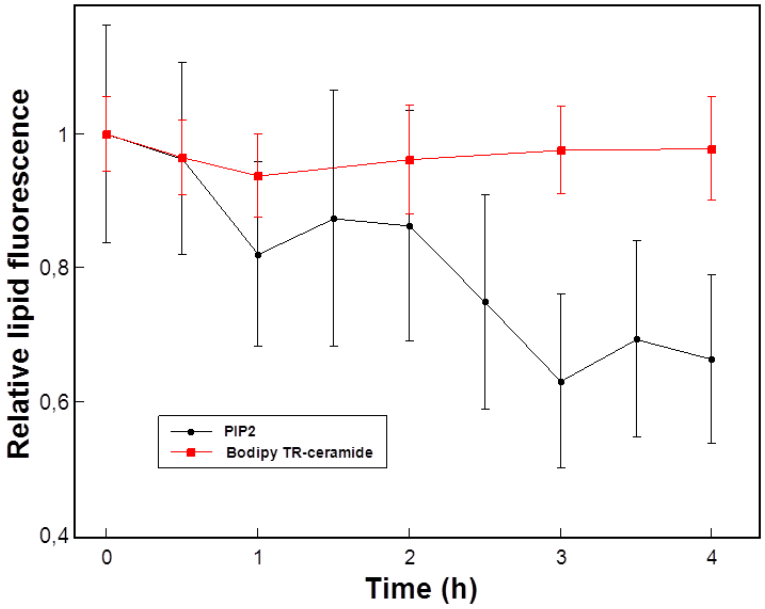


***Figure 68 – PI(4,5)P2 solubilizes over time***

*Variation of the fluorescence of PI(4,5)P2 (black dots) and Bodipy TR-ceramide (red squares) over time. The value is normalized by the initial fluorescence value.*

While the fluorescence levels of GUVs containing Bodipy TR-ceramide remained constant over the course of 4 hours, the signal intensity of GUVs containing fluorescent PI(4,5)P2 droped by approximately 30% over 4 hours.

The observed changes in fluorescence do not come from bleaching but most likely from lipid solubilization. This hypothesis was confirmed by mixing together two batches of GUVs grown with different fluorescent PI(4,5)P2. GUVs doped with 0.5% of either red or green fluorescent PI(4,5)P2 and 7.5% of non-fluorescent PI(4,5)P2 were grown. We then measured the incorporation of solubilized fluorescent PI(4,5)P2 by measuring the evolution of green signal of initially red-only GUVs and the red signal of initially green-only GUVs. With time, red GUVs started to show green signal and green GUVs started to show red signal. The results are shown in Figure 69.

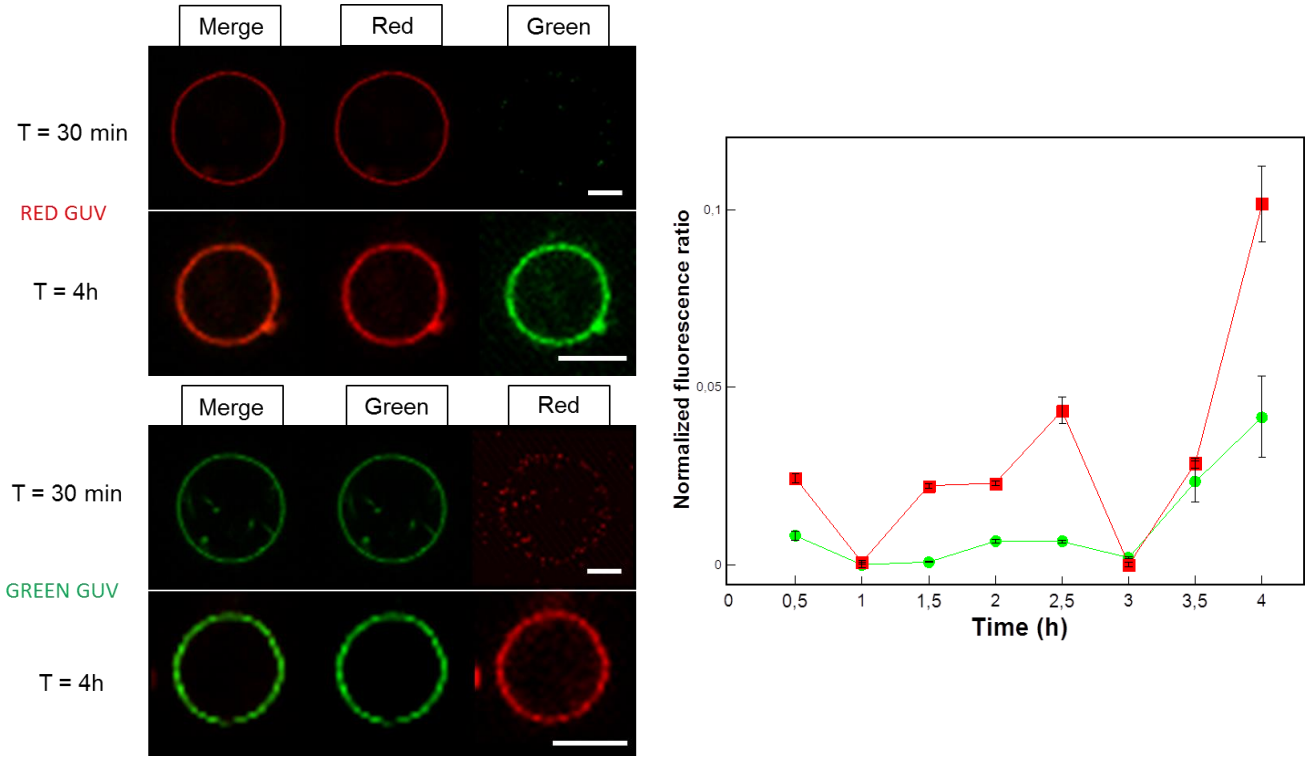


***Figure 69 – Mixing two population of GUVs containing fluorescent PI(4,5)P2***

*Left – Confocal images of red (top) GUVs at T=30 min and T=4 h after extraction, the constrast of the green signal has been greatly increased on the third row and confocal images of green (bottom) GUVs at T=30 min and T=4 h after extraction, the constrast of the red signal has been grealy increased on the third row. Scale bars are 3 µm. Right - Ratio of green over red fluorescence signal in initially red-only GUVs (green circles) and red over green fluorescence signal in initially green-only GUVs (red squares).*

As we can see on the confocal images (Figure 69), red (respectively green) GUVs display no green (respectively red) signal at short times after extraction. At longer times, we start to visualize red on green GUVs and vice versa (the contrast has been increased). This is displayed more quantitatively in the measurement of the fluorescence ratio where we see a

3-fold increase after 4h for both GUVs populations. This evidences that the PI(4,5)P2 in both GUVs populations is solubilized and exchanged.

If we consider that fluorescent PI(4,5)P2 behaves similarly as the non-fluorescent one, we can estimate from the data in Figure 68 that only 70% of the initial PI(4,5)P2 remains in the membrane whereas the 30% are solubilized after 4 hours. This would indicates that from the supposed 8% initial PI(4,5)P2 molar fraction, only 5,6% are still present. Even though it could account for a small reduction in the measured septin density after 4 hours, this alone cannot explain the absence of interaction we observed in our other experiments. Moreover, the fluorescence of the initial color was still measurable even after 4 hours, indicating that a proportion of the PI(4,5)P2 did not get solubilized. To explore other possibilities such as PI(4,5)P2 hydrolysis into PIP, we performed spectrometry lipodomics experiments on pure lipids in aqueous solution (lipodomics facility in Toulouse, F. Viars, J. Bertrand-Michel). Solutions of lipids in Tris pH8 10 mM were flash frozen at different times after solubilization and sent to perform spectrometry. While we couldn't measure the absolute value of PI(4,5)P2 and PIP concentrations, we were able to get the relative concentrations over time. The results are shown in Figure 70.

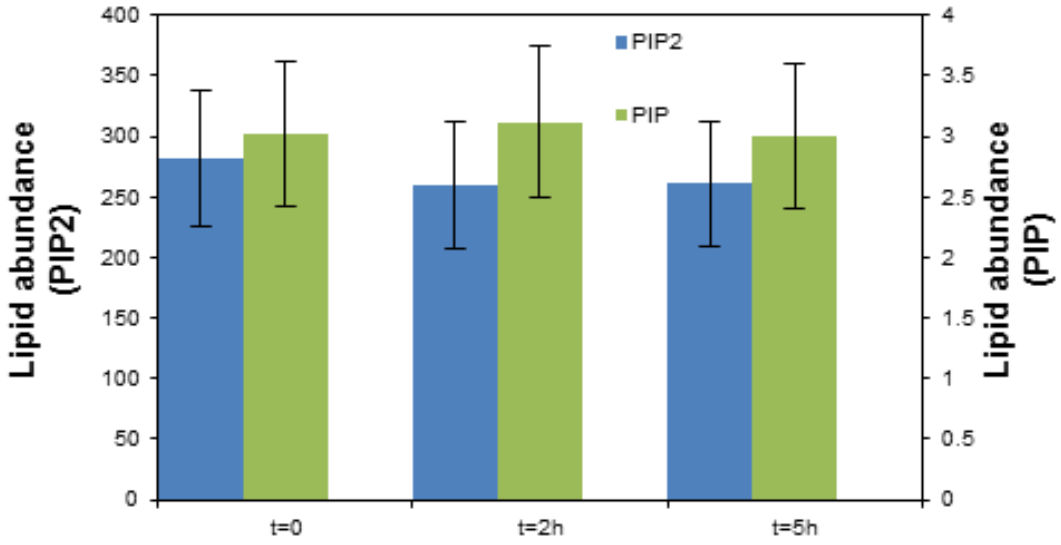


***Figure 70 – Spectrometry experiment***

*Abundance of PI(4,5)P2 and PIP in aqueous solutions over time. No unit.*

We measured no significant difference in the level of hydrolysis of PI(4,5)P2 and abundance of PIP even after 5 hours. Hence, PI(4,5)P2 does not get significantly hydrolyzed. Another possible mechanisms of PI(4,5)P2 degradation is by the formation of free radical through

oxidation[247]. For technical reasons, the lipodomics facility could not test for oxidation. For all further experiments, GUVs were utilized right after extraction and never for more than 4 hours.

To conclude, we saw that several parameters related to the growth of GUVs (voltage, composition, time of growth…) as well as external parameters (buffer composition, time after GUV extraction) play a role in tuning the interaction between the membrane and septins. Now that the interaction conditions have been optimized, we can confidently use those biomimetic systems to explore the different properties of septin-membrane interaction, namely their curvature sensing and membrane deformations capabilities.

## Summary

- **Septins interaction with PI(4,5)P2 is more selective than PLC-δ.**
- **GUVs formation has been optimized with electroformation on platinum wires being the most adapted method.**
- **GUVs lose their integrity after 4 hours, which arises mainly from PI(4,5)P2 resolubilization.**

## 3.2 Membrane deformation by septins

In cells, septins are located at places where the membrane is deformed. The most striking example is during cytokinesis where the neck between the two cells is constricted to a thin tube about 1 µm in diameter. However, it is still not clear whether septins are directly involved in those deformations or not. The constriction of the neck seems to arise mostly from the acto-myosin contractile ring. In rare occasion during the optimization process, we could observe GUVs having peculiar morphologies instead of the regular spherical shape that one could expect (see Figure 71). Indeed, at concentrations around 200 nM, septins would sometime induce deformations on GUVs such as sharp angles, flattened vesicles and invaginations. These deformations were static and not the result of thermal fluctuations. These morphologies were still rare. Less than 1% of the GUVs would display such shapes while the rest would display a regular spherical shape. Nevertheless, their frequency increased with the septin concentration increased. This led us to hypothesize that septins could form rigid scaffold on GUVs that would constrain the GUVs into these interesting shapes. To test this hypothesis we performed several experiment aiming to investigate the ability of septin to deform and rigidify vesicles starting with osmotic shocks experiments.

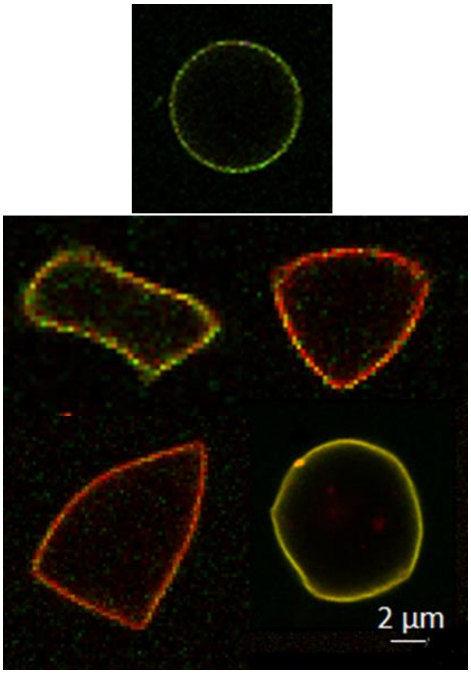


***Figure 71 – Septin induced GUV deformations***

*GUVs displaying sharp angles induced by the presence of septins, instead of their usual spherical shape (top).*

### 3.2.1 Osmotic shock experiments

In order to test the possibility that septins could create rigid scaffolds on membranes, we first performed osmotic shock experiments. We grew vesicles using the standard procedure and incubated them in an isotonic buffer inside the observation chamber (NaCl 75 mM, Tris pH 7.4 10 mM) with 200 nM septins or without septins as control. We then added a hypo-osmotic or hyper-osmotic solution and waited 15 minutes for homogenization and equilibration. The hypo-osmotic and hyper-osmotic solutions consisted of Tris pH 7.4 10 mM and NaCl 1 M Tris pH 7.4 10 mM respectively, added gradually. Using confocal microscopy, we collected images of GUVs under different osmolar stresses. The results are reported in Figure 72.

For hypo-osmotic solutions, an osmotic difference about 20% (30 mOsm) induced vesicle bursting in the control while septin-coated GUVs resisted the osmotic difference and this up to a 50% osmotic pressure difference (75 mOsm). For osmotic differences beyond that point, GUVs busted even when coated with septins. Using of hyper-osmotic solutions, control GUVs became wobbly up to a 40% osmotic pressure difference (60 mOsm). An osmotic pressure difference greater than 40% was sufficient to make the vesicles collapse and thus only lumps of lipids were found in the observation chamber. However, in the presence of septins, GUVs remained spherical for osmotic pressure differences up to 80% (120 mOsm). After a 100% osmotic pressure difference (150 mOsm), deformed vesicles started to be observable. Their shapes were reminiscent of vesicles collapsing but still maintained an internal volume instead of fully collapsing like a naked vesicle would (see Figure 72). This phenomenon persisted for osmotic pressure differences up to 300% (450 mOsm) indicating the capacity of septins to create a rigid shell around the GUVs and resist mechanical stress.

Given these first results, we wanted to further investigate the role of septins in membrane deformations and their impact on mechanical properties. Thus, we used hallmark systems to measure two mechanical properties of GUVs: the bending modulus and the stretching modulus.

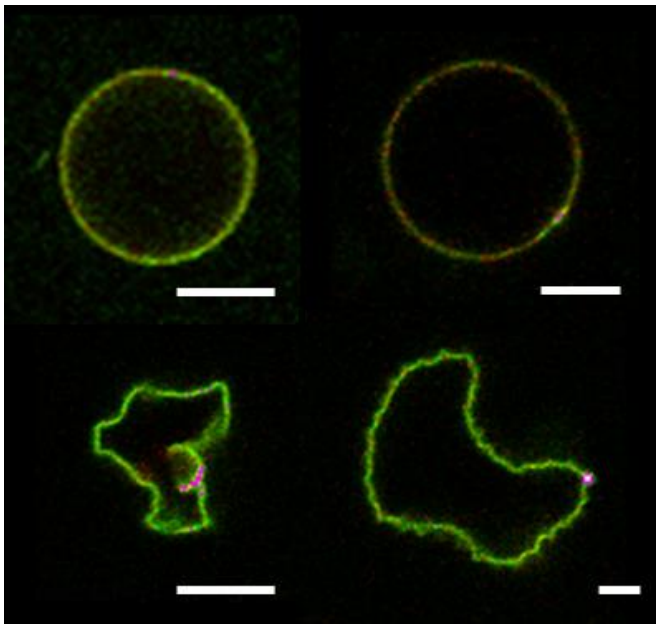

***Figure 72 – GUVs under osmotic shocks***

*Confocal images of septin-coated vesicles in an isoosmotic solution (top left), an hypo-osmotic solution (top right, osmolarity difference = 75 mOsm) and an hyper-osmotic solution (bottom left and right, osmolarity difference = 300 mOsm). Scale bars = 5 µm.*

### 3.2.2 Pipette aspiration as a way to measure membrane reshaping

Following the work of Baumgart[179,222] on α-synuclein and the N-BAR domain of endophilin (a protein and protein domain known to induce membrane deformation and sense curvature[64,229,248,249]), we used a micropipette assay to monitor in time a reshaping of the membranes induced by septins. A first micropipette was used to hold a GUV while a second one was used to inject septins locally. Confocal microscopy was used to record any changes in the size of the vesicles. After inserting them in the observation chamber, GUVs were held at a fixed tension (at a tension low enough to still be in the thermal regime where the GUV has a fluctuating membrane reservoir, $\sigma < 0.5$ mN.m$^{-1}$). Confocal images of the GUV were taken before the onset of protein injection sequentially every minute until the GUV was saturated with septins. The flow of the injection pipette was carefully regulated. An excessively strong flow would induce fast tongue retraction (in the order of a few seconds) because of the induced shear stress. It can also induce fluctuations that perturb the measurement. The septin concentration inside the injection pipette was about 400 nM which translates into a local bulk concentration of 200 nM around the GUV. The salt concentration inside the pipette was 75 mM to match the osmolarity of the observation buffer. We were able to record changes in the projected area and volume (correlated to a change in the

length of the part inside the pipette called the tongue and the diameter of the GUV) as the density of bound septin increased for $N = 54$ GUVs for 6 separate experiments. Figure 73 shows a typical experiment and the corresponding curve. As we can see on the curve in Figure 73, septins accumulate quickly on the membrane and saturate after a few minutes. This causes the tongue to retract which we characterize by a reduction of the projected area. This happened at a fixed volume, excluding any volume effect like changes in pressure due to osmolarity differences. In the meantime, the projected surface area decreases.

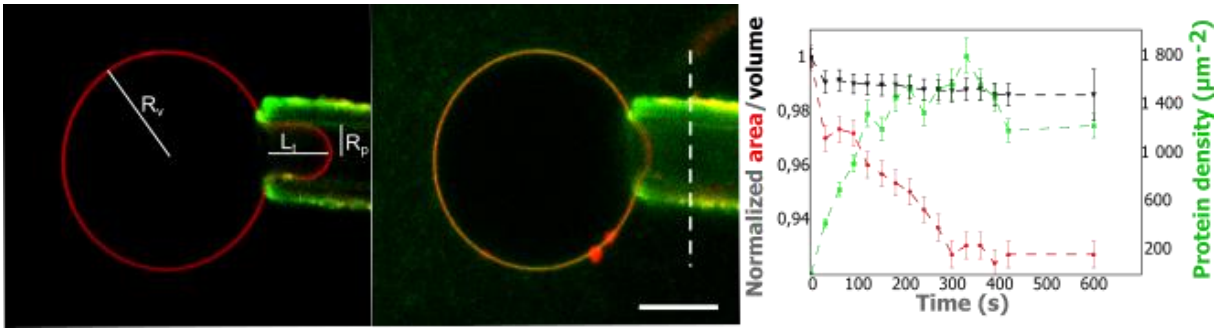


***Figure 73 – Membrane remodeling by pipette aspiration***

*Left – confocal images of a GUV before (left) and after (right, t = 10 min) septin injection. The white dashed line corresponds to the initial length of the tongue, scale bar = 10 µm. Right – Plot of the variation of the area and volume normalized by their initial value and the bound septin density as a function of time. The black dots correspond to the volume, the green dots to the bound septin density and the red dots to the projected area.*

Once the GUVs reached saturation (approximately after 10 minutes), the injection was stopped. The injection pipette was then moved away from the GUV. A final image was taken 1 minute after displacing the pipette and any subsequent area change was attributed to the injection pipette (osmolarity or high flow effects). If this was the case, the experiment was discarded and some adjustments were made (more gentle flow, osmolarity changes). This usually applied to the few first trials. Once the flow of the injection pipette was set and controlled, the next experiments did not need further adjustment. For each experiment, the projected area and volume were measured accord to the method described in section 1.5.3.1. We measured changes in projected area around 1-2% and up to 7%.

To understand how relevant these values are, we need to calculate the energy necessary for a pore to rupture a vesicle. Let us consider a lipid vesicle of radius $R_v \approx 10\mu m$ constituted of neutral lipids only, neglecting possible electrostatic interactions. Under tension, a pore of radius $r$ can be nucleated and its energy is linked to parameters: its line tension $\Gamma$ and its

surface tension $\sigma$, this gives us a critical pore radius after which rupture is initiated. Using typical values found in the literature, the critical radius can be estimated as $r_c \approx 100$ nm. If we consider an expansion of the vesicle which increase the length of the perimeter $P$ by $r_c$. The new radius can be written as $R_v' = R_v + \frac{r_c}{2\pi}$ and the relative area expansion $\frac{\Delta A}{A_0} = \frac{4\pi\left(R_v+\frac{r_c}{2\pi}\right)^2 - 4\pi R_v}{4\pi {R_v}^2} \approx 0.9\%$ . A 0.9% increase in surface area would be enough to nucleate a pore that would generate vesicle rupture. This implies that even small membrane remodeling processes that modify the total area by a few percent are relevant.

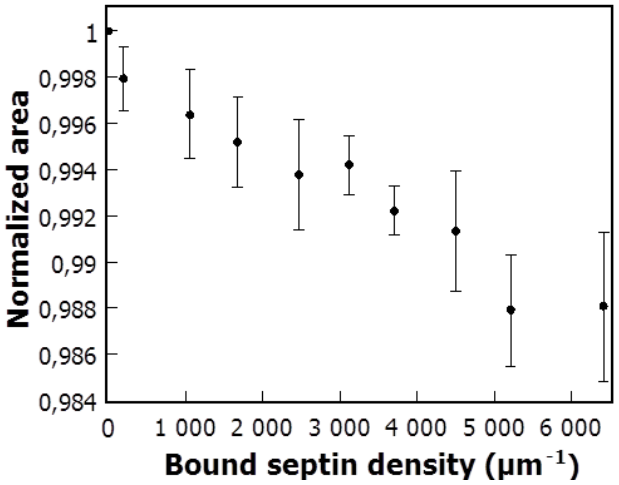


***Figure 74 – Average area reduction***

*Area reduction normalized by the initial area after septin injection. All points are averaged over 54 GUVs. Error bars represent standard deviations.*

Figure 74 reports for the experiments. Each point is an average out of 54 GUVs. For each GUV, we measured the bound density and the corresponding surface area variation. Matching values of bound septin density were grouped to obtain average values. On average, the surface area of the GUVs is reduced by 1.5% after saturation of bound septins which occurs at 6400 septins.µm$^{-1}$. The fact that septins induce a variation of the projected area was consistent over the 54 GUVs observed and led us to formulate two hypotheses:

First, the interaction with septins could directly affect the mechanical properties of the membrane and rigidify it, making it more difficult to create a tongue inside the pipette for a given applied tension. This would result in a shorter tongue. *In vivo*, membrane specific geometries need to be stable throughout a whole process (for instance, the constriction site

during cell division for about 2 hours). We hypothesize that the septin network could help increasing locally the membrane rigidity to maintain a given shape and geometry.

Second, septins could deform and remodel the membrane. Indeed, in the low tension regime investigated in these experiments, membrane undulations persist and septins could create small membrane deformations in the same fashion as BAR domain proteins that are able to induce membrane protrusion. This hypothesis would be supported by the *in vivo* observation that septins regulate membrane shape in migrating T cells and axons[71,72]. We decided to test both hypotheses and first tested whether septins have a role in controlling the mechanical properties of the membrane.

### 3.2.3 Measurement of the effect of septins on the mechanical properties of GUVs

In order to test the hypothesis that septins might influence the mechanical properties of GUVs, we decided to use our micropipette assay to probe two parameters: the bending and the stretching moduli. The bending modulus is a measurement of the response of the membrane to a deformation in a direction perpendicular to it. In that case, the angle between adjacent molecules is changed with the local mean curvature $C$. The energy necessary to bend the membrane can be written as:

$$F_{bending} = \frac{\kappa}{2} C^2$$

With $\kappa$ being the bending modulus. It can be measured (on a GUV for instance) with our micropipette assay by studying the variation of projected area as a function of the applied tension. Under low tension ($\sigma < 0.5$ mN.m$^{-1}$), the vesicles are still subjected to thermal fluctuation and the strain $\Delta\alpha = \frac{\Delta A}{A_0}$ can be expressed as (see section 1.5.1):

$$ln\frac{\sigma}{\sigma_0} \approx \frac{8\pi\kappa}{k_b T}\frac{\Delta A}{A_0}$$

Where $k_b T$ is the thermal energy and $\sigma_0$ an initial state of tension.

Experimentally, GUVs were pre-stretched at a tension $\sigma \approx 0.5$ mN.m$^{-1}$ to smooth out the surface and discard possible defects and brought to a lower tension $\sigma \approx 10^{-2}$ mN.m$^{-1}$. A control initial image was collected and septins were injected until saturation for 10 minutes after which the injection was stopped and the second pipette removed from the field of view. A second image was taken and the tension was increased from the initial value to $\sigma \approx 0.3$ mN.m$^{-1}$ by small increments. After each increment, we waited for 1 minute to ensure that equilibrium was reached and that the tension was homogeneous on the GUV before an image was taken. The projected area was extracted from the confocal images and plotted against the logarithm of the applied tension. The experiment was performed on N = 37 and N = 32 GUVs for the control and with septins respectively out of 6 different experiments each time. Figure 75 shows a plot of the logarithm of the applied tension versus the strain for a single GUV and a plot of the average for all GUVs.

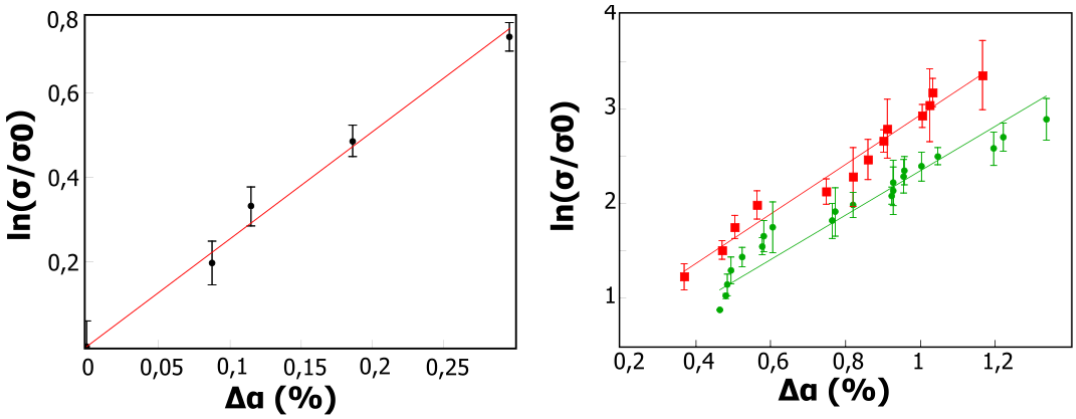


***Figure 75 - Bending modulus measurement***

*Plot of the logarithm of the applied tension versus the strain at low tension ($\sigma < 0.5$ mN.m-1 ) for a single GUV (left) and the average over 37 GUVs for the control (no septin added, red, right) and over 32 (septins added, green, right). The slope of these curves gives* $8\pi\kappa$.

The values of the bending moduli were extracted from these curved: $\kappa_{control} = 10.5 \pm 0.5$ $k_bT$ for the control and $\kappa_{septin} = 9.3 \pm 0.7$ $k_bT$ on septin-coated GUVs. Surprisingly, the average values where not significantly different. Given the result obtained with the osmotic shock experiments and the *in vivo* data, we were expecting to reveal differences between naked and septin-coated GUVs, namely an increase in the value of the bending modulus. To confirm the absence of effect, we decided to repeat the measurement by using a different methodology: optical tweezers to pull a membrane nanotube. Indeed, using a micropipette to pull a tube attached to a glass bead held by optical tweezers, it is possible to measure the bending modulus by controlling the tension applied by the micropipette and record the force

generated by the tube on the bead and they are related by the following relation (see section 1.5.3.2):

$$F_{tube} = 2\pi\sqrt{2\kappa\sigma}$$

Where $F_{tube}$ is the force generated on the tube and measured on the bead, $\sigma$ is the tension applied by the micropipette and $\kappa$ is the bending modulus (see section 1.5.3.2 for details).

To perform the experiment, we grew GUVs using the standard conditions and added 0.5% molar fraction of biotinylated PE lipids. A nanotube was pulled and septins were injected in the same fashion as described in the previous experiments. Once the GUV was fully covered with septins, the injection micropipette was removed and we started recording the position of the bead with the camera. The tension was increased stepwise (always kept at low tensions under 0.3 mN.m$^{-1}$ to prevent the tube from retracting) and we waited at least a minute between each increment to ensure equilibrium. For the control, no septins were added and the tension increments were applied right after the tube was pulled. We extracted the force curve from the tracking of the bead position and plotted it against the applied tension to obtain a measurement of the bending modulus. An example of this experiment is presented in Figure 76.

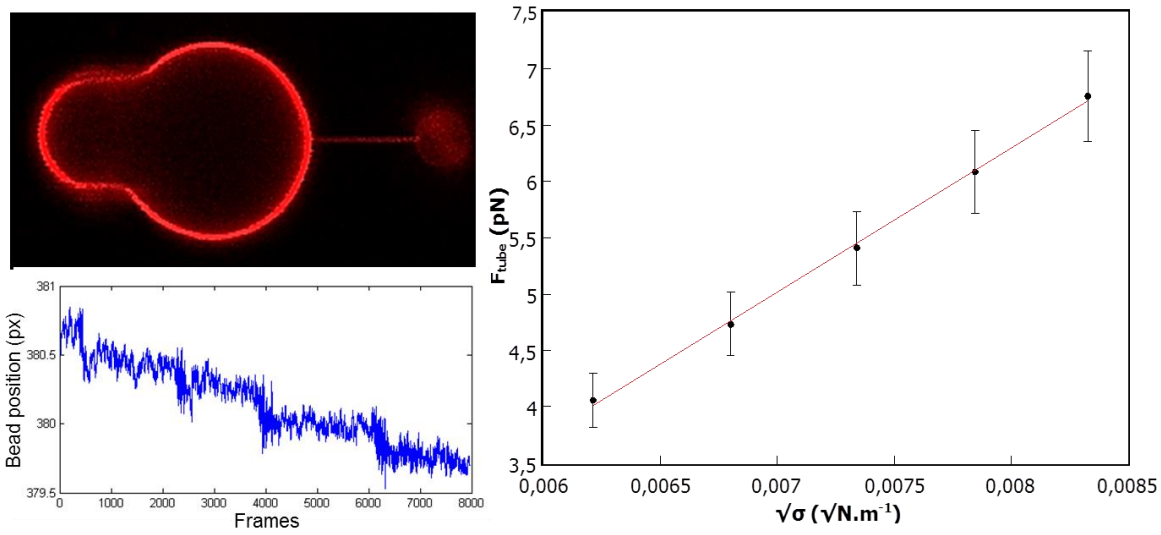


***Figure 76 – Tube pulling example***

*Left – confocal image of a tube pulled out of a GUV (top left) and tracking of the position of the bead (bottom left).Pixel size 56 nm is and framerate is 30 fps.*
*Right – plot of the force measured on the bead versus the square root of the applied tension for the same GUV, we can extract the bending modulus from the slope* $\kappa = 9.8 \pm 0.8$ *kbT*

We were able to obtain the bending modulus for the control condition ($\kappa_{control} = 11.3 \pm 1.2$ $k_bT$, $N_{GUVs} = 6$) and for septin-coated GUVs ($\kappa_{septins} = 11.5 \pm 1.2$ $k_bT$, $N_{GUVs} = 5$). Again, the value of the bending modulus is not significantly different in the presence of the absence of septins. The values measured using tube pulling are slightly different from the values measured with the micropipette aspiration experiments. Indeed, it is known that measurement of the absolute value of mechanical properties of GUVs can differ from one experimental setup to another. However, the results are consistent. In both cases, we did not measure any difference in the bending modulus upon septin injection.

In addition, we decided to use again our micropipette experiment to measure the stretching modulus of GUVs with and without septins. The stretching modulus is another mechanical property that assesses the resistance to lateral deformations. It can be measured at a higher tension regime. The experiments were performed similarly to the bending modulus measurement, except that the tensions applied were higher ($\sigma > 0.5$ mN.m$^{-1}$). In these conditions, thermal fluctuations of the membrane vanish and the deformation of the GUV results in an increase of the lateral spacing between lipids, effectively reducing the density. In the high tension regime, the relation between the strain and the applied tension can be expressed as (see section 1.5.3.1):

$$\frac{\Delta A}{A_0} = \frac{\sigma}{S}$$

With $S$ being the stretching modulus. The results are shown in Figure 77.

Surprisingly, we observe a slight softening of the membrane in the case of septin binding (the measured stretching moduli were $42 \pm 8$ with septins versus $65 \pm 9$ mN.m$^{-1}$ for the control). It is possible that the stretching of the membrane at high tension allows septins to insert between lipids. Indeed, numerical simulations have shown that the functions of budding yeast septin is best conserved when shallowly inserted (1.2 nm)[250]. By stretching the membrane, septins can insert further into the membrane and push the surrounding lipids, effectively increasing the stretching of the membrane. Similar results were obtained in the case of streptavidin-coated GUVs[251].

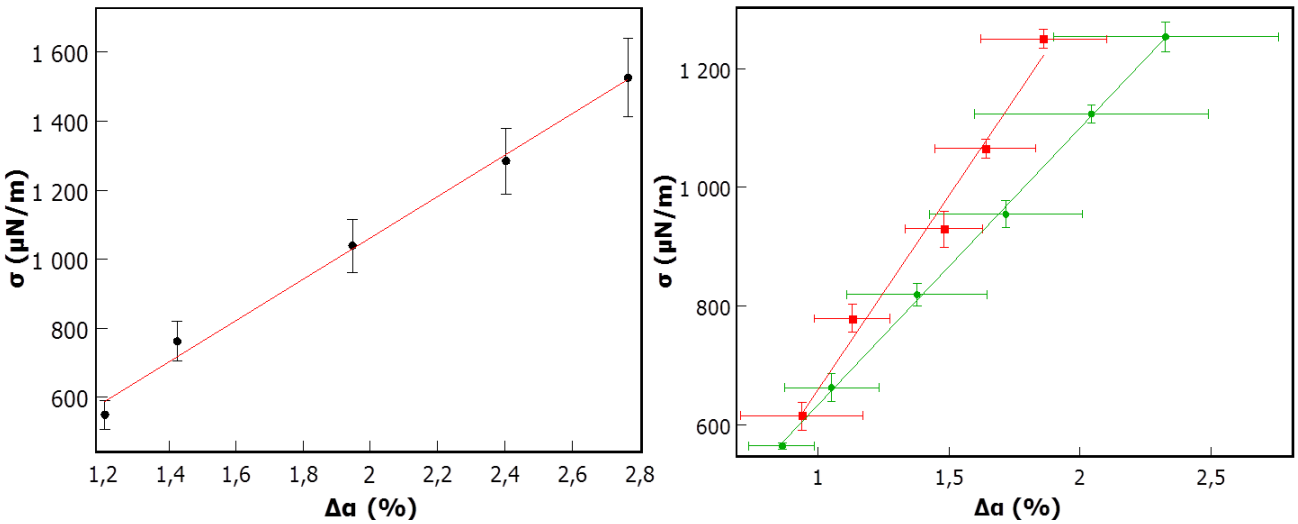


***Figure 77 – Measurement of the stretching modulus***

*Plot of the tension σ versus the strain at high tensions ($\sigma > 0.5$ mN.m-1) for a single GUV with septins (left) and the for the average (right) for the control (red dots, N=30) and septin conditions (green squares, N=29). The extracted values of the stretching moduli are* $S_{\text{control}} = 65 \pm 9$ *mN.m-1 and* $S_{\text{septins}} = 42 \pm 8$ *mN.m-1.*

We showed that although septins can protect GUVs against osmotic shock, the measured bending and stretching moduli did not increase in their presence. We believe that the explanation resides in the fact that this method is not suited to measure those parameters on protein-coated GUVs. Indeed, the measurement of the bending modulus relies on the thermal fluctuation at low tensions. By adding a rigid protein network around the vesicle, we effectively stop these fluctuations and the measurement becomes hard to interpret. It is also possible that the septin network is non-elastic (as seen by the plastic deformations seen in section 3.2) and applying mechanical stress induces non-linear deformations. This will be elaborated in the discussion section3.4.

### 3.2.4 Systematic deformation of GUVs by high concentrations of septins

Given or previous results, we decided to test the hypothesis that septins can directly remodel the membrane. It was shown in section 3.2 that at a sufficient concentration ($\approx 200$ nM), septins were able to induce membrane deformation at the micron scale. Those GUVs displayed abnormal shapes with sharp angles instead of their usual spherical shapes. We decided to incubate free GUVs with various concentrations of septins and monitor their shapes.

GUVs were grown using the standard conditions and put into the observation chamber with septins at concentrations ranging from 200 nM up to 600 nM in a low-salt observation buffer (NaCl 75 mM, Tris pH 7.4 10 mM). Images were taken after 1h of incubation. Figure 78 shows different morphologies that can be found in the lower concentration range (between 200 and 300 nM).

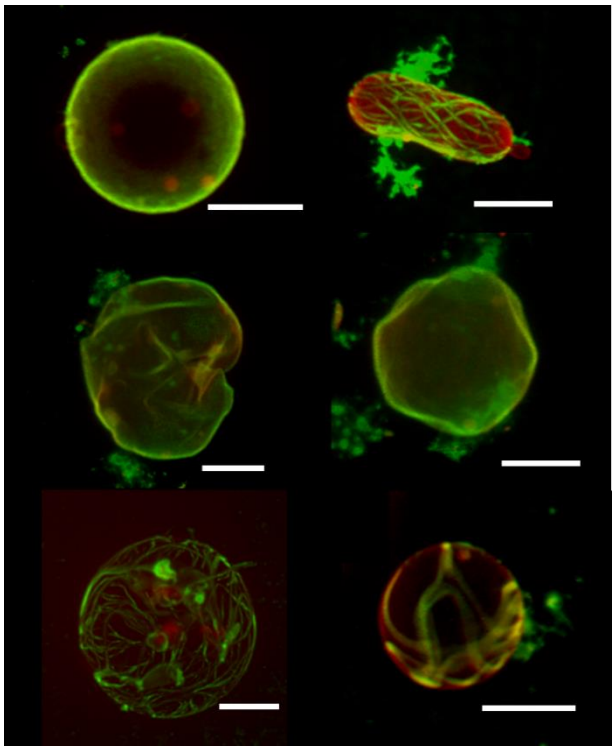

***Figure 78 – 3D reconstitution of septin-coated GUVs***

*3D reconstitution of z-stacks of spinning-disk microscopy images of GUVs. Regular spherical shape (top left), cylindrical shape (top right), rugged surface (middle row) and network of thick bundles (bottom row). Scale bars are 5µm. Septin concentrations are between 200 and 600 nM*

As shown previously, GUVs with abnormal shapes (different from a sphere, Figure 78 top left) are present. GUVs with folds in the micrometer range and a rugged surface (Figure 78 middle row) are formed by the presence of a septin network. The coverage of the septin on the surface remains homogeneous. In some cases, we could observe septins create a non-homogeneous network on the GUVs by forming thick (several hundreds of nm) bundles that propagate all around the GUV (Figure 78, bottom row) while some parts are devoid of septins. So far, no correlation has been found to explain the appearance of rugged (i.e. not smooth) GUVs rather than thick septin bundles. We believe that the bundles were pre-

polymerized in solution and assembled onto the GUVs while rugged homogeneous coverage of the GUVs corresponds to smaller filaments.

With higher protein concentrations (400 to 600 nM), new morphologies were visible with seemingly conserved features and abnormal shapes became more and more frequent (~33%). Indeed, at higher concentrations, septins would induce the formation of spike-like structures on the GUVs (see Figure 79, bottom row). We analyzed different parameters: the amplitude $A$, the lateral spacing $\lambda$ and the curvature radius $R$ (see Figure 79, top left) using the measuring tools from ImageJ. As shown in the histograms, the features of the spike-like protrusion are well defined and conserved. The mean spike amplitude measured is $A_{mean} = 0.9 \pm 0.2$ µm and the mean radius $R_{mean} = 1.1 \pm 0.2$ µm. These values indicate that, at high enough concentrations (> 400 nM) septins are able to deform the membrane and create structures in a conserved manner. The fact that all the spikes all similar dimensions lead us to believe that septins arrange specifically on micrometric structures, which is in agreement with a previous study on lipid-coated beads[177].

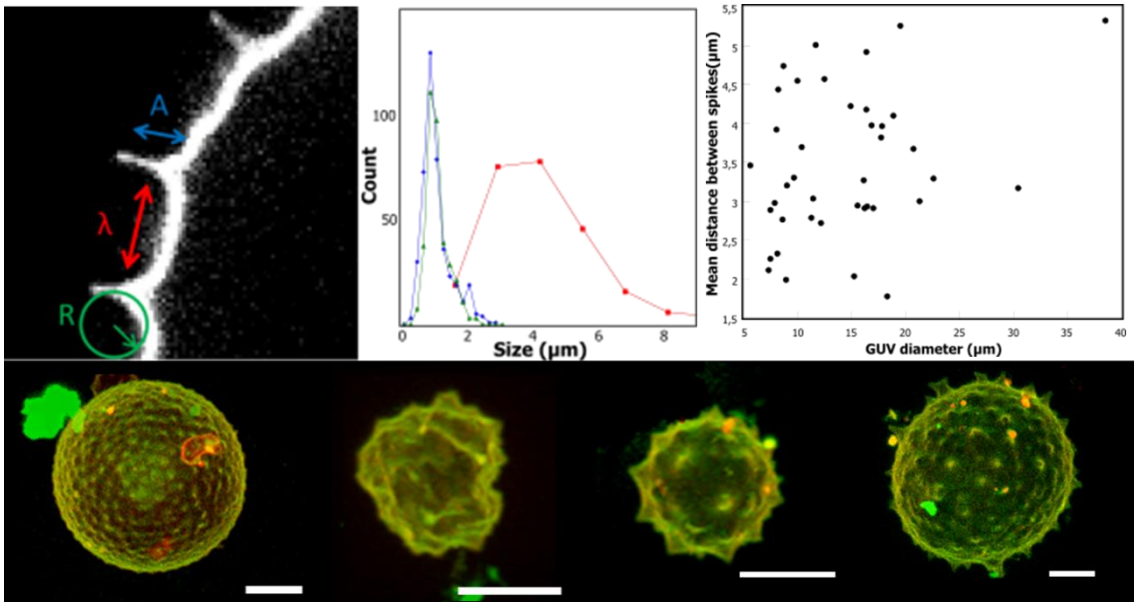


***Figure 79 – Spiky GUVs at higher septin concentrations***

*Top left – confocal image of a spiky GUV showing the different measured parameters: the amplitude of the spikes* A*, the distance between spikes* λ*, and the curvature radius* R*.*
*Top middle – Size distribution for the three parameters* A *(blue),* λ *(red) and* R *(green) out of 35 different vesicles.*
*Top right – Mean spike distance plotted against the GUV diameter.*
*Bottom row – 3D reconstitution of confocal image stacks of GUVs deformed by the binding of septins. Scale bars are 10 µm.*

Our experimental values of A and λ are consistent with the curvatures and geometries where septin localize *in vivo* (from 300 nm to 2 µm during the different steps of cytokinesis in *S. cerevisae*, measured by SEM[147]). We also measured the lateral spacing between the spikes $\lambda_{mean} = 3.9 \pm 1.4$ µm which is less regular. The incertitude might stem from the fact that we measure the lateral spacing on 2D image (slices) of objects positioned on a sphere, thus measuring effectively a projection of the distance between spikes. We also compared the mean spike distance to the GUV diameter and found no correlation (see Figure 79, top right). The two conserved features were the amplitude and the curvature radius given the distribution of the mean distance shows a much larger spread.

We then tested the influence of the observation buffer, namely the salt concentration, to understand the role of pre-formed filaments into the generation of those spikes. We used a NaCl 300 mM, Tris pH 7.4 10 mM observation buffer (with the osmolarity of the growth buffer adjusted with NaCl 50 mM, Sucrose 500 mM, Tris pH 7.4 10 mM. At this salt concentration, the septins added in the observation chamber remain in their octameric form while they can still bind the membrane and polymerize by diffusion-driven annealing[173,174]. We found no difference between the deformation induced by septins in a low-salt or high-salt environment, meaning that septins can still form these higher order structures on the membrane and not only in solution (see Figure 80).

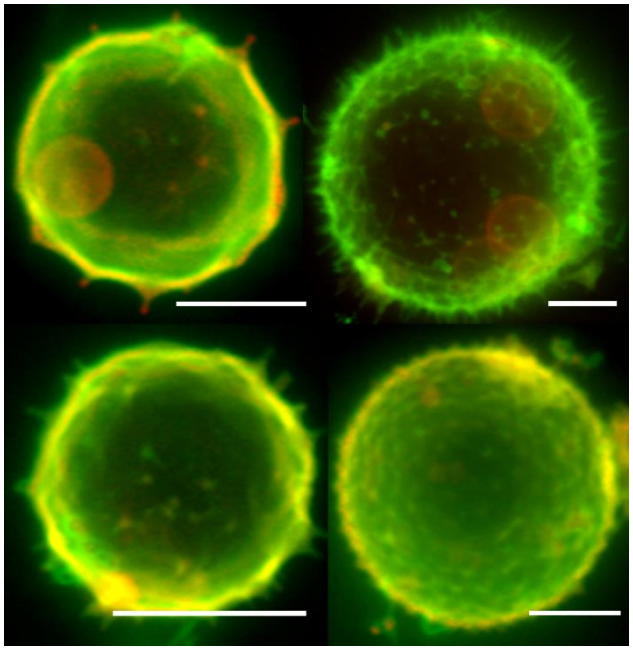

***Figure 80 – Spiky GUVs at high septin and high salt concentration***

*3D reconstitution of confocal image stacks of GUVs deformed by the binding of septins at high salt (NaCl 300 mM) condition. Scale bars are 5 µm.*

Last, we hypothesized that these structures could be mechanically unstable and would be able to relax on time scale longer that the ones explored during our experiments (typically 1 to 3 hours). We decided to incubate septins with GUVs for 24 hours and observe the deformation that would occur. We observed in rare occasions dramatically deformed small vesicles that displayed large spikes (see Figure 81).

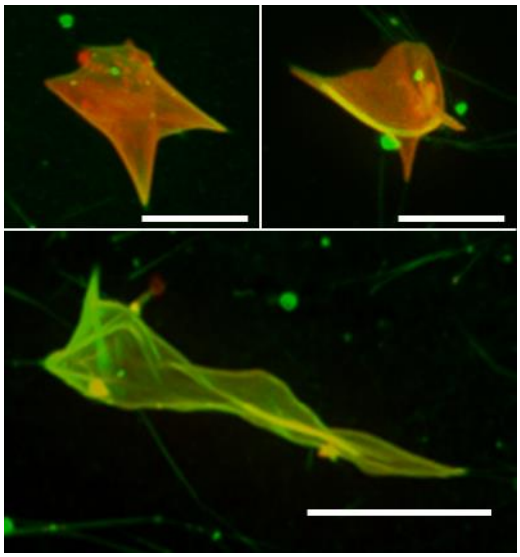

***Figure 81 – Large spikes on smaller vesicles***

*GUVs incubated for 24h with septins at high concentration (600 nM) displaying a low number of larger spikes. Scale bars are 2 µm.*

This indicates that the spikes seen at lower incubation time might be transient structures that equilibrate by coalescing into larger spikes. This phenomenon seems to be faster for smaller vesicles. The morphology of those GUVs are very reminiscent of the deformation induced by FtsZ, the bacterial homologue of tubulin[226] and suggests a possible universal mode of deformation by filament-forming proteins. This protein, like septins can discriminate between different curvatures and because of this, we decided to investigate further the ability of septins to sense curvature.

## Summary

- **Septins increase the resistance of GUVs to osmotic shocks.**
- **No difference in the bending modulus of GUVs was measured in the presence of septins.**
- **A decrease in the stretching modulus of GUVs was measured in the presence of septins.**
- **Septins can induce deformations on GUVs which can adopt spike-like features at the micron scale.**

## 3.3 Curvature sensing ability of septins

As described in the previous chapter, septins have a tendency to deform membrane *in* vitro by forming spike-like structure with a well-defined amplitude and curvature radius around 1 µm. To investigate the curvature sensing ability of septins, we decided to develop a novel *in vitro* tool.

### 3.3.1 Septins enrichment on positive curvatures

A handful of *in vitro* studies on septins have been conducted in the recent years. The laboratory of Amy Gladfelter at the University of North Carolina (USA) has performed experiments showing that septins can discriminate between positive and negative curvatures *in vivo* at branching points. They also found that budding yeast septin filaments accumulate at different densities depending on the curvature with a maximum at 2 $\mu m^{-1}$ using lipid-coated beads (see section 1.3.4)[177]. These findings are interesting since they show that septins have a natural ability to discriminate between different curvatures in value and sign. However, the geometry chosen in those experiments was restricted to a fixed shape and a fixed curvature. Moreover, positive curvatures were exclusively explored. With that in mind, we used a novel tool to investigate positive, negative and null curvatures simultaneously. The system is composed of a piece of polymer (we used either PDMS or NOA81) 100 µm thick displaying a sinusoidal pattern on top of it (see Figure 82). The dimension of the pattern can vary from several hundreds of nm to several µm in wavelength $\lambda$ and height $H$ (for a more detailed description of the system and its fabrication process, see section 2.4).

Since the surface presents a sinusoidal pattern, we can assess the exact curvature $C$ which depends on the vertical position $z$ (see section 2.4 for details). These values are bound by the maximum values given by $[-C_{max}; +C_{max}]$ and correspond to the bottom (“valley”, highlighted in green in Figure 82) and top (“hill”, highlighted in blue in Figure 82) of the substrate respectively.

Typically, we used samples with a maximum curvature ranging from 1 to 5 $\mu m^{-1}$ in absolute value. This corresponds to an amplitude ranging from 0.6 to 0.8 µm and a wavelength ranging from 1.1 to 4 µm. Besides, the second main axis of curvature of the substrate is always zero (in the direction perpendicular to the sinusoidal pattern) which means that the Gaussian curvature (the product of the two main curvatures) is always zero.

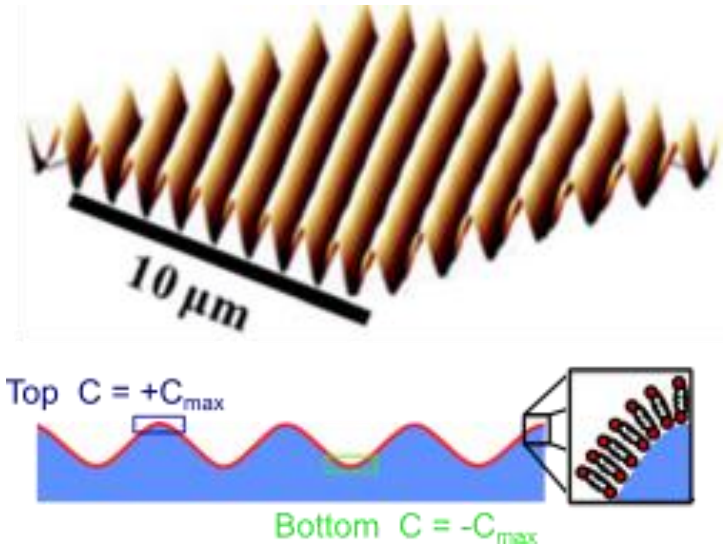


***Figure 82 – Patterned substrates***

*3D representation of the patterned substrates (top) and side view of the sinusoidal pattern coated with a lipid bilayer (bottom) indicating the two regions where the absolute value of the curvature is maximum in green and blue.*

We used the substrates by first making a replicate using the original that were sent to us as stamps then by coating them with a lipid bilayer. The lipid bilayer was formed by fusing SUVs to the surface using the following lipid composition: EPC 56.5%, Cholesterol 15%, DOPS, 10%, DOPE 10%, PI(4,5)P2 8%, Bodipy TR-Ceramide 0.5%, all in molar fractions. The detailed protocol of the bilayer formation can be found in section 2.3. Once the bilayers were formed, we incubated the substrates with a solution of septins at 250 nM in NaCl 75 mM Tris pH 7.4 10 mM for 15 minutes. We then carried out a washing step with the same buffer to remove septins in excess and reduce the background noise.

We used confocal microscopy to collect images starting from the top of the sample until the bottom of the sample was reached by taking care of spacing each images by at least 250 nm (twice the size of our PSF, see section 2.6.1). We thus obtained images of the positions $C = +C_{max}$ , $C = -C_{max}$, , $C = 0$ and sometimes other intermediate values. Some pictures were also taken several µm above and under the sample to get noise data that would be subtracted from the images during the analysis. Confocal images of the substrates are shown in Figure 83 for both lipids and septins (in red and green respectively).

The periodic feature of the sample can be seen on the images and more closely on their respective intensity profiles on the left where we determine see the wavelength of the sample $\lambda = 2.2$ µm. To measure the intensity on the sample (and not on the dark parts), I developed a MatLab script to scan the images, identify the position where septins were present and measure their density while ignoring the dark parts (see section 2.8.6 for details). The advantage of this method is that it allows for the measurement over the whole image (field of view = 150x150 µm²), thus increasing the statistics greatly.

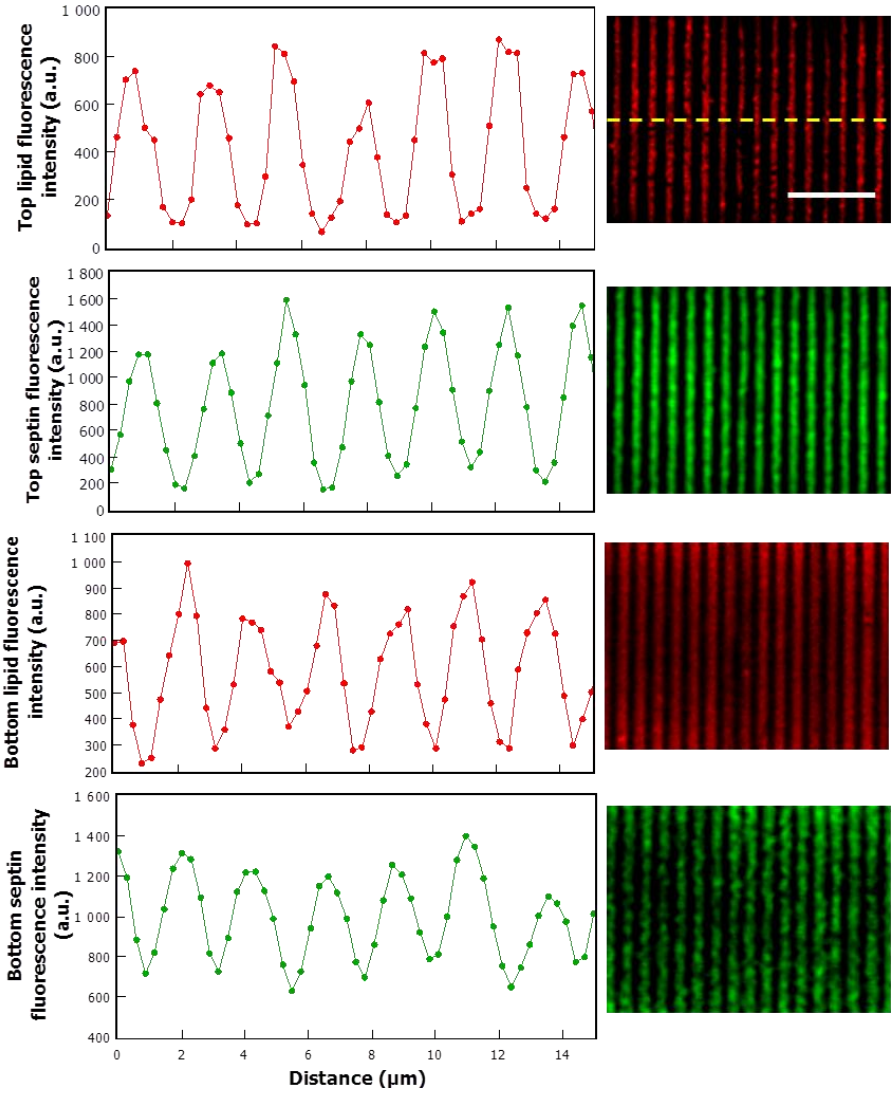


***Figure 83 – Intensity profile of the patterned substrates***

*Confocal images of the patterned substrates at the top and the bottom for both lipids (red) and septins (green) of the sample and their corresponding intensity profiles along le center of the image (dotted line). Scale bar is 10 µm. The substrate dimensions are λ=2.2 µm, H=0.8 µm,* $C_{max} = 3$ *µm*$^{-1}$

The drawback of this method is that the images have to be manually rotated first (so that all lines become vertical) losing some information in the process. Moreover, it requires a manual component in the workflow of image analysis.

We conducted this experiment and analysis on several samples with maximum curvatures ranging from -5.3 to +5.3 $\mu m^{-1}$. The resulting curve gathers averaging over many different experiments (N = 8) and replicates (N = 24). It is displayed in Figure 84, where we plotted the lipids and septin (red/orange and green respectively) density normalized by the value in the midpoint (where the curvature is equal to zero) versus the curvature. The lipid density is used as a control to make sure that a difference in septin density is not related to a difference in lipid enrichment.. Besides, we ensure that the SLB is homogeneous. Specifically, we show that the PI(4,5)P2 density is homogeneous too. We expected the lipid density to be independent of the curvature given the dimensions of the substrates. At $C = -5.3$ $\mu m^{-1}$, we found that the lipids and septin density increased. This is probably due to the fact that SUVs do not fuse correctly with this highly convex region. This was later confirmed by SEM studies of the substrates. For that reason, we decided to discard the points at $C = -5.3$ $\mu m^{-1}$ (Figure 84, gray part).

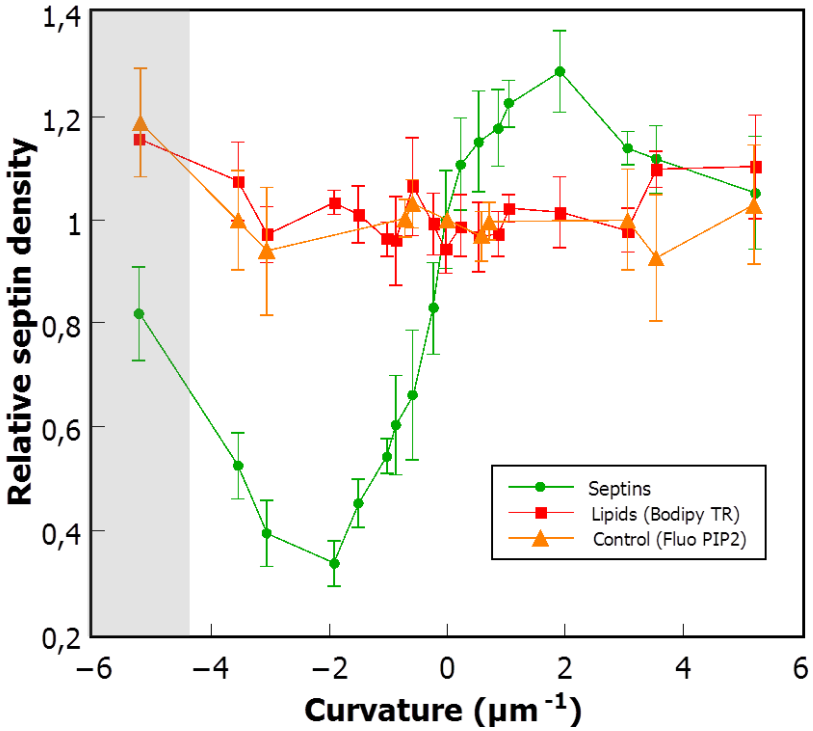


***Figure 84 – Relative septin and lipid densities at different curvatures***

*Bodipy TR-ceramide (red), septin (green) and fluorescent PI(4,5)P2 (orange) relative densities versus the curvature. The density is normalized by the value at* $C = 0$.

As expected, the lipid densities remained relatively constant over the range of curvatures presented. We can then safely believe that any change in septin density is due to geometric effect alone, namely the value of the curvature. Two things can be extracted from this study. First, septins bind with higher density at positive curvatures compared to negative curvatures. For positive curvatures, they show a local maximum for curvatures around $C = 2$ µm$^{-1}$ as it was observed with silica beads coated with lipids[177]. This indicates that not only septins are able to discriminate between different values of curvature but that the sign of the curvature also plays an important role. Next, we wanted to investigate how septin filaments assemble *in vitro* on different curvatures using the same patterned substrates coated with a lipid bilayer. We used scanning electron microscopy (SEM) to reach higher resolution and visualize individual filaments.

### 3.3.2 Septins orientation on different curvatures

For SEM imaging, the samples were coated with a 1.1 nm layer of platinum (for a more detailed protocol, see section 2.6.3). Figure 85 shows 3 images of the same patterned sample at different locations and magnifications (1 to 3, the dimensions are $\lambda = 2.2$ µm $H = 0.8$ µm and $C_{max} = 3$ µm$^{-1}$), an image of another patterned sample (4, the dimensions are $\lambda = 2.5$ µm $H = 0.5$ µm and $C_{max} = 1.6$ µm$^{-1}$) and their colored version. To be able to better discern the filaments and their orientations, we used OrientationJ, an ImageJ plug-in developed by the Biomedical imaging group of Ecole polytechnique de Lausanne (Switzerland). This tool can be used to detect objects and their orientation and color them accordingly (with green colors corresponding to the horizontal axis and red colors corresponding to the vertical axis, see color map figure Figure 85.2). It is suited to analyze the orientation of filament because their elongated shape follows a discernible orientation.

In the first image, the patterned substrate is shown at low magnification. Some defects can be seen. Indeed, three big lines (pink lines) cross the pattern perpendicularly and some cracks in the middle which result from the replication process can be visualized. In the second image, two “hills” and one “valley” within the substrates as well as septin filaments and small spherical objects about 50-300 nm in diameter are visible. These objects are most likely SUVs that couldn’t fuse with the substrate to form the bilayer and did not wash out properly even after several rinses. It is also possible that they appeared after the addition of septins. Their small sizes make them devoid of any septin filament. The septin filaments are not randomly oriented on the sample but rather possess a local organization which is different when looking at positives or negatives curvatures.

This phenomenon can be clearly seen in the colored version of the picture. At positive curvatures, we see a majority of green colors which means that the filaments are all oriented along the ridge of the pattern, where the curvature is zero. As a consequence, the filaments lay flat and avoid being positively curved. Another example in the third image shows a picture of septin filaments following a defect (horizontal structure in the middle) crossing the pattern to finally follow the ridge and remaining flat.

On negative curvatures, we see a majority of red/purple color indicating that the filaments are negatively bent. In image 4, the maximum curvature of the sample is lower than the sample showed in the 3 previous pictures (1.6 instead of 3 $\mu m^{-1}$). In image 4, the filaments aligned along the axis of zero curvature for positive curvatures at the top. For negative curvatures, we see a slight difference between the two images. In image 4, the filaments are still negatively bent but the orientation of the filaments seems more disperse as the one in image 2 (as seen by the broader color palette).

To get a more quantitative understanding of the orientation of septin filaments, we used the distribution tool of the OrientationJ plug-in which measures the amount of pixels with a certain orientation (color). We thus obtained the orientation distribution function (ODF) of septin filaments at different curvatures (for a detailed explanation, see section 2.6.3). Figure 86 shows the orientation distribution of the images shown in Figure 85 and their respective corresponding pictures. The distributions have been shifted so that the value for 0° corresponds to the direction perpendicular to the axis of the undulation. This implies an imagine rotation of about 12° (given their orientation) but is a preferred solution because it does not modify the images. From the orientation ODF, we were able to extract the mean orientation $\alpha$ an order parameter usually used in liquid crystal theory. The ODF can be developed as a series of Legendre polynomial and the average of the second parameters can be used to describe the order of liquid crystal and predict their phase. Here we used it to compare the order of different alignments of septin filaments. The order parameter $m$ was calculated using the following formula:

$$m = \langle \frac{3}{2} \cos(\theta)^2 - \frac{1}{2} \rangle$$

Where $\theta$ is the angle between a filament and the mean orientation and the brackets stand for the average over all orientations.

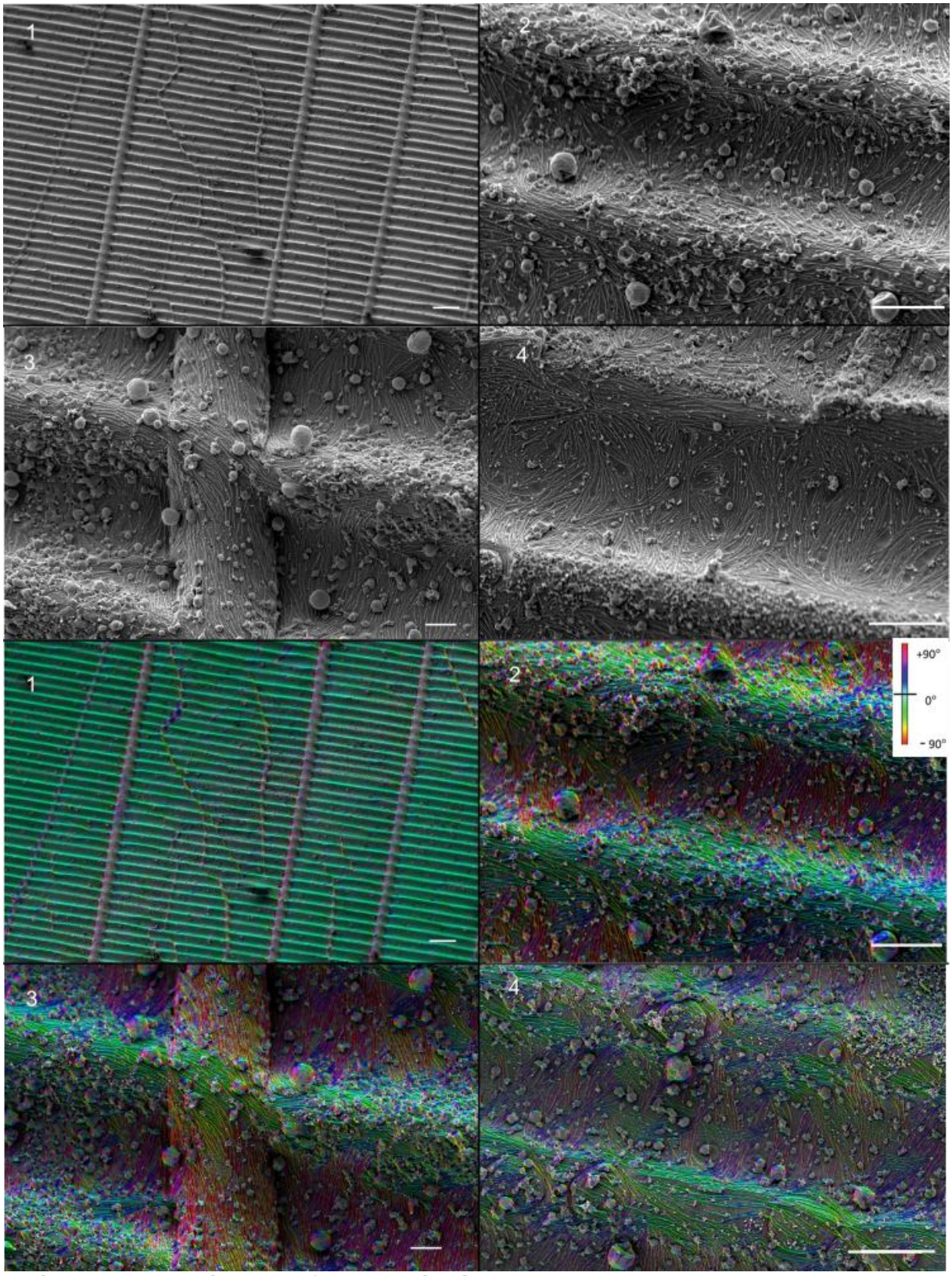


***Figure 85 – SEM images of patterned substrates***

*SEM images of the patterned substrates coated with a lipid bilayer and septin filaments (top) and their colored versions (bottom). N°1 shows a low magnification image (scale bar is 5 µm). The three remaining images are a close-up of different parts of the sample, scale bars are: 2,4 = 1 µm, 3 = 300 nm. The color map is showed in image 2 and is the same for all images.*

For liquid crystals, a value $m = 1$ corresponds to a completely ordered phase where all the molecules are aligned in the same direction. Unlike a solid crystal however, the distances between the molecules are not equal. The value $m = 0$ corresponds to a completely isotropic phase with a random distribution. Intermediate values of $0.8 \geq m \geq 0.4$ correspond to a semi-ordered phase known as the nematic phase (see Figure 86, top drawing).

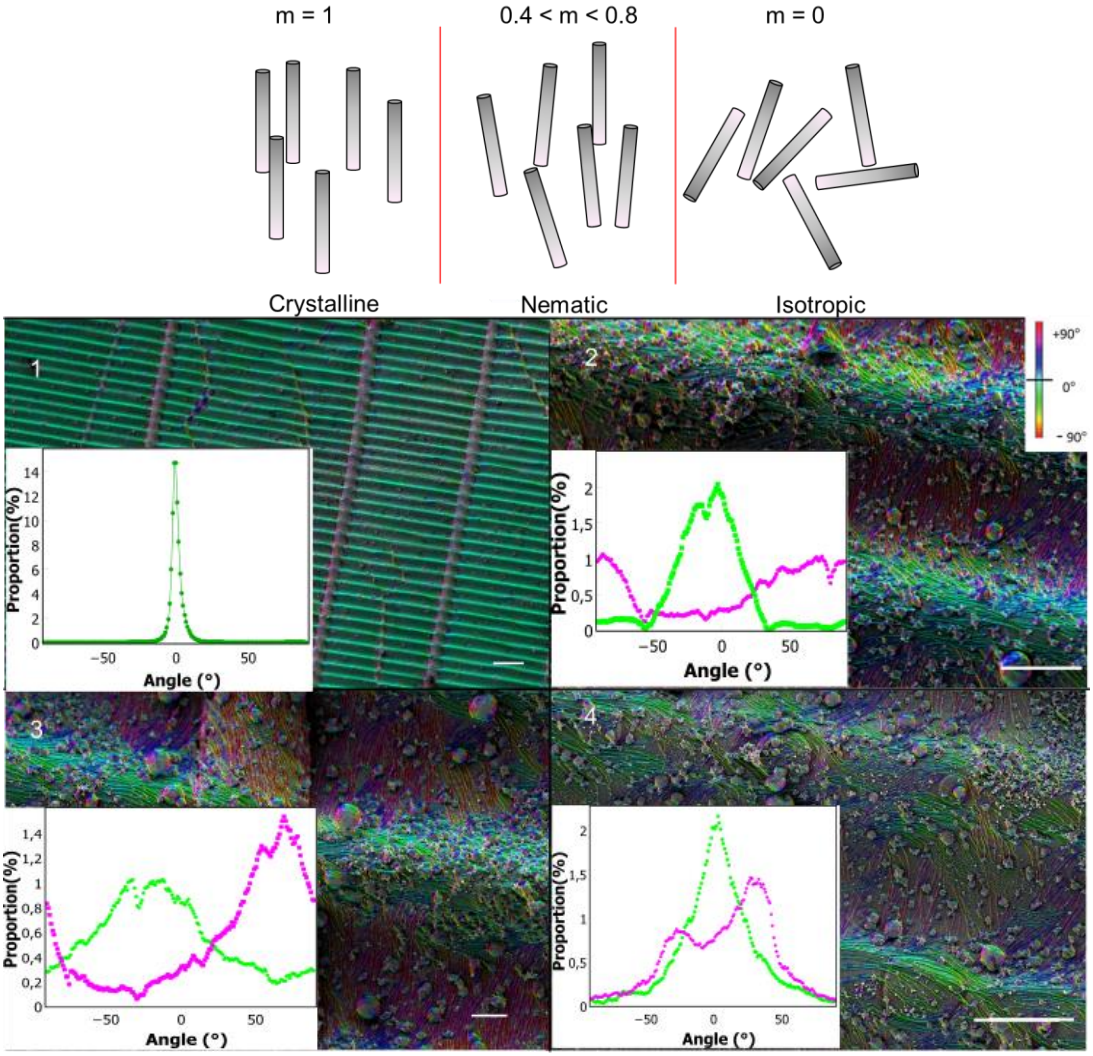


***Figure 86 – SEM images and orientation distributions***

*Drawing of the different phases found in liquid crystals and their corresponding value of m. SEM images of the patterned substrates coated with a lipid bilayer and septin filaments and their respective orientation distribution obtained after filtering of the impurities. For images 2 to 4, the green curve corresponds to positive curvature and the magenta to negative curvature. Scale bars are 1: 5 µm, 2 and 4: 1 µm, 3: 300 nm.*

As a control and to validate the use of the OrientationJ plug-in, we measured the orientation distribution of the low magnification image of the sample. Given the periodic nature of the sample and the very organized features, we expected to obtain a mean orientation of 0° and a value of $m$ close to 1. The values obtained were $\alpha = 0 \pm 2$ ° and $m = 0.97$ and were thus in good agreement with the expected values. The resulting mean angles and order parameter are presented in Figure 87 for images 2, 3 and 4 and separated into values measured at positive ($\alpha_+$, $m_+$) and negative ($\alpha_-$, $m_-$) curvatures.

| | 2 | 3 | 4 |
|---|---|---|---|
| $\alpha_+$ | 1±15° | -17±30° | 3±9° |
| $m_+$ | 0.78 | 0.5 | 0.75 |
| $C_{max}$ | 3 µm$^{-1}$ | 3 µm$^{-1}$ | 1.6 µm$^{-1}$ |

| | 2 | 3 | 4 |
|---|---|---|---|
| $\alpha_-$ | 82±32° | 66±22° | ±35±12° |
| $m_-$ | 0.59 | 0.57 | 0.45 |
| $C_{max}$ | 3 µm$^{-1}$ | 3 µm$^{-1}$ | 1.6 µm$^{-1}$ |

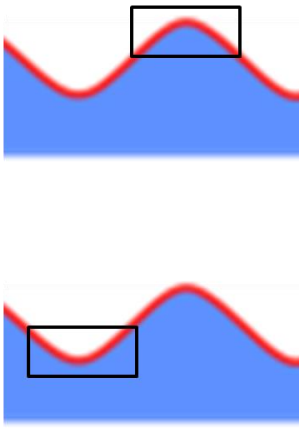

***Figure 87 – Mean orientation and order parameter***

*Mean orientations α and order parameter m measured at positive and negative curvatures for the images present in Figure 86.2,3 and 4.*

The first striking result is the organization that septin filaments adopt at positive curvatures and reflected by the values of $m_+ = 0.78$ and $0.75$. On positive curvatures, septin filaments collectively remained flat and all align in the same direction. We observed similar results for two different curvatures. We believe this phenomenon might be enhanced by the fact that these long septin filaments expose a large surface for lateral interaction, strengthening their orientational order. In the vicinity of defects, the septin filaments were less ordered as expected. On negative curvatures, the ODF was more dispersed and the resulting order parameter values were lower. We also observe a different behavior for the two different curvatures observed, with the lower value of $C_{max}$ resulting in less ordered septin networks. Septin filaments seem to behave completely differently depending on the sign of the curvature. On positive curvatures, they will avoid being bent and this, independently on the value of the curvature. On negative curvatures however, they can bend and show different orientations depending on its value.

We also used these data to compare the relative density of septin filaments bound on positive and negative curvatures obtained by SEM or confocal imaging. Using the data from Figure 84 and Figure 86, we compared the density of bound septins at $+3$ and $-3$ µm$^{-1}$ as well as +1.6 and -1.6 µm$^{-1}$ and found $\frac{C_{3,+}}{C_{3,-}} = 2.3 \pm 0.4$ and $\frac{C_{1.6,+}}{C_{1.6,-}} = 2.2 \pm 0.4$ with the confocal data and $\frac{C_{3,+}}{C_{3,-}} = 2.1 \pm 0.4$ and $\frac{C_{1.6,+}}{C_{1.6,-}} = 1.9 \pm 0.4$ with the SEM data. Both methods point out to an accumulation of septins at positive curvatures as compared with negative curvatures. At first, we were puzzled by the seemingly contradictory results that septins would rather orient themselves away from the positive curvature and follow the axis of zero curvature and accumulate there while they would sense the negative curvature and orient in its direction. We hypothesize that, since septin filaments all orient themselves along the same axis in the case of positive curvatures, they are more likely to laterally interact and participate into the creation of septin pairs or bundles. On negative curvatures, the filaments are not as organized. Indeed, the order parameter $m$ is lower and thus septin filaments are more likely to be single, reducing the overall septin density.

As septins seem to be sensitive to curvature, we wanted to compare the findings described above with a control where septins organized on a flat surface of NOA81. NOA81 was spincoated at 500 rpm for 10 s on a glass coverslip and put under UV light for 10 minutes for polymerization. The bilayer formation, septin incubation and metallization were performed in the same fashion as described previously for the patterned substrates. Figure 90 shows a SEM picture of septin filaments bound to a flat sample as well as the colored version and the corresponding ODF which has been calculated on the whole image. The mean orientation is $\alpha_{flat} = -1°$ and the order parameter $m_{flat} = 0.22$.

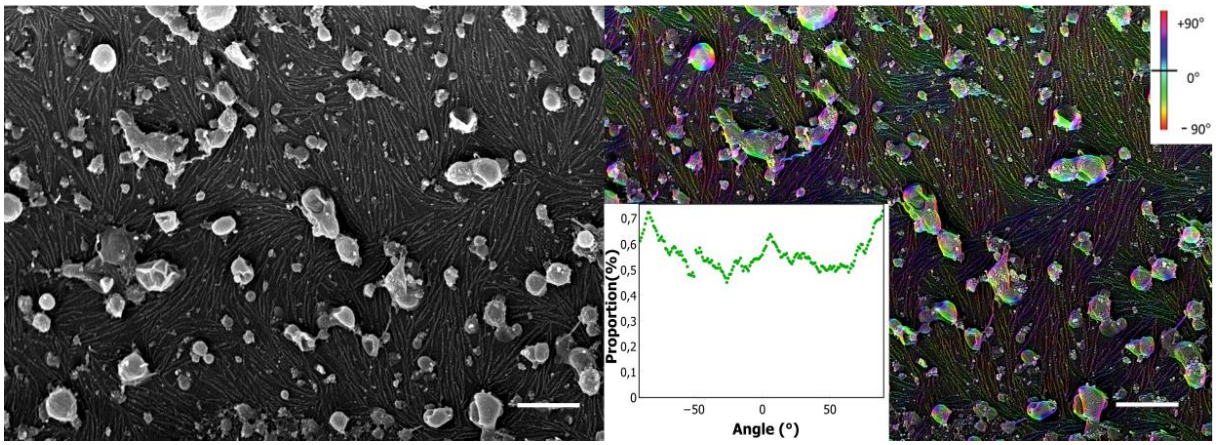


***Figure 88 – SEM images of septin filaments on a flat surface***

*SEM image of septin filaments bound on a lipid bilayer deposited on a flat PDMS sample (left) and the colored version (right) with the color scale and the corresponding ODF. Scale bars are 200 nm.*

As shown by the orientation distribution, septin filaments are no longer oriented in one particular direction. Instead they have an isotropic behavior with an order parameter close to 0. However, by looking at the picture, we see that septin filaments seem to show some organization at a short scale where patches of filaments are oriented in the same direction. To measure the range of this local order, we obtained the local ODF by segmenting the pictures into small squares of length $L$ centered on these septin patches (see Figure 89, left). By considering squares of increasing sizes a decrease in the order parameter was observed. Therefore a small scale order exists but decreases as the size of the observed network becomes larger.

As shown in the curve in Figure 89, at low scale (0.1-0.5 µm, $m = 0.9 - 0.7$), septin filaments show a crystalline order and are aligned in the same direction. Going to larger scales, the values of m keeps decreasing until it reaches a value close to $m_{flat} = 0.22$ at micrometric scales. An exponential fit of the curve in Figure 89 revealed a characteristic length of $1.1 \pm 0.1$ µm.

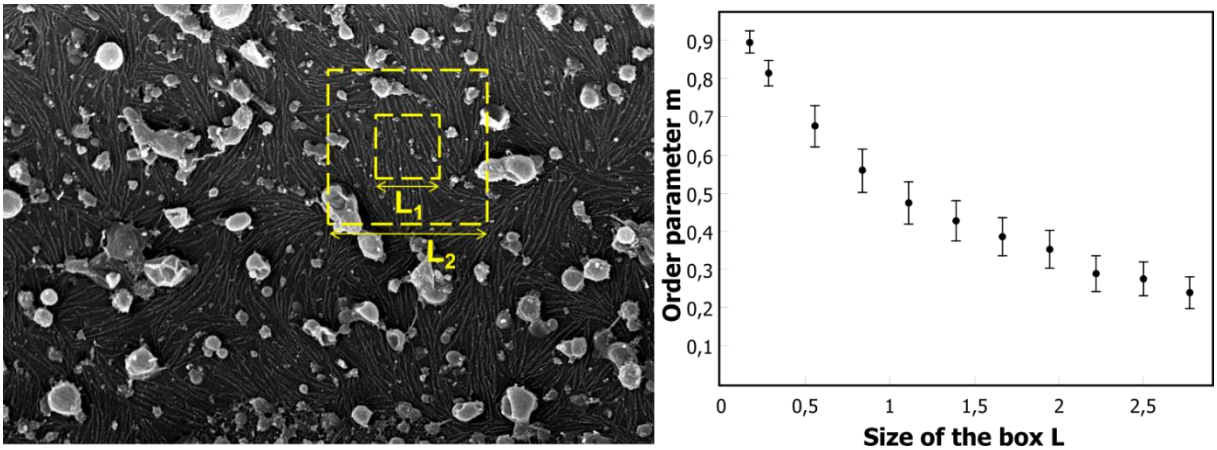


***Figure 89 – Order parameter at different scales***

*SEM image of the flat sample coated with a lipid bilayer and septin filaments showing two boxes of increasing sizes where the order parameter* m *has been calculated (left). The process has been repeated on different part of the sample and the images. The graph shows the decrease of* m *as a function of the box size (right).*

A recent study showed that septin bundling is promoted by the presence of nucleotides (GDP or GTP) and $Mg^{2+}$ [163], indicating that septin filament lateral interaction might arise from electrostatic interaction as shown for actin bundles[252] or from conformational changes inducing increased exposed binding interface as demonstrated for FtsZ[253]. A cdc11 D65T mutant later revealed that lateral interactions responsible for bundling were most likely based on conformational changes. It is possible that these interactions are of shorter range than electrostatic interactions and promote filament lateral association while at larger scales electrostatic repulsions dominate, resulting in a less ordered state of septin filaments.

In addition to aligned parallel filaments, we were able to observe locally small networks of short (about hundreds of nm) septin filaments crossing each other, creating a ‘gauze-like’ pattern (see Figure 90).

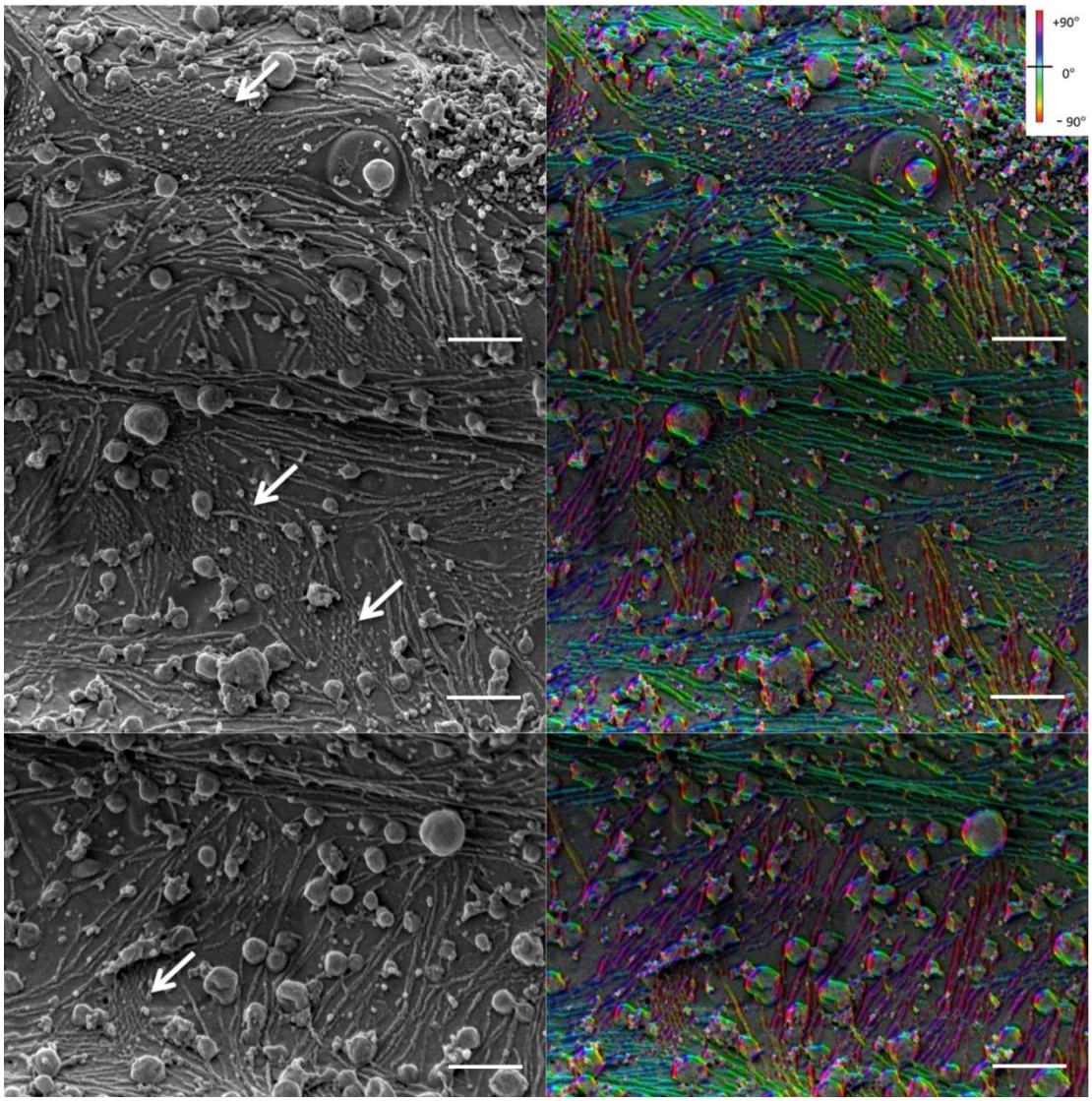


***Figure 90 – SEM images of small septin networks***

*SEM images of short septin filaments network (left) and their colored version (right) on a sample where* $C_{max} = 3$ *µm-1. The network are pointed by the white arrows. Scale bars are 300 nm.*

The small networks were found at different locations on the sample independently on the local curvature (see Figure 90, top images correspond to positive curvatures, middle are intermediate and bottom are negative ones). The sizes of the filaments and the network were found to be conserved. The mean filament length was $L_{mean} = 166 \pm 31$ nm and the mean area covered by these networks was $A_{mean} = 0.36 \times 0.36 \pm 0.05 \times 0.05$ µm$^{-2}$. In these structures, septin filaments have two main orientations and create a mesh by crossing one another with a mean angle $\theta_{mean} = 32 \pm 5$ ° (see Figure 91, colored filaments).

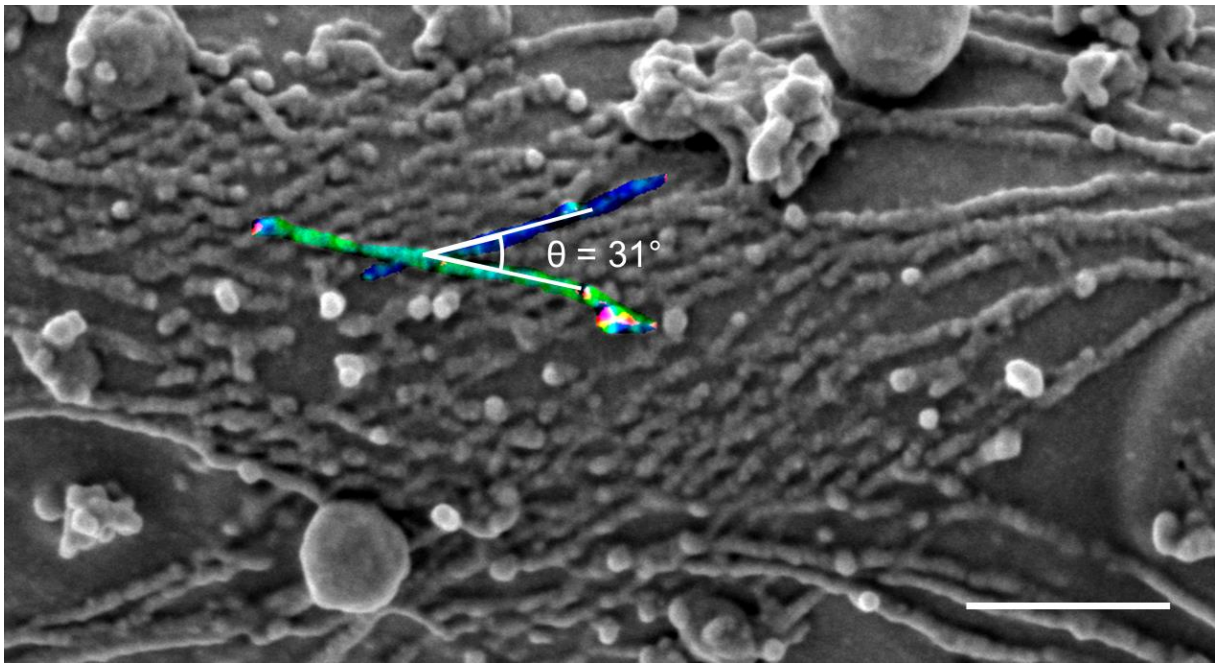


***Figure 91 – SEM image of a septin mesh***

*SEM image of short septin filaments forming a mesh. Image is a zoom of Figure 90 (top left). Septin filaments show two main orientations which have been highlighted and colored, the angle between these two filaments is 31°.*

These structures are reminiscent of septin networks *in vivo* during cytokinesis in budding yeast. Indeed, SEM experiments showed that short filaments (~300 nm) organize into meshes of perpendicular filaments[147]. While it makes sense that short filaments (~150 nm) would not be able to sense micrometric curvatures like long filaments have been observed to do, it is still unclear what drives them to organize with a specific angle. Unlike branched actin networks where actin filaments bind to Arp2/3 complexes to polymerize and form networks with 70° angles between individual filaments, these septin networks are only constituted of short filaments and we are still unsure of the biological relevance of such structures.

To assess the possibility the arrangement of septin on undulated surfaces might be transient, we tested longer incubation time (24 hours instead of just 1 hour) to ensure that chemical and mechanical equilibrium was reached. Figure 92 show several pictures of these long incubation time and their ODF.

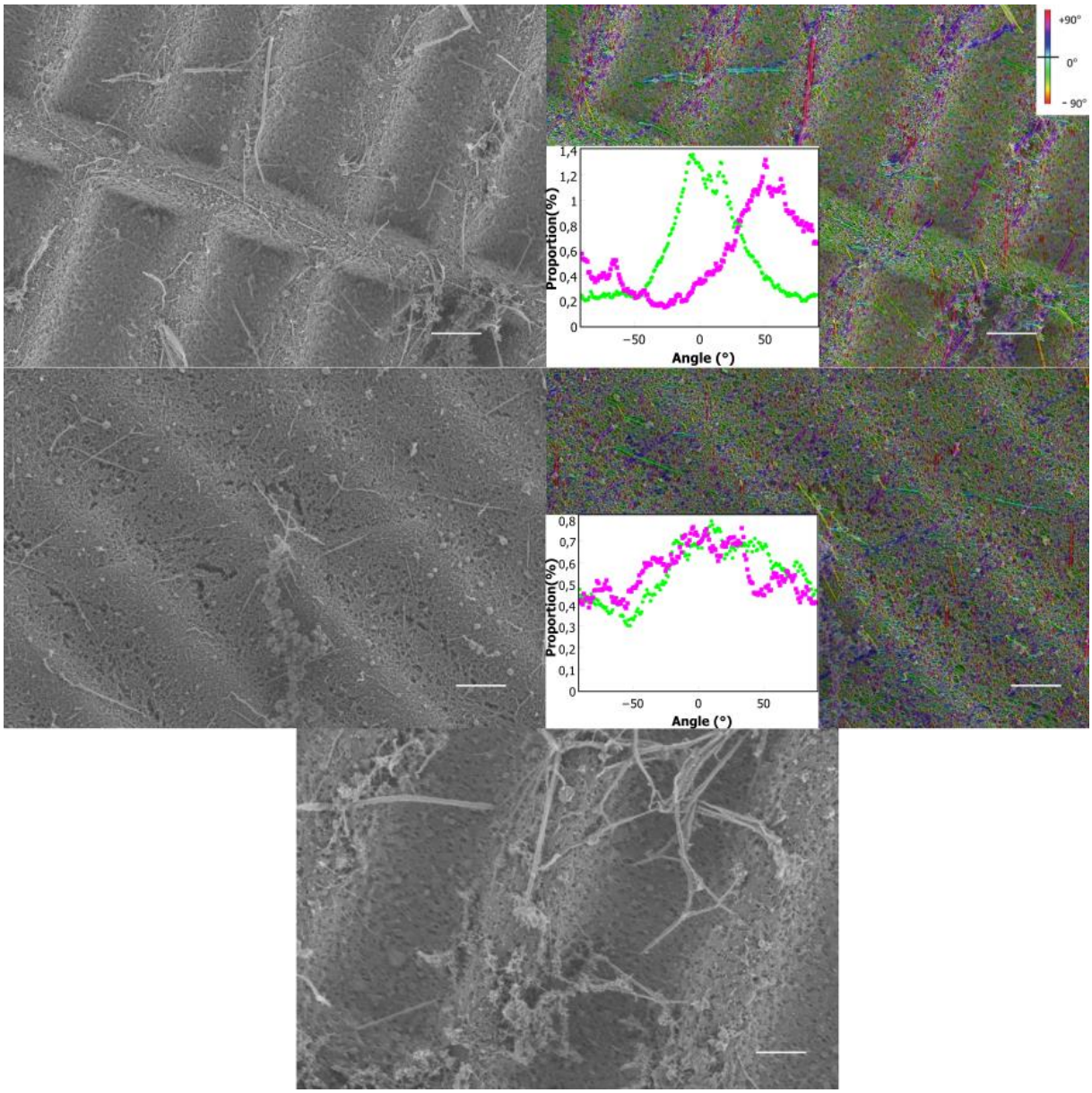


***Figure 92 – SEM images of long incubation time***

*SEM images of patterned substrates coated with a lipid bilayers and incubated with 250 nM septin for 24 hours and the respective ODF, green curves correspond to positive curvatures and magenta to negative ones. Scale bars are top and bottom : 1 µm, middle : 500 nm.*

We have first noticed that septin filaments tend to bundle and form thicker structures (about 50 nm in diameter) when left to incubate for a long time. These thick filaments were mostly present at positive curvatures (Figure 92, top) and would still follow the axis of null curvature but could sometimes be observed to cross the main axis of curvature (Figure 92, middle). On negative curvatures, shorter and thinner filaments were present but the difference in orientation still persisted between positive and negative curvatures. Another striking consequence of leaving septins incubated for a long time is the appearance of many holes in the lipid bilayer, thus disrupting the order of assembly of septin filaments since they don't have a continuous surface to bind on (Figure 92, middle). This is not completely surprising because we already know that septins are able to deform the membrane. Thick septin bundles would also sometimes assemble into large patches (Figure 92, bottom).

Finally, we wanted to test whether the curvature sensing ability of septins was a property of being filamentous or whether non-polymerized octamers were also able to sense curvature after annealing on a membrane. In order to investigate that, we expressed a cdc11 mutant truncated at its $\alpha_0$ helix located at the C-terminus which impedes end-to-end interaction between octamers, thus preventing filament formation in solution. This mutant is still able to polymerize, to some extent, once bound to a lipid membrane[173]. The cdc11Δα$_0$-cdc10-cdc12-cdc3 septins octamers at 200 nM were incubated for 1 hour before metallic deposition for SEM imaging. Figure 93 shows a SEM image of this experiment and the corresponding ODF extracted from it. The measured mean angle and order parameters are $\alpha_{mutant} = 5.8$ ° and $m_{mutant} = 0.25$ respectively.

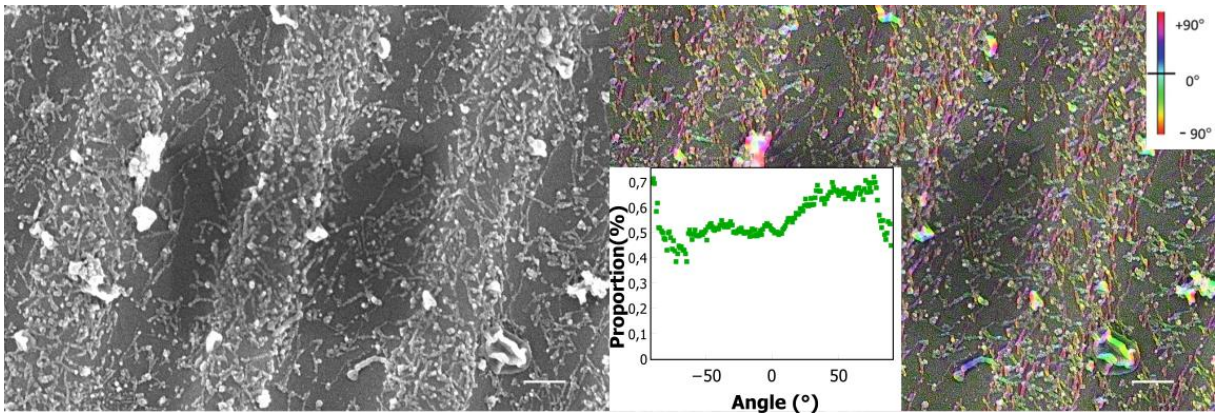


***Figure 93 – SEM images of septin mutants on patterned substrates***

*SEM images of cdc11Δα0-cdc10-cdc12-cdc3 septins bound to a patterned substrate ($C_{max} = 5$ µm-1) coated with a lipid bilayer (left) and the corresponding colored version and ODF extracted from it (right). Scale bars are 200 nm.*

As expected, the filaments observed are much shorter than wild type filaments ($L_{mutant} = 164 \pm 28$ nm, about 5 octamers) since they do not have the ability to polymerize in solution prior to binding to the membrane. Importantly, their orientation is not curvature-dependent. They display an isotropic orientation as shown by the ODF and the value of the order parameter. Their organization is thus similar to this of wild type filaments on a flat surface. These results indicate that the curvature-sensing ability of septins stems from long filaments and is absent at the octameric level and that these long filaments are necessary to generate the small scale order observed on flat membranes. With that in mind, we developed a theoretical model based on filament mechanics, membrane interaction and geometry that describes the behavior of septins on curved membranes.

## Summary

- **Septins are enriched at positive curvatures.**
- **Septins adopt a flat and ordered conformation on positive curvatures. Independently on the value.**
- **Septins adopt a curved and less ordered conformation on negative curvatures. This depends on the value.**
- **Septins adopt an isotropic conformation on flat surfaces but show a small-scale order.**
- **Septins can form small gauze-like pattern, independently on the curvature.**
- **The Δα0 mutant of septins does not display the properties mentioned above.**

### 3.3.3 Theoretical model

Given our results, it seems clear that septins are sensitive to curvature whether it is by forming spike-like structures of micrometric size on deformable membrane or by orienting differently on positive and negative curvatures. In that direction, we developed a theoretical model with the help of Hervé Isambert, a theoretician working at the Curie institute. With this model, we try to explain how septin filaments assemble and orient themselves on a membrane with a cylindrical topography (much like our patterned substrates, where one axis has a curvature $C$ which can be positive or negative and the other axis, called the axis of null curvature, has a zero curvature) by comparing the binding energy of filaments $F_{bind}$ and the bending energy $F_{bend}$ to describe their free energy per unit length. These two energy terms can be written as:

$$F_{bind} = \frac{k_b T}{8a} \ln K_d$$

With $K_d$ being the dissociation constant between septins and lipids and $a$ the width of a septin subunit and equal to 4 nm. The factor $\frac{1}{8}$ is due to the fact that septin complexes are octameric and present 8 binding sites to the membrane. The value of $F_{bind}$ is always negative otherwise no binding would occur. The bending energy of a filament depends on its persistence length $L_p$ and can be expressed as:

$$F_{bend} = \frac{k_b T}{2} L_p C^2$$

Where $C$ is the curvature of the bent filament. To be able to use this model and predict how septin organize on cylindrical membranes, the parameters $K_d$ and $L_p$ have to be determined. The value of $K_d$ was experimentally measured on a flat glass coverslip coated with a lipid bilayer using the same lipid composition as the one used in the previous experiments. The fluorescence intensity of bound septins at increasing septin concentration was measured (for the detailed protocol, see section 2.8.2) to be was $K_d = 220 \pm 27$ nM. We measured the $K_d$ on undulated samples with curvatures of $C = \pm 3$ µm$^{-1}$ and found sensibly the same values (199 and 225 nM). In addition, the low logarithmic dependency of the binding energy with the dissociation constant makes it not very sensitive and we decided to keep the value of $K_d = 220 \pm 27$ nM as a constant. The persistence length was measured as described in section 2.8.3 with a value of $L_p = 7.8 \pm 1.1$ µm.

The free energy per unit length of a bound filament on a flat surface has been described earlier as $F_{bind} = \frac{k_b T}{8a} \ln K_d$. When a filament binds to a curved surface, the contact surface will be different as explicated in the Euler-Bernoulli beam theory. To understand that, let us consider a filament that we describe as a rectangular cuboid of length $L$, width and height $a$ and incompressible (see Figure 94, left).

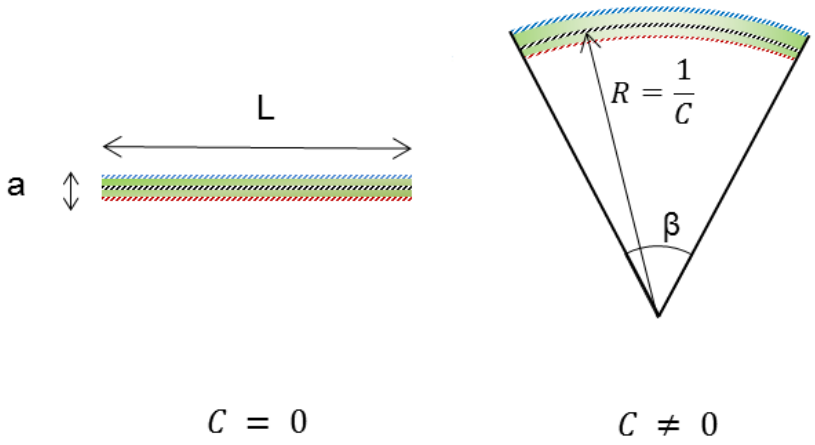


***Figure 94 – Model filaments***

*Straight filament represented as a rectangular cuboid of length* L*, width and height* a *(left). The same filament curved at a radius* $\mathrm{R} = \frac{1}{\mathrm{C}}$ *(right).*

When the filament is not under stress, it has a straight shape and its length $L$ is the same at the bottom (represented by a dashed red line in Figure 94), the center (dashed black line) and the top of the filament (dashed blue line). When the filament is curved with a curvature radius $= \frac{1}{C}$, it describes an angle $\beta$ and the length of the center line (dashed black line) is still $L$ which means the corresponding arc length is $\xi_{center} = R\beta = L$. However, the bottom and top part (red and blue lines respectively), while still describing the same angle $\beta$, form an arc length at a radius $R' = R \pm \frac{a}{2}$, the red line being shorter and the blue line being longer. This implies that the corresponding arc lengths are $\xi_{bottom} = R\left(1 - \frac{a}{2R}\right)\beta$ and $\xi_{top} = R\left(1 + \frac{a}{2R}\right)\beta$ that we can rewrite and $\xi' = L\left(1 - \frac{a}{2}C\right)$ when orienting the surfaces (using the convention that a negatively curved filament binds to a positively curved membrane and vice versa). Consequently, a bent filament will present less or more contact area whether it is positively (red) or negatively (blue) curved. This geometrical observation is the center point of the model and the driving force of the organization of filaments. With that in mind, we can rewrite the binding energy per unit length of a curved filament:

$$F_{bind}(C) = \frac{k_b T}{8a} \ln K_d \left(1 - \frac{a}{2} C\right) = F_{bind}^0 \left(1 - \frac{a}{2} C\right)$$

And the total free energy per unit length of a curved filament:

$$F(C) = F_{bind}^0 \left(1 - \frac{a}{2} C\right) + \frac{k_b T}{2} L_p C^2$$

The minimum of energy is then obtained at a critical value:

$$C^* = -\frac{F_{bind}^0 a}{2 k_b T \, L_p}$$

This corresponds to an optimum of energy for a negatively bent filament. This model can be generalized for association $n$ of filaments as septin filaments have a tendency to assemble. If we assume a circular section of an association of filaments, the different parameters can be expected to scale as:

$$a_n \approx a_1 \sqrt{n}$$

$$L_{pn} \approx L_{p1} n^2$$

$$F_{bind,n}^0 \approx F_{bind}^0 \sqrt{n}$$

$$C_n^* \approx C_1^* n^{-1}$$

In solution, budding yeast septin usually assemble into paired filaments[165]. This means that the value of $L_p$ that we measured by analyzing the fluctuation of septin filaments on a passivated surface by TIRF microscopy is the value of $L_{p2} \approx 8$ µm. For a single filament, we have $L_{p1} \approx \frac{L_{p2}}{4} \approx 2$ µm. The optimum curvature for a single filament is then $C_1^* \approx -1.4$ µm$^{-1}$ and for a double filament $C_2^* \approx 0.7$ µm$^{-1}$, which is in good agreement with the dimensions of the deformations induced by septin filaments on GUVs we observed by spinning disk microscopy ($C_{spikes} = 0.9 \pm 0.2$ µm$^{-1}$).

Next, we can use this model to predict the orientation of septin filaments on a cylindrical topography by comparing the free energy per unit length of a flat filament and a curved filament:

$$\Delta F = F(C) - F(0) = -\frac{F_{bind}^{0} a}{2} C + \frac{k_b T}{2} L_p C^2$$

When the value of $\Delta F$ is positive, it means that the energy required to bend the filament is greater that the energy gained by increasing the contact area with the substrate. In that case, the filament will avoid being curved by remaining straight and will bind to the membrane along the axis of null curvature. Interestingly, this value is always positive for positively curved filament. In that case, the filaments will always avoid being positively bent and always lay flat on negatively curved surfaces. This result is reminiscent of the observations made on septin filaments bound to patterned substrates in section 3.3.2, at the top of the sample where filaments are positively curved, they always follow the ridge of the sample and adopt a flat configuration and this, independently of the value of the curvature as long as it is positive. For $\Delta F$ negative, the filament will bind and align with the axis of curvature $C$ for values $0 > C > C'$ with $C' = \frac{F_{bind}^{0} a}{k_b T L_p} = 2C^*$ which corresponds to $\Delta F = 0$ and sets the limit between the two regimes. For values lower than $C'$, the filaments will orient themselves to follow the axis of null curvature as the bending energy becomes too big to be compensated by the gain in binding energy. This assessment is supported by the results shown by SEM images in section 3.3.2 where we see septin filaments negatively curved following the curvature of the sample. Another interesting feature of this model is that it predicts that the value of $C_n'$ depends on the number of filaments bundled together with $C_n' \approx C_1' n^{-1}$. For instance, we can calculate the values $C_1' \approx -2.8$ µm$^{-1}$, $C_2' \approx -1.4$ µm$^{-1}$ and $C_4' \approx -0.7$ µm$^{-1}$. This implies that a different number of bundled filaments (single, double…) will have different critical values at which they go from a curved configuration to a flat configuration, leading to the possibility of having septin filaments arranged with different orientations. This is the case *in vivo* as shown by SEM observations on budding yeast spheroplasts where single and double septin filaments were found to organize perpendicular to one another with the double filaments on top of the single filaments[147]. For intermediary negative curvatures $0 > C^* > C > C'$, we expect septin filaments to be curved and not completely parallel to the axis of curvature but rather with a certain angle with it as orientations other than the one aligned with the axis of curvature will have a lower energy states.

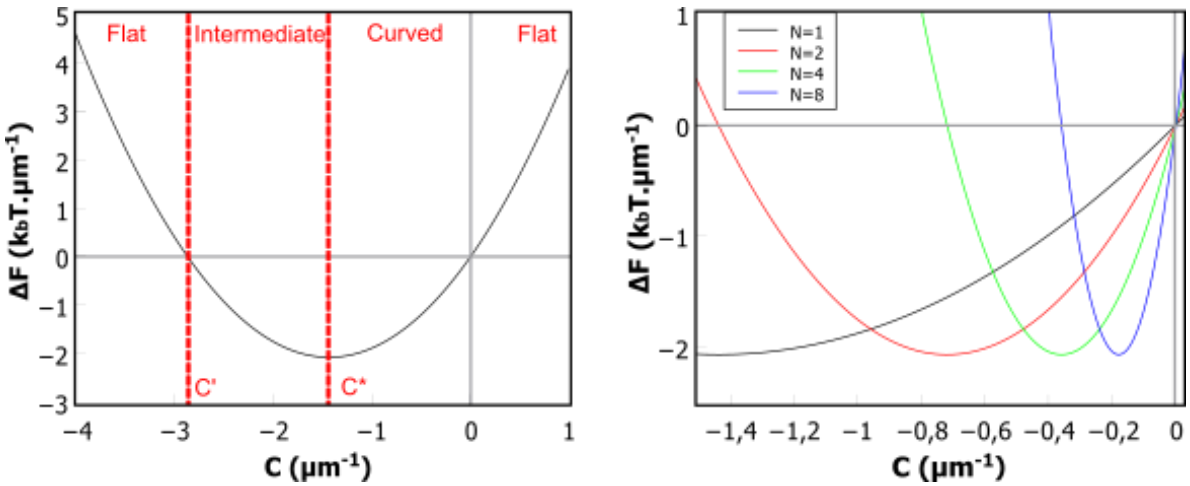


***Figure 95 – Energy profile of bound septin filaments***

*Left - Energy profile of a single septin filament bound on a membrane of curvature* $C$*. The value* $C^* = -1.44$ *µm corresponds to a minimum of energy and the value* $C' = -2.88$ *µm corresponds to the border between a flat and intermediately curved filaments (dashed lines). Right – Energy profile of a single filament (black), double (red), quadruple (green) and octuple (blue) filaments.*

During cell divison, septins assemble onto the plasma membrane at the neck between the mother and daughter cell which undergoes several remodeling processes. First, the bud resembles a spherical cap and then turns to a tubular shape that later shrinks to finally collapse as the scission occurs. In the meantime, septins accumulate at the onset of budding into a radial arrangement and switch to an hourglass shaped structure to finally split into two rings during cytokinesis. To explain the different orientations that septins can adopt on those morphologies, we generalized of this model by considering this time a membrane with axial symmetry with two axis of main curvature where both can be positive, negative or zero. We will try to predict radial or circumferential adsorption of septin filaments, respectively to parallel ($C_{||}$) or orthogonal ($C_{\perp}$). The equations can be easily transposed as:

$$F(C_{||}) = F^0_{bind}\left(1 - \frac{a}{2}C_{||}\right) + \frac{k_b T}{2}L_p {C_{||}}^2$$

$$F(C_{\perp}) = F^0_{bind}\left(1 - \frac{a}{2}C_{\perp}\sin\theta\right) + \frac{k_b T}{2}L_p {C_{\perp}}^2$$

Where $\theta$ is the angle between the filament and the plane of circumferential orientations (see Figure 96).

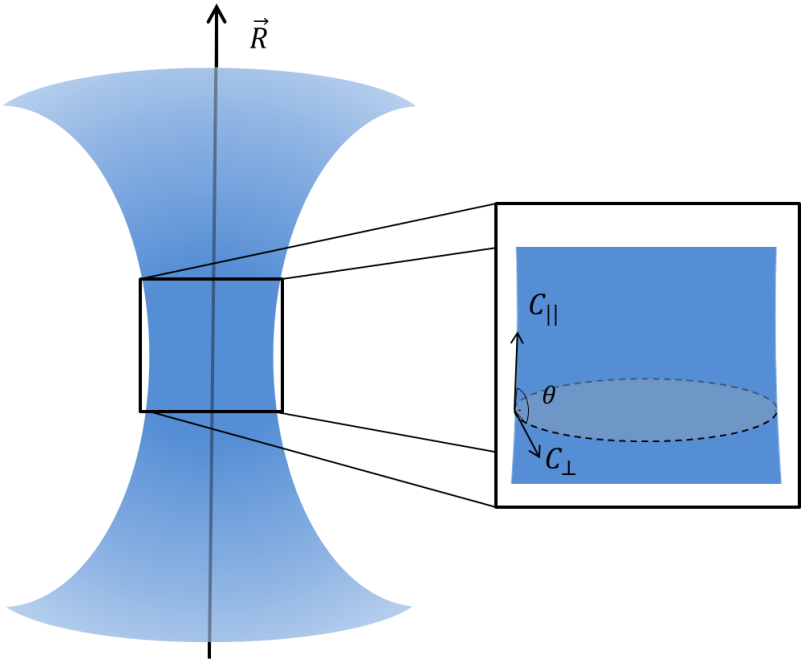


***Figure 96 – Object with axial symmetry***

*Sketch of an object with an axis of symmetry $\vec{R}$. The two main curvatures $C_{||}$ and $C_{\perp}$ and the angle $\theta$ are represented in the zoomed portion of the image.*

Two special cases are of particular interest, namely a spherical shape where $\sin\theta = \frac{R_{\perp}}{R_{||}}$ and an oblong shape where $\sin\theta \approx 1$.

First, for spherical shape, we have $\sin\theta C_{\perp} = C_{||}$ which cancels the contribution linked to the increase of contact area between radial or circumferential orientations:

$$\Delta F_{sphere} = F(C_{||}) - F(C_{\perp}) = \frac{k_b T}{2} L_p \left({C_{||}}^2 - {C_{\perp}}^2\right)$$

In that case, septins will always adopt a radial rather than circumferential orientation as $R_{\perp} \leq R_{||}$ or $|C_{\perp}| \geq |C_{||}|$, with $C_{\perp}$ corresponding to a plane cutting a section of the sphere (see Figure 97). In the limit case where $R_{\perp} = R_{||}$ which corresponds to a half-sphere, filaments could arrange both way as the two orientations become similar.

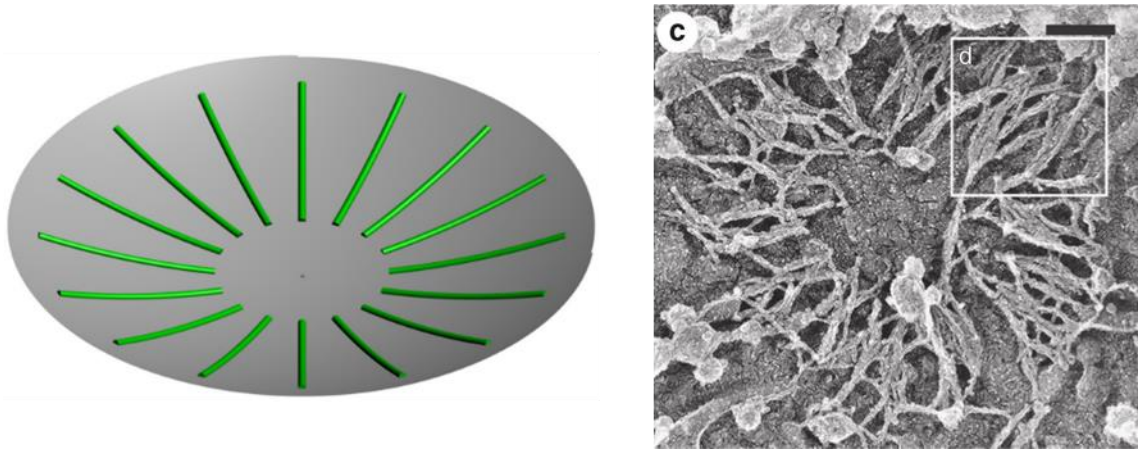


***Figure 97 – Septin on a spherical topography***

*Sketch of septin filaments arranged radially on a section of a sphere (left). SEM image of septin filaments arranged radially during the onset of budding, which has a locally spherical topography, in budding yeast spheroplasts*[147]*. Scale bar is 50 nm.*

This radial orientation is consistent with the orientation of septin filaments at the onset of budding where they show an exclusively radial arrangement. We will now consider a more general oblong shape of the neck of a diving cell with an axial symmetry, close to a cylinder (see Figure 96). The membrane and the circumferential plane are close to orthogonal and we can consider $\theta \approx 90°, \sin\theta \approx 1$. The two equations become:

$$F(C_{||}) = F^0_{bind}\left(1 - \frac{a}{2}C_{||}\right) + \frac{k_bT}{2}L_p{C_{||}}^2$$

$$F(C_{\perp}) = F^0_{bind}\left(1 - \frac{a}{2}C_{\perp}\right) + \frac{k_bT}{2}L_p{C_{\perp}}^2$$

Again, we can compare the adsorption of radial versus circumferential filaments:

$$\Delta F_{oblong} = F(C_{||}) - F(C_{\perp}) = \frac{F^0_{bind}a}{2}(C_{\perp} - C_{||}) + \frac{k_bT}{2}L_p({C_{||}}^2 - {C_{\perp}}^2)$$

This leads to a transition of orientation from radial to circumferential as the membrane goes to an oblong shape where $C_{||} > 0$, to a cylinder for $C_{||} = 0$ to an hourglass shape for $C_{||} < 0$. The value of $C_{||}$ will then keep decreasing as the neck constricts more and more. This transition will happen as the following condition is reached:

$$(C_{||} - C_{\perp})(C_{\perp} + C_{||} - C_n') > 0$$

With $C_n' = \frac{F_{bind}^0 a_n}{k_b T L_{pn}} = C_1' n^{-1}$. Therefore, we expect a different number of septin filaments connected (single, double…) to undergo this transition at different critical values of the local curvature $C_{\perp} + C_{||}$. For instance, for an oblong shape where $|C_{||}| < |C_{\perp}|$, we expect single filament to adopt a circumferential orientation while double filaments (or more) are expected to arrange radially, following the axis of revolution as long as $C_2 > C_{\perp} + C_{||} > C_1$ (see Figure 98, B). Then, upon further constriction of the membrane, both single and double filaments will adopt the circumferential orientation under the condition that $C_2 > C_1 > C_{\perp} + C_{||}$ (see Figure 98, C). Finally, as the neck becomes very small, we expect septin bundles to reach their minimum curvature under membrane adsorption. Under those conditions, the energy gain from the addition of contact area can be neglected as $\frac{Ca_n}{2} \ll 1$ and the energy per unit length can be written as:

$$F_n(C) = F_{bind}^0 + \frac{k_b T}{2} L_{pn} C^2$$

Which leads to a maximum curvature of septin bundles:

$$C_n^{max} = \sqrt{\frac{-2F_{bind}^0}{k_b T L_{pn}}}$$

And $R_n^{min} = \frac{1}{C_n^{max}}$. For single filaments, $R_1^{min} \approx 84\ nm$ and octuplet filaments $R_8^{min} \approx 397$ nm. Ultimately, this minimum radius of curvature might drive the separation of the septin assembly at the neck into characteristics double rings that include dozens of filaments on each side of a thinner membrane bridge across the two cells (see Figure 98, D). Indeed, the typical value of these rings is in the range $0.5 - 1$ µm.

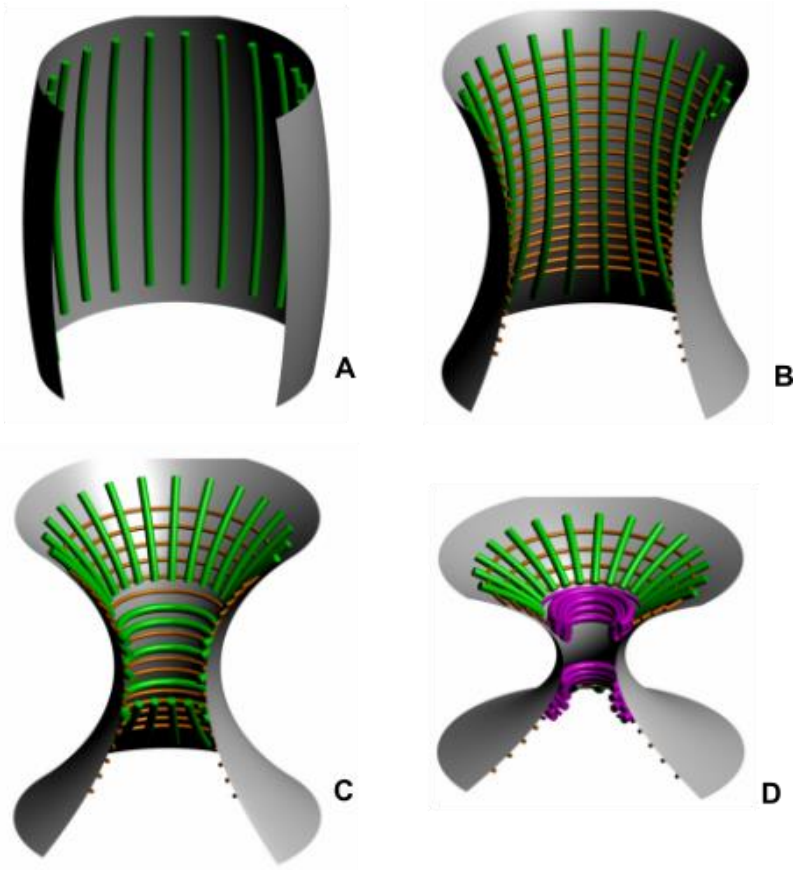


***Figure 98 – Membrane constriction and septin reorganization***

*Sketch of septin filaments bound to an oblong-shaped membrane. Starting from a barrel-shaped membrane, double filaments (green) will bind and orient radially (A). As the membrane switches to an hourglass-shaped structure, at low curvatures, double filaments will maintain their radial orientation while single filaments (orange) will prefer a circumferential orientation (B). As the neck of the membrane constricts, two populations of single and double filaments will coexist: only circumferential filaments at the center of the constriction surrounded by radial single filaments and circumferential double filaments (C). As the neck constricts further, thick filaments are expected to lie at both sides of the center of the constriction (D).*

Other processes such as the molecular interaction with partners, cooperation with the cytoskeleton and other filamentous proteins might be at play during the remodeling of the septin network during cell division. Our model explains the behavior of septin filaments under several geometrical configurations and its conclusion seems to corroborate observations made by SEM both *in vivo and in vitro*. Hence we can assume that geometrical and physical parameters may facilitate the cytokinetic process driven by biological pathwaysAn interesting feature of this model is that it makes no hypothesis on the nature of the filament and no

specific coupling with the membrane is assumed, which also might play a role as septins interact specifically with PI(4,5)P2. The only parameters are the binding energy and the gain of binding energy that occurs by exposing more contact area when the filament is curved and the bending energy that acts as an opposing force. In theory, this model could work for other time of membrane-binding filaments, given they have the correct ratio of binding over bending energy.

## Summary

- **The model describes the orientation of n filaments on a cylindrical topography.**
- **It is based on filament mechanics and geometrical considerations.**
- **The model predicts 4 regimes depending on the sign and the value of the curvature.**
- **A generalization of the model predicts reorientation of the filaments as the curvature of the surface increases.**

## 3.4 Conclusion and discussion

The first goal of this study was to use *in* vitro assays to understand the role of the septin cytoskeleton in the plasma membrane mechanics of budding yeast using purified cdc11-GFPcdc10-cdc12-cdc3 complexes. We also investigated the septins ability to sense curvature and analyzed how they assemble onto curved membranes. My main results are gathered within two articles. A technical report on the optimization of septin-GUVs interaction has been accepted for publication in cytoskeleton. An additional article (in revision in nature communications) describes how septins, being curvature sensitive can remodel membrane. The results are summarized as follows:

The interaction of septin assemblies with our biomimetic systems was optimized. Using the specificity of septins with PI(4,5)P2, we compared their affinity with a commonly used PI(4,5)P2 reporter: PLC-δ. We showed that septins are more specific to PI(4,5)P2 since they did not interact with PI(4,5)P2-depleted GUVs while PLC-δ still did. PLC-δ is a human enzyme that specifically interacts with PI(4,5)P2 *in vivo*. It was shown that it can also specifically interact with PI(4,5)P2-doped vesicles *in vitro*, even at low concentrations[254]. The same study also reported that PLC-δ could interact with LUVs deprived of PI(4,5)P2 in the presence of 50% DOPS. This shows that PLC-δ can interact non-specifically with anionic lipids. The presence of several anionic lipids, including 10% DOPS, in our GUVs might be enough to observe this non-specific interaction. A screen for 388 PI(4,5)P2-interacting proteins showed that the specificity of septins was among the highest[255]. Taken together, this indicates that septins are reliable PI(4,5)P2-reporter candidates.

Growing artificial vesicles using PI(4,5)P2 can be quite challenging. The optimization process we went through during this study was the subject of a published paper[243]. We compared different growing conditions (lipid composition, buffer composition, growth methods) to optimize the septin/membrane interaction. As a result, the optimal interacting conditions were determined and used for the rest of the study. One of the main challenges when using reconstituted lipid systems to study membrane-associated proteins is the specificity of the interactions, which is empirical. Because research on septins is still a blooming field, we have provided a tool to facilitate the implementation of biomimetic membranes into future septin studies.

While we were still optimizing our system, we found that, on rare occasions, septins were able to induce peculiar GUV morphologies such as sharp angles and flattened facets instead

of displaying a regular spherical shape. These deformations were not transient within the experimental timescale (tens of minutes to hours), resembling plastic deformations. This, along with several *in vivo* studies showing their implication in the remodeling of the plasma membrane of living cells, led us to hypothesize that septins could be directly involved in the remodeling of model membrane. To test this hypothesis, we used a micropipette assay to hold and fix the tension of GUVs. Inspired by two studies on $\alpha$-synuclein and endophilin[178,222], we used confocal microscopy to record possible changes in the projected area induced by the local injection of septins. We were able to see that the projected surface area of GUVs decreased (by about 1-2%) when interacting with septins. This experiment alone was not able to give us a definite answer on the mechanism of action. We hypothesized that this drop in projected area results from two different phenomena. First, the septin network could act as a rigid scaffold and effectively increase the mechanical resistance of the GUVs. Since the area expansion of the GUV under tension depends on its bending and stretching moduli, an increase in those values would consequently result in a lower area expansion. This has been reported with clathrins, which increase the bending rigidity of GUVs by a factor of 10[256]. Second, septins could also remodel the membrane reservoir present in the thermal fluctuations at a scale that was not resolved at optical resolution. Membrane remodeling by membrane-bound proteins is common. These hypotheses would corroborate the *in vivo* observations which show that septins are necessary to maintain the shape of the membrane[71,72].

We tested the first hypothesis by performing osmotic shock experiments on septin-coated GUVs. We showed that the presence of septin filaments was sufficient to prevent the collapse or bursting of GUVs compared to naked vesicles up to osmolarity differences of +450 mOsm or -75 mOsm. In response to osmotic shocks, vesicles can equilibrate their pressure by two mechanisms. If the fluctuations are small enough (about the size of the membrane thickness), the vesicle rapidly exchanges solutes with the external medium through small pores. When the osmotic pressure is too high and the membrane fluctuations become comparable to the vesicle radius (i.e. “floppy” vesicles), the vesicle can either rupture (hypo-osmotic shock) or shrink by nucleating small daughter vesicles that can even lead to pearling (hyper-osmotick shock)[257]. In the case of hypo-osmotic shocks, the presence of the septin network reduces the total surface area of the membrane in contact with the outer medium, thus reducing the permeability of the membrane. This promotes the nucleation of bigger pores that can lead to vesicle rupture. Although the presence of the septin network does not greatly affect the resistance of the membrane to swelling, it changes the dynamics of the permeation process. In the case of hyper-osmotic shocks, the vesicle cannot regulate its osmolarity as efficiently because the rigid septin scaffold weakens the

membrane fluctuations that lead to budding of smaller vesicles. The vesicle has then to resort to permeation to equilibrate the osmolarity. This results in an increased surface area by creating folds, as observed. Those highly curved folds can promote pore nucleation as numerical simulation have suggested[258]. A study performed similar experiments using avidin or streptavidin as membrane-binding proteins[257]. They found significantly different behaviors when comparing the two, with avidin-coated vesicles showing relatively normal shapes under osmotic stress. Avidin creates a soft coating on the vesicles that can elastically expand, which does not affect the vesicle mechanics. Conversely, streptavidin which forms a crystalline network on the membrane would induce crumpling of vesicles under hyper-osmotic conditions, in the same fashion as our septin-coated GUVs. This strengthened the idea that septins formed a rigid scaffold that could effectively tune the mechanical properties of the membrane.

The mechanical properties of GUVs, namely the bending and stretching moduli, were measured in the presence or not of septins using hallmark tools: a micropipette assay and optical tweezers. We reported a decrease (~ -50%) in the value of the stretching modulus in the presence of septins compared to the naked membrane. This is probably due to the shallow insertion of budding yeast septins into the membrane (about 1.2 nm) to fulfill their function, as shown by numerical simulations[250]. Because of their insertion, the surrounding lipids are pushed away, resulting in an increase of the stretching of the membrane. This effect would reduce the apparent stretching modulus. Surprisingly, we found no difference in the measurement of the bending modulus in the presence or not of septins even though osmotic shock experiments tend to show the opposite. This result was consistent over the two experimental tools we used (micropipette aspiration and nanotube pulling). A first explanation could be that the interaction between the septin network and the GUVs is weaker than the energy necessary to bend the membrane, resulting in a detachment of the network when applying mechanical stress. This is unlikely as the binding energy per unit length is higher than the bending modulus of our GUVs ($F_{binding} \approx 50 k_b T.\mu m^{-1}$ and $\kappa_{GUV} \approx 10\ k_b T$). With these values, we can undoubtedly believe that the septin network is tightly connected to the membrane upon its deformation. A second hypothesis would be that the rigidity of the septin network is too low compared to the rigidity of the GUV, making the effective bending modulus of the complex GUV+septins sensibly the same. However, the bending modulus of a double filament was measured to be $\kappa_s = k_b T L_{p2} \approx 8\ k_b T.\mu m$. This value is comparable to the bending modulus of the whole GUVs. One would find it reasonable to think that the effective bending modulus of the whole network, composed of many intertwined and bundled filaments would be higher than the value of a double filament, rejecting the hypothesis of a

soft septin network. Measurement of the bending modulus by micropipette aspiration relies on the thermal fluctuations of the membrane at low tensions. The presence of the septin network impedes these fluctuations. The relationship between the area variation and the tension for low tensions regimes includes the ratio of thermal and bending energy as seen by the following equation:

$$\frac{\Delta A}{A_0} \approx \frac{k_b T}{8\pi\kappa} ln \frac{\sigma_0}{\sigma}$$

It is thus possible that the increase in rigidity by the septin network is effectively compensated by the dampening of the thermal fluctuations, resulting in an apparent similar bending modulus. Another hypothesis would be that non-linear local deformations of the network are induced on the septin network. We used a theory describing semiflexible filaments and networks[259] and specifically the Heussinger-Frey model on non-affine deformation of 2D networks[260,261]. First, let us consider a 2D network of area $A$ composed of $N$ filaments that are randomly distributed and oriented within the network. This isotropic distribution of filaments gives an isotropic distribution of angles $\theta$ between two intersecting filaments $P(\theta) = \frac{\sin(\theta)}{2}$ and the distribution of the mesh size $\xi$ (which is equivalent to the mean distance between two contact points in the network) can be written as:

$$P(\xi) = \frac{e^{\left[\frac{-\xi}{\langle\xi\rangle}\right]}}{\xi}$$

Using the measurement of the filament bending modulus $\kappa = k_b T L_p$ where $L_p$ is the persistence length of the filament and $k_b T$ the thermal energy, numerical simulations have shown that such a network has two distinct regimes characterized by a length scale:

$$l_c = \frac{L_f}{\left(\delta\rho L_f\right)^{\nu}}$$

With $L_f$ being the full length of a filament, $\delta$ corresponds to the axial displacement of the filament induced by the deformation of the network and is comparable to $\xi$, $\rho$ is the filament density and $\nu \approx 2.84$. For filaments with a radius $\gg l_c$ , the deformations spread evenly throughout all the network. These deformations are affine (meaning they can be described by linear transformations such a rotation, strain, and translation). In that case, the elastic

response mainly arises from the stretching of the network. For filaments with a radius $a \ll l_c$ the non-affine deformations dominate the network (non-linear transformations, resulting from a stress that is transmitted inhomogeneously). In this model, the filament length is large compared to the mesh-size and the radius. To estimate which regime was being investigated during the micropipette experiments, we need a measurement of the different parameters. With our SEM data we were able to obtain the values $L_f = 1.4 \pm 0.2$ µm, $\delta \approx 0.7 \pm 0.2$ µm and $\rho = 30 \pm 9$ µm$^{-2}$ which give a value of $l_c \approx 60$ nm which is well above the value of $a \approx 2$ nm. As a consequence, the mechanical behavior of the septin network *in vitro* arises mainly from non-affine deformations. Unfortunately, this observation means that these two methods might not be suited to investigate the mechanical properties of GUVs coated with a non-flexible protein network. The same hypothesis has been proposed when measuring the mechanical properties of streptavidin-coated GUVs[251]. The streptavidin coating forms a crystal and the mechanical stress applied by a micropipette induced ruptures points in the crystal, making the data hard to interpret. The same study showed that AFM was better suited to investigate those properties. Finally, it is also possible that the mechanical properties of the GUVs are unaffected by the presence of septins but the osmotic shock experiments, combined with the similar behavior of clathrin- and streptavidin-coated GUVs strongly suggest the opposite. Additional AFM measurements would potentially remove any doubt by giving a more reliable quantitative answer.

Separately, we tested the hypothesis of direct membrane remodeling by septins. By incubating GUVs with different amount of septins, we were able to show that they can induce strong deformations of the membrane. Different kinds of deformations were observed within the investigated concentrations ($200 \leq [septins] \leq 600$ nM). At lower concentrations, GUVs appeared faceted with sharp angles between the different facets. However, reproducible deformations were hard to obtain, with very rare events (<1%) and we observed a wide zoology of deformed GUVs. At higher concentrations, septins were able to induce more drastic membrane remodeling by forming spike-like structures. The deformations were much more consistent and reproducible (~33%). Direct membrane remodeling was already observed *in vitro* with the human septin complex SEPT2/6/7[180]. However the mechanism of deformation seems to be different because the human septins induce long fluctuating protrusions rather than shorter and stable micron-sized spikes. Similar spiky morphologies were found on vesicles incubated with FtsZ, a bacterial homologue of tubulin[262,263], indicating a possible universal mode of deformation by a certain category of membrane-binding filaments. After testing different conditions, we concluded that the size of these structures was conserved (about 1 µm in length and 1 µm in curvature radius) and independent on the

GUVs size, indicating preferential dimensions of septin assemblies. The fact that septins consistently assemble into these structures at sufficient concentrations indicates a curvature-dependent mechanisms of membrane deformation. However, unlike BAR domains, septins do not possess an intrinsic curvature. This suggests that septins operate with a different mechanism of membrane deformation.

Several studies both *in vivo* and *in vitro* have already shown that septins can, to some extent, sense and accumulate at specific curvatures. In the current study, we used a novel tool consisting of a surface with a sinusoidal pattern coated with a lipid bilayer to investigate how septin assemble on a cylindrical topography. Using confocal microscopy, we were able to confirm that septins accumulate at positive curvatures compared to negative curvatures with a maximum around 2 $\mu m^{-1}$, as it was already observed on lipid-coated beads[177]. We then used SEM to have a better resolution and be able to see how filaments orient and organize on the patterned bilayers. We showed that septin filaments orient differently on positive or negative curvatures (i.e. on a hill or a valley respectively).

On positive curvatures, septin filaments avoid being positively bent by aligning with the axis of null curvature while on negative ones septins will follow the axis of curvature and bend accordingly. We obtained the distribution of filaments orientation and derived an order parameter from our data. Its values vary from 0 corresponding to a completely random distribution to 1 for a perfect crystal and intermediate values between 0.4 and 0.8 for a nematic order. We found values near 0.8 for positive curvatures indicating that they assemble into an ordered state and this independently on the absolute value of the curvature. For negatively curved filaments, we found a slight difference between filaments with a curvature of -3 and -1.6 $\mu m^{-1}$ with order parameters of 0.59 and 0.45 respectively. We compared those results with a flat sample as a control and found a more isotropic distribution with an order parameter of 0.22, although at lower scale (<1 µm), filaments would show a higher organization and be parallel. We also found small patches ($0.36 \times 0.36$ µm²) of short septin filaments organized into a gauze-like pattern with filament forming a mean angle of 30° between them. These structures were found for all curvatures, positive, negative or null. Finally, we used a mutant: cdc11$\Delta\alpha_0$-cdc10-cdc12-cdc3 that prevents end to end polymerization in solution while keeping the possibility to assemble when bound to a membrane. Again, the filaments showed a random organization compared to regular septin filaments. This result contradicts the hypothesis that septins could sense curvature at the scale of the septin monomer/oligomer via its amphipathic helix[264]. This led us to hypothesize that the curvature-sensing ability of septin is a property of the whole filament and not the

octamer. With these results, we developed a theoretical model, with the help of Hervé Isambert, to predict the orientation of curved (or flat) septin filaments based on filament mechanics and membrane binding energy.

In this model, we describe the free energy per unit length of a filament bound on a curved membrane with a cylindrical topography as a function of two terms: (1) the binding energy that depends on the dissociation constant between the septins and the membrane that we measured on flat lipid bilayers and (2) a bending energy which depends on the persistence length that was measured using fluctuating septin filaments constrained on a surface. These two terms can be generalized to multiple filaments using simple geometrical considerations by approximating filament groups with a cylinder.

To predict whether septin filaments will bend and follow the curvature or will avoid it and remain flat, we compared the free energy per unit **length** of a curved versus a flat filament. By bending a filament at a curvature $C$, the face that is positively bent will be shorter by a factor $\frac{a}{2}C$, with $a$ being the filament width and the negatively-curved side will be longer by the same factor. This is a consequence of the conservation of the volume of the filament. From this, we were able to extract two parameters $C_n^*$ and $C_n'$, the minimum of energy curvature and the transition curvature respectively. These two values correspond to negative curvatures with $C_n'$, < $C_n^* < 0$. For curvatures > 0, septin filaments will always avoid being curved and remain flat by following the axis of null curvature, showing a preferential bending orientation. For curvature between 0 and $C_n^*$, filament will align with the axis of curvature while at curvature between $C_n^*$ and $C_n'$, filaments will adopt an intermediate orientation since states of lower energy at higher curvatures will exist. For curvatures greater than $C_n'$, the bending energy cost will not be compensated by the energy gain related to the increase of contact area with the membrane. The filaments will thus follow the axis of null curvature like they would for positive curvatures. The existence of a minimum of energy at a negative curvature indicates that septins could possibly induce membrane deformations, given that the sum of the energy coming from the bending of the membrane and the bending of the filament is lower than the energy gain. The formation of spikes on the membrane of septins strongly supports this idea. Nevertheless, it is only triggered at high septin concentrations (>400 nM) and it remains unclear whether this mechanism is biologically relevant.

We then developed a more generalized version of the model with two main axes of curvatures instead of a single one with the other being zero. We included a higher variety of geometries including spherical geometries where filaments arrange radially like septin

filaments would in budding yeast at the onset of budding. For oblong geometries, resembling the neck between the two cells at later stages of cell division, septin filaments will cross each other depending on the number of filaments involved (single, double…) and the value of the curvature. It implies that different types of filaments would be able to assemble with different orientation and reorient as the curvature changes during the remodeling of the cell membrane during the division. This model is consistent with our SEM data and the *in vivo* data showing septin filaments crossing each other and reorganizing throughout the different steps of cells division. One limitation of the model however, is that it doesn't take into account septin-septin interaction. *In vivo* studies have shown that septin filaments cooperate to form supramolecular structures while *in vitro* studies revealed that septin filament rarely form single filaments, especially in the presence of membrane[165]. Additionally, the stoichiometry of shs1 and cdc11 subunits is a key component in regulating the organization of septin filaments[97,147]. Whether the curvature sensing ability of septin filaments only depends on binding energy and filament mechanics or not is still an open question. An interesting feature of the model is that it makes no assumption on the nature of the interaction between the filament and the membrane other than regular coupling and simple mechanics, meaning that it could be generalized to other type of membrane-associated filaments, as long as the binding energy is high enough compared to the bending energy. It would be interesting to use similar filaments to repeat those experiments. A good candidate to test this model could be MreB, a bacterial protein essential for the maintain of their rod shape that has been shown to polymerize into filament and to sense micrometric curvatures like septins[265,266]. Another candidate could be the bacterial homologue to tubulin, FtsZ which shows similar properties and can also induce micrometric spikes on model membranes[263,267]. Recent Monte-Carlo simulations successfully predicted the spiky shapes of FtsZ-coated vesicles, bearing a striking resemblance with the morphologies we described[268]. In these simulations, they consider the FtsZ network bound on the membrane as a nematic fluid. The spikes are generated by local nematic defects and depend on the tangent and orthogonal curvatures induced by the filaments. Their model requires that the filamentous network possess a bending rigidity higher than the vesicle modulus. This strengthens our hypothesis that septins can rigidify the membrane and that further measurements are necessary. Taken together, these results strongly suggest that these filaments possess similar properties. Confronting our model with experimental results from those two candidates (FtsZ and MreB) could reveal a universal mode of membrane deformation by membrane-binding filaments.

## Future of the project

Because the processes aforementioned are all dynamic, we tried to perform single molecule experiments on our patterned substrates. The goal was to be able to directly see filament polymerization on curved surfaces and obtain a diffusivity map of these filaments using photoactivated localization microscopy (PALM) techniques. Unfortunately, meaningful data in that direction could not be obtained but we still aim to achieve it as a continuity of my PhD project and continue to optimize the experimental conditions.

An example of dynamic septin process is the assembly of the septin ring, especially during cell division where it undergoes several drastic remodeling. Many *in vivo* studies show that this septin ring is crucial for the establishment of a diffusion barrier for membrane proteins. However, the mechanism by which it restricts membrane-protein diffusion is still unknown. So far, three modes of action have been proposed. The first one explains that membrane-associated objects offer a physical confinement to transmembrane proteins. For instance, the actin cytoskeleton, known for being closely associated to the membrane by anchor proteins, has been shown to reduce their diffusion by providing steric constraints and transient behavior when in contact with actin filaments[269,270]. The endoplasmic reticulum is another candidate for physical diffusion barrier since it has been identified in close contact with other plasma membranes and is a relatively large and immobile structure[271,272]. The extracellular matrix, also known as the glycocalix, have been shown to mechanically constrain integrins to certain locations in cancer cells[273]. Finally, protein crowding and the formation of big proteins clusters can also form obstacles to each other and significantly reduce diffusion[274]. Numerical simulations have shown that septin filaments could act as fences as long as they were sufficiently embedded into the membrane[250]. Moreover, the establishment of the septin fences was completely dependent on PI(4,5)P2 distribution. Additionally to physical collisions, electrostatic interaction in regions of highly charged lipids or proteins can also hinder transmembrane protein diffusion. Phosphoinositides, especially PI(4,5)P2 which is tetravalent, are known to cluster at specific sites[275] and coat some proteins with a cationic barrier[276]. Local composition, specifically saturated lipids and cholesterol rich region known as lipid rafts, can also play a role in modifying the diffusion of proteins by tuning the viscosity of the membrane[277]. Recently, an emphasis on the importance of curvature and curvature-generating proteins in relation to diffusion as well as other mechanical parameters such as membrane tension has been made[178,278,279]. Finally, membrane thinning can also restrict

proteins by creating a mismatch of accessible thickness of lipid tails for the hydrophobic domain of the proteins[280]. Although septins have been identified to be essential for the creation of a diffusion barrier in many tissues and organisms, no definitive model on their mechanism has yet been established. Given their close association with the plasma membrane, it is possible that septin create a physical network of obstacle but they also interact superficially with the ER in yeast and accumulate at region of high PI(4,5)P2 density[172] and their diffusion barrier are localized in places of relatively high curvature. It is also possible that all the aforementioned mechanisms play a role in the diffusion barrier by restricting different type of proteins. Proteins with large cytoplasmic domains would be constrained physically by either the ER or septin filaments and the presence of PI(4,5)P2 enriched region could create a plasma membrane mismatch while larger proteins would be more sensible to curvature and electrostatic repulsions by having a larger coating. Finally, it could be possible that septins are only responsible in the formation of the barrier diffusion while not being actually part of it as they are known to recruit and interact with a lot of proteins. By using this work as a stepping stone, we hope to answer these questions by investigating the diffusive behavior of several membrane proteins in the presence of a septin network. This will be the subject of another PhD project that will be conducted using this study as a working ground.

# *References*


1. Hartwell, L. H. Macromolecule synthesis in temperature-sensitive mutants of yeast. *J. Bacteriol.* **93,** 1662–1670 (1967).

2. HARTWELL, L. Genetic control of the cell division cycle in yeast. *Exp. Cell Res.* **69,** 265–276 (1971).

3. Hartwell, L. H., Culotti, J., Pringle, J. R. & Reid, B. J. Genetic control of the cell division cycle in yeast. *Exp. Cell Res.* **67,** 389–401 (1974).

4. Byers, B. A highly ordered ring of membrane-associated filaments in budding yeast. *J. Cell Biol.* **69,** 717–721 (1976).

5. Byers, B. in *The Molecular Biology of the Yeast Saccharomyces: Life Cycle and Inheritance* 59–96 (1981).

6. Ford, S. K. & Pringle, J. R. Cellular morphogenesis in the Saccharomyces cerevisiae cell cycle: Localization of the CDC11 gene product and the timing of events at the budding site. *Dev. Genet.* **12,** 281–292 (1991).

7. Longtine, M. S. *et al.* The septins: Roles in cytokinesis and other processes. *Curr. Opin. Cell Biol.* **8,** 106–119 (1996).

8. Kim, H. B. Cellular morphogenesis in the Saccharomyces cerevisiae cell cycle: localization of the CDC3 gene product and the timing of events at the budding site. *J. Cell Biol.* **112,** 535–544 (1991).

9. Cao, L. *et al.* Phylogenetic and evolutionary analysis of the septin protein family in metazoan. *FEBS Lett.* **581,** 5526–5532 (2007).

10. Pan, F., Malmberg, R. L. & Momany, M. Analysis of septins across kingdoms reveals orthology and new motifs. *BMC Evol. Biol.* **7,** 1–17 (2007).

11. Nishihama, R., Onishi, M. & Pringle, J. R. New insights into the phylogenetic

distribution and evolutionary origins of the septins. *Biol. Chem.* **392,** 681–687 (2011).

12. NEUFELD, T. The Drosophila peanut gene is required for cytokinesis and encodes a protein similar to yeast putative bud neck filament proteins. *Cell* **77,** 371–379 (1994).

13. Field, C. M. *et al.* A purified Drosophila septin complex forms filaments and exhibits GTPase activity. *J. Cell Biol.* **133,** 605–616 (1996).

14. Weirich, C. S., Erzberger, J. P. & Barral, Y. The septin family of GTPases: Architecture and dynamics. *Nat. Rev. Mol. Cell Biol.* **9,** 478–489 (2008).

15. Bi, E. & Park, H. O. Cell polarization and cytokinesis in budding yeast. *Genetics* **191,** 347–387 (2012).

16. Oh, Y. & Bi, E. Septin structure and function in yeast and beyond. *Trends Cell Biol.* **21,** 141–148 (2011).

17. Kusch, J., Meyer, A., Snyder, M. P. & Barral, Y. Microtubule capture by the cleavage apparatus is required for proper spindle positioning in yeast. *Genes Dev.* **16,** 1627–1639 (2002).

18. Sanders, S. L. & Herskowitz, I. The Bud4 protein of yeast, required for axial budding, is localized to the mother/bud neck in a cell cycle-dependent manner. *J. Cell Biol.* **134,** 413–427 (1996).

19. Chant, J. & Pringle, J. R. Patterns of bud-site selection in the yeast Saccharomyces cerevisiae. *J. Cell Biol.* **129,** 751–65 (1995).

20. Lippincott, J. & Li, R. Sequential assembly of myosin II, an IQGAP-like protein, and filamentous actin to a ring structure involved in budding yeast cytokinesis. *J. Cell Biol.* **140,** 355–366 (1998).

21. Bi, E. *et al.* Involvement of an actomyosin contractile ring in Saccharomyces cerevisiae cytokinesis. *J. Cell Biol.* **142,** 1301–1312 (1998).

22. Dobbelaere, J. & Barral, Y. Spatial coordination of cytokinetic events by compartmentalization of the cell cortex. *Science (80-. ).* **305,** 393–396 (2004).

23. Korinek, W. S. *et al.* Cyk3, a novel SH3-domain protein, affects cytokinesis in yeast. *Curr. Biol.* **10,** 947–950 (2000).

24. Vallen, E. A., Caviston, J. & Bi, E. Roles of Hof1p, Bni1p, Bnr1p, and Myo1p in Cytokinesis in Saccharomyces cerevisiae. *Mol. Biol. Cell* **11,** 593–611 (2000).

25. Fares, H., Peifer, M. & Pringle, J. R. Localization and possible functions of Drosophila septins. *Mol. Biol. Cell* **6,** 1843–59 (1995).

26. Field, C. M. Characterization of anillin mutants reveals essential roles in septin localization and plasma membrane integrity. *Development* **132,** 2849–2860 (2005).

27. Maddox, A. S., Lewellyn, L., Desai, A. & Oegema, K. Anillin and the Septins Promote Asymmetric Ingression of the Cytokinetic Furrow. *Dev. Cell* **12,** 827–835 (2007).

28. Adam, J. C., Pringle, J. R. & Peifer, M. Evidence for functional differentiation among Drosophila septins in cytokinesis and cellularization. *Mol. Biol. Cell* **11,** 3123–3135 (2000).

29. Echard, A., Hickson, G. R. X., Foley, E. & O'Farrell, P. H. Terminal Cytokinesis Events Uncovered after an RNAi Screen. *Curr. Biol.* **14,** 1685–1693 (2004).

30. Eggert, U. S., Mitchison, T. J. & Field, C. M. Animal Cytokinesis: From Parts List to Mechanisms. *Annu. Rev. Biochem.* **75,** 543–566 (2006).

31. Kinoshita, M. *et al.* Nedd5, a mammalian septin, is a novel cytoskeletal component interacting with actin-based structures. *Genes Dev.* **11,** 1535–1547 (1997).

32. Surka, M. C., Tsang, C. W. & Trimble, W. S. The Mammalian Septin MSF Localizes with Microtubules and Is Required for Completion of Cytokinesis. *Mol. Biol. Cell* **13,** 3532–3545 (2002).

33. Spiliotis, E. T. A Mitotic Septin Scaffold Required for Mammalian Chromosome Congression and Segregation. *Science (80-. ).* **307,** 1781–1785 (2005).

34. Estey, M. P., Di Ciano-Oliveira, C., Froese, C. D., Bejide, M. T. & Trimble, W. S. Distinct roles of septins in cytokinesis: SEPT9 mediates midbody abscission. *J. Cell Biol.* **191,** 741–749 (2010).

35. Addi, C., Bai, J. & Echard, A. Actin, microtubule, septin and ESCRT filament remodeling during late steps of cytokinesis. *Curr. Opin. Cell Biol.* **50,** 27–34 (2018).

36. Finger, F. P., Kopish, K. R. & White, J. G. A role for septins in cellular and axonal migration in C. elegans. *Dev. Biol.* **261,** 220–234 (2003).

37. Xie, Y. *et al.* The GTP-Binding Protein Septin 7 Is Critical for Dendrite Branching and Dendritic-Spine Morphology. *Curr. Biol.* **17,** 1746–1751 (2007).

38. Tada, T. *et al.* Role of Septin Cytoskeleton in Spine Morphogenesis and Dendrite Development in Neurons. *Curr. Biol.* **17,** 1752–1758 (2007).

39. Ageta-Ishihara, N. *et al.* Septins promote dendrite and axon development by negatively regulating microtubule stability via HDAC6-mediated deacetylation. *Nat. Commun.* **4,** 2532 (2013).

40. Cho, S. J. *et al.* Septin 6 regulates the cytoarchitecture of neurons through localization at dendritic branch points and bases of protrusions. *Mol. Cells* **32,** 89–98 (2011).

41. Sheffield, P. J. *et al.* Borg/Septin interactions and the assembly of mammalian septin heterodimers, trimers, and filaments. *J. Biol. Chem.* **278,** 3483–3488 (2003).

42. Li, X., Serwanski, D. R., Miralles, C. P., Nagata, K. I. & De Blas, A. L. Septin 11 is present in GABAergic synapses and plays a functional role in the cytoarchitecture of neurons and GABAergic synaptic connectivity. *J. Biol. Chem.* **284,** 17253–17265 (2009).

43. Ewers, H. *et al.* A Septin-Dependent Diffusion Barrier at Dendritic Spine Necks. *PLoS*

*One* **9,** e113916 (2014).

44. Spiliotis, E. T. Regulation of microtubule organization and functions by septin GTPases. *Cytoskeleton (Hoboken).* **67,** 339–45 (2010).

45. Bai, X., Karasmanis, E. P. & Spiliotis, E. T. Septin 9 interacts with kinesin KIF17 and interferes with the mechanism of NMDA receptor cargo binding and transport. *Mol. Biol. Cell* **27,** 897–906 (2016).

46. Webber, W. A. & Lee, J. Fine structure of mammalian renal cilia. *Anat. Rec.* **182,** 339–343 (1975).

47. Adams, M., Smith, U. M., Logan, C. V. & Johnson, C. A. Recent advances in the molecular pathology, cell biology and genetics of ciliopathies. *J. Med. Genet.* **45,** 257–267 (2008).

48. Hu, Q. *et al.* A septin diffusion barrier at the base of the primary cilium maintains ciliary membrane protein distribution. *Science* **329,** 436–439 (2010).

49. Ghossoub, R. *et al.* Septins 2, 7 and 9 and MAP4 colocalize along the axoneme in the primary cilium and control ciliary length. *J. Cell Sci.* **126,** 2583–2594 (2013).

50. Fliegauf, M., Kahle, A., Häffner, K. & Zieger, B. Distinct localization of septin proteins to ciliary sub-compartments in airway epithelial cells. *Biol. Chem.* **395,** 151–156 (2014).

51. Kim, S. K. *et al.* Planar Cell Polarity Acts Through Septins to Control Collective Cell Movement and Ciliogenesis. *Science (80-. ).* **329,** 1337–1340 (2010).

52. Collier, S., Lee, H., Burgess, R. & Adler, P. The WD40 repeat protein fritz links cytoskeletal planar polarity to Frizzled subcellular localization in the Drosophila epidermis. *Genetics* **169,** 2035–2045 (2005).

53. Dash, S. N. *et al.* Sept7B Is Essential for Pronephric Function and Development of Left-Right Asymmetry in Zebrafish Embryogenesis. *J. Cell Sci.* **127,** 1476–1486

(2014).

54. Sharma, N., Kosan, Z. A., Stallworth, J. E., Berbari, N. F. & Yoder, B. K. Soluble levels of cytosolic tubulin regulate ciliary length control. *Mol. Biol. Cell* **22,** 806–816 (2011).

55. Cesario, M. M., Ensrud, K., Hamilton, D. W. & Bartles, J. R. Biogenesis of the Posterior-Tail Plasma Membrane Domain of the Mammalian Spermatozoon: Targeting and Lateral Redistribution of the Posterior-Tail Domain-Specific Transmembrane Protein CE9 during Spermiogenesis. *Dev. Biol.* **169,** 473–486 (1995).

56. Ihara, M. *et al.* Cortical organization by the septin cytoskeleton is essential for structural and mechanical integrity of mammalian spermatozoa. *Dev. Cell* **8,** 343–352 (2005).

57. Steels, J. D. *et al.* Sept12 is a component of the mammalian sperm tail annulus. *Cell Motil. Cytoskeleton* **64,** 794–807 (2007).

58. Peterson, E. A. *et al.* Characterization of a SEPT9 interacting protein, SEPT14, a novel testis-specific septin. *Mamm. Genome* **18,** 796–807 (2007).

59. Kuo, Y.-C. *et al.* SEPT12 orchestrates the formation of mammalian sperm annulus by organizing core octameric complexes with other SEPT proteins. *J. Cell Sci.* **128,** 923–934 (2015).

60. Kissel, H. *et al.* The Sept4 septin locus is required for sperm terminal differentiation in mice. *Dev. Cell* **8,** 353–364 (2005).

61. Ono, R. *et al.* Disruption of Sept6, a fusion partner gene of MLL, does not affect ontogeny, leukemogenesis induced by MLL-SEPT6, or phenotype induced by the loss of Sept4. *Mol. Cell. Biol.* **25,** 10965–78 (2005).

62. Lin, Y. H. *et al.* The expression level of septin12 is critical for spermiogenesis. *Am. J. Pathol.* **174,** 1857–1868 (2009).

63. Lin, Y. H. *et al.* SEPT12 deficiency causes sperm nucleus damage and developmental

arrest of preimplantation embryos. *Fertil. Steril.* **95,** 363–365 (2011).

64. Gallop, J. L. *et al.* Mechanism of endophilin N-BAR domain-mediated membrane curvature. *EMBO J.* **25,** 2898–2910 (2006).

65. Bonifacino, J. S. & Glick, B. S. The Mechanisms of Vesicle Budding and Fusion. *Cell* **116,** 153–166 (2004).

66. Beites, C. L., Xie, H., Bowser, R. & Trimble, W. S. The septin CDCrel-1 binds syntaxin and inhibits exocytosis. *Nat. Neurosci.* **2,** 434–439 (1999).

67. Beites, C. L., Campbell, K. A. & Trimble, W. S. The septin Sept5/CDCrel-1 competes with alpha-SNAP for binding to the SNARE complex. *Biochem. J.* **385,** 347–53 (2005).

68. Ihara, M. *et al.* Sept4, a Component of Presynaptic Scaffold and Lewy Bodies, Is Required for the Suppression of α-Synuclein Neurotoxicity. *Neuron* **53,** 519–533 (2007).

69. Dolat, L. & Spiliotis, E. T. Septins promote macropinosome maturation and traffic to the lysosome by facilitating membrane fusion. *J. Cell Biol.* **214,** 517–527 (2016).

70. Tokhtaeva, E. *et al.* Septin dynamics are essential for exocytosis. *J. Biol. Chem.* **290,** 5280–8297 (2015).

71. Gilden, J. K., Peck, S., Chen, Y. C. M. & Krummel, M. F. The septin cytoskeleton facilitates membrane retraction during motility and blebbing. *J. Cell Biol.* **196,** 103–114 (2012).

72. Patzig, J. *et al.* Septin/anillin filaments scaffold central nervous system myelin to accelerate nerve conduction. *Elife* **5,** 1–21 (2016).

73. Goebbels, S. *et al.* Elevated Phosphatidylinositol 3,4,5-Trisphosphate in Glia Triggers Cell-Autonomous Membrane Wrapping and Myelination. *J. Neurosci.* **30,** 8953–8964 (2010).

74. Østevold, K. *et al.* Septin remodeling is essential for the formation of cell membrane protrusions (microtentacles) in detached tumor cells. *Oncotarget* **8,** 76686–76698 (2017).

75. Heasley, L. R. & McMurray, M. A. Roles of septins in prospore membrane morphogenesis and spore wall assembly in Saccharomyces cerevisiae. *Mol. Biol. Cell* **27,** 442–450 (2016).

76. Takizawa, P. A., DeRisi, J. L., Wilhelm, J. E. & Vale, R. D. Plasma membrane compartmentalization in yeast by messenger RNA transport and a septin diffusion barrier. *Science (80-. ).* **290,** 341–344 (2000).

77. Barral, Y., Mermall, V., Mooseker, M. S. & Snyder, M. Compartmentalization of the cell cortex by septins is required for maintenance of cell polarity in yeast. *Mol. Cell* **5,** 841–851 (2000).

78. Clay, L. *et al.* A sphingolipid-dependent diffusion barrier confines ER stress to the yeast mother cell. *Elife* **3,** (2014).

79. Kwitny, S., Klaus, A. V. & Hunnicutt, G. R. The Annulus of the Mouse Sperm Tail Is Required to Establish a Membrane Diffusion Barrier That Is Engaged During the Late Steps of Spermiogenesis1. *Biol. Reprod.* **82,** 669–678 (2010).

80. Mostowy, S. & Cossart, P. Septins: the fourth component of the cytoskeleton. *Nat. Rev. Mol. Cell Biol.* (2012). doi:10.1038/nrm3284

81. Kinoshita, M., Field, C. M., Coughlin, M. L., Straight, A. F. & Mitchison, T. J. Self- and actin-templated assembly of mammalian septins. *Dev. Cell* **3,** 791–802 (2002).

82. Mavrakis, M. *et al.* Septins promote F-actin ring formation by crosslinking actin filaments into curved bundles. *Nat. Cell Biol.* **16,** 322–334 (2014).

83. Schmidt, K. & Nichols, B. J. Functional interdependence between septin and actin cytoskeleton. *BMC Cell Biol.* **5,** 43 (2004).

84. Norden, C., Liakopoulos, D. & Barral, Y. Dissection of septin actin interactions using actin overexpression in Saccharomyces cerevisiae. *Mol. Microbiol.* **53,** 469–483 (2004).

85. Verdier-Pinard, P. *et al.* Septin 9-i2 is downregulated in tumors, impairs cancer cell migration and alters subnuclear actin filaments. *Sci. Rep.* **7,** 1–18 (2017).

86. Osaka, M., Rowley, J. D. & Zeleznik-Le, N. J. MSF (MLL septin-like fusion), a fusion partner gene of MLL, in a therapy-related acute myeloid leukemia with a t(11;17)(q23;q25). *Proc. Natl. Acad. Sci. U. S. A.* **96,** 6428–33 (1999).

87. Kalikin, L. M., Sims, H. L. & Petty, E. M. Genomic and Expression Analyses of Alternatively Spliced Transcripts of the MLL Septin-like Fusion Gene (MSF) That Map to a 17q25 Region of Loss in Breast and Ovarian Tumors. *Genomics* **63,** 165–172 (2000).

88. Hu, J. *et al.* Septin-Driven Coordination of Actin and Microtubule Remodeling Regulates the Collateral Branching of Axons. *Curr. Biol.* **22,** 1109–1115 (2012).

89. Mizutani, Y. *et al.* Possible role of a septin, SEPT1, in spreading in squamous cell carcinoma DJM-1 cells. *Biol. Chem.* **394,** (2013).

90. Huang, Y.-W. *et al.* Mammalian Septins Are Required for Phagosome Formation. *Mol. Biol. Cell* **19,** 1717–1726 (2008).

91. Smith, C. *et al.* Septin 9 Exhibits Polymorphic Binding to F-Actin and Inhibits Myosin and Cofilin Activity. *J. Mol. Biol.* **427,** 3273–3284 (2015).

92. Tojkander, S., Gateva, G., Husain, A., Krishnan, R. & Lappalainen, P. Generation of contractile actomyosin bundles depends on mechanosensitive actin filament assembly and disassembly. *Elife* **4,** 1–28 (2015).

93. Bowen, J. R., Hwang, D., Bai, X., Roy, D. & Spiliotis, E. T. Septin GTPases spatially guide microtubule organization and plus end dynamics in polarizing epithelia. *J. Cell Biol.* **194,** 187–197 (2011).

94. Menon, M. B. *et al.* Genetic Deletion of SEPT7 Reveals a Cell Type-Specific Role of Septins in Microtubule Destabilization for the Completion of Cytokinesis. *PLoS Genet.* **10,** e1004558 (2014).

95. Nagata, K. ichi *et al.* Filament formation of MSF-A, a mammalian septin, in human mammary epithelial cells depends on interactions with microtubules. *J. Biol. Chem.* **278,** 18538–18543 (2003).

96. Zhu, M. *et al.* Septin 7 interacts with centromere-associated protein E and is required for its kinetochore localization. *J. Biol. Chem.* **283,** 18916–18925 (2008).

97. Garcia, G. *et al.* Subunit-dependent modulation of septin assembly: Budding yeast septin Shs1 promotes ring and gauze formation. *J. Cell Biol.* **195,** 993–1004 (2011).

98. Bai, X. *et al.* Novel septin 9 repeat motifs altered in neuralgic amyotrophy bind and bundle microtubules. *J. Cell Biol.* **203,** 895–905 (2013).

99. Amos, L. A. & Schlieper, D. in 257–298 (2005). doi:10.1016/S0065-3233(04)71007-4

100. Spiliotis, E. T., Hunt, S. J., Hu, Q., Kinoshita, M. & Nelson, W. J. Epithelial polarity requires septin coupling of vesicle transport to polyglutamylated microtubules. *J. Cell Biol.* **180,** 295–303 (2008).

101. Mains, P. E., Sulston, I. A. & Wood, W. B. Mammalian Septins regulate microtubule stability through interaction with the microtubule-binding protein MAP4. *Genetics* **125,** 351–369 (2005).

102. Drummond, D. R. Regulation of microtubule dynamics by kinesins. *Semin. Cell Dev. Biol.* **22,** 927–934 (2011).

103. Russell, S. E. *et al.* Isolation and mapping of a human septin gene to a region on chromosome 17q, commonly deleted in sporadic epithelial ovarian tumors. *Cancer Res.* **60,** 4729–34 (2000).

104. Scott, M. *et al.* Multimodality expression profiling shows SEPT9 to be overexpressed

in a wide range of human tumours. *Oncogene* **24,** 4688–4700 (2005).

105. Kissel, H., Brown, S., Gorenc, T. & Schile, A. J. Sept4 / ARTS is required for stem cell apoptosis and tumor suppression. *Genes Dev.* 2282–2293 (2010). doi:10.1101/gad.1970110.tumor

106. Montagna, C., Bejerano-sagie, M. & Zechmeister, J. R. Mammalian septins in health and disease. 59–72 (2015). doi:10.2147/RRBC.S59060

107. Bongiovanni, L. *et al.* Bradeion (SEPT4) as a Urinary Marker of Transitional Cell Bladder Cancer: A Real-Time Polymerase Chain Reaction Study of Gene Expression. *J. Urol.* **187,** 2223–2227 (2012).

108. Warren, J. D. *et al.* Septin 9 methylated DNA is a sensitive and specific blood test for colorectal cancer. *BMC Med.* **9,** 133 (2011).

109. Angelis, D. & Spiliotis, E. T. Septin Mutations in Human Cancers. *Front. Cell Dev. Biol.* **4,** 1–17 (2016).

110. Cortez, B. A., Teixeira, P. R., Redick, S., Doxsey, S. & Machado-Santelli, G. M. Multipolar mitosis and aneuploidy after chrysotile treatment: a consequence of abscission failure and cytokinesis regression. *Oncotarget* **7,** 8979–8992 (2016).

111. Diesenberg, K., Beerbaum, M., Fink, U., Schmieder, P. & Krauss, M. SEPT9 negatively regulates ubiquitin-dependent downregulation of EGFR. *J. Cell Sci.* **128,** 397–407 (2015).

112. Marcus, E. A. *et al.* Septin oligomerization regulates persistent expression of ErbB2/HER2 in gastric cancer cells. *Biochem. J.* **473,** 1703–1718 (2016).

113. Füchtbauer, A. *et al.* Septin9 is involved in septin filament formation and cellular stability. *Biol. Chem.* **392,** (2011).

114. Liu, Z., Vong, Q. P., Liu, C. & Zheng, Y. Borg5 is required for angiogenesis by regulating persistent directional migration of the cardiac microvascular endothelial

cells. *Mol. Biol. Cell* **25,** 841–851 (2014).

115. Chacko, A. D. *et al.* SEPT9_v4 expression induces morphological change, increased motility and disturbed polarity. *J. Pathol.* **206,** 458–465 (2005).

116. Shankar, J. *et al.* Pseudopodial actin dynamics control epithelial-mesenchymal transition in metastatic cancer cells. *Cancer Res.* **70,** 3780–3790 (2010).

117. Yeh, Y. T. *et al.* Matrix Stiffness Regulates Endothelial Cell Proliferation through Septin 9. *PLoS One* **7,** 1–13 (2012).

118. Loong, H. H. & Yeo, W. Microtubule-targeting agents in oncology and therapeutic potential in hepatocellular carcinoma. *Onco. Targets. Ther.* **7,** 575–585 (2014).

119. Xu, M. *et al.* Identification of a novel role of Septin 10 in paclitaxel-resistance in cancers through a functional genomics screen. *Cancer Sci.* **103,** 821–827 (2012).

120. Amir, S. & Mabjeesh, N. J. SEPT9_V1 protein expression is associated with human cancer cell resistance to microtubule-disrupting agents. *Cancer Biol. Ther.* **6,** 1926–31 (2007).

121. Froidevaux-Klipfel, L. *et al.* Modulation of septin and molecular motor recruitment in the microtubule environment of the Taxol-resistant human breast cancer cell line MDA-MB-231. *Proteomics* **11,** 3877–3886 (2011).

122. Chacko, A. D. *et al.* Expression of the SEPT9_i4 isoform confers resistance to microtubule-interacting drugs. *Cell. Oncol.* **35,** 85–93 (2012).

123. Larisch, S. *et al.* A novel mitochondrial septin-like protein, ARTS, mediates apoptosis dependent on its P-loop motif. *Nat. Cell Biol.* **2,** 915–921 (2000).

124. Elhasid, R. & Larisch, S. ARTS-based anticancer therapy: taking aim at cancer stem cells. *Futur. Oncol.* **7,** 1185–1194 (2011).

125. Zhang, Y. *et al.* Parkin functions as an E2-dependent ubiquitin- protein ligase and

promotes the degradation of the synaptic vesicle-associated protein, CDCrel-1. *Proc. Natl. Acad. Sci.* **97,** 13354–13359 (2000).

126. Son, J. H. *et al.* Neurotoxicity and behavioral deficits associated with Septin 5 accumulation in dopaminergic neurons. *J. Neurochem.* **94,** 1040–1053 (2005).

127. Ihara, M. *et al.* Association of the Cytoskeletal GTP-binding Protein Sept4/H5 with Cytoplasmic Inclusions Found in Parkinson's Disease and Other Synucleinopathies. *J. Biol. Chem.* **278,** 24095–24102 (2003).

128. Musunuri, S. *et al.* Quantification of the Brain Proteome in Alzheimer's Disease Using Multiplexed Mass Spectrometry. *J. Proteome Res.* **13,** 2056–2068 (2014).

129. Kinoshita, A. *et al.* Identification of Septins in Neurofibrillary Tangles in Alzheimer's Disease. *Am. J. Pathol.* **153,** 1551–1560 (1998).

130. Pissuti Damalio, J. C. *et al.* Self assembly of human septin 2 into amyloid filaments. *Biochimie* **94,** 628–636 (2012).

131. Garcia, W. *et al.* An Intermediate Structure in the Thermal Unfolding of the GTPase Domain of Human Septin 4 (SEPT4/Bradeion-β) Forms Amyloid-like Filaments in Vitro †. *Biochemistry* **46,** 11101–11109 (2007).

132. Mostowy, S. *et al.* Septins regulate bacterial entry into host cells. *PLoS One* **4,** (2009).

133. Mostowy, S. *et al.* Septins Regulate Bacterial Entry into Host Cells. *PLoS One* **4,** e4196 (2009).

134. Weiner, A. *et al.* Macropinosomes are Key Players in Early Shigella Invasion and Vacuolar Escape in Epithelial Cells. *PLOS Pathog.* **12,** e1005602 (2016).

135. Mostowy, S. *et al.* Entrapment of intracytosolic bacteria by septin cage-like structures. *Cell Host Microbe* **8,** 433–444 (2010).

136. Sirianni, A. *et al.* Mitochondria mediate septin cage assembly to promote autophagy of

*Shigella*. *EMBO Rep.* **17,** 1029–1043 (2016).

137. Mostowy, S. *et al.* The Zebrafish as a New Model for the In Vivo Study of Shigella flexneri Interaction with Phagocytes and Bacterial Autophagy. *PLoS Pathog.* **9,** 12–16 (2013).

138. Kumar, Y. & Valdivia, R. H. Actin and Intermediate Filaments Stabilize the Chlamydia trachomatis Vacuole by Forming Dynamic Structural Scaffolds. *Cell Host Microbe* **4,** 159–169 (2008).

139. Volceanov, L. *et al.* Septins arrange F-Actin-Containing fibers on the chlamydia trachomatis inclusion and are required for normal release of the inclusion by extrusion. *MBio* **5,** 1–12 (2014).

140. McMurray, M. A. *et al.* Septin Filament Formation Is Essential in Budding Yeast. *Dev. Cell* **20,** 540–549 (2011).

141. Bertin, A. *et al.* Three-dimensional ultrastructure of the septin filament network in Saccharomyces cerevisiae. *Mol. Biol. Cell* **23,** 423–432 (2012).

142. Bertin, A. & Nogales, E. in **1369,** 113–123 (2016).

143. Vissa, A. *et al.* Single-molecule localization microscopy of septin bundles in mammalian cells. *Cytoskeleton* (2018). doi:10.1002/cm.21481

144. Kaplan, C. *et al.* Absolute Arrangement of Subunits in Cytoskeletal Septin Filaments in Cells Measured by Fluorescence Microscopy. *Nano Lett.* **15,** 3859–3864 (2015).

145. Vrabioiu, A. M. & Mitchison, T. J. Structural insights into yeast septin organization from polarized fluorescence microscopy. *Nature* **443,** 466–469 (2006).

146. Willis, A., Mazon-Moya, M. & Mostowy, S. *Investigation of septin biology in vivo using zebrafish*. *Methods in Cell Biology* **136,** (Elsevier Ltd, 2016).

147. Ong, K., Wloka, C., Okada, S., Svitkina, T. & Bi, E. Architecture and dynamic

remodelling of the septin cytoskeleton during the cell cycle. *Nat. Commun.* **5,** 5698 (2014).

148. McQuilken, M. *et al.* Analysis of Septin Reorganization at Cytokinesis Using Polarized Fluorescence Microscopy. *Front. Cell Dev. Biol.* **5,** 1–14 (2017).

149. Takahashi, Y. *et al.* Smt3, a SUMO-1 homolog, is conjugated to Cdc3, a component of septin rings at the mother-bud neck in budding yeast. *Biochem. Biophys. Res. Commun.* **259,** 582–587 (1999).

150. Johnson, E. S. & Blobel, G. Cell cycle-regulated attachment of the ubiquitin-related protein SUMO to the yeast septins. *J. Cell Biol.* **147,** 981–94 (1999).

151. Ribet, D. *et al.* SUMOylation of human septins is critical for septin filament bundling and cytokinesis. *J. Cell Biol.* **216,** 4041–4052 (2017).

152. Mitchell, L. *et al.* Regulation of Septin Dynamics by the Saccharomyces cerevisiae Lysine Acetyltransferase NuA4. *PLoS One* **6,** e25336 (2011).

153. Garcia, W. *et al.* Dissection of a Human Septin: Definition and Characterization of Distinct Domains within Human SEPT4. *Biochemistry* **45,** 13918–13931 (2006).

154. Sirajuddin, M. *et al.* Structural insight into filament formation by mammalian septins. *Nature* **449,** 311–315 (2007).

155. Zhang, J. *et al.* Phosphatidylinositol polyphosphate binding to the mammalian septin H5 is modulated by GTP. *Curr. Biol.* **9,** 1458–1467 (1999).

156. Weems, A. D. & McMurray, M. A. The step-wise pathway of septin hetero-octamer assembly in budding yeast. *Elife* **6,** (2017).

157. Sirajuddin, M., Farkasovsky, M., Zent, E. & Wittinghofer, A. GTP-induced conformational changes in septins and implications for function. *Proc. Natl. Acad. Sci. U. S. A.* **106,** 16592–7 (2009).

158. Weems, A. D., Johnson, C. R., Argueso, J. L. & McMurray, M. A. Higher-order septin assembly is driven by GTP-promoted conformational changes: Evidence from unbiased mutational analysis in Saccharomyces cerevisiae. *Genetics* **196,** 711–727 (2014).

159. Mendoza, M., Hyman, A. A. & Glotzer, M. GTP binding induces filament assembly of a recombinant septin. *Curr. Biol.* **12,** 1858–1863 (2002).

160. Versele, M. & Thorner, J. Septin collar formation in budding yeast requires GTP binding and direct phosphorylation by the PAK, Cla4. *J. Cell Biol.* **164,** 701–715 (2004).

161. Abbey, M. *et al.* GTPase domain driven dimerization of SEPT7 is dispensable for the critical role of septins in fibroblast cytokinesis. *Sci. Rep.* **6,** 1–15 (2016).

162. Huang, Y. W., Surka, M. C., Reynaud, D., Pace-Asciak, C. & Trimble, W. S. GTP binding and hydrolysis kinetics of human septin 2. *FEBS J.* **273,** 3248–3260 (2006).

163. Khan, A., Newby, J. & Gladfelter, A. S. Control of septin filament flexibility and bundling by subunit composition and nucleotide interactions. *Mol. Biol. Cell* **29,** 702–712 (2018).

164. Sala, F. A., Valadares, N. F., Macedo, J. N. A., Borges, J. C. & Garratt, R. C. Heterotypic Coiled-Coil Formation is Essential for the Correct Assembly of the Septin Heterofilament. *Biophys. J.* **111,** 2608–2619 (2016).

165. Bertin, A. *et al.* Saccharomyces cerevisiae septins: supramolecular organization of heterooligomers and the mechanism of filament assembly. *Proc. Natl. Acad. Sci. U. S. A.* **105,** 8274–8279 (2008).

166. de Almeida Marques, I. *et al.* Septin C-Terminal Domain Interactions: Implications for Filament Stability and Assembly. *Cell Biochem. Biophys.* **62,** 317–328 (2012).

167. John, C. M. *et al.* The Caenorhabditis elegans septin complex is nonpolar. *EMBO J.* **26,** 3296–3307 (2007).

168. Unit, C. B. Septins. **496,** 491–496 (2003).

169. Frazier, J. A. *et al.* Polymerization of purified yeast septins: Evidence that organized filament arrays may not be required for septin function. *J. Cell Biol.* **143,** 737–749 (1998).

170. Versele, M. *et al.* Protein–Protein Interactions Governing Septin Heteropentamer Assembly and Septin Filament Organization in Saccharomyces cerevisiae. *Mol. Biol. Cell* **15,** 4568–4583 (2004).

171. Xie, H., Surka, M., Howard, J. & Trimble, W. S. Characterization of the mammalian septin H5: Distinct patterns of cytoskeletal and membrane association from other septin proteins. *Cell Motil. Cytoskeleton* **43,** 52–62 (1999).

172. Casamayor, A. & Snyder, M. Molecular dissection of a yeast septin: distinct domains are required for septin interaction, localization, and function. *Mol. Cell. Biol.* **23,** 2762–2777 (2003).

173. Bertin, A. *et al.* Phosphatidylinositol-4,5-bisphosphate Promotes Budding Yeast Septin Filament Assembly and Organization. *J. Mol. Biol.* **404,** 711–731 (2010).

174. Bridges, A. A. *et al.* Septin assemblies form by diffusion-driven annealing on membranes. *Proc. Natl. Acad. Sci.* **111,** 2146–2151 (2014).

175. Rothwell, S. W., Grasser, W. A. & Murphy, D. B. End-to-end annealing of microtubules in vitro. *J. Cell Biol.* **102,** 619–627 (1986).

176. Murphy, D. B., Gray, R. O., Grasser, W. A. & Pollard, T. D. Direct demonstration of actin filament annealing in vitro. *J. Cell Biol.* **106,** 1947–1954 (1988).

177. Bridges, A. A., Jentzsch, M. S., Oakes, P. W., Occhipinti, P. & Gladfelter, A. S. Micron-scale plasma membrane curvature is recognized by the septin cytoskeleton. *J. Cell Biol.* jcb.201512029 (2016). doi:10.1083/jcb.201512029

178. Zhu, C., Das, S. L. & Baumgart, T. Nonlinear sorting, curvature generation, and

crowding of endophilin N-BAR on tubular membranes. *Biophys. J.* **102,** 1837–1845 (2012).

179. Shi, Z., Sachs, J. N., Rhoades, E. & Baumgart, T. Biophysics of α-synuclein induced membrane remodelling. *Phys. Chem. Chem. Phys.* **17,** 15561–15568 (2015).

180. Tanaka-Takiguchi, Y., Kinoshita, M. & Takiguchi, K. Septin-Mediated Uniform Bracing of Phospholipid Membranes. *Curr. Biol.* **19,** 140–145 (2009).

181. Tolias, K. F. & Cantley, L. C. Pathways for phosphoinositide synthesis. *Chem. Phys. Lipids* **98,** 69–77 (1999).

182. Rameh, L. E., Tolias, K. F., Duckworth, B. C. & Cantley, L. C. A new pathway for synthesis of phosphatidylinositol-4,5-bisphosphate. *Nature* **390,** 192–196 (1997).

183. Desrivières, S., Cooke, F. T., Parker, P. J. & Hall, M. N. MSS4, a phosphatidylinositol-4-phosphate 5-kinase required for organization of the actin cytoskeleton in Saccharomyces cerevisiae. *J. Biol. Chem.* **273,** 15787–93 (1998).

184. Yamamoto, A. *et al.* Novel PI(4)P 5-kinase homologue, Fab1p, essential for normal vacuole function and morphology in yeast. *Mol. Biol. Cell* **6,** 525–39 (1995).

185. Berridge, M. J. & Irvine, R. F. Inositol phosphates and cell signalling. *Nature* **341,** 197–205 (1989).

186. Hilgemann, D. W., Feng, S. & Nasuhoglu, C. The Complex and Intriguing Lives of PIP2 with Ion Channels and Transporters. *Sci. Signal.* **2001,** re19-re19 (2001).

187. Suh, B.-C. & Hille, B. Regulation of ion channels by phosphatidylinositol 4,5-bisphosphate. *Curr. Opin. Neurobiol.* **15,** 370–378 (2005).

188. Padrón, D., Wang, Y. J., Yamamoto, M., Yin, H. & Roth, M. G. Phosphatidylinositol phosphate 5-kinase Iβ recruits AP-2 to the plasma membrane and regulates rates of constitutive endocytosis. *J. Cell Biol.* **162,** 693–701 (2003).

189. Boucrot, E., Saffarian, S., Massol, R., Kirchhausen, T. & Ehrlich, M. Role of lipids and actin in the formation of clathrin-coated pits. *Exp. Cell Res.* **312,** 4036–4048 (2006).

190. Botelho, R. J. *et al.* Localized biphasic changes in phosphatidylinositol-4,5-bisphosphate at sites of phagocytosis. *J. Cell Biol.* **151,** 1353–68 (2000).

191. Haga, Y., Miwa, N., Jahangeer, S., Okada, T. & Nakamura, S. CtBP1/BARS is an activator of phospholipase D1 necessary for agonist-induced macropinocytosis. *EMBO J.* **28,** 1197–1207 (2009).

192. Hoeller, O. *et al.* Two distinct functions for PI3-kinases in macropinocytosis. *J. Cell Sci.* **126,** 4296–4307 (2013).

193. Eze, M. O. Phase transitions in phospholipid bilayers: Lateral phase separations play vital roles in biomembranes. *Biochem. Educ.* **19,** 204–208 (1991).

194. Dietrich, C., Volovyk, Z. N., Levi, M., Thompson, N. L. & Jacobson, K. Partitioning of Thy-1, GM1, and cross-linked phospholipid analogs into lipid rafts reconstituted in supported model membrane monolayers. *Proc. Natl. Acad. Sci.* **98,** 10642–10647 (2001).

195. W. Helfrich. Elastic Properties of Lipid Bilayers—Theory and Possible Experiments. *Zeitschrift fur Naturforsch. Tl. C Biochem. Biophys. Biol. Virol.* **28,** 693–703 (1973).

196. Rawicz, W., Olbrich, K. C., McIntosh, T., Needham, D. & Evans, E. Effect of chain length and unsaturation on elasticity of lipid bilayers. *Biophys. J.* **79,** 328–339 (2000).

197. Sackmann, E. Molecular and global structure and dynamics of membranes and lipid bilayers. *Can. J. Phys.* **68,** 999–1011 (1990).

198. Kwok, R. & Evans, E. Thermoelasticity of large lecithin bilayer vesicles. *Biophys. J.* **35,** 637–652 (1981).

199. Olbrich, K., Rawicz, W., Needham, D. & Evans, E. Water Permeability and Mechanical Strength of Polyunsaturated Lipid Bilayers. *Biophys. J.* **79,** 321–327 (2000).

200. Evans, E. & Rawicz, W. Entropy-driven tension and bending elasticity in condensed-fluid membranes. *Phys. Rev. Lett.* **64,** 2094–2097 (1990).

201. Helfrich, W. & Servuss, R. M. Undulations, steric interaction and cohesion of fluid membranes. *Nuovo Cim. D* **3,** 137–151 (1984).

202. Fricke, K., Wirthensohn, K., Laxhuber, R. & Sackmann, E. Flicker spectroscopy of erythrocytes. *Eur. Biophys. J.* **14,** 67–81 (1986).

203. Esposito, C. *et al.* Flicker Spectroscopy of Thermal Lipid Bilayer Domain Boundary Fluctuations. *Biophys. J.* **93,** 3169–3181 (2007).

204. Lasic, D. D. & Martin, F. J. On the mechanism of vesicle formation. *J. Memb. Sci.* **50,** 215–222 (1990).

205. Szoka, F. AND METHODS OF PREPARATION OF LIPID VESICLES ( LIPOSOMES ) l. *Cancer Res.* 467–508 (1980). doi:10.1073/pnas.73.11.3862

206. Dietrich, C. *et al.* Lipid rafts reconstituted in model membranes. *Biophys. J.* **80,** 1417–1428 (2001).

207. Richter, R. P., Bérat, R. & Brisson, A. R. Formation of solid-supported lipid bilayers: An integrated view. *Langmuir* **22,** 3497–3505 (2006).

208. Reeves, J. P. & Dowben, R. M. Formation and properties of thin- walled phospholipid vesicles. *J. Cell. Physiol.* **73,** 49–60 (1969).

209. Kirchner, S. R. *et al.* Membrane composition of jetted lipid vesicles: A Raman spectroscopy study. *J. Biophotonics* **5,** 40–46 (2012).

210. Shum, H. C., Lee, D., Yoon, I., Kodger, T. & Weitz, D. A. Double emulsion templated monodisperse phospholipid vesicles. *Langmuir* **24,** 7651–7653 (2008).

211. van Swaay, D. & deMello, A. Microfluidic methods for forming liposomes. *Lab Chip* **13,** 752 (2013).

212. Blosser, M. C., Horst, B. G. & Keller, S. L. cDICE method produces giant lipid vesicles under physiological conditions of charged lipids and ionic solutions. *Soft Matter* **12,** 7364–71 (2016).

213. Brian, A. A. & McConnell, H. M. Allogeneic stimulation of cytotoxic T cells by supported planar membranes. *Proc. Natl. Acad. Sci.* **81,** 6159–6163 (1984).

214. Ekeroth, J., Konradsson, P. & Höök, F. Bivalent-Ion-Mediated Vesicle Adsorption and Controlled Supported Phospholipid Bilayer Formation on Molecular Phosphate and Sulfate Layers on Gold. *Langmuir* **18,** 7923–7929 (2002).

215. Richter, R. P. & Brisson, A. R. Following the formation of supported lipid bilayers on mica: a study combining AFM, QCM-D, and ellipsometry. *Biophys. J.* **88,** 3422–33 (2005).

216. Ashkin, A. Acceleration and Trapping of Particles by Radiation Pressure. *Phys. Rev. Lett.* **24,** 156–159 (1970).

217. Van Der Honing, H. S., De Ruijter, N. C. A., Mie, A., Emons, C. & Ketelaar, T. Actin and myosin regulate cytoplasm stiffness in plant cells: a study using optical tweezers. *New Phytol.* **185,** 90–102 (2010).

218. Murai, S. *et al.* © 19 9 3 Nature Publishing Group. *Nature* **366,** 529–531 (1993).

219. Wang, M. D., Yin, H., Landick, R., Gelles, J. & Block, S. M. Stretching DNA with optical tweezers. *Biophys. J.* **72,** 1335–1346 (1997).

220. Cuvelier, D., Chiaruttini, N., Bassereau, P. & Nassoy, P. Pulling long tubes from firmly adhered vesicles. *Europhys. Lett.* **71,** 1015–1021 (2005).

221. Zhang, H. & Liu, K. K. Optical tweezers for single cells. *J. R. Soc. Interface* **5,** 671–690 (2008).

222. Shi, Z. & Baumgart, T. Membrane tension and peripheral protein density mediate membrane shape transitions. *Nat. Commun.* **6,** 5974 (2015).

223. Prévost, C. *et al.* IRSp53 senses negative membrane curvature and phase separates along membrane tubules. *Nat. Commun.* **6,** 8529 (2015).

224. Roux, A. *et al.* Membrane curvature controls dynamin polymerization. *Proc. Natl. Acad. Sci.* **107,** 4141–4146 (2010).

225. Heinrich, M., Tian, A., Esposito, C. & Baumgart, T. Dynamic sorting of lipids and proteins in membrane tubes with a moving phase boundary. *Proc. Natl. Acad. Sci.* **107,** 7208–7213 (2010).

226. Arumugam, S. *et al.* Surface Topology Engineering of Membranes for the Mechanical Investigation of the Tubulin Homologue FtsZ. *Angew. Chemie Int. Ed.* **51,** 11858–11862 (2012).

227. Baumann, E. Lipid Bilayers on Planes and in Micropipettes - Two model systems to study binding of DivIVA to flat and negatively curved membranes. (Lund university, 2016).

228. Hsieh, W.-T. *et al.* Curvature Sorting of Peripheral Proteins on Solid-Supported Wavy Membranes. *Langmuir* **28,** 12838–12843 (2012).

229. Galic, M. *et al.* External push and internal pull forces recruit curvature-sensing N-BAR domain proteins to the plasma membrane. *Nat. Cell Biol.* **14,** 874–881 (2012).

230. Bayley, F. A., Liao, J. L., Stavrinou, P. N., Chiche, A. & Cabral, J. T. Wavefront Kinetics of Plasma Oxidation of Polydimethylsiloxane: Limits for Sub-μm Wrinkling. *Soft Matter* **10,** 1155–66 (2014).

231. Nania, M., Matar, O. K. & Cabral, J. T. Frontal vitrification of PDMS using air plasma and consequences for surface wrinkling. *Soft Matter* 3067–3075 (2015). doi:10.1039/C4SM02840F

232. Chiche, A., Stafford, C. M. & Cabral, J. T. Complex micropatterning of periodic structures on elastomeric surfaces. *Soft Matter* **4,** 2360 (2008).

233. Zhu, T. F., Budin, I. & Szostak, J. W. Preparation of Fatty Acid Amides.Pdf. *Methods Enzymol.* **533,** 267–274 (2013).

234. Okumura, Y. & Iwata, Y. Electroformation of giant vesicles on indium tin oxide (ITO)-coated poly(ethylene terephthalate) (PET) electrodes. *Membranes (Basel).* **1,** 109–118 (2011).

235. Rodriguez, N., Pincet, F. & Cribier, S. Giant vesicles formed by gentle hydration and electroformation: A comparison by fluorescence microscopy. *Colloids Surfaces B Biointerfaces* **42,** 125–130 (2005).

236. Montes, L. R., Alonso, A., Goñi, F. M. & Bagatolli, L. A. Giant unilamellar vesicles electroformed from native membranes and organic lipid mixtures under physiological conditions. *Biophys. J.* **93,** 3548–3554 (2007).

237. Angelova, M. I. & Dimitrov, D. S. Liposome Electro formation. *Faraday Discuss. Chem. SOC* **81,** 303–311 (1986).

238. Horger, K. S., Estes, D. J., Capone, R. & Mayer, M. Films of Agarose Enable Rapid Formation of Giant Liposomes in Solutions of Physiologic Ionic Strength. *J. Am. Chem. Soc.* **131,** 1810–1819 (2009).

239. Weinberger, A. *et al.* Gel-assisted formation of giant unilamellar vesicles. *Biophys. J.* **105,** 154–164 (2013).

240. Sorre, B. Role of Membrane Curvature in Intracellular Traficking. (2010).

241. Galush, W. J., Nye, J. A. & Groves, J. T. Quantitative fluorescence microscopy using supported lipid bilayer standards. *Biophys. J.* **95,** 2512–2519 (2008).

242. Nagle, J. F. & Tristram-Nagle, S. Structure of lipid bilayers. *Biochim. Biophys. Acta - Rev. Biomembr.* **1469,** 159–195 (2000).

243. Beber, A. *et al.* Septin-based readout of PI(4,5)P2 incorporation into membranes of giant unilamellar vesicles. *Cytoskeleton* (2018). doi:10.1002/cm.21480

244. Pawelczyk, T. & Lowensteint, J. M. Binding of phospholipase C51 to phospholipid vesicles. *Biochem. J.* **291,** 693–696 (1993).

245. Roy, A., Dutta, R., Kundu, N., Banik, D. & Sarkar, N. A Comparative Study of the Influence of Sugars Sucrose, Trehalose, and Maltose on the Hydration and Diffusion of DMPC Lipid Bilayer at Complete Hydration: Investigation of Structural and Spectroscopic Aspect of Lipid–Sugar Interaction. *Langmuir* **32,** 5124–5134 (2016).

246. Houen, G. & Hansen, K. Interference of sugars with the binding of biotin to streptavidin and avidin. *J. Immunol. Methods* **210,** 115–123 (1997).

247. Reis, A. & Spickett, C. M. Chemistry of phospholipid oxidation. *Biochim. Biophys. Acta - Biomembr.* **1818,** 2374–2387 (2012).

248. Pranke, I. M. *et al.* -Synuclein and ALPS motifs are membrane curvature sensors whose contrasting chemistry mediates selective vesicle binding. *J. Cell Biol.* **194,** 89–103 (2011).

249. Jiang, Z., de Messieres, M. & Lee, J. C. Membrane remodeling by alpha-synuclein and effects on amyloid formation. *J Am Chem Soc* **135,** 15970–15973 (2013).

250. Lee, K. I., Im, W. & Pastor, R. W. Langevin dynamics simulations of charged model phosphatidylinositol lipids in the presence of diffusion barriers: Toward an atomic level understanding of corralling of PIP<inf>2</inf> by protein fences in biological membranes. *BMC Biophys.* **7,** 3–12 (2014).

251. Dieluweit, S. *et al.* Mechanical properties of bare and protein-coated giant unilamellar phospholipid vesicles. A comparative study of micropipet aspiration and atomic force microscopy. *Langmuir* **26,** 11041–11049 (2010).

252. Tang, J. X. & Janmey, P. A. The polyelectrolyte nature of F-actin and the mechanism of actin bundle formation. *J. Biol. Chem.* **271,** 8556–8563 (1996).

253. Marrington, R., Small, E., Rodger, A., Dafforn, T. R. & Addinall, S. G. FtsZ fiber bundling is triggered by a conformational change in bound GTP. *J. Biol. Chem.* **279,**

48821–48829 (2004).

254. Rebecchi, M., Peterson, a & McLaughlin, S. Phosphoinositide-specific phospholipase C-delta 1 binds with high affinity to phospholipid vesicles containing phosphatidylinositol 4,5-bisphosphate. *Biochemistry* **31,** 12742–12747 (1992).

255. Catimel, B. *et al.* The PI(3,5)P2 and PI(4,5)P2 Interactomes. *J. Proteome Res.* **7,** 5295–5313 (2008).

256. Saleem, M. *et al.* A balance between membrane elasticity and polymerization energy sets the shape of spherical clathrin coats. *Nat. Commun.* **6,** 6249 (2015).

257. Csiszár, A., Hoffmann, B. & Merkel, R. Double-shell giant vesicles mimicking gram-negative cell wall behavior during dehydration. *Langmuir* **25,** 5753–5761 (2009).

258. Awasthi, N. & Hub, J. S. Simulations of Pore Formation in Lipid Membranes: Reaction Coordinates, Convergence, Hysteresis, and Finite-Size E ff ects. (2016). doi:10.1021/acs.jctc.6b00369

259. Meng, F. & Terentjev, E. M. Theory of semiflexible filaments and networks. *Polymers (Basel).* **9,** 1–28 (2017).

260. Heussinger, C. & Frey, E. Floppy modes and nonaffine deformations in random fiber networks. *Phys. Rev. Lett.* **97,** (2006).

261. Heussinger, C., Schaefer, B. & Frey, E. Nonaffine rubber elasticity for stiff polymer networks. *Phys. Rev. E - Stat. Nonlinear, Soft Matter Phys.* **76,** 1–12 (2007).

262. Cabré, E. J. *et al.* Bacterial Division Proteins FtsZ and ZipA Induce Vesicle Shrinkage and Cell Membrane Invagination. *J. Biol. Chem.* **288,** 26625–26634 (2013).

263. Osawa, M., Anderson, D. E. & Erickson, H. P. Curved FtsZ protofilaments generate bending forces on liposome membranes. *EMBO J.* **28,** 3476–3484 (2009).

264. Cannon, K. S., Woods, B. L., Crutchley, J. M. & Gladfelter, A. S. An amphipathic helix

enables septins to sense micron-scale membrane curvature. *bioRxiv* 379982 (2018). doi:10.1101/379982

265. Ursell, T. S. *et al.* Rod-like bacterial shape is maintained by feedback between cell curvature and cytoskeletal localization. *Proc. Natl. Acad. Sci.* **111,** E1025–E1034 (2014).

266. Hussain, S. *et al.* MreB filaments align along greatest principal membrane curvature to orient cell wall synthesis. *Elife* **7,** (2018).

267. Arumugam, S. *et al.* Surface topology engineering of membranes for the mechanical investigation of the tubulin homologue FtsZ. *Angew. Chemie - Int. Ed.* **51,** 11858–11862 (2012).

268. Kumar, G., Ramakrishnan, N. & Sain, A. Spontaneous tubulation of membrane vesicles coated with bio-active filaments. *arXiv* 1–8 (2018).

269. Fujiwara, T., Ritchie, K., Murakoshi, H., Jacobson, K. & Kusumi, A. Phospholipids undergo hop diffusion in compartmentalized cell membrane. *J. Cell Biol.* **157,** 1071–1081 (2002).

270. Funakoshi, K., Suzuki, H. & Takeuchi, S. Formation of giant lipid vesiclelike compartments from a planar lipid membrane by a pulsed jet flow. *J. Am. Chem. Soc.* **129,** 12608–12609 (2007).

271. Hönscher, C. & Ungermann, C. A close-up view of membrane contact sites between the endoplasmic reticulum and the endolysosomal system: From yeast to man. *Crit. Rev. Biochem. Mol. Biol.* **49,** 262–268 (2014).

272. Rowland, A. A. & Voeltz, G. K. Endoplasmic reticulum-mitochondria contacts: Function of the junction. *Nat. Rev. Mol. Cell Biol.* **13,** 607–615 (2012).

273. Paszek, M. J. *et al.* The cancer glycocalyx mechanically primes integrin-mediated growth and survival. *Nature* **511,** 319–325 (2014).

274. Guigas, G. & Weiss, M. Effects of protein crowding on membrane systems. *Biochim. Biophys. Acta - Biomembr.* **1858,** 2441–2450 (2016).

275. McLaughlin, S. & Murray, D. Plasma membrane phosphoinositide organization by protein electrostatics. *Nature* **438,** 605–611 (2005).

276. van den Bogaart, G. *et al.* Membrane protein sequestering by ionic protein–lipid interactions. *Nature* **479,** 552–555 (2011).

277. Lingwood, D. & Simons, K. Lipid Rafts As a Membrane-Organizing Principle. *Science (80-. ).* **327,** 46–50 (2010).

278. Sorre, B. *et al.* Nature of curvature coupling of amphiphysin with membranes depends on its bound density. *Proc. Natl. Acad. Sci. U. S. A.* **109,** 173–8 (2012).

279. Simunovic, M. & Voth, G. A. Membrane tension controls the assembly of curvature-generating proteins. *Nat Commun* **6,** 7219 (2015).

280. Bigay, J. & Antonny, B. Curvature, Lipid Packing, and Electrostatics of Membrane Organelles: Defining Cellular Territories in Determining Specificity. *Dev. Cell* **23,** 886–895 (2012).

## Résumé :

Les septines constituent une nouvelle classe de protéines du cytosquelette. Les septines de levure s'auto-assemblent en filaments non-polaires liés à la face interne de la membrane plasmique à travers des interactions spécifiques avec le L- α-phosphatidylinositol-4,5-bisphosphate (PI(4,5)P2. Les septines sont localisées au niveau de sites de constriction durant la cytokinèse et ont un impact sur le remodelage de la membrane. Nous avons utilisé une plage d'outils biomimétiques in vitro pour examiner comment les septines de levure se comportent sur des membranes courbées et déformables.
Des tests in vitro utilisant des Vesicules Unilamellaires Géantes (GUVs) sont des outils pertinents pour obtenir des informations sur l'interaction protéine-lipide, la mécanique de membrane et la sensibilité à la courbure. Obtenir des GUVs dopées au PI(4,5)P2 peut être difficile. Nous avons d'abord optimisé l'incorporation de PI(4,5)P2 dans des GUVs en étudiant l'interaction entre les septines et les GUVs. Nous montrons que cette interaction est plus spécifique qu'en utilisant un rapporteur usuel (phospholipase Cδ1). Nous avons montré que l'électro-formation sur fils de platines est la méthode la plus appropriée pour atteindre une interaction septines-lipides optimale. De plus, nous avons montré que les GUVs contenant du PI(4,5)P2 doivent être utilisées quelques heures après leur préparation. En effet, avec le temps, le PI(4,5)P2 est éjecté de la membrane des GUVs et la concentration de PI(4,5)P2 dans la bicouche diminue.

Ensuite, nous avons analysé comment les septins peuvent contrôler les propriétés mécaniques de la membrane et analysé comment les déformations de la membrane pouvaient être induites par la sensibilité des septines à des courbures spécifiques. En effet, nous avons montré que les septines reforment la membrane de GUVs avec l'apparition de piques périodiques. Nous avons montré que ces déformations sont associées à la préférence de courbure des filaments de septine. En se liant à des bicouches supportées posées sur des substrats possédant un motif ondulé présentant des courbures positives et négatives, les filaments de septine restent droits et perpendiculaires à la courbure aux endroits convexes et se plient négativement pour suivre les géométries concaves. En se basant sur ces résultats, nous proposons un modèle théorique qui décrit quantitativement les déformations et la sensibilité à la courbure micrométrique observée in vitro. Le modèle capture la réorganisation des filaments de septines durant la cytokinèse in vivo, fournissant des informations sur la mécanique de la division cellulaire.


Mots clés : Septines, biophysique, GUV, courbure, membrane.


## Abstract :

Septins constitute a novel class of cytoskeletal proteins. Budding yeast septins self-assemble into non-polar filaments bound to the inner plasma membrane through specific interactions with L- α-phosphatidylinositol-4,5-bisphosphate (PI(4,5)P2). Septins localize at constriction sites during cytokinesis and impact membrane remodeling processes. We have analyzed a range of in vitro biomimetic tools to examine how yeast septins behave on curved and deformable membranes.
In vitro assays using Giant Unilamellar Vesicles (GUVs) are relevant tools to reveal insights in proteins-lipids interactions, membrane mechanics and curvature sensitivity. GUVs doped with PI(4,5)P2 are challenging to prepare. We first optimized the incorporation of PI(4,5)P2 lipids into GUVs by probing the proteins-PI(4,5)P2 GUVs interactions. We show that the interaction between budding yeast septins and PI(4,5)P2 is more specific than using usual reporters (phospholipase Cδ1). We have shown that electro-formation on platinum wires is the most appropriate method to achieve an optimal septin-lipid interaction. Besides, we have shown that PI(4,5)P2 GUVs have to be used within a few hours after their preparation. Indeed, over time, PI(4,5)P2 is expelled from the GUV membrane and the PI(4,5)P2 concentration in the bilayer decreases .

Next, we analyzed how septins can control the mechanical properties of membranes and analyzed how membrane deformations could be induced by a specific curvature sensitivity of septins. Indeed, we have shown that septins reshape the membranes of Giant Unilamellar Vesicles with the formation of periodic spikes. We have shown that membrane deformations are associated to septin filament curvature arrangement preferences. When binding to bilayers supported on custom-designed periodic wavy patterns displaying positive and negative micrometric radii of curvatures, septin filaments remain straight and perpendicular to the curvature of the convex parts, while bending negatively to follow concave geometries. Based on these results, we propose a theoretical model that quantitatively describes the deformations and micrometric curvature sensitivity observed in vitro. The model captures the reorganizations of septin filaments throughout cytokinesis in vivo, providing mechanistic insights into cell division.


Keyword : Septins, biophysics, GUV, curvature, membrane.